

Nonlinear Theoretical Models of Nanofluid with Heat Flux



By

Misbah Ijaz

A THESIS SUBMITTED IN THE PARTIAL FULFILLMENT OF THE REQUIREMENT
FOR THE DEGREE OF
DOCTOR OF PHILOSOPHY
IN
MATHEMATICS

Supervised By

Prof. Dr. Muhammad Ayub

**Department of Mathematics
Quaid-I-Azam University
Islamabad, Pakistan
2019**

Author's Declaration

I, **Misbah Ijaz**, hereby state that my PhD thesis titled **Nonlinear Theoretical Models of Nanofluids with Heat Flux** is my own work and has not been submitted previously by me for taking any degree from the Quaid-I-Azam University Islamabad, Pakistan or anywhere else in the country/world.

At any time if my statement is found to be incorrect even after my graduate the university has the right to withdraw my PhD degree.



Name of Student: **Misbah Ijaz**

Date: **28-Nov-2019**

Plagiarism Undertaking

I solemnly declare that research work presented in the thesis titled "**Nonlinear Theoretical Models of Nanofluids with Heat Flux**" is solely my research work with no significant contribution from any other person. Small contribution/help wherever taken has been duly acknowledged and that complete thesis has been written by me.

I understand the zero tolerance policy of the HEC and **Quaid-i-Azam University** towards plagiarism. Therefore, I as an Author of the above titled thesis declare that no portion of my thesis has been plagiarized and any material used as reference is properly referred/cited.

I undertake that if I am found guilty of any formal plagiarism in the above titled thesis even afterward of PhD degree, the University reserves the rights to withdraw/revoke my PhD degree and that HEC and the University has the right to publish my name on the HEC/University Website on which names of students are placed who submitted plagiarized thesis.



Student/Author Signature

Name: **Misbah Ijaz**

**Nonlinear Theoretical Models of Nanofluids
with Heat Flux**

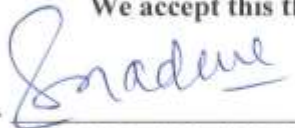
By

Misbah Ijaz

CERTIFICATE


A THESIS SUBMITTED IN THE PARTIAL FULFILLMENT OF THE
REQUIREMENTS FOR THE DEGREE OF THE
DOCTOR OF PHILOSOPHY IN MATHEMATICS

We accept this thesis as conforming to the required standard

1. 
Prof. Dr. Sohail Nadeem
(Chairman)

2. 
Prof. Dr. Muhammad Ayub
(Supervisor)

3. 
Dr. Rahmat Ellahi
(External Examiner)

4. 
Dr. Muhammad Mushtaq
(External Examiner)

Department of Mathematics
International Islamic University
Sector H-10 Islamabad.

Department of Mathematics
COMSATS University, Park Road Chak
Shahzad, Islamabad.

**Department of Mathematics
Quaid-I-Azam University
Islamabad, Pakistan
2019**

Certificate of Approval

This is to certify that the research work presented in this thesis entitled **Nonlinear Theoretical Models of Nanofluids with Heat Flux** was conducted by **Ms. Misbah Ijaz** under the kind supervision of **Prof. Dr. Muhammad Ayub**. No part of this thesis has been submitted anywhere else for any other degree. This thesis is submitted to the Department of Mathematics, Quaid-i-Azam University, Islamabad in partial fulfillment of the requirements for the degree of Doctor of Philosophy in field of Mathematics from Department of Mathematics, Quaid-i-Azam University Islamabad, Pakistan.

Student Name: **Misbah Ijaz**

Signature: 

External committee:

a) **External Examiner 1:**

Signature: 

Name: **Dr. Rahmat Ellahi**

Designation: Associate Professor

Office Address: Department of Mathematics, International Islamic University, H-10, Islamabad.

b) **External Examiner 2:**

Signature: 

Name: **Dr. Muhammad Mushtaq**

Designation: Assistant Professor

Office Address: Department of Mathematics, COMSATS University, Park Road Chak Shahzad, Islamabad.

c) **Internal Examiner**

Signature: 

Name: **Prof. Dr. Muhammad Ayub**

Designation: Professor

Office Address: Department of Mathematics, QAU Islamabad.

Supervisor Name:

Signature: 

Prof. Dr. Muhammad Ayub

Name of Dean/ HOD

Signature: 

Prof. Dr. Sohail Nadeem

DEDICATED TO

MY PARENTS

&

MY BELOVED SON

SAAIM ASRAR

Acknowledgement

In the name of almighty **Allah**, the creator and sustainer of the heavens and the earth, and everything between them, who gave me the potential and ability to complete this dissertation. Also, my respect goes to his holy prophet **Muhammad** (peace be upon him) who showed humanity the right path and brought message of peace and love.

It is a matter of great honor for me to express my immense gratitude and profound thanks to my worthy supervisor **Prof. Dr. Muhammad Ayub** upon their guidance, constant help and encouragement throughout my studies. Without his generous help and support, the timely completion of this task would not have been possible for me.

I am very much obliged to my mentor **Prof. Dr. Sohail Nadeem**, Chairman, Department of Mathematics on providing research-oriented environment and constant encouragement throughout my studies.

My special thanks are for my respected teachers on their support and encouragement during my studies. This dissertation could not have been completed without generous support and guidance of my respected teachers **Prof. Dr. Tasawer Hayat** and **Prof. Dr. Muhammad Yousaf Malik**. Their fabulous provision, valuable suggestions and careful readings are extremely accredited in the completion of this work.

I can't forget my research fellows (Ms Sumaira Qayyum, Ms. Sadaf Nawaz, Ms. Samia, Dr. Adnan Saeed Butt, Dr. Noor Muhammad, Dr. Muhammad Waqas, Dr. Muhammad Azam, Mr. Muhammad Ijaz Khan) for their company.

Finally, my sincere gratitude goes to my parents and my family, my son (**Saaim Asrar**) on their great concern and prayers. Words are countless to say thanks to those benevolent hands that sincerely raised me with gentle love, care and patience. Without their prayers I could not successfully complete this difficult task. May almighty Allah reward all of them with great honor in this world and the world hereafter.

Misbah Ijaz

28-11-2019

Preface

Fluid dynamics is a branch of engineering science which deals with the analysis of different fluids flow in different geometries under their rheological behavior. Analysis of non-Newtonian fluids is now recognized for its several industrial and engineering applications. Motivation of researchers in these material is through biological stuff (chemicals, vaccines, syrups, blood, synovial fluid etc.), chemical material (cosmetics, grease, pharmaceutical chemicals, shampoos, tooth paste, paints, oil reservoirs etc.) and food products (ketchup, ice creams, mayonnaise, apple sauce etc.). Such materials do not obey the Newton's law of viscosity. All characteristics of non-Newtonian liquids are not completely described by a single constitutive relation (model). Therefore, numerous models of such complex liquids have been suggested for the discussion about their rheological characteristics. The non-Newtonian fluids are categorized through three main classification (i.e., rate type, differential type and integral type). In addition, the features of such materials within the frame of different domain have benchmark importance in polymer and metal extrusion mechanisms, cooling of metallic surfaces and crystal growth, paper production and glass fibres. The analysis of heat transfer mechanism through cooling rate is an essential requirement of present industrial technologies. Features of heat and mass transfer is based through various mechanisms like heat generation/absorption, thermal radiation, Fourier's law of heat conduction, convection, binary chemical reaction, activation energy and Fick's laws.

Keeping all these aspects in mind, the prime objective of this thesis is to study nonlinear mathematical models subject to chemical reaction and Cattaneo-Christov heat and mass fluxes. Solutions and analysis are performed by utilizing homotopy analysis technique and shooting method. Finally, the structure of thesis is as follows:

Chapter one consists of literature survey of relevant published works and some basic conservation laws. The basic concepts of homotopy analysis method (HAM) and shooting technique are presented.

Chapter two addresses the axisymmetric convective, stagnation point flow of electrically conducting nanofluid induced by a permeable cylinder. The Darcy-Forchheimer relation is accounted to specify the flow nature in porous medium. Formulation of mathematical model is given by using Tiwari-Das nanofluid model. The velocity and thermal slip conditions are considered for present analysis. Implementation of appropriate transformation leads to nonlinear coupled systems of momentum and energy. Resulting systems are cracked through homotopic technique. The physical quantities namely, the skin friction coefficient and the local Nusselt number are calculated at the cylindrical surface and elucidated through graphs and tables. The contents of this chapter are published in “**Results in Physics, 9 (2018): 771–778**”.

(<https://doi.org/10.1016/j.rinp.2018.02.073>)

Chapter three describes dual stratified flow of Maxwell nanofluid subjected to Cattaneo-Christov double diffusion scheme by nonlinearly stretched inclined cylinder. Key objective of this chapter is to explore the physical aspects of Maxwell nanofluid flow by nonlinearly stretched inclined cylinder in corporation with Arrhenius activation energy, non-uniform heat generation/absorption, nonlinearly convection, dual stratification and binary chemical reaction. Homotopy procedure yields convergence series solutions. Graphs are plotted to see the behaviour of physical variables. Expression of Nusselt and Sherwood numbers are examined numerically. The results of this chapter are published in “**Heliyon 5 (2019): e01121**”.

(<https://doi.org/10.1016/j.heliyon.2019.e01121>)

Chapter 4 reports the novel characteristics of Jeffrey nanofluid flow due to an inclined permeable stretching cylinder manifested within the frame of homogeneous-heterogeneous reactions, thermal stratification, mixed convection and stagnation point. Energy expression is

modelled by Cattaneo-Christov heat flux. The derived nonlinear systems are solved analytically. Intervals of convergence are identified. The dimensionless fluid velocity, temperature and nanoparticle concentration on varying physical parameters are demonstrated by means of graphical and tabular outcomes. The contents of this chapter are submitted to “**Heliyon**”.

Chapter five describes nonlinear mixed convective flow of Jeffrey nanofluid with Arrhenius activation energy over an inclined permeable stretched cylinder. Features of non-uniform heat generation/absorption, binary chemical reaction, thermal and solutal stratification are utilized through no slip condition. The novel binary chemical reaction model is implemented to characterize the impact of activation energy. Generalized versions of Fourier’s and Fick’s law through Cattaneo–Christov double diffusion are employed to configure heat and mass transfer. Graphs and tables are created to analyse the impact of governing parameters on interested physical entities. The contents of this chapter are submitted in “**The European Physical Journal**”

Chapter six explores the novel aspects of activation energy in nonlinearly convective flow of Walter-B nanofluid subjected to Cattaneo-Christov double diffusion model over a permeable stretched sheet. Generalized forms of Fourier's and Fick's law are utilized through Cattaneo-Christov double diffusion. Walter-B nanomaterial model is used that describes the significant slip mechanism namely Brownian and thermophoresis diffusion. Activation energy, dual stratification, heat generation/absorption and binary chemical reaction are considered. Mathematical problems are computed for convergent series solutions. Discussion is made for dimensionless velocity, temperature and nanoparticle concentration. The outcomes of this chapter are published in “**Heliyon 5 (2019): e01815**”. (<https://doi.org/10.1016/j.heliyon.2019.e01815>).

Chapter seven aims to examine the novel features of activation energy in MHD nonlinear convective flow of Casson nanomaterial within the frame of Cattaneo-Christov heat flux model. Physical significance of heat transfer is based through nonlinear thermal radiation and non-uniform heat generation/absorption. Formulation for Brownian motion and thermophoresis is made through Buongiorno model. Additionally, impact of binary chemical reaction, thermal and solutal stratification are studied. A validation of the work is offered by comparing the current results with published literature. The contents of this chapter are submitted in "**Physica Scripta**".

Chapter eight is dedicated to discover the physical aspects of ferromagnetic Maxwell fluid flow over a stretched sheet in the presence of magnetic dipole, non-uniform heat source/sink, thermal and concentration stratification. Highlights of Brownian movement and thermophoresis are also explored through Buongiorno model. The numerical solution is obtained by using shooting method with the aid of fifth order Runge-Kutta-Fehlberg algorithm. Skin friction coefficient, local Nusselt and Sherwood numbers are tabulated and analysed. The contents of this chapter are published in "**Physica Scripta, (2018)**".
(<https://doi.org/10.1088/1402-4896/aaf6df>)

Nomenclature

A	Velocity ratio parameter
B_0	Magnetic field strength
(\hat{B}_1, \hat{B}_2)	Heat generation/absorption parameters
C	Fluid concentration
(C_0, C_w, C_∞)	Reference, wall and ambient concentration
C_F	Skin friction coefficient
$(c_1, d_1, d_2, d_3, d_4)$	Constants
(D_B, D_T)	Brownian diffusion and thermophoretic coefficients
Ec	Eckert number
E_1	Activation energy
E_a	Activation energy parameter
$F(\xi)$	Similarity function
\hat{F}_r	Forchheimer inertia coefficient
\hat{g}_1	Gravitational acceleration
Gr	Grashof number
J_w	Wall mass flux
J_1	Mass flux
(k_f, k_s, k_{nf})	Thermal conductivity of (fluid, solid fractions, nanofluid)
(K_m, K_t)	Homogeneous and heterogeneous reaction strength

k^*	Boltzmann constant
\hat{K}_1	Reaction rate parameter
\hat{K}_3	Mean absorption coefficient
\hat{K}_r^2	Chemical reaction rate constant
L	Scale length
Le	Lewis number
\hat{M}	Magnetic parameter
M_1	Porosity parameter
\hat{N}_b	Brownian motion parameter
\hat{N}_t	Thermophoresis parameter
Nu_z	Local Nusselt number
\hat{N}_1	Buoyancy ratio parameter
p	Fitted rate constant
Pr	Prandtl number
\hat{q}	Embedding parameter
\hat{q}_r	Radiative heat flux
q_w	Wall heat flux
q_1	Heat flux
R_0	Radius of cylinder
(S_t, S_v)	Thermal and velocity slip parameters
Sc	Schmidt number
Sh_z	Sherwood number

(S_1, S_2)	Thermal and solutal stratification parameters
T	Fluid temperature
(T_0, T_w, T_∞)	Reference, surface and ambient temperature
(u_z, u_r)	Axial and radial velocity
(U_0, U_w, U_∞)	Reference, stretching and ambient velocity
V_1	Mass transfer velocity
V_p	Mass suction/injection parameter
Greek symbols	
ξ	Similarity variable
α^*	Thermal diffusivity
$(\rho_f, \rho_s, \rho_{nf})$	Density of (fluid, solid fractions, nanofluid)
μ_f	Dynamic viscosity of base fluid
(ν_f, ν_{nf})	Kinematic viscosity of (fluid, nanofluid)
$\theta(\xi)$	Dimensionless temperature
γ_1	Curvature parameter
γ_2	Chemical reaction parameter
γ_3	Chemical reaction rate constant
ζ_0	Magnetic permeability
$(\hat{\beta}_t, \hat{\beta}_c)$	Nonlinear thermal and solutal convection parameters
β_1	Buoyancy parameter
β_2	Deborah number
δ	Temperature relative parameter

(δ_e, δ_c)	Thermal and solutal relaxation parameters
ϕ	Nanoparticle volume fraction
ϕ_a	Angle of inclination
τ_w	Shear stress at surface
$(\omega_1, \omega_2, \omega_3, \omega_4, \omega_5, \omega_6)$	Arbitrary constants
$((\rho C_p)_f, (\rho C_p)_p, (\rho C_p)_{nf})$	Heat capacity of (base fluid, nanoparticle, nanofluid)
(E_F, E_θ, E_Φ)	Auxiliary linear operators
$\Phi(\xi)$	Dimensionless nanoparticle concentration
$(\Gamma_1, \Gamma_2, \Gamma_3, \Gamma_4)$	Thermal and solutal expansion coefficients (linear & nonlinear)
$(\hat{\Gamma}_e, \hat{\Gamma}_c)$	Thermal and solutal relaxation time
Ψ_1	Stream function

Contents

CHAPTER 1	4
Literature Review	4
1.1 Introduction	4
1.2 Background	4
1.3 Fundamental laws	10
1.3.1 Law of mass conservation.....	10
1.3.2 Law of momentum conservation.....	10
1.3.3 Law of energy conservation.....	12
1.3.4 Law of mass conservation.....	12
1.3.5 Law of energy conservation for nanofluid.....	13
1.3.6 Law of mass conservation for nanofluid.....	13
1.4 Mathematical formulation of heat flux models.....	14
1.4.1 Fourier's law of heat conduction	14
1.4.2 Maxwell-Cattaneo model	14
1.4.3 Cattaneo-Fox model	15
1.4.4 Cattaneo-Christov model.....	15
1.4.5 Fick's law	16
1.5 Solution procedures.....	16
1.5.1 Homotopy analysis method (HAM)	16
1.5.2 Shooting technique.....	18
CHAPTER 2	19
Mixed convective flow of nanofluid with Darcy-Fochheimer relation and partial slip	19
2.1 Introduction	19
2.2 Mathematical formulation.....	19
2.3 Methodology.....	23
2.3.1 Zeroth-order systems	24
2.3.2 <i>mth</i> – order systems	25
2.4 Convergence analysis.....	27
2.5 Results and discussion	30
2.6 Graphical outcomes	33
2.7 Conclusions	40

CHAPTER 3	41
Nonlinearly convective stratified flow of Maxwell nanofluid with activation energy	41
3.1 Introduction	41
3.2 Mathematical formulation.....	41
3.3 Methodology.....	47
3.4 Convergence analysis.....	48
3.5 Results and discussion	52
3.6 Graphical outcomes	55
3.7 Conclusions	68
CHAPTER 4	69
Thermally stratified flow of Jeffrey fluid with homogeneous-heterogeneous reactions and non-Fourier heat flux model	69
4.1 Introduction	69
4.2 Mathematical formulation.....	69
4.3 Methodology.....	74
4.3.1 Zeroth-order systems	75
4.3.2 <i>mth</i> -order systems	76
4.4 Convergence analysis.....	79
4.5 Results and discussion	81
4.6 Graphical outcomes.....	83
4.5 Conclusions	90
CHAPTER 5	91
Aspects of activation energy for Jeffrey nanofluid with Cattaneo-Christov double diffusion model	91
5.1 Introduction	91
5.2 Mathematical formulation.....	92
5.3 Methodology.....	97
5.3.1 Zeroth-order systems.....	98
5.3.2 <i>mth</i> -order systems.....	100
5.4 Convergence analysis.....	103
5.5 Results and discussion	106
5.6 Graphical outcomes	109
5.7 Conclusions	121
CHAPTER 6	122

Dual stratification effects for Walter-B fluid flow in view of Cattaneo–Christov double diffusion	122
6.1 Introduction	122
6.2 Mathematical formulation.....	122
6.3 Methodology.....	127
6.4 Convergence analysis	129
6.4 Results and discussion	130
6.5 Graphical outcomes	132
6.6 Conclusions	143
CHAPTER 7	144
Numerical simulation of nonlinear radiative flow of Casson nanofluid with Cattaneo-Christov heat flux model	144
7.1 Introduction	144
7.2 Mathematical formulation.....	145
7.3 Methodology.....	150
7.4 Results and discussion	151
7.5 Graphical outcomes	160
7.6 Conclusions	170
CHAPTER 8	172
Stratified flow of ferromagnetic nanofluid with heat generation/absorption	172
8.1 Introduction	172
8.2 Mathematical formulation.....	172
8.3 Magnetic Potential.....	175
8.4 Methodology.....	176
8.5 Results and discussion	178
8.6 Graphical outcomes	183
8.7 Conclusions	190
Bibliography	191

CHAPTER 1

Literature Review

1.1 Introduction

This chapter is devoted to review the published articles related to the work presented in this thesis (e.g. heat and mass transfer with activation energy, nonlinear mixed convection, thermal radiation, nonuniform heat generation/absorption, homogeneous-heterogeneous reactions and dual stratification) and the constitutive equations representing Maxwell, Walter-B, Jeffrey and Casson fluid models are included to analyze the flow regime. For the solution of the models homotopy analysis method (HAM) and built-in-shooting technique are employed.

1.2 Background

Investigation of non-Newtonian liquids has attained notable consideration in recent couple of years on account of its broad applications in engineering and industries. Some examples of non-Newtonian materials are gypsum paste, yogurt, clays, printing ink, drilling mud, blood, hydrogenated castor oil, paints, colloidal suspension, butter, ketchup, soup, jam and so on. The intricate idea of non-Newtonian liquids offers great challenge to physicists, mathematicians and engineers. Several models have been offered for the investigation of non-Newtonian liquids in the literature. Since there is no single constitutive relation (model) that completely predict all characteristics of non-Newtonian liquids. Various

constitutive equations were modelled to predict the rheological characteristics of such type of materials. Additionally, there are various rheological complex fluid models which do not display the features of relaxation and retardation time. These fluids are categorized as rate and differential types [1-5]. To predict the characteristics of relaxation/retardation time, Maxwell, Walter-B, Jeffrey and Casson fluid models were developed [6]. Mustafa et al. [7] completed numerical computations for rotating flow of Maxwell liquid in view of Cattaneo-Christov heat flux mode. Hayat et al. [8] considered the problem of Maxwell fluid with the effects of melting heat transfer via homotopic technique. Ijaz and Ayub [9] presented nonlinear convective flow of Maxwell nanofluid in the presence of heat generation/absorption and activation energy. Hayat et al. [10] discussed about thermally stratified flow of Maxwell liquid with radiation. Ijaz et al. [11] focused on stratified flows with ferromagnetic Maxwell fluid by including heat generation/absorption. Hayat et al. [12] examined the radiative flow of Jeffrey fluid in the presence of heat generation/absorption. Hamad et al. [13] inspected stagnation point flow of Jeffrey fluid with variable thermal conductivity over permeable surface. Physical features of Jeffrey liquid with different assumptions are delineated (see [14-18]).

Mixed convective flow with stretched surface has practical implementations in industries and engineering. Basically, it is coalition of forced and free convections. Key role of main factors in the particle deposition include convection, Brownian diffusion, turbulence, sedimentation, thermophoresis electrophoresis, inertial effect and surface geometry. Some significant applications of convection phenomenon are nuclear reactor, heat exchanger, solar thermal collectors and electronic equipment. Mixed convection 2D flow on stagnation point through vertical surface is investigated by Ramachandran et al.

[19]. Hayat et al. [20] explained mixed convection impacts on viscous nanofluid flow towards the stagnation point over a linearly stretched cylinder. Mixed convection influencing the nanofluid flow through cylinder along with heat source/sink was discussed by Hayat et al. [21]. Unsteady radiative and mixed convective flow over stretched surface embedded through porous medium was analysed by Mukhopadhyay [22].

Fourier [23] proposed a model to analyze heat transfer phenomenon for different materials. This model was quite beneficiary in case of solids. But for fluids, this model has some flaws; one of major flaws is of parabolic nature in its mathematical system which does not predict the heat transfer in fluid flow accurately. This deficiency was overcome by Cattaneo [24] by adding thermal relaxation term (effects of thermal inertia). Christov [25] revised the Cattaneo model by taking Oldroyd's upper convected derivative for thermal inertia. Ciarletta and Straughan [26] proved the uniqueness and stability of Christov-Cattaneo model. Han et al. [27] described the slip flow of viscoelastic fluid through stretched surface with non-Fourier heat flux model. Hayat et al. [28] discussed Jeffrey model with Cattaneo-Christov heat and mass diffusion on stretched surface. Some significant work has been presented in [29-34].

Ferrofluids has demonstrated some remarkable physical properties and their usage in many smart appliances. Its electrical application has fascinated scientists and engineers over the years. Ferrofluids are used in various equipments like lasers, avionics, cooling agents, filtration, robotic, metal spinning etc. Firstly, Anderson and Vanes [35] discussed the features of magnetic dipole and heat transfer on ferrofluid flow due to stretchable surface. Titus and Abraham [36] examined ferroliquid flow and warmth transfer over a stretchable sheet. Neuringer and Rosensweig [37] inspected thermophysical characteristics

of ferrohydrodynamics. Mixed convective flow of ferrofluids with homogeneous/heterogeneous reactions and magnetic dipole is deliberated by Yasmeen et al. [38]. Impact of suction/injection in the presence of magnetic dipole for flow of viscoelastic material is considered by Zeeshan and Majeed [39]. Vtulkina and Elfimova [40] deliberated magnetic characteristics of ferrofluids due to external magnetic field. Few recent articles identified with ferrofluid flow are introduced in [41–43].

Chemical reaction and activation energy to study mass transfer phenomenon has attracted many researchers after its number of applications in industry (i.e. chemical engineering, cooling of nuclear reactors, thermal oil recovery and food processing). The law of Arrhenius is generally of the form [44]:

$$K = B^*(T - T_\infty)^p \exp\left[-\frac{E_a}{\kappa(T - T_\infty)}\right], \quad (1.1)$$

here K denotes the rate constant of chemical reaction, B^* the prefactor (constant) based on the fact enhancing the temperature that frequently causes remarkable increase in the rate of reactions, E_a the activation energy and $\kappa (= 8.61 \times 10^{-5} \text{ eV/K})$ the Boltzmann constant. Besides experimental study, theoretical efforts are acknowledged for activation energy analysis in different flow problems. Shortcomings of theoretical study are also found in literature. The complexities in predicting chemical reaction processes were main hurdle. These types of problems are very difficult to handle. Practical problems representing chemical kinetic reaction become very complicated, but if this is limited to binary type reaction a lot of achievements are possible in this field. On the basis of thermomechanics, Truesdell [45,46] initially formulated the balance equations for general materials. Afterwards, [47,48] obtained exact solutions of incompressible Newtonian fluids

with a binary chemical reaction in boundary layer regime. Bestman [49] explored the activation energy effects through porous matrix. Recently, Kandasamy et al. [50] discussed chemical reaction effects on viscous fluid flow over a wall of wedge with different physical assumptions. Bestman [51] analyzed the radiative heat transfer with effects of the Arrhenius activation energy under the various physical conditions through a vertical cylinder.

Heat generation/absorption directly changes heat distribution that ultimately effects the rate of particle deposition in the medium. Heat source/sink have different situations, it may be constant, space or temperature dependent. Abo-Eldahab and El-Aziz [52] investigated hydrodynamic viscous fluid flow with heat generation/absorption. Abel et al. [53] also described the heat generation/absorption phenomenon in viscoelastic fluid flow with various assumptions. Abel and Mahesha [54] analyzed non-uniform heat source in viscoelastic fluid flow past a stretching sheet. In [55-60] some related articles on heat source/sink are presented.

The character of radiative heat transfer is quite phenomenal in various engineering processes like nuclear power plants, process of solar heat generation hypersonic flights, space vehicles, gas turbines, gas coolant nuclear reactors etc. Radiation phenomenon is not medium-dependent while it varies against arrangement of geometry, properties between temperature and surface which is emitting or absorbing heat. The influences of linear radiation are not noticeable for excessive temperature difference because in this case the involved parameter i.e., linearized Rosseland approximation has negligible effects [61], whereas nonlinear radiation phenomenon is delineated with the aid of radiation parameter, Prandtl number and temperature ratio parameter. Heat exchange with thermal radiation has

marvellous uses in numerous procedures including satellites, missiles and space vehicles. Pantokratoras [62] investigated the both linear and nonlinear Rosseland radiations on natural convective flow over isothermal plate by means of a novel radiation parameter named as film radiation parameter. Cortell [63] discussed the nonlinear radiations influence on viscous fluid flow past a stretched surface. Refs. [64-69] also described the nonlinear radiations impacts on MHD fluids.

Although number of researchers has discussed various nanofluid models with flat surfaces under different situations by taking stratified flow. So far, the chemical reaction and Arrhenius activation energy under stretched cylindrical domain has not been considered. Due to its various applications in industry main focus of this thesis will be to examine Cattaneo-Christov heat and mass flux models by taking various viscoelastic materials in the presence of chemical reaction. Features of double stratification, stagnation point, non-uniform heat generation/absorption, MHD, binary chemical reaction, homogeneous-heterogeneous reactions and activation energy are also taken into account. Viscoelastic materials are one of the major subclasses of non-Newtonian models. These materials have so many applications (e.g. in automobile bumpers, on computer drives to protect from mechanical shock, in helmets (the foam padding inside), in wrestling mats, in shoe insoles to reduce the impact transmitted to a person's skeleton etc.). Moreover, synthetic viscoelastic materials can be injected directly into an osteoarthritic knee, enveloping cartilage-deficient joints and acting as a lubricant and shock absorber. In the formulation of mathematical models Tiwari-Das nanofluid model and Buongiorno model are taken with careful consideration.

1.3 Fundamental laws

1.3.1 Law of mass conservation

According to the law of conservation of mass, mass can neither be created and nor can be destroyed. Mathematically for compressible fluid it can be expressed as

$$\frac{\partial \rho}{\partial t} + \nabla \cdot (\rho \mathbf{V}_1) = 0, \quad (1.2)$$

in which ρ denotes the density and \mathbf{V}_1 fluid velocity. After considering incompressible fluid (ρ is constant), Eq. (1.2) implies:

$$\nabla \cdot \mathbf{V}_1 = 0. \quad (1.3)$$

For rectangular coordinate system it is written as

$$\frac{\partial u}{\partial x} + \frac{\partial v}{\partial y} + \frac{\partial w}{\partial z} = 0, \quad (1.4)$$

whereas in cylindrical form we have

$$\frac{1}{r} \frac{\partial}{\partial r} (r u_r) + \frac{1}{r} \frac{\partial}{\partial \theta} (u_\theta) + \frac{\partial}{\partial z} (u_z) = 0. \quad (1.5)$$

For axisymmetric incompressible flow the continuity equation is reduced as follows:

$$\frac{u_r}{r} + \frac{\partial}{\partial \theta} (u_\theta) + \frac{\partial}{\partial z} (u_z) = 0. \quad (1.6)$$

1.3.2 Law of momentum conservation

This law states that linear momentum remains conserved of whole system. Newton's second law is used to derive it. Mathematically it becomes

$$\rho \frac{d\mathbf{V}_1}{dt} = \nabla \cdot \boldsymbol{\tau} + \rho \mathbf{b}. \quad (1.7)$$

For incompressible fluid the Cauchy stress tensor is described as

$$\boldsymbol{\tau} = -P\mathbf{I} + \mathbf{S}, \quad (1.8)$$

here P denotes pressure, \mathbf{I} an identity tensor, \mathbf{S} extra stress tensor and $\frac{d}{dt}$ the material time differentiation.

For $\mathbf{V}_1 = [u(x, y, t), v(x, y, t), w(x, y, t)]$, momentum equation in components form (by using cartesian coordinates) can be written as

$$\rho \left[\frac{\partial u}{\partial t} + u \frac{\partial u}{\partial x} + v \frac{\partial u}{\partial y} + w \frac{\partial u}{\partial z} \right] = \frac{\partial \tau_{xx}}{\partial x} + \frac{\partial \tau_{xy}}{\partial y} + \frac{\partial \tau_{xz}}{\partial z} + \rho b_x, \quad (1.9)$$

$$\rho \left[\frac{\partial v}{\partial t} + u \frac{\partial v}{\partial x} + v \frac{\partial v}{\partial y} + w \frac{\partial v}{\partial z} \right] = \frac{\partial \tau_{yx}}{\partial x} + \frac{\partial \tau_{yy}}{\partial y} + \frac{\partial \tau_{yz}}{\partial z} + \rho b_y, \quad (1.10)$$

$$\rho \left[\frac{\partial w}{\partial t} + u \frac{\partial w}{\partial x} + v \frac{\partial w}{\partial y} + w \frac{\partial w}{\partial z} \right] = \frac{\partial \tau_{zx}}{\partial x} + \frac{\partial \tau_{zy}}{\partial y} + \frac{\partial \tau_{zz}}{\partial z} + \rho b_z, \quad (1.11)$$

where $(\tau_{xx}, \tau_{yy}, \tau_{zz}, \tau_{xy}, \tau_{xz}, \tau_{yx}, \tau_{yz}, \tau_{zx}, \tau_{zy})$ shows components of Cauchy stress tensor and (b_x, b_y, b_z) the body force components.

Using $\mathbf{V}_1 = [u_r(r, \theta, z), u_\theta(r, \theta, z), u_z(r, \theta, z)]$ momentum equation in cylindrical coordinate system can be expressed as

$$\rho \left[\frac{\partial u_r}{\partial t} + u_r \frac{\partial u_r}{\partial r} + \frac{u_\theta}{r} \frac{\partial u_r}{\partial \theta} + u_z \frac{\partial u_r}{\partial z} - \frac{u_\theta^2}{r} \right] = \frac{1}{r} \frac{\partial}{\partial r} (r \tau_{rr}) + \frac{1}{r} \frac{\partial}{\partial \theta} (\tau_{r\theta}) + \frac{\partial}{\partial r} (\tau_{rz}) - \frac{\tau_{\theta\theta}}{r} + \rho b_r, \quad (1.12)$$

$$\rho \left[\frac{\partial u_\theta}{\partial t} + u_r \frac{\partial u_\theta}{\partial r} + \frac{u_\theta}{r} \frac{\partial u_\theta}{\partial \theta} + u_z \frac{\partial u_\theta}{\partial z} - \frac{u_r u_\theta}{r} \right] = \frac{1}{r^2} \frac{\partial}{\partial r} (r^2 \tau_{\theta r}) + \frac{1}{r} \frac{\partial}{\partial \theta} (\tau_{\theta \theta}) + \frac{\partial}{\partial z} (\tau_{\theta z}) + \rho b_\theta, \quad (1.13)$$

$$\rho \left[\frac{\partial u_z}{\partial t} + u_r \frac{\partial u_z}{\partial r} + \frac{u_\theta}{r} \frac{\partial u_z}{\partial \theta} + u_z \frac{\partial u_z}{\partial z} \right] = \frac{1}{r} \frac{\partial}{\partial r} (r \tau_{zr}) + \frac{1}{r} \frac{\partial}{\partial \theta} (\tau_{z\theta}) + \frac{\partial (\tau_{zz})}{\partial z} + \rho b_z. \quad (1.14)$$

In the above expressions $(\tau_{rr}, \tau_{r\theta}, \tau_{rz}, \tau_{\theta r}, \tau_{\theta\theta}, \tau_{\theta z}, \tau_{zr}, \tau_{z\theta}, \tau_{zz})$ represent Cauchy stress tensor components and (b_r, b_θ, b_z) denotes components of body force.

1.3.3 Law of energy conservation

This law physically interprets that total energy of the framework remains conserved. It is developed from first law of thermodynamics. Mathematically, we have

$$\rho C_p \frac{dT}{dt} = \boldsymbol{\tau} \cdot \mathbf{L} - \text{div}(\mathbf{q}) - \text{div}(\mathbf{q}_r), \quad (1.15)$$

where $\rho C_p \frac{dT}{dt}$ indicates internal energy, $\boldsymbol{\tau} \cdot \mathbf{L}$ viscous dissipation, $\text{div}(\mathbf{q})$ thermal heat flux and $\text{div}(\mathbf{q}_r)$ radiative heat flux respectively. While C_p, T, \mathbf{q} and \mathbf{q}_r represent for specific heat, density, thermal and radiative heat fluxes respectively.

1.3.4 Law of mass conservation

It is defined as the total concentration of framework remains conserved. It is derived from Fick's second law. The concentration equation in view of Fick's law can be expressed as

$$\frac{dC}{dt} = D(\nabla^2 C), \quad (1.16)$$

where C symbolize for concentration and D for mass diffusivity.

1.3.5 Law of energy conservation for nanofluid

The energy expression within the frame of nanofluid can be defined as

$$(\rho C_p)_f \frac{dT}{dt} = -div(\mathbf{q}) + h_p(\nabla \cdot \mathbf{J}_p), \quad (1.17)$$

where T for temperature, $\hat{\mathbf{q}}$ for energy flux, \mathbf{J}_p for mass diffusion flux of nanoparticles, C_p for specific heat of nanofluid and h_p for specific enthalpy for nanoparticles. Energy and mass fluxes $(\hat{\mathbf{q}}, \mathbf{J}_p)$ are defined as

$$\mathbf{q} = -k\nabla T + h_p \mathbf{J}_p, \quad (1.18)$$

$$\mathbf{J}_p = -\rho_p D_B \nabla C - \rho_p D_T \frac{\nabla T}{T_\infty}, \quad (1.19)$$

in which ρ_p defines for mass density of nanoparticles, k for thermal conductivity, D_B for Brownian diffusion and D_T for thermophoretic diffusion.

The energy expression for nanfluid in view of Eqs. (1.18) and (1.29) is written as

$$\rho C_p \frac{dT}{dt} = k\nabla^2 T + \rho_p C_p \left[D_B \nabla C \cdot \nabla T + D_T \frac{\nabla T \cdot \nabla T}{T_\infty} \right]. \quad (1.20)$$

1.3.6 Law of mass conservation for nanofluid

The concentration equation within the frame of nanofluid is

$$\frac{\partial C}{\partial t} + \mathbf{v}_1 \cdot \nabla C = -\frac{1}{\rho_p} (\nabla \cdot \mathbf{J}_p). \quad (1.21)$$

The concentration expression for nanofluids in view of Eq. (1.19) is given as

$$\frac{\partial C}{\partial t} + \mathbf{V}_1 \cdot \nabla C = D_B \nabla^2 C + D_T \frac{\nabla^2 T}{T_\infty}. \quad (1.22)$$

1.4 Mathematical formulation of heat flux models

1.4.1 Fourier's law of heat conduction

In 1822, Fourier states that rate of heat transfer with the passage of time is directly proportional to the product of negative temperature gradient and area. Mathematically, it is written as

$$\mathbf{Q} \propto -A_1 \nabla T, \quad (1.23)$$

where A_1 denotes cross sectional area of the fluid flow and ∇T is defining the temperature gradient. Now heat flux \hat{q} relation is

$$\mathbf{q} = -\frac{\mathbf{Q}}{A_1}, \quad (1.24)$$

hence conduction Fourier law takes the following form

$$\mathbf{q} = -k \nabla T. \quad (1.25)$$

Fundamental deficiency of this law is that constitutional interruption is instantly sensed by medium under consideration. In fact it is infeasible, so this is recognized as “Paradox of heat conduction”. To resolve this issue various modifications have been proposed by the scientists.

1.4.2 Maxwell-Cattaneo model

In 1948, Cattaneo resolved the paradox of Fourier's law by introducing thermal relaxation time which characterizes the time necessitated for heat conduction to build in a volume

element when temperature gradient is imposed across it. Mathematical expression of Maxwell-Cattaneo (MC) model is

$$\mathbf{q} + \lambda \frac{\partial \mathbf{q}}{\partial t} = -k \nabla T, \quad (1.26)$$

here λ represents the relaxation time and the modified form involved in above equation

(i. e., $\lambda \frac{\partial \mathbf{q}}{\partial t}$) is known as "thermal inertia".

1.4.3 Cattaneo-Fox model

In 1984, Straughan and Franchi [70] proposed a new theory for heat flux. In this model they introduced Juamann derivative for \mathbf{q} in Maxwell-Cattaneo model. Thus Cattaneo-Fox model is

$$\mathbf{q}_i + \lambda \left[\frac{\partial \mathbf{q}}{\partial t} - \epsilon_{ijk^*} w_j \mathbf{q}_{k^*} \right] = -k \nabla T, \quad (1.27)$$

where $k^* = (0,0,1)$ and $w = \frac{1}{2} \text{curl}(\mathbf{V}_1)$.

1.4.4 Cattaneo-Christov model

In 2009, Christov swapped the ordinary derivative by upper convective derivatives. After this modification of Maxwell-Cattaneo theory, main advantage is that one can eliminate \mathbf{q} thus yielding a single equation for thermal field. Finally, the Cattaneo-Christov model becomes:

$$\mathbf{q} + \lambda \left[\frac{\partial \mathbf{q}}{\partial t} + \mathbf{V}_1 \cdot \nabla \mathbf{q} - \mathbf{q} \cdot \nabla \mathbf{V}_1 + (\nabla \cdot \mathbf{V}_1) \mathbf{q} \right] = -k \nabla T, \quad (1.28)$$

1.4.5 Fick's law

The concentration equation is based on the Fick's law [71] and it is of the form

$$\frac{\partial C}{\partial t} + \mathbf{V}_1 \cdot \nabla C = -\nabla \cdot \mathbf{J}, \quad (1.29)$$

here normal mass flux \mathbf{J} mass is defined as

$$\mathbf{J} = -D\nabla C, \quad (1.30)$$

from Eqs. (1.29) and (1.30), one has

$$\frac{\partial C}{\partial t} + \mathbf{V}_1 \cdot \nabla C = -D\nabla^2 C. \quad (1.31)$$

1.5 Solution procedures

1.5.1 Homotopy analysis method (HAM)

According to Liao [72], this analytical method has the following advantages on other techniques:

- It provides a series solution without depending upon small/ large physical parameters involved in series solution and applicable for not only weakly but also strongly nonlinear problems.
- It guarantees the convergence of series solutions for nonlinear problems.
- It provides us great choice to select the base function of the required solution and the corresponding auxiliary linear operator of the homotopy.

Brief mathematical description of HAM is as follows:

Consider a nonlinear differential equation:

$$N^*[w(r)] + u(r) = 0, \quad (1.32)$$

where N^* denotes nonlinear operator, $u(r)$ for a known function and $w(r)$ is unknown function to be determined. The homotopic equation is

$$(1 - q)\mathcal{L}[\bar{w}(r; q) - w_0(r)] = q\hbar H(r)N^*[\bar{w}(r; q) - w_0(r)], \quad (1.33)$$

here $q \in [0,1]$ is the embedding parameter, $H(r) \neq 0$ is an auxiliary function, $\hbar (\neq 0)$ is a nonzero parameter, \mathcal{L} is an auxiliary linear operator, $w_0(r)$ is an initial guess of $w(r)$ and $\bar{w}(r; q)$ is an unknown function, respectively. It is significant, that one has great freedom to choose auxiliary parameters in HAM. Noticeably, when $q = 0$ and $q = 1$, following holds

$$\bar{w}(r; 0) = w_0(r) \text{ and } \bar{w}(r; 1) = w(r), \quad (1.34)$$

expanding $\bar{w}(r; q)$ in Taylor series with respect to q , one obtains

$$\bar{w}(r; q) = w_0(r) + \sum_m^{\infty} w_m(r) q^m \text{ where } w_m(r) = \frac{1}{m!} \left. \frac{\partial^m \bar{w}(r; q)}{\partial q^m} \right|_{q=0}. \quad (1.35)$$

For convergence of above series solution, the value of \hbar play important role. Substituting $q = 1$, one gets

$$w(r) = w_0(r) + \sum_m^{\infty} w_m(r), \quad (1.36)$$

by defining a vector $w = (w_0(r), w_1(r), w_2(r) \dots w_n(r))$ and differentiating Eq. (1.30) m -times w. r. t. (q) at $q = 0$, one obtain deformation of m^{th} –order as

$$w(r) = w_0(r) + \sum_m^{\infty} w_m(r), \quad (1.37)$$

$$\mathcal{L}[w_m(r) - \chi_m w_{m-1}(r)] = \hbar H(r) R_m[w_{m-1}], \quad (1.38)$$

$$\chi_m = \begin{cases} 0 & m \leq 1, \\ 1 & m > 1. \end{cases} \quad (1.39)$$

where

$$R_m[w_{m-1}] = \frac{1}{m!} \left. \frac{\partial^{m-1} N^*[\bar{w}(r; q)]}{\partial q^{m-1}} \right|_{q=0}. \quad (1.40)$$

Taking \mathcal{L}^{-1} of Eq. (1.38),

$$w_m(r) = \chi_m w_{m-1}(r) + \hbar H(r) R_m[w_{m-1}]. \quad (1.41)$$

In this way one can obtain w_m for $m \geq 1$, at m^{th} – order

$$w(r) = \sum_{m=1}^M w_m(r). \quad (1.42)$$

1.5.2 Shooting technique

Shooting method [73] deals only initial values problems. Thus, modeled equations are converted into first order ODE's.

CHAPTER 2

Mixed convective flow of nanofluid with Darcy-Fochheimer relation and partial slip

2.1 Introduction

This chapter addresses axisymmetric mixed convective, stagnation point flow of electrically conducting nanofluid with velocity and thermal slip conditions by a permeable cylinder. The Darcy-Forchheimer relation is taken due to porous media. Tiwari-Das [74] nanofluid constitutive law has been utilized to configure flow situation. Water-based nanofluid with nanoparticle of titanium oxide, aluminum oxide and copper is considered. After using similarity variables, the flow-govern system is transferred into nonlinear ordinary differential equations. Analytical approach HAM has been utilized to solve flow-govern system. Thermophysical features of problems are discussed by computing velocity, temperature and concentration profiles versus physical parameters. Physical characteristics in surface vicinity are described by coefficients of wall friction, wall heat and mass fluxes

2.2 Mathematical formulation

Here we analyze mixed convective stagnation point flow of nanofluids by a permeable stretched cylinder having radius R_0 . The physical sketch of the flow problem is presented in Fig. 2.1. The flow analysis is considered under Darcy-Forchheimer law. The velocity

components along cylinder and radial direction are symbolized by u_z and u_r respectively. The flow is generated due to stretching velocity of the form $U_w \left(= \frac{U_0 z}{L} \right)$ and wall temperature $T_w = T_\infty + \frac{\Delta T}{L}$. Free stream velocity and ambient temperature are represented by $U_1(z) = \frac{zU_\infty}{L}$ and T_∞ . The mathematical model has been formulated based on Tiwari-Das nanofluid model. Using boundary layer approximation, one can get the following governing equations [75]:

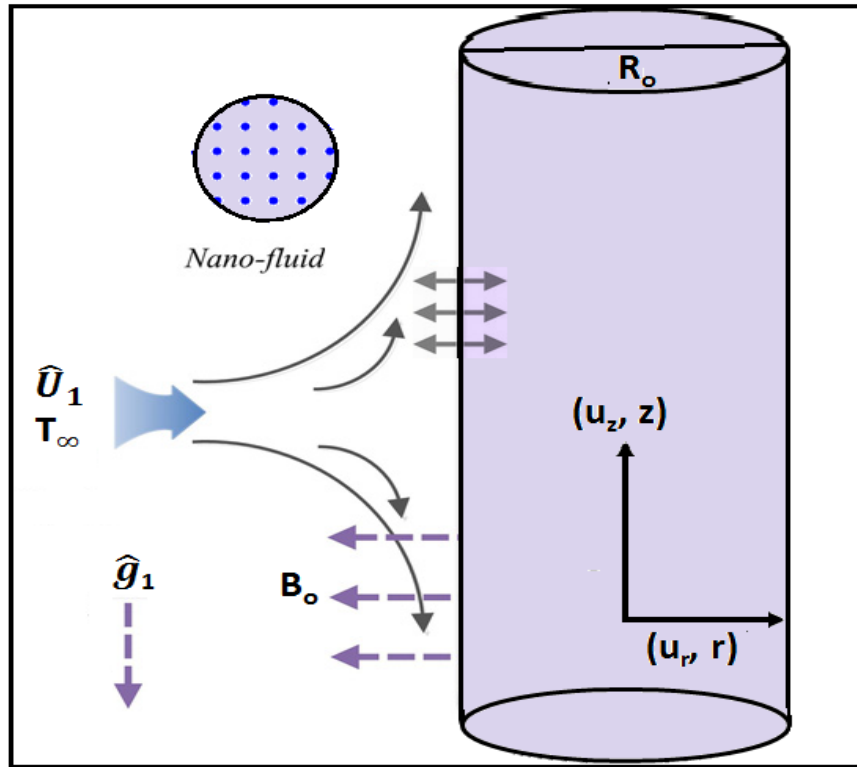


Fig. 2.1: Physical model.

$$\frac{\partial}{\partial r}(ru_r) + \frac{\partial}{\partial z}(ru_z) = 0, \quad (2.1)$$

$$u_z \frac{\partial u_z}{\partial z} + u_r \frac{\partial u_z}{\partial r} = U_1 \frac{\partial U_1}{\partial z} + v_{nf} \left(\frac{\partial^2 u_z}{\partial r^2} + \frac{1}{r} \frac{\partial u_z}{\partial r} \right) + \frac{\sigma B_0^2}{\rho_{nf}} (U_1 - u_z) - \frac{v_{nf}}{\hat{k}_1} u_z - f_r u_z^2 + \frac{\phi \rho_s \beta_s + (1 - \phi) \rho_f \beta_f}{\rho_{nf}} \hat{g}_1 (T - T_\infty), \quad (2.2)$$

$$u_z \frac{\partial T}{\partial z} + u_r \frac{\partial T}{\partial r} = \frac{k_{nf}}{(\rho C_p)_{nf}} \left(\frac{\partial^2 T}{\partial r^2} + \frac{1}{r} \frac{\partial T}{\partial r} \right). \quad (2.3)$$

The definitions are [76]

$$v_{nf} = \frac{\mu_f}{(1 - \phi)^{2.5} [(1 - \phi) \rho_f + \phi \rho_s]}, \quad (2.4)$$

$$\rho_{nf} = (1 - \phi) \rho_f + \phi \rho_s, \quad (2.5)$$

$$\frac{k_{nf}}{k_f} = \frac{(k_s + 2k_f) - 2\phi(k_f - k_s)}{(k_s + 2k_f) + \phi(k_f - k_s)}, \quad (2.6)$$

$$(\rho C_p)_{nf} = (1 - \phi)(\rho C_p)_f + \phi(\rho C_p)_s. \quad (2.7)$$

The associated boundary conditions are:

$$\begin{aligned} u_z &= U_w + V_2 \frac{\partial u_z}{\partial r}, \quad u_r = V_1, \quad T = T_w + V_3 \frac{\partial T}{\partial r} \quad \text{at } r = R_0, \\ u_z &= U_1 = \frac{U_\infty z}{L}, \quad u_r = 0, \quad T \rightarrow T_\infty \quad \text{as } r \rightarrow \infty. \end{aligned} \quad (2.8)$$

By considering inappropriate transformations [77]

$$\begin{aligned} \Psi_1 &= \left(\frac{U_0 v_f R_0^2}{L} \right) z F(\xi) \quad \xi = \sqrt{\frac{U_0 v_f L}{R_0^2}} \left(\frac{r^2 - R_0^2}{2v_f L} \right), \\ T - T_\infty &= \frac{\Delta T z}{L} \theta(\xi), \end{aligned} \quad (2.9)$$

where, Ψ_1 is the stream function, which equitably satisfies the continuity Eq. (2.1) and is defined as

$$u_z = \frac{1}{r} \frac{\partial \Psi_1}{\partial r}, \quad u_r = -\frac{1}{r} \frac{\partial \Psi_1}{\partial z}. \quad (2.10)$$

After applying Eqs. (2.9) and (2.10) incompressibility condition is trivially satisfied and flow Eqs. (2.2) – (2.3) become

$$\begin{aligned} & \frac{1}{(1-\phi)^{2.5} \left(1 - \phi + \phi \frac{\rho_s}{\rho_f}\right)} \left((1 + 2\gamma_1 \xi) F'''' + 2\gamma_1 F''' - M_1 F' \right. \\ & \quad \left. + \hat{M}^2 (1-\phi)^{2.5} (A - F') \right) + FF'' + A^2 \\ & - (1 + \hat{F}_r) F'^2 + \frac{\left(1 - \phi + \phi \frac{\rho_s \beta_s}{\rho_f \beta_f}\right)}{\left(1 - \phi + \phi \frac{\rho_s}{\rho_f}\right)} \beta_1 \theta = 0, \end{aligned} \quad (2.11)$$

$$\frac{k_{nf}/k_f}{\left(1 - \phi + \phi \frac{(\rho C_p)_s}{(\rho C_p)_f}\right)} [(1 + 2\gamma_1 \xi) \theta'' + 2\gamma_1 \theta'] + Pr [F\theta' - F'\theta] = 0, \quad (2.12)$$

with

$$\begin{aligned} F(\xi) = V_p, \quad F'(\xi) = 1 + S_v F''(\xi), \quad \theta(\xi) = 1 + S_t \theta'(\xi) \quad \text{at } \xi = 0, \\ F'(\xi) = A, \quad \theta(\xi) = 0, \quad \text{as } \xi \rightarrow \infty. \end{aligned} \quad (2.13)$$

Different dimensionless parameters are defined as

$$\begin{aligned} \gamma_1 = \sqrt{\frac{\nu_f L}{U_0 R_0^2}}, \quad \beta_1 = \frac{Gr}{Re_z^2}, \quad Gr = \frac{\hat{g}_1 \beta_f \Delta T L^3}{\nu_f^2}, \quad S_t = \frac{V_3 r}{R_0} \sqrt{\frac{U_0}{\nu_f L}}, \quad A = \frac{U_\infty}{U_0}, \\ \hat{M}_1 = \frac{\nu_f L}{U_0 \hat{k}_1}, \quad S_v = \frac{V_2 r}{R_0} \sqrt{\frac{U_0}{\nu_f L}}, \quad \hat{F}_r = \frac{\hat{C}_b}{z \sqrt{\hat{k}_1}}, \quad \hat{M} = \frac{\sigma B_0^2 L}{\rho_f U_0}, \quad Pr = \frac{\mu C_p}{\hat{k}_f}. \end{aligned} \quad (2.14)$$

The skin friction C_F and local Nusselt number Nu_z are described as

$$C_F = \frac{\tau_w}{\rho_f U_w^2}, \quad Nu_z = \frac{L q_w}{\hat{k}_f \Delta T}. \quad (2.15)$$

In which τ_w and q_w (i.e., surface shear stress and surface heat flux) are

$$\begin{aligned}\tau_w &= \mu_{nf} \left. \frac{\partial u_z}{\partial r} \right|_{r=R_0}, \\ q_w &= -k_{nf} \left. \frac{\partial T}{\partial r} \right|_{r=R_0}.\end{aligned}\tag{2.16}$$

In non-dimensional form, C_F and Nu_z are

$$\begin{aligned}C_F(Re_z)^{\frac{1}{2}} &= \frac{L_1}{(1-\phi)^{2.5}} F''(0), \\ Nu_z(Re_z)^{-\frac{1}{2}} &= -\frac{k_{nf}}{k_f} L_1 \theta'(0).\end{aligned}\tag{2.17}$$

In which $Re_z \left(= \frac{U_0 L}{\nu_f} \right)$ is local Reynold number and setting $L_1 = \frac{z}{L}$.

2.3 Methodology

The nonlinear coupled Eqs. (2.11)-(2.12) along with the boundary conditions, Eq. (2.13) has been solved with the help of Homotopy technique. The initial solutions $(F^0(\xi), \theta^0(\xi))$ are

$$\begin{aligned}F^0(\xi) &= V_p + A\xi + \frac{1-A}{1+S_v} - \frac{1-A}{1+S_t} \exp(-\xi), \\ \theta^0(\xi) &= \frac{1}{1+S_t} \exp(-\xi),\end{aligned}\tag{2.21}$$

$$\mathcal{E}_F[F] = F''' - F', \quad \mathcal{E}_\theta[\theta] = \theta'' - \theta',\tag{2.22}$$

with

$$\mathcal{E}_F[\omega_1 + \omega_2 \exp(\xi) + \omega_3 \exp(-\xi)] = 0,\tag{2.23}$$

$$\mathcal{E}_\theta[\omega_4 \exp(\xi) + \omega_5 \exp(-\xi)] = 0,\tag{2.24}$$

in which ω_j ($j = 1 - 5$) are arbitrary constants. The problems at zeroth and m^{th} -order are as follows:

2.3.1 Zeroth-order systems

The relevant deformation problems at this order are

$$(1 - \hat{q})\mathcal{E}_F[\hat{F}(\xi; \hat{q}) - F^0(\xi)] = qh_F\hat{N}_F[\hat{F}(\xi; \hat{q}), \hat{\theta}(\xi; \hat{q})], \quad (2.25)$$

$$(1 - \hat{q})\mathcal{E}_\theta[\hat{\theta}(\xi; \hat{q}) - \theta^0(\xi)] = qh_\theta\hat{N}_\theta[\hat{F}(\xi; \hat{q}), \hat{\theta}(\xi; \hat{q})], \quad (2.26)$$

$$\hat{F}(0; \hat{q}) = V_p, \quad \hat{F}'(0; \hat{q}) = 1 + S_v\hat{F}''(0; \hat{q}) \quad \text{and} \quad \hat{\theta}(0; \hat{q}) = 1 + S_t\hat{\theta}'(0; \hat{q}), \quad (2.27)$$

$$\hat{F}(\xi; \hat{q}) = A \quad \text{and} \quad \hat{\theta}(\xi; \hat{q}) \rightarrow 0 \quad \text{as} \quad \xi \rightarrow \infty, \quad (2.28)$$

$$\begin{aligned} \hat{N}_F[\hat{F}(\xi; \hat{q}), \hat{\theta}(\xi; \hat{q})] = & \frac{1}{(1 - \phi)^{2.5} \left(1 - \phi + \phi \frac{\rho_s}{\rho_f}\right)} \left((1 + 2\gamma_1\xi)\hat{F}'''' + 2\gamma_1\hat{F}''' - M_1\hat{F}' \right. \\ & \left. + \hat{M}^2(1 - \phi)^{2.5}(A - \hat{F}') \right) \\ & + \hat{F}\hat{F}'' + A^2 - (1 + \hat{F}_r)\hat{F}'^2 + \frac{\left(1 - \phi + \phi \frac{\rho_s\beta_s}{\rho_f\beta_f}\right)}{\left(1 - \phi + \phi \frac{\rho_s}{\rho_f}\right)} \beta_1\hat{\theta}, \end{aligned} \quad (2.29)$$

$$\begin{aligned} \hat{N}_\theta[\hat{F}(\xi; \hat{q}), \hat{\theta}(\xi; \hat{q})] = & \frac{k_{nf}/k_f}{\left(1 - \phi + \phi \frac{(\rho C_p)_s}{(\rho C_p)_f}\right)} [(1 + 2\gamma_1\xi)\hat{\theta}'' + 2\gamma_1\hat{\theta}'] \\ & + Pr[\hat{F}\hat{\theta}' - \hat{F}'\hat{\theta}]. \end{aligned} \quad (2.30)$$

The values of embedding parameter \hat{q} lies in the interval $[0,1]$. For $\hat{q} = 0$ and $\hat{q} = 1$ we have

$$\hat{F}(\xi; 0) = F^0(\xi), \quad \hat{\theta}(\xi; 0) = \theta^0(\xi),$$

$$\hat{F}(\xi; 1) = F(\xi), \quad \hat{\theta}(\xi; 1) = \theta(\xi). \quad (2.31)$$

2.3.2 m^{th} – order systems

The deformation system at this order are

$$\mathcal{E}_F[F_m(\xi) - \chi_m F_{m-1}(\xi)] = h_F R_m^F(\xi), \quad (2.32)$$

$$\mathcal{E}_\theta[\theta_m(\xi) - \chi_m \theta_{m-1}(\xi)] = h_\theta R_m^\theta(\xi), \quad (2.33)$$

$$F_m(0) = 0, \quad F'_m(0) = S_\nu F''_m(0) \quad \text{and} \quad \theta_m(0) = S_t \theta'_m(0), \quad (2.34)$$

$$F'_m \rightarrow 0 \quad \text{and} \quad \theta_m \rightarrow 0 \quad \text{as} \quad \xi \rightarrow \infty. \quad (2.35)$$

Nonlinear operators for momentum and energy equations are

$$\begin{aligned} R_m^F(\xi) &= \frac{1}{(1-\phi)^{2.5} \left(1 - \phi + \phi \frac{\rho_s}{\rho_f}\right)} \left((1 + 2\gamma_1 \xi) F'''_{m-1} + 2\gamma_1 F''_{m-1} - M_1 F'_{m-1} \right) \\ &+ \sum_{k=0}^{m-1} \left(F_{m-1-k} F''_k - (1 + \hat{F}_r) F'_{m-1-k} F'_k - \frac{\hat{M}^2}{\left(1 - \phi + \phi \frac{\rho_s}{\rho_f}\right)} F'_k \right) \\ &+ \left(\frac{\hat{M}^2 A}{\left(1 - \phi + \phi \frac{\rho_s}{\rho_f}\right)} + A^2 \right) (1 - \chi_m) + \frac{\left(1 - \phi + \phi \frac{\rho_s \beta_s}{\rho_f \beta_f}\right)}{\left(1 - \phi + \phi \frac{\rho_s}{\rho_f}\right)} \beta_1 \theta_{m-1}, \end{aligned} \quad (2.36)$$

$$\begin{aligned} R_m^\theta(\xi) &= \frac{k_{nf}/k_f}{\left(1 - \phi + \phi \frac{(\rho C_p)_s}{(\rho C_p)_f}\right)} \left((1 + 2\gamma_1 \xi) \theta''_{m-1} + 2\gamma_1 \theta'_{m-1} \right) \\ &+ Pr \sum_{k=0}^{m-1} (F_{m-1-k} \theta'_k - F'_{m-1-k} \theta_k). \end{aligned} \quad (2.37)$$

By Taylor series expansion

$$F(\xi; \hat{q}) = F^0(\xi) + \sum_{m=1}^{\infty} F_m(\xi) \hat{q}^m,$$

$$F_m(\xi) = \frac{1}{m!} \frac{\partial^m}{\partial \hat{q}^m} F(\xi; \hat{q}) \Big|_{\hat{q}=0}, \quad (2.38)$$

$$\hat{\theta}(\xi; \hat{q}) = \theta^0(\xi) + \sum_{m=1}^{\infty} \theta_m(\xi) \hat{q}^m,$$

$$\theta_m(\xi) = \frac{1}{m!} \frac{\partial^m}{\partial \hat{q}^m} \theta(\xi; \hat{q}) \Big|_{\hat{q}=0}. \quad (2.39)$$

The above series (2.38) and (2.39) converge at $q = 1$ by selecting appropriate auxiliary parameter and thus one has written

$$F(\xi) = F^0(\xi) + \sum_{m=1}^{\infty} F_m(\xi), \quad (2.40)$$

$$\theta(\xi) = \theta^0(\xi) + \sum_{m=1}^{\infty} \theta_m(\xi). \quad (2.41)$$

General solutions $(F_m(\xi), \theta_m(\xi))$ of Eqs. (2.32) and (2.33) in view of special solutions $(F_m^*(\xi), \theta_m^*(\xi))$

$$F_m(\xi) = F_m^*(\xi) + \omega_1 + \omega_2 \exp(\xi) + \omega_3 \exp(-\xi), \quad (2.42)$$

$$\theta_m(\xi) = \theta_m^*(\xi) + \omega_5 \exp(\xi) + \omega_4 \exp(-\xi). \quad (2.43)$$

Using boundary conditions (2.34 and 2.35), the values of constants ω_j ($j = 1 - 5$) are

$$\begin{aligned}
\omega_3 &= \frac{1}{1+S_v} \frac{\partial F_m^*(\xi)}{\partial \xi} \Big|_{\xi=0} - \frac{S_v}{1+S_v} \frac{\partial F_m^{*2}(\xi)}{\partial \xi^2} \Big|_{\xi=0}, & \omega_1 &= -\omega_3 - F_m^*(0), \\
\omega_5 &= -\frac{S_t}{1+S_t} \frac{\partial \theta_m^*(\xi)}{\partial \xi} \Big|_{\xi=0} - \frac{1}{1+S_t} \theta_m^*(0), & \omega_2 &= \omega_4 = 0.
\end{aligned} \tag{2.44}$$

2.4 Convergence analysis

The h -curves of Al_2O_3 – water, Cu –water and TiO_2 –water nanofluids have been displayed in Figs. (2.2) – (2.4) for $F''(0)$ and $\theta'(0)$. It is observed that acceptable ranges of h_F and h_θ –curves for Al_2O_3 , Cu and TiO_2 with water base nanofluid ranges are $(-1.0 \leq h_F \leq -0.2, -0.9 \leq h_\theta \leq -0.2)$, $(-1.1 \leq h_F \leq -0.4, -0.9 \leq h_\theta \leq -0.2)$ and $(-1.0 \leq h_F \leq -0.3, -0.9 \leq h_\theta \leq -0.2)$ respectively. The admissible values of physical parameters for plotting h –curves of $Al_2O_3 - H_2O, Cu - H_2O$ and $TiO_2 - H_2O$ nanofluids include $\phi = 0.1, \hat{M} = 0.02, M_1 = \hat{F}_r = 0.01, S_v = A = \gamma_1 = V_p = 0.2, S_t = 1.0$ and $\beta_1 = 0.1$ (see Figs. (2.2) – (2.4)). Table 2.1 shows thermophysical effects of nanoparticles. Table 2.2 demonstrates convergence of homotopic solutions for the momentum and energy. It is examined that 25th, 22nd and 32th orders seems to be acceptable for velocity convergence when Al_2O_3 – water, Cu –water and TiO_2 –water nanofluids are under consideration. Further 22nd, 20th and 32th approximations are appropriate for the convergence of $\theta'(0)$ for Al_2O_3 – water, Cu – water and TiO_2 –water nanofluids.

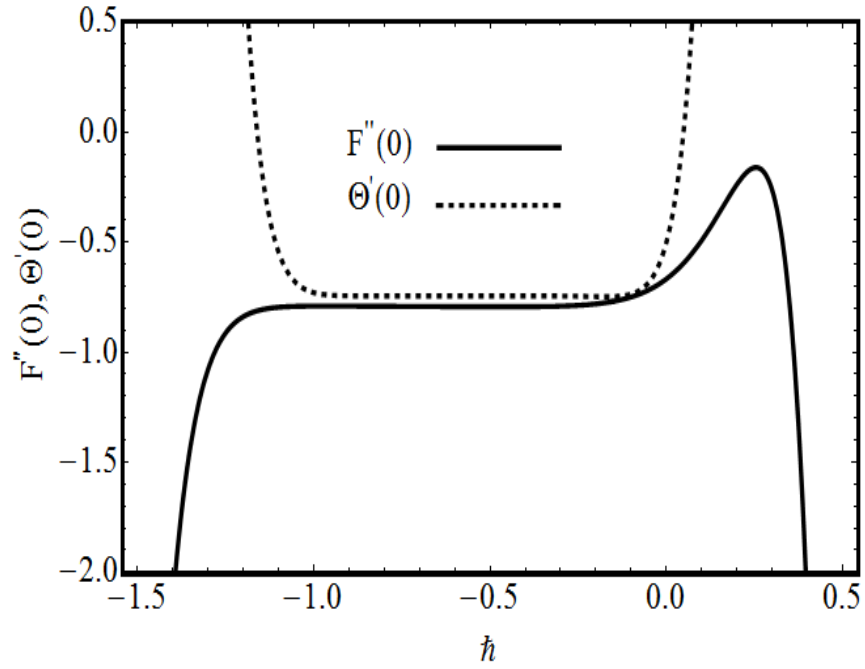


Fig. 2.2: h -curves for $Al_2O_3 - H_2O$.

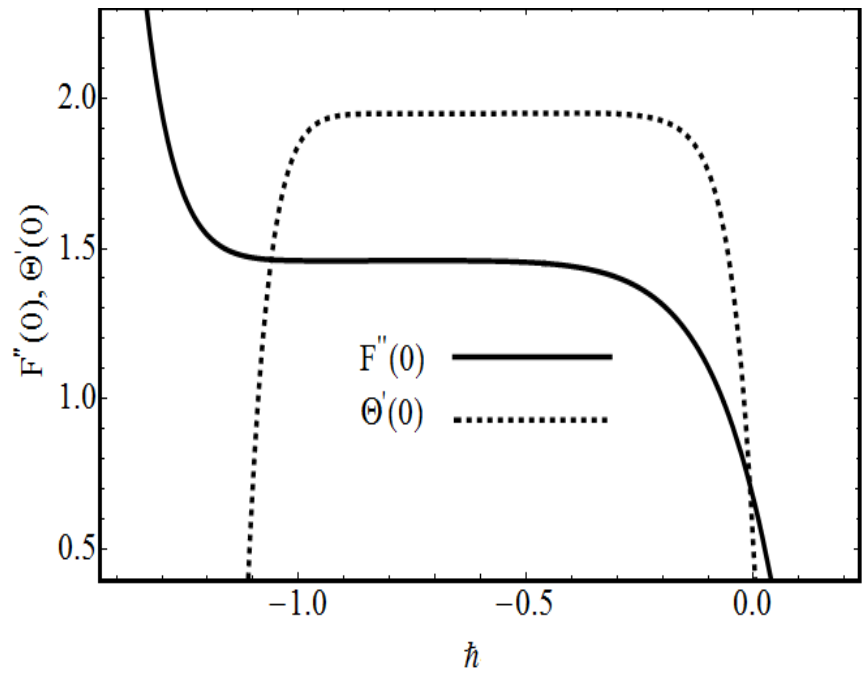


Fig. 2.3: h -curves for $Cu - H_2O$.

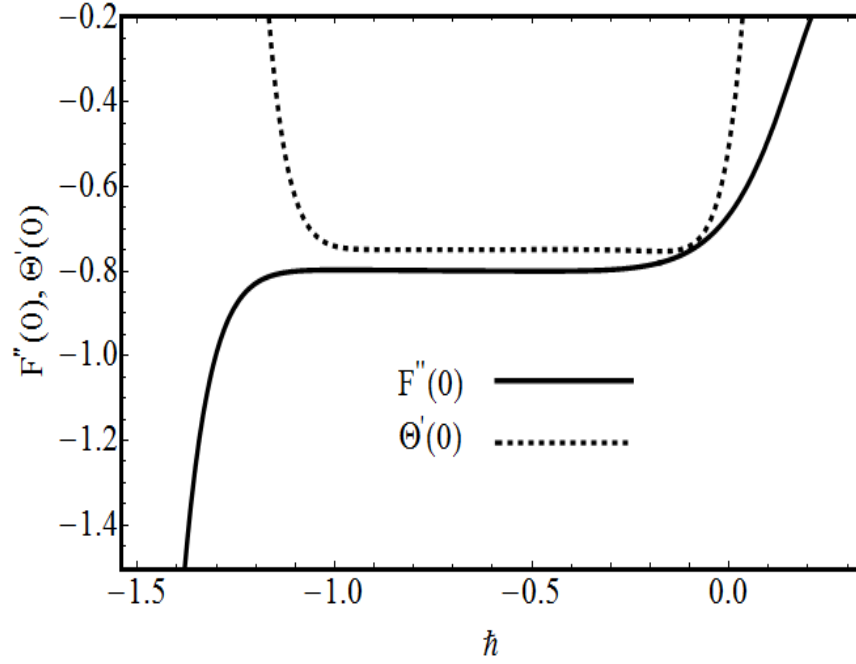


Fig. 2.4: h -curves for $TiO_2 - H_2O$.

Table 2.1: The properties of Al_2O_3 , Cu , TiO_2 and base fluid H_2O .

Formula	$\alpha \times 10^7$ m^2/sce	$\beta \times 10^{-5}$ $1/K$	k W/mK	ρ Kg/m^3	C_p J/kgK	ρC_p j/m^3k
Al_2O_3	131.7	0.85	40	3970	765	3037050
Cu	1163.1	1.67	400	8933	385	3439205
TiO_2	30.07	0.9	8.954	4250	686.2	2916350
H_2O	1.47	21	0.613	997.1	4179	4166880.9

Table 2.2: Solutions convergence for $Al_2O_3 - H_2O, Cu - H_2O, TiO_2 - H_2O$ when $S_v = A = \gamma_1 = V_p = 0.2, \phi = \beta_1 = 0.1, \hat{M} = 0.02, M_1 = \hat{F}_r = 0.01$ and $S_t = 1.0$.

Conv.	$Al_2O_3 - H_2O$		Conv.	$Cu - H_2O$		Conv.	$TiO_2 - H_2O$	
Order	$F''(0)$	$\theta'(0)$	Order	$F''(0)$	$\theta'(0)$	Order	$F''(0)$	$\theta'(0)$
1	0.72093	0.70113	1	0.74036	0.70109	1	0.70250	0.70260
10	0.79640	0.74402	8	0.89195	0.74042	8	0.70650	0.74905
15	0.78721	0.74425	15	0.89451	0.74067	13	0.74905	0.74922
22	0.77391	0.74500	20	0.88342	0.74004	22	0.77866	0.74980
25	0.77342	0.74500	22	0.88072	0.74074	30	0.77079	0.75041
30	0.77342	0.74500	28	0.88072	0.74074	35	0.77079	0.75041
32	0.77342	0.74500	35	0.88072	0.74074	40	0.77079	0.75041

2.5 Results and discussion

This section presents outcome of various pertinent variables on velocity, temperature, skin friction and local Nusselt number. Here impact of involved parameters on interested physical quantities is discussed. Velocity behavior for A is revealed in Fig. 2.5. Here velocity $F'(\xi)$ increases both for $A > 1$ and $A < 1$. The increase in A boosts up free stream velocity that ultimately enhances $F'(\xi)$. This growing behaviour of $F'(\xi)$ remained same when either free stream velocity dominates or followed. Thickness of boundary layer has reverse effects. Fig. 2.6 reflects the effect of volume fraction of nanoparticles ϕ on $F'(\xi)$. Decrease in $F'(\xi)$ is notified for increasing ϕ because with increase in nanoparticles more resistance produces consequently motion slows down. The present

study depicts the thinning effect of boundary layer due to existence of Al_2O_3 , Cu and TiO_2 nanoparticles. Here effect of Cu and TiO_2 nanoparticles are prominent when compared with copper. Figs.(2.7 and 2.8) deliberates mixed convection parameter β_1 on velocity profile for the cases known as assisting, forced and opposing convection flows. Fig. 2.7 predicts that nanofluid velocity escalates against mixed convection parameter β_1 . Basically, mixed convection parameter states the measure of buoyancy force as compare to inertia of external/free stream flow. The physical reason of an increase in velocity is due to increase in buoyancy force that acts as a favorable pressure gradient. This pressure gradient ultimately forces the fluid to be fast. A significant reduction in magnitude of velocity is noticed through Fig. 2.8 i.e. for opposing flow ($\beta_1 < 0$). For positive values of β_1 the effect of copper nanoparticles is less while for negative values opposite behavior is observed. Permeability parameter V_p effects on linear momentum are exhibited in Fig. 2.9. The fluid velocity $F'(\xi)$ decreases in the presence of nanoparticles. From Fig. 2.9 one can see the decrease in boundary layer for suction parameter. The variation of M_1 on $F'(\xi)$ is checked in Fig. 2.10. Here parameter M_1 reduces the fluid velocity because for higher values of M_1 , adhesive forces reduces. As a result, velocity and boundary layer thickness of nanofluid declines. Less velocity is noticed for Cu nanoparticles. Effect of velocity slip parameter S_v for $F'(\xi)$ is displayed in Fig. 2.11. The expected outcome of slip parameter S_v is a reduction of velocity in the neighborhood of boundary and hence declines the boundary layer thickness. This resulting behavior of velocity $F'(\xi)$ is due to decline of adhesive forces between cylindrical surface and fluid. The influences of thermal slip parameter S_t on fluid energy are delineated through Fig. 2.12. The results show the decreasing temperature with an increase in S_t . Physically decrease of temperature

difference in ambient fluid and cylinder surface is identified by diminish in temperature curves. Velocity profile for inertia coefficient \hat{F}_r is displayed via Fig. 2.13. The result shows decreasing behavior of velocity with increase of \hat{F}_r . As the increase in \hat{F}_r produces more resistance in flow field that declines velocity curve. Nusselt number and skin friction coefficients for numerous parameters such as volume fraction ϕ , curvature parameter γ_1 , permeability V_p and mixed convection parameter β_1 are displayed in Figs. (2.14 – 2.17). Increase in Nusselt number was noticed (see Figs. 2.14 and 2.15) for increasing volume fraction ϕ of nanoparticles and curvature parameter γ_1 respectively.

Increasing behavior of skin friction coefficient is also observed (see Figs. 2.16 and 2.17) versus permeability parameter V_p and mixed convection parameter β_1 , respectively. For opposing flow, reduction of skin friction coefficient is identified for larger mixed convective parameter (see Fig. 2.17).

2.6 Graphical outcomes

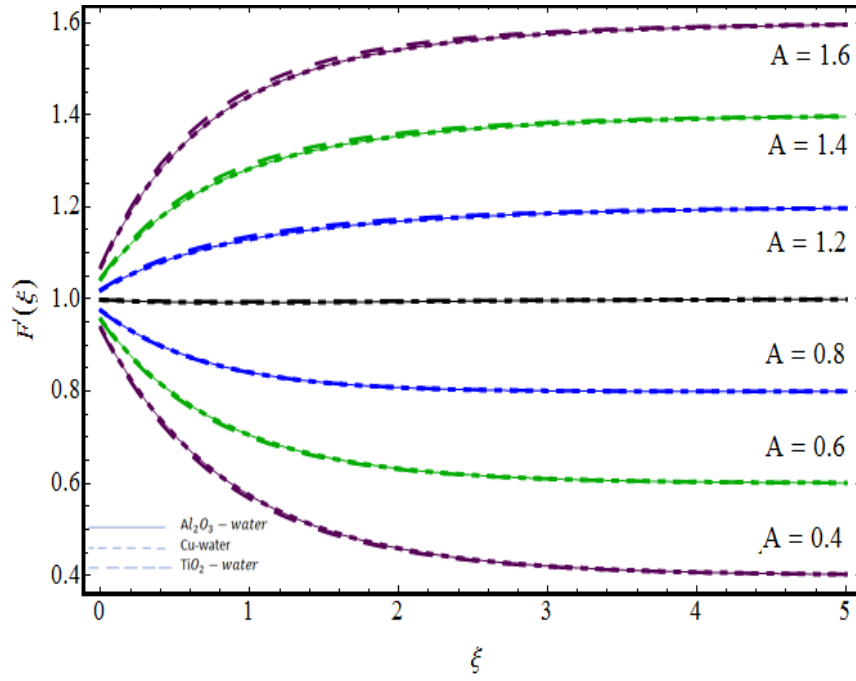


Fig. 2.5: Variation of A on $F'(\xi)$.

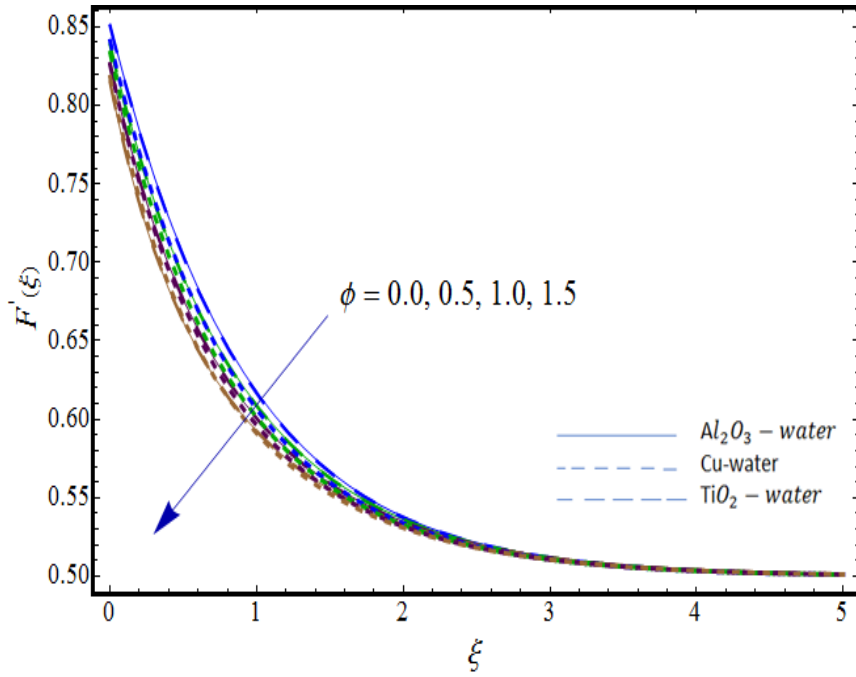


Fig. 2.6: Variation of ϕ on $F'(\xi)$.

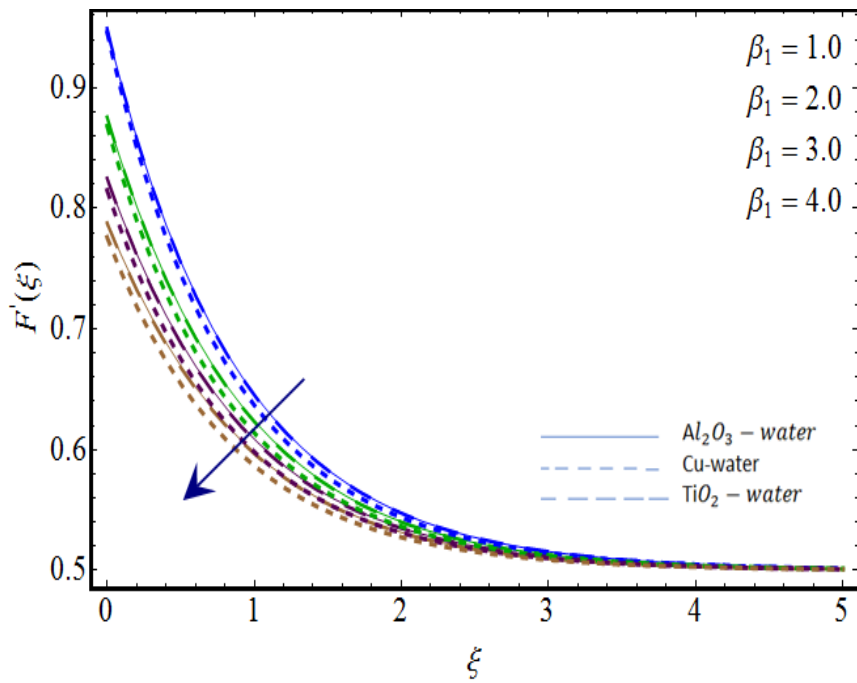


Fig. 2.7: Variation of $\beta_1 > 0$ on $F'(\xi)$.

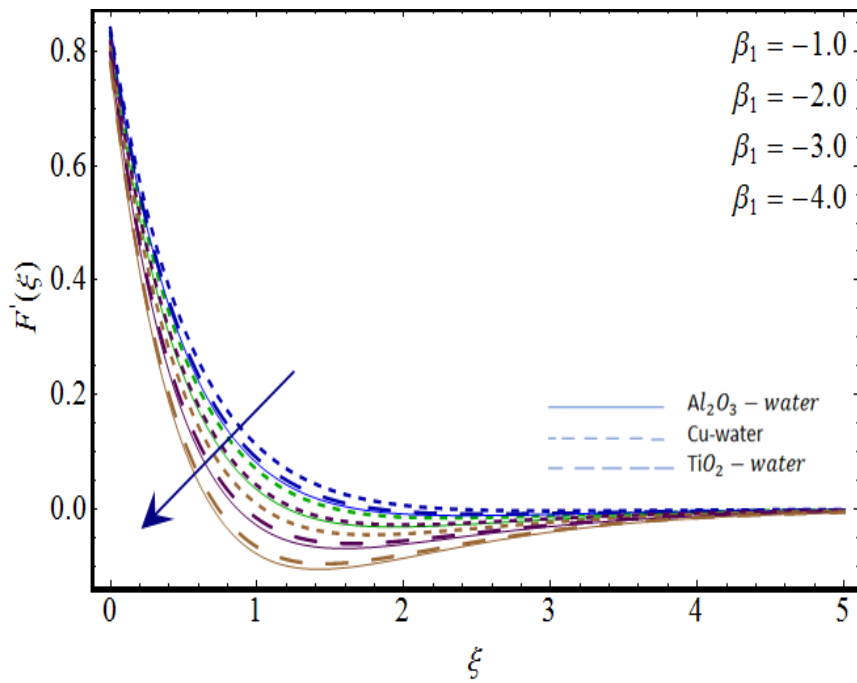


Fig. 2.8: Variation of $\beta_1 < 0$ on $F'(\xi)$.

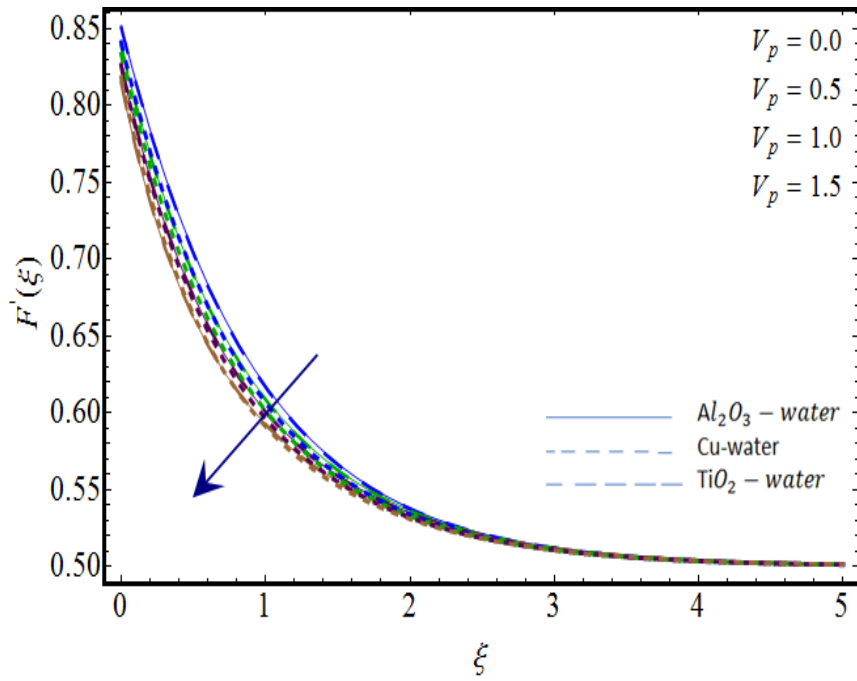


Fig. 2.9: Variation of V_p on $F'(\xi)$.

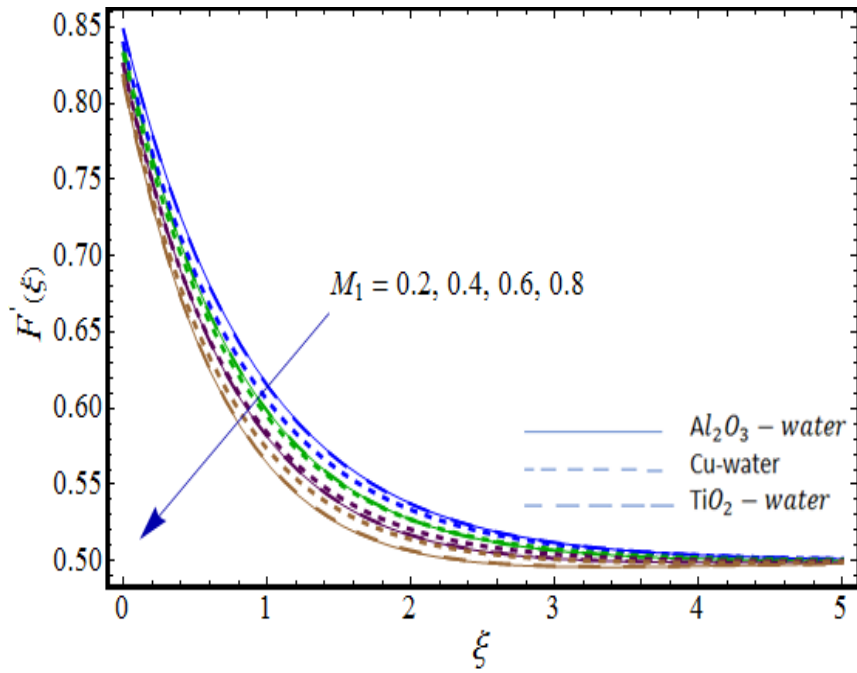


Fig. 2.10: Variation of M_1 on $F'(\xi)$.

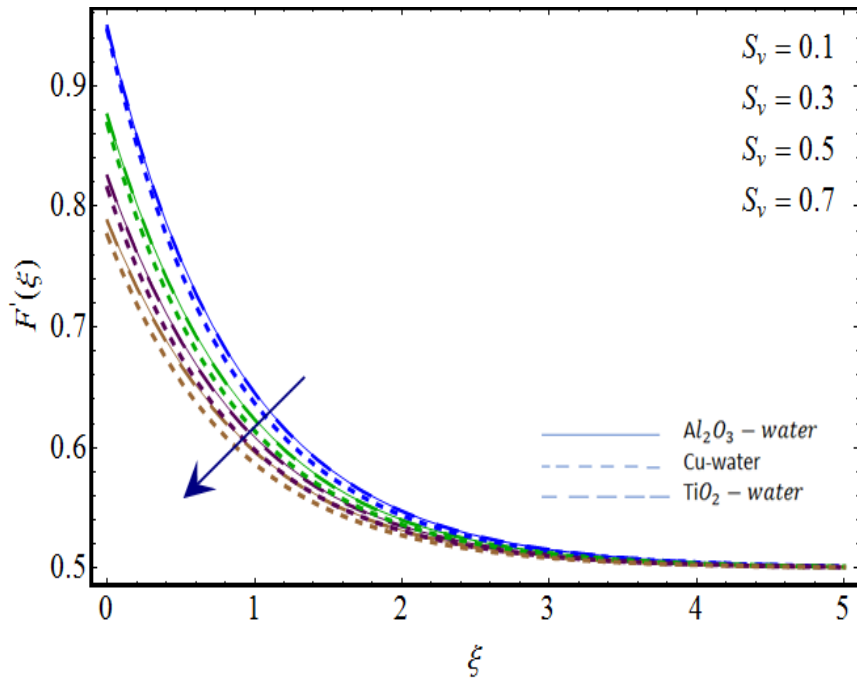


Fig. 2.11: Variation of S_v on $F'(\xi)$.

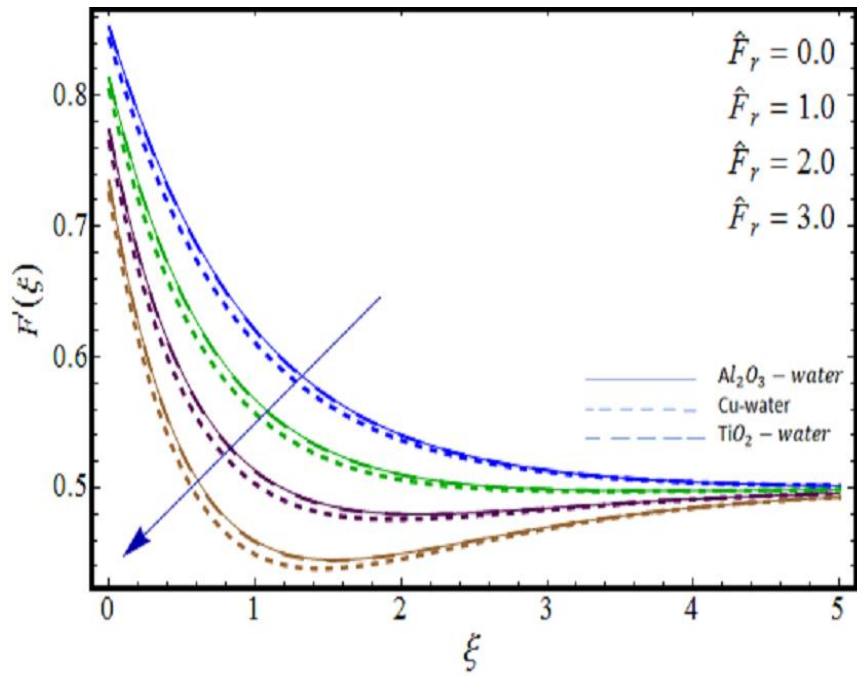


Fig. 2.12: Variation of \hat{F}_γ on $F'(\xi)$.

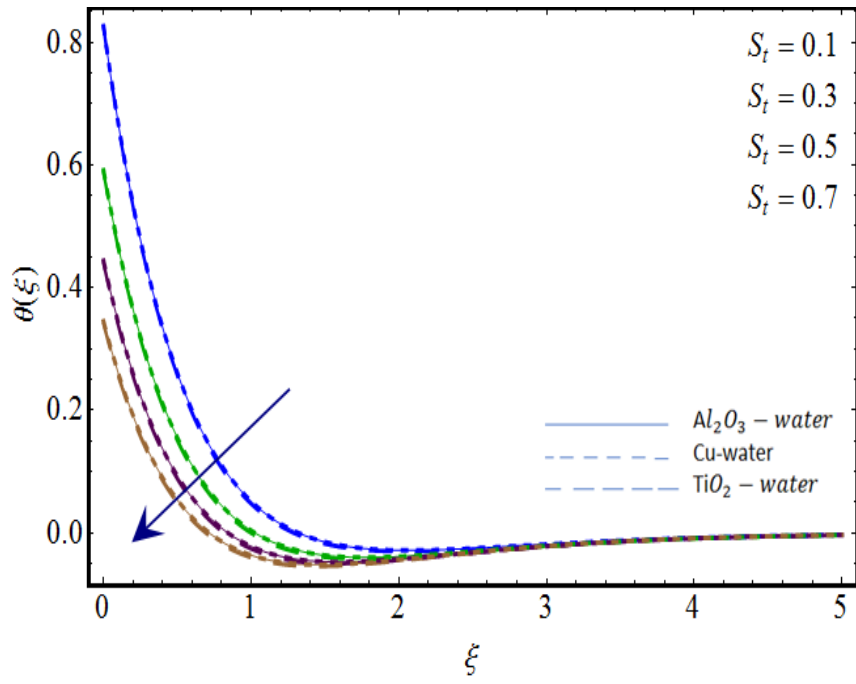


Fig. 2.13: Variation of S_t on $\theta(\xi)$.

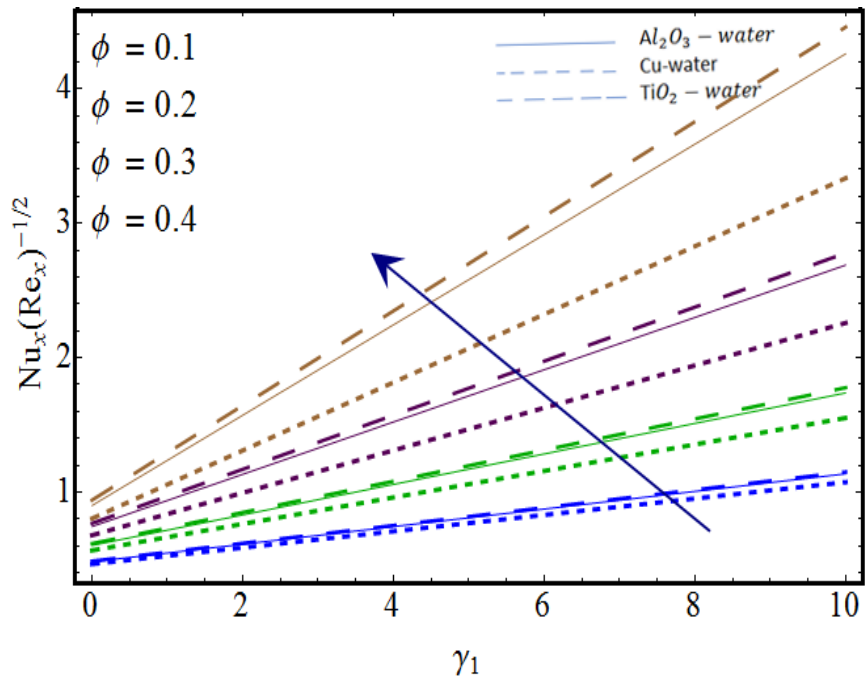


Fig. 2.14: Variation of $Nu_x(Re_x)^{-\frac{1}{2}}$ on ϕ .

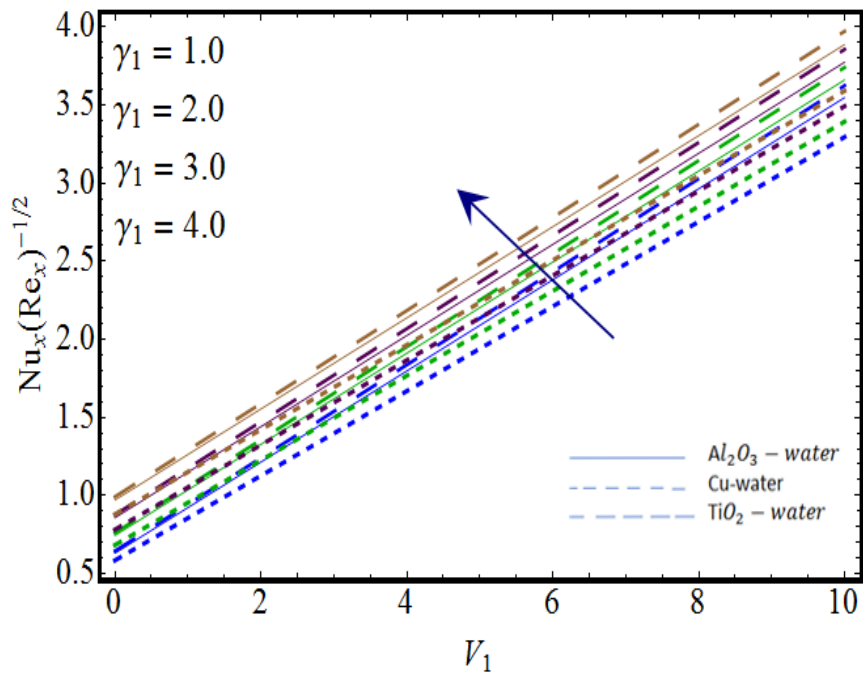


Fig. 2.15: Variation of $Nu_z(Re_z)^{-\frac{1}{2}}$ on γ_1 .

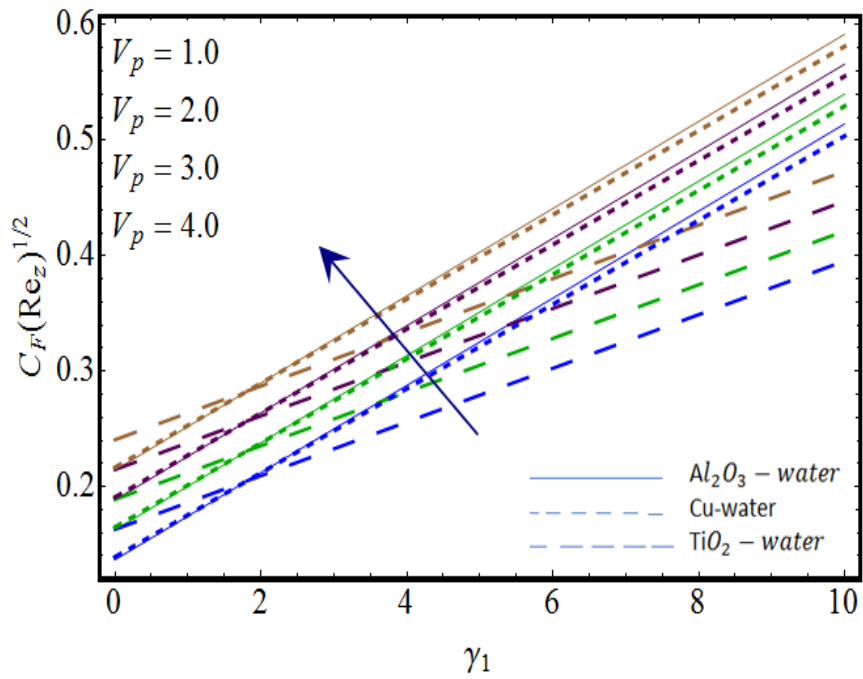


Fig. 2.16: Variation of $C_F(Re_z)^{\frac{1}{2}}$ on ϕ .

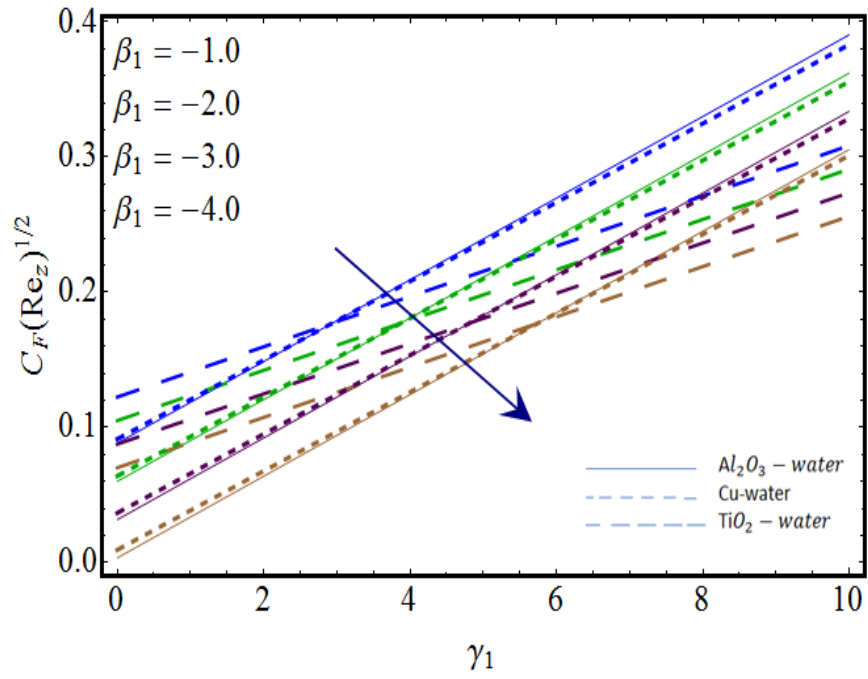


Fig. 2.17: Variation of $C_F(Re_z)^{\frac{1}{2}}$ on β_1 .

2.7 Conclusions

Major findings of presented study are as follows:

- Fluid velocity is an increasing function of volume fraction ϕ of nanoparticles.
- Impact of velocity slip parameter S_v and thermal slip parameter S_t leads to reduction in velocity and temperature respectively.
- An increase in inertia coefficient \hat{F}_r and local porosity parameter M_1 reduces velocity.
- For larger V_p and β_1 , skin friction coefficient enhances.
- Rate of heat transfer increases via larger γ_1 and ϕ .
- Velocity in all cases is noticed less for Cu nanoparticles when compared to Al_2O_3 and TiO_2 nanoparticles.

CHAPTER 3

Nonlinearly convective stratified flow of Maxwell nanofluid with activation energy

3.1 Introduction

Main objective of present chapter is to configure stratified flow of Maxwell nanofluid driven by nonlinearly stretched inclined cylinder with activation energy. Cattaneo-Christov double diffusion scheme is utilized for heat and mass transfer analysis. Brownian and thermophoresis diffusions are focused in this analysis. The non-uniform heat generation/absorption and binary chemical reaction are considered for current flow configuration. Modified Arrhenius formula for activation energy is implemented. The governing flow equations are solved with the aid of homotopy technique. Velocity, temperature and concentration profiles are computed, and effects of involved flow parameters are analyzed via graphs. Both interested physical quantities i.e., Nusselt and Sherwood numbers are calculated numerically. Computed results are compared with published results in limiting case.

3.2 Mathematical formulation

Consider the nonlinear convective flow of Maxwell nanofluid with Cattaneo-Christov heat and mass diffusion model. Fluid flow is investigated by nonlinearly stretching velocity

$U_w \left(\frac{U_0 z^n}{L} \right)$ with stretching rate $U_0 > 0$. Here focus will be to analyze the effects of non-uniform heat source/sink, binary reaction, dual stratification and Arrhenius energy. Buongiorno model of nanoparticles is incorporated. The flow configuration of the system is displayed in Fig. 3.1. Temperature and concentration at cylindrical surface are $T_w = T_0 + \frac{d_1 z}{L}$ and $C_w = C_0 + \frac{d_3 z}{L}$. where as ambient temperature and concentration are stratified as $T_\infty = T_0 + \frac{d_2 z}{L}$ and $C_\infty = C_0 + \frac{d_4 z}{L}$, respectively. The modelled governing equations are:

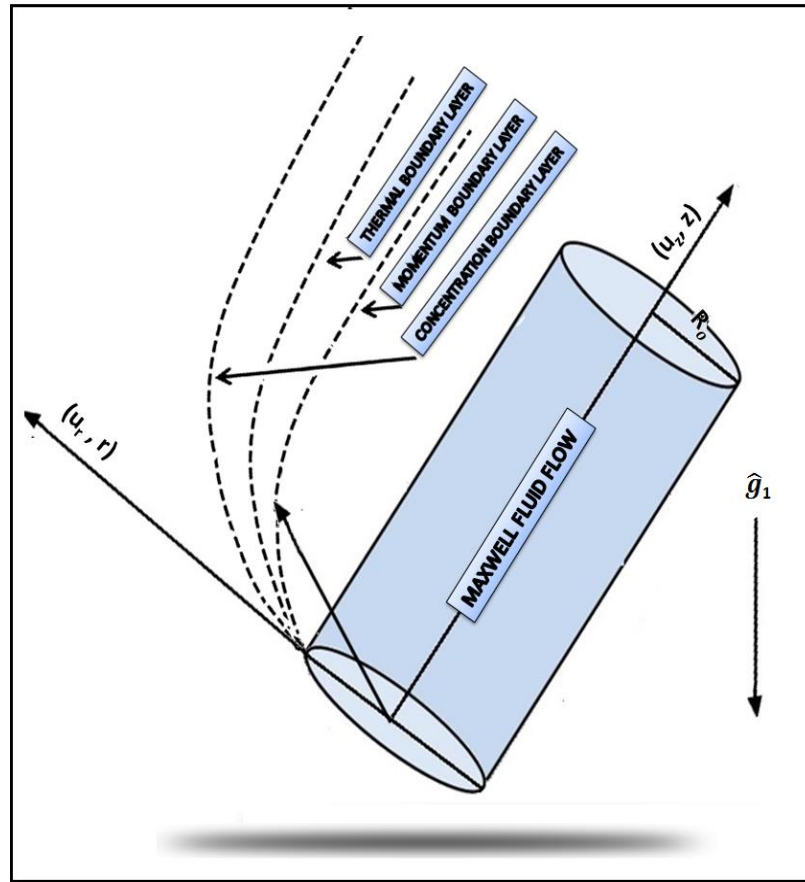


Fig. 3.1: Physical model.

$$\frac{\partial}{\partial r}(ru_r) + \frac{\partial}{\partial z}(ru_z) = 0, \quad (3.1)$$

$$\begin{aligned}
& u_z \frac{\partial u_z}{\partial z} + u_r \frac{\partial u_z}{\partial r} + \lambda_m \left(u_z^2 \frac{\partial^2 u_z}{\partial z^2} + u_r^2 \frac{\partial^2 u_z}{\partial r^2} + 2u_z u_r \frac{\partial^2 u_z}{\partial r \partial z} \right) = v_1 \frac{\partial^2 u_z}{\partial r^2} \\
& + \frac{\hat{g}_1}{\rho_f} [\Gamma_1(T - T_\infty) + \Gamma_2(T - T_\infty)^2 + \Gamma_3(C - C_\infty) + \Gamma_4(C - C_\infty)^2] \cos \phi_a.
\end{aligned} \tag{3.2}$$

According to Cattaneo-Christove double diffusive scheme [78], we have

$$\mathbf{q}_1 + \hat{\Gamma}_e \left[\frac{\partial \mathbf{q}_1}{\partial t} + \mathbf{V}_1 \cdot \nabla \mathbf{q}_1 - (\mathbf{q}_1 \cdot \nabla) \mathbf{V}_1 + (\nabla \cdot \mathbf{V}_1) \mathbf{q}_1 \right] = -\hat{k}_f \nabla T, \tag{3.3}$$

$$\mathbf{J}_1 + \hat{\Gamma}_e \left[\frac{\partial \mathbf{J}_1}{\partial t} + \mathbf{V}_1 \cdot \nabla \mathbf{J}_1 - (\mathbf{J}_1 \cdot \nabla) \mathbf{V}_1 + (\nabla \cdot \mathbf{V}_1) \mathbf{J}_1 \right] = -D_B \nabla C. \tag{3.4}$$

By taking $\hat{\Gamma}_e = \hat{\Gamma}_c = 0$, the generalized models reduce to classical form. For steady

($\frac{\partial \mathbf{q}_1}{\partial t} = \frac{\partial \mathbf{J}_1}{\partial t} = 0$) and for incompressible fluid ($\nabla \cdot \mathbf{V}_1 = 0$) one has

$$\mathbf{q}_1 + \hat{\Gamma}_e [\mathbf{V}_1 \cdot \nabla \mathbf{q}_1 - (\mathbf{q}_1 \cdot \nabla) \mathbf{V}_1] = -\hat{k}_f \nabla T, \tag{3.5}$$

$$\mathbf{J}_1 + \hat{\Gamma}_e [\mathbf{V}_1 \cdot \nabla \mathbf{J}_1 - (\mathbf{J}_1 \cdot \nabla) \mathbf{V}_1] = -D_B \nabla C. \tag{3.6}$$

The energy and concentration equations for non-uniform heat source/sink, Arrhenius energy, thermophoresis and Brownian motion are

$$\begin{aligned}
& u_r \frac{\partial T}{\partial r} + u_z \frac{\partial T}{\partial z} + \hat{\Gamma}_e \Pi_e = \frac{\hat{k}_f}{(\rho C_p)_f} \frac{1}{r} \frac{\partial}{\partial r} \left(r \frac{\partial T}{\partial r} \right) + \frac{\hat{Q}_m}{(\rho C_p)_f} \\
& + \tau_1 D_B \frac{\partial C}{\partial r} \frac{\partial T}{\partial r} + \frac{\tau_1 D_T}{T_\infty} \left(\frac{\partial T}{\partial r} \right)^2,
\end{aligned} \tag{3.7}$$

$$\begin{aligned}
& u_r \frac{\partial C}{\partial r} + u_z \frac{\partial C}{\partial z} + \hat{\Gamma}_c \Pi_c = D_B \frac{\partial}{\partial r} \left(r \frac{\partial C}{\partial r} \right) + \frac{D_T}{T_\infty} \frac{1}{r} \frac{\partial}{\partial r} \left(r \frac{\partial T}{\partial r} \right) \\
& - \hat{K}_1 (C - C_\infty) - \hat{K}_r^2 (C_w - C_0) \left(\frac{T}{T_\infty} \right)^p \exp \left[-\frac{E_1}{T k^*} \right],
\end{aligned} \tag{3.8}$$

with

$$\left. \begin{aligned} u_z &= \frac{U_0 z^m}{L}, & T &= T_w = T_0 + \frac{d_1 z}{L}, \\ u_r &= V_1, & C &= C_w = C_0 + \frac{d_3 z}{L} \end{aligned} \right| \text{at } r = R_0, \quad (3.9)$$

$$\left. \begin{aligned} u_z &\rightarrow 0, & T &\rightarrow T_\infty = T_0 + \frac{d_2 x}{L}, \\ u_r &\rightarrow 0, & C &\rightarrow C_\infty = C_0 + \frac{d_4 x}{L}. \end{aligned} \right| \text{when } r \rightarrow \infty, \quad (3.10)$$

$$\begin{aligned} \Pi_e &= u_r^2 \frac{\partial^2 T}{\partial r^2} + u_z^2 \frac{\partial^2 T}{\partial z^2} + \frac{\partial T}{\partial r} \left(u_z \frac{\partial u_r}{\partial z} + u_r \frac{\partial u_r}{\partial r} \right) + 2u_z u_r \frac{\partial^2 C}{\partial r \partial z} \\ &+ \frac{\partial T}{\partial z} \left(u_z \frac{\partial u_z}{\partial z} + u_r \frac{\partial u_r}{\partial r} \right), \end{aligned} \quad (3.11)$$

$$\begin{aligned} \Pi_c &= u_r^2 \frac{\partial^2 C}{\partial r^2} + u_z^2 \frac{\partial^2 C}{\partial z^2} + \frac{\partial C}{\partial r} \left(u_z \frac{\partial u_r}{\partial z} + u_r \frac{\partial u_r}{\partial r} \right) + 2u_r u_z \frac{\partial^2 C}{\partial r \partial z} \\ &+ \frac{\partial C}{\partial z} \left(u_z \frac{\partial u_z}{\partial z} + u_r \frac{\partial u_r}{\partial r} \right). \end{aligned} \quad (3.12)$$

The non-uniform heat source/sink \hat{Q}_m [79] is defined as

$$\hat{Q}_m = \frac{U_w \hat{k}_f}{z \nu_1} \left[\hat{B}_1 (T_w - T_0) \frac{\partial F}{\partial \xi} + \hat{B}_2 (T - T_\infty) \right], \quad (3.13)$$

where \hat{B}_1 and \hat{B}_2 are for space and temperature dependent coefficients of heat source /sink. By introducing the following transformations [80]

$$\begin{aligned} \xi &= \sqrt{\frac{(m+1)U_0 z^{m-1}}{2Lv_1} \left(\frac{r^2 - R_0^2}{2R_0} \right)}, & \Psi_1(\xi) &= \sqrt{\frac{2}{m+1} \frac{\nu_1 U_0 z^{m+1}}{L}} F(\xi), \\ \theta(\xi) &= \frac{T - T_\infty}{T_w - T_0}, & \Phi(\xi) &= \frac{C - C_\infty}{C_w - C_0}, & u_z(\xi) &= \frac{U_0 z^m}{L} F'(\xi), \\ u_r(\xi) &= -\frac{R_0}{r} \sqrt{\frac{(m+1)\nu_1 U_0 z^{m-1}}{2L}} \left[F(\xi) + \xi \left(\frac{m-1}{m+1} \right) F'(\xi) \right]. \end{aligned} \quad (3.14)$$

The flow expressions under above transformations take the form

$$\begin{aligned}
& (1 + 2\gamma_1\xi)F'''' - \frac{2m}{m+1}F'^2 + FF'' + \gamma_1F'' - \beta_2 \left((3m-1)F''F'F + \frac{2m(m-1)}{m+1}F'^3 \right) \\
& - \beta_2 \left(\frac{m+1}{2} \left(F'''F^2 + \gamma_1(1+2\gamma_1\xi)^{-1} \left(F + \xi \frac{m-1}{m+1} F' \right)^2 \right) F'' \right) - \beta_2 \left(\frac{m-1}{2} \right) \xi F'^2 F'' \\
& + \frac{2}{m+1} \beta_1 [(1 + \hat{\beta}_t \theta) \theta + \hat{N}_1 (1 + \hat{\beta}_c \Phi)] \cos \phi_a = 0,
\end{aligned} \tag{3.15}$$

$$\begin{aligned}
& (1 + 2\gamma_1\xi) \left[\theta'' + Pr \hat{N}_b \left(\theta' \Phi' + \frac{\hat{N}_t}{\hat{N}_b} \theta'^2 + Ec F''^2 \right) \right] + 2\gamma_1 \theta' + Pr \theta \theta' \\
& - Pr \delta_e \left[\frac{m+1}{2} (\theta'' F^2 - FF' \theta') + \frac{2}{m+1} (S_1 + \theta) \left(m F'^2 - \frac{m+1}{2} FF'' \right) \right] \\
& + \frac{2}{m+1} (\hat{B}_1 F' + \hat{B}_2 \theta) - \frac{2}{m+1} Pr (S_1 + \theta) F' = 0,
\end{aligned} \tag{3.16}$$

$$\begin{aligned}
& (1 + 2\gamma_1\xi) \left(\Phi'' + \frac{\hat{N}_t}{\hat{N}_b} \theta'' \right) + 2\gamma_1 \Phi' + Sc F \Phi' + 2\gamma_1 \left(\frac{\hat{N}_t}{\hat{N}_b} \right) \theta' - \frac{2}{m+1} Sc \gamma_2 \Phi \\
& - Sc \delta_c \left[\left(\frac{m+1}{2} \right) (\Phi'' F^2 - FF' \Phi') + \frac{2}{m+1} (S_2 + \Phi) \left(m F'^2 - \frac{m+1}{2} FF'' \right) \right] \\
& - \frac{2}{m+1} Sc (S_2 + \Phi) F' - Sc \gamma_3 (1 + \delta \theta)^p \exp \left[-\frac{E_a}{1 + \delta \theta} \right] = 0,
\end{aligned} \tag{3.17}$$

with

$$\begin{aligned}
& F'(\xi) = 1, \quad F(\xi) = 0, \quad \theta(\xi) = 1 - S_1, \quad \Phi(\xi) = 1 - S_2 \quad \text{at } \xi = 0, \\
& F'(\xi) = 0, \quad \theta(\xi) = 0, \quad \Phi(\xi) = 0, \quad \text{as } \xi \rightarrow \infty,
\end{aligned} \tag{3.18}$$

where physical flow parameters are defined as

$$\begin{aligned}
\gamma_1 &= \sqrt{\frac{2}{m+1} \frac{Lv_1}{R_0^2 U_0}} z^{-\frac{m-1}{2}}, \delta_e = \frac{U_0 \hat{\Gamma}_e z^{m-1}}{L}, \hat{N}_1 = \frac{\Gamma_3 (C_w - C_0)}{\Gamma_1 (T_w - T_0)}, Sc = \frac{\nu_1}{D_B}, S_1 = \frac{d_2}{d_1}, \\
\hat{\beta}_c &= \frac{\Gamma_4 (C_w - C_0)}{\Gamma_3}, Gr = \frac{\hat{g}_1 \Gamma_1 (T_w - T_0) z^3}{\nu_1^2}, \hat{N}_t = \frac{\tau_1 D_T (T_w - T_0)}{T_\infty \nu_1}, E_a = \frac{E_1}{T_\infty k^*}, \\
\hat{N}_b &= \frac{\tau_1 D_B (C_w - C_0)}{\nu_1}, Ec = \frac{U_w^2}{C_p (T_w - T_0)}, Gr^* = \frac{\hat{g}_1 \Gamma_3 (C_w - C_0) z^3}{\nu_1^2}, \\
\gamma_2 &= \frac{K_1 L}{U_0 z^{m-1}}, \gamma_3 = \frac{L \hat{K}_r^2}{U_0 z^{m-1}}, \delta = \frac{(T_w - T_0)}{T_\infty}, \hat{\beta}_t = \frac{\Gamma_2 (T_w - T_0)}{\Gamma_1}.
\end{aligned} \tag{3.19}$$

Physical entities near surface are defined as

$$C_F = \frac{2\tau_w}{\rho_f U_w^2}, \quad Nu_z = \frac{zq_w}{\hat{k}_f (T_w - T_0)}, \quad Sh_z = \frac{zj_w}{D_B (C_w - C_0)}, \tag{3.20}$$

where wall shear stress, wall heat and mass flux are defined as

$$\tau_w = (1 + \beta_2) \frac{\partial u_z}{\partial r} \Big|_{r=R_0}, \quad q_w = -\hat{k}_f \frac{\partial T}{\partial r} \Big|_{r=R_0}, \quad j_w = -D_B \frac{\partial C}{\partial r} \Big|_{r=R_0}. \tag{3.21}$$

In non-dimensional variables we have

$$\begin{aligned}
\frac{1}{2} C_F (Re_z)^{\frac{1}{2}} &= \left(\frac{m+1}{2} \right)^{\frac{1}{2}} (1 + \beta_2) F''(0), \\
Nu_z (Re_z)^{-\frac{1}{2}} &= - \left(\frac{m+1}{2} \right)^{\frac{1}{2}} \theta'(0), \\
Sh_z (Re_z)^{-\frac{1}{2}} &= - \left(\frac{m+1}{2} \right)^{\frac{1}{2}} \Phi'(0),
\end{aligned} \tag{3.22}$$

here $Re_z = \frac{z^{m+1} U_0}{Lv_1}$ is the local Reynold number.

3.3 Methodology

The coupled nonlinear system (3.15) to (3.18) is tackled analytically with the help of HAM. The comprehensive description of HAM is provided below:

The initial approximations $(F^0(\xi), \theta^0(\xi), \Phi^0(\xi))$ and auxiliary linear operators $(\mathcal{E}_F, \mathcal{E}_\theta, \mathcal{E}_\Phi)$ are

$$\begin{aligned} F^0(\xi) &= 1 - \exp(-\xi), \\ \theta^0(\xi) &= (1 - S_1) \exp(-\xi), \\ \Phi^0(\xi) &= (1 - S_2) \exp(-\xi), \end{aligned} \quad (3.24)$$

$$\mathcal{E}_F[F] = F''' - F', \quad \mathcal{E}_\theta[\theta] = \theta'' - \theta, \quad \mathcal{E}_\Phi[\Phi] = \Phi'' - \Phi, \quad (3.25)$$

with properties

$$\begin{aligned} \mathcal{E}_F[\omega_2 \exp(-\xi) + \omega_1 + \omega_3 \exp(\xi)] &= 0, \\ \mathcal{E}_\theta[\omega_4 \exp(-\xi) + \omega_5 \exp(\xi)] &= 0, \\ \mathcal{E}_\Phi[\omega_6 \exp(-\xi) + \omega_7 \exp(\xi)] &= 0. \end{aligned} \quad (3.26)$$

According to procedure (see Ref. [81]), one has

$$F_m(\xi) = F_m^*(\xi) + \omega_1 + \omega_2 \exp(-\xi) + \omega_3 \exp(\xi), \quad (3.27)$$

$$\theta_m(\xi) = \theta_m^*(\xi) + \omega_5 \exp(\xi) + \omega_4 \exp(-\xi), \quad (3.28)$$

$$\Phi_m(\xi) = \Phi_m^*(\xi) + \omega_7 \exp(\xi) + \omega_6 \exp(-\xi), \quad (3.29)$$

where $(F_m^*(\xi), \theta_m^*(\xi), \Phi_m^*(\xi))$ are the special solutions and w_j ($j = 1 - 7$) are the arbitrary constant given by

$$\begin{aligned}
\omega_1 &= -\hat{F}'_m(0) + \left. \frac{\partial F^*_m(\xi)}{\partial \xi} \right|_{\xi=0}, & \omega_2 &= \left. \frac{\partial F^*_m(\xi)}{\partial \xi} \right|_{\xi=0}, & \omega_4 &= -\theta^*_m(\xi)|_{\xi=0}, \\
\omega_6 &= -\Phi^*_m(\xi)|_{\xi=0} & \omega_3 &= \omega_5 = \omega_7 = 0.
\end{aligned} \tag{3.30}$$

3.4 Convergence analysis

Auxiliary parameters involved in HAM provide great freedom to find region of convergence for velocity $F''(0)$, temperature $\theta'(0)$, and concentration $\Phi'(0)$ profiles. Therefore, h -curves of 20th order approximation are shown in Fig. 3.2. Permissible values of h_F , h_θ and h_Φ lie in the ranges $(-1.7 \leq h_F \leq -0.7)$, $(-1.6 \leq h_\theta \leq -0.9)$ and $(-1.5 \leq h_\Phi \leq -0.8)$. Table 3.1 suggested that 26th, 30th and 20th order of approximations for $F''(0)$, $\theta'(0)$ and $\Phi'(0)$ are sufficient for convergence. For the present analysis, we have considered the following values of emerging parameters.

$$\gamma_1 = \beta_2 = S_1 = \delta_c = 0.3, \quad Pr = Sc = 1.5, \quad \hat{\beta}_t = S_2 = \hat{B}_1 = \hat{\beta}_c = \delta_e = \hat{B}_2 = 0.2, \quad \gamma_3 = \hat{N}_1 = E_a = \delta = 1.0, \quad p = \hat{N}_t = m = \beta_1 = \hat{N}_b = 0.5, \quad \gamma_2 = 0.9, \quad Ec = 1.0 \quad \text{and} \quad \phi_a = \frac{\pi}{4}.$$

Table 3.2 shows local Nusselt number Nu_z and Sherwood number Sh_z variations versus involving parameters. Local Nusselt number enlarges against δ_e , Pr and S_2 while reverse effects are recorded against \hat{B}_1 , \hat{N}_t , S_1 and δ_c on it. Additionally, Sherwood number enhances versus δ_e , \hat{N}_b , S_2 , Pr and \hat{B}_1 while it declines against S_1 and \hat{N}_t . Tables 3.3 and 3.4 are computed to compare numerical results of $F''(0)$ and $\theta'(0)$ with literature. This comparison shows that current results have good agreement with reported literature.

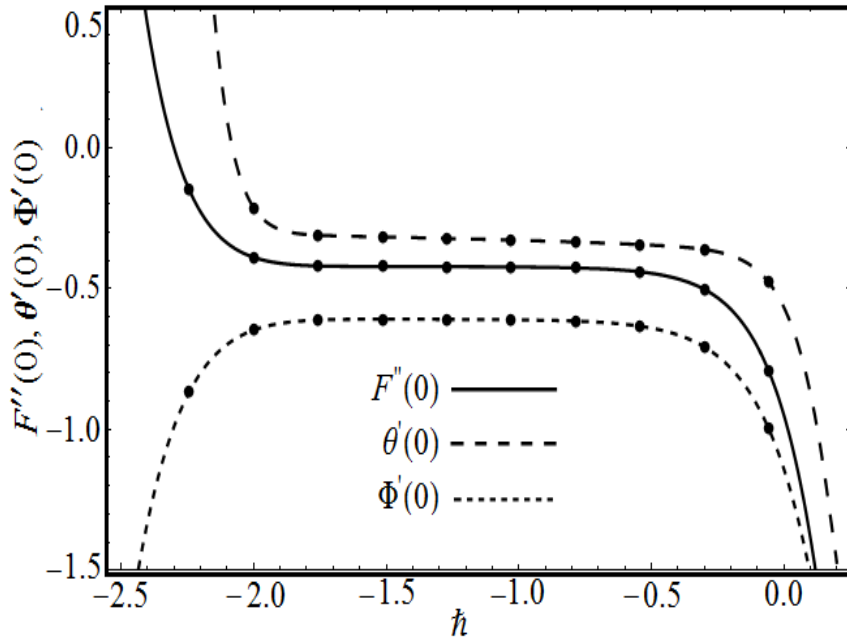


Fig. 3.2: h -curves.

Table 3.1: Convergence analysis of $F''(0), \theta'(0)$ and $\Phi'(0)$ when $\gamma_1 = \beta_2 = S_1 = \delta_c = 0.3, Sc = Pr = 1.5, \hat{B}_1 = \hat{\beta}_c = S_2 = \hat{\beta}_t = \delta_e = \hat{B}_2 = 0.2, \hat{N}_1 = 1.0, p = m = \hat{N}_t = \beta_1 = \hat{N}_b = 0.5, \gamma_1 = 0.9, Ec = \gamma_3 = E_a = \delta = 1.0$ and $\phi_a = \frac{\pi}{4}$.

Approximation Order	$-F''(0)$	$-\theta'(0)$	$-\Phi'(0)$
1	0.38642	0.30745	0.58247
5	0.39123	0.32012	0.58479
11	0.39627	0.31426	0.58640
16	0.40878	0.32562	0.58718
20	0.41403	0.32766	0.58956
26	0.42891	0.33412	0.58956
30	0.42891	0.33694	0.58956
36	0.42891	0.33694	0.58956

Table 3.2: Computed results of $Nu_z(Re_z)^{-\frac{1}{2}}$ and $Sh_z(Re_z)^{-\frac{1}{2}}$ when $\gamma_2 = 0.9$, $\gamma_1 = \beta_2 = 0.3, \gamma_3 = \hat{N}_1 = E_a = \delta = Ec = 1.0, Sc = 1.5, \hat{\beta}_t = \hat{\beta}_c = 0.2$, $n = \beta_1 = p = 0.5$ and $\phi_a = \frac{\pi}{4}$.

Pr	\hat{N}_b	\hat{N}_t	S_1	S_2	δ_c	δ_e	B_1	$-\left(\frac{n+1}{2}\right)^{\frac{1}{2}} \theta'(0)$	$-\left(\frac{n+1}{2}\right)^{\frac{1}{2}} \Phi'(0)$
0.6	0.5	0.5	0.3	0.2	0.3	0.2	0.2	0.63743	0.58893
1.4								0.85856	0.75205
2.0								1.01772	1.00130
1.5	0.1	0.5	0.3	0.2	0.3	0.2	0.2	0.80632	0.05884
	0.6							0.78427	0.87407
	0.8							0.73593	0.98916
1.5	0.5	0.1	0.3	0.2	0.3	0.2	0.2	0.86094	0.93704
		0.6						0.77561	0.49833
		0.8						0.70283	0.12053
1.5	0.5	0.5	0.0	0.2	0.3	0.2	0.2	0.86719	0.87640
			0.3					0.83011	0.82077
			0.5					0.77059	0.76344
1.5	0.5	0.5	0.3	0.0	0.3	0.2	0.2	0.75056	1.27534
				0.3				0.77575	1.34103
				0.5				0.79540	0.84569
1.5	0.5	0.5	0.3	0.2	0.1	0.2	0.2	0.88566	0.86745
					0.4			0.88539	0.87342
					0.5			0.87520	0.89011
1.5	0.5	0.5	0.3	0.2	0.3	0.1	0.2	0.76876	0.85878
						0.4		0.78456	0.87453
						0.5		0.79348	0.88324
1.5	0.5	0.5	0.3	0.2	0.3	0.2	0.1	0.85432	0.95759
							0.3	0.81672	0.98432
							0.5	0.76043	1.21434

Table 3.3: Comparative values of $-\theta'(0)$ via m and Ec when $Pr = 1.5$.

Ec	m	Ref. [82]	Present results
0.0	0.5	0.595277	0.59538
	1.5	0.574537	0.57457
	3.0	0.564472	0.56452
1.0	0.5	0.556623	0.55671
	1.5	0.530966	0.53085
	3.0	0.517977	0.51788

Table 3.4: Comparative values of $-F''(0)$ when $\gamma_1 = \beta_1 = \hat{\beta}_t = \hat{N}_1 = \hat{\beta}_c = \phi_a = 0$.

β_2	Ref. [83]	Ref. [84]	Present results
0.0	0.999978	0.999962	1.00001
0.3	1.101848	1.101850	1.10196
0.6	1.150160	1.150163	1.15019
0.8	1.196690	1.196692	1.19676
1.2	1.285253	1.285257	1.28538
1.6	1.368641	1.368641	1.36867
2.0	1.447616	1.447617	1.44783

3.5 Results and discussion

In current section calculated results are described briefly and concisely. Figs. (3.3) – (3.7) are revealed to show the influence of γ_1 , β_2 , $\hat{\beta}_t$, $\hat{\beta}_c$ and ϕ_a on $F'(\xi)$. Fig. 3.3 shows the feature of curvature parameter γ_1 on $F'(\xi)$. This figure strengthens the physical phenomenon that curved cylindrical surface is favourable for fluid movement i.e. enhancement in curvature causes acceleration in velocity. Impacts of Deborah number β_2 on $F'(\xi)$ are presented through Fig. 3.4. This figure shows that β_2 enlarges velocity profile. It happens because larger values of β_2 enhances the relaxation time which resists the fluid motion and as a result $F'(\xi)$ decreases. Variations of $\hat{\beta}_t$ and $\hat{\beta}_c$ on velocity distribution $F'(\xi)$ are shown in Figs. 3.5 and 3.6. For higher estimation of $\hat{\beta}_t$, velocity is accelerated because $\hat{\beta}_t$, enlarges enthalpy i.e. $(T_w - T_\infty)$ which alternatively enhances velocity. Also, velocity $F'(\xi)$ has increasing behaviour versus $\hat{\beta}_c$ (see Fig. 3.6). Fig. 3.7 portrays that effects of angle of inclination ϕ_a causes reduction in $F'(\xi)$. This holds physically because influences of gravity become small for greater ϕ_a about z-axis and alternatively velocity profile declines. Figs. (3.8 – 3.15) exhibit variations in temperature profile $\theta(\xi)$ against Ec , δ_e , \hat{N}_b , S_1 , \hat{N}_t , Pr , \hat{B}_1 and \hat{B}_2 , respectively. Behavior of temperature $\theta(\xi)$ for large estimation of Ec is delineated through Fig. 3.8. As larger values of Eckert number Ec corresponds to accelerate the conversion of mechanical into thermal energy, thus fluid temperature rises. Fig. 3.9 deliberates the influences of thermal relaxation parameter δ_e on fluid temperature. As enhancement in relaxation time decreases the heat transfer through fluid molecules, as a result, fluid temperature reduces. Fig. 3.10 reveals fluctuations in $\theta(\xi)$ against Brownian motion parameter \hat{N}_b . This figure predicts that temperature $\theta(\xi)$ rises versus larger values of \hat{N}_b (see Fig. 3.10) because Brownian motion disperses fluid

particles which alternatively enhance temperature. Fig. 3.11 explained the significance of thermal stratification S_1 on fluid temperature $\theta(\xi)$. As stratification phenomenon reduces the temperature difference between surface and fluid, as a result, temperature profile $\theta(\xi)$ falls down. Fig. 3.12 elaborated the \hat{N}_t effects on temperature $\theta(\xi)$. This graph suggests that fluid temperature increases against thermophoresis parameter. Fig. 3.13 depicted the impacts of Prandtl number Pr on temperature profile. As Prandtl number reduces the thermal conductance (i.e. capability of heat transfer) and hence temperature. Figs. (3.14 and 3.15) elaborated the consequences of space and temperature dependent heat source/sink parameters \hat{B}_1 and \hat{B}_2 on temperature $\theta(\xi)$. These graphs predict that both parameters incline the temperature profile. Figs. (3.16 – 3.25) examines the influence of \hat{N}_t , δ_c , Sc , γ_3 , \hat{N}_b , γ_2 , E_a , δ , S_2 and \hat{B}_1 on $\Phi(\xi)$. Fig. 3.16 illustrates the effects of \hat{N}_t on $\Phi(\xi)$. This graph shows that thermophoresis phenomenon leads to enlarge nanoparticle concentration. Concentration profile $\Phi(\xi)$ in frame of solutal relaxation time δ_c is displayed in Fig. 3.17. Here concentration $\Phi(\xi)$ diminishes due to controlling influence of δ_c . Impact of Schmidt number Sc on $\Phi(\xi)$ is disclosed through Fig. 3.18. One can observed that $\Phi(\xi)$ declines versus higher values of Sc . It is true because Sc is responsible to lessen mass diffusivity and hence concentration. Declining impact of concentration $\Phi(\xi)$ is observed for larger γ_3 in Fig. 3.19. The growing nature of γ_3 is responsible for rise in the expression $(1 + \delta\theta)^p \exp\left[-\frac{E_a}{1+\delta\theta}\right]$. Physically, destructive rate of chemical reaction upsurges for greater estimation of γ_3 . This is used to dissolve/ terminate the fluid species more efficiently. Fig. 3.20 is remarked for the impact of \hat{N}_b on $\Phi(\xi)$. Declining conduct of $\Phi(\xi)$ and relevant boundary thickness is identified for greater \hat{N}_b . An enhancement in Brownian motion leads to dispersion of liquid particles more rapidly, as a

result, concentration $\Phi(\xi)$ reduces. Impact of generative/destructive chemical reaction γ_2 on concentration $\Phi(\xi)$ is outlined in Fig. 3.21. There is an increase in $\Phi(\xi)$ in vision of destructive chemical reaction variable $\gamma_2 > 0$. However, opposite trend is seen for generative chemical reaction $\gamma_2 < 0$. Fig. 3.22 elucidates the increasing trend of activation energy E_a on nanoparticle concentration $\Phi(\xi)$. The modified Arrhenius function declines when E_a increases. This holds practically because generative chemical reaction increases which rises concentration. Fig. 3.23 shows the effect of concentration $\Phi(\xi)$ against temperature difference parameter δ . Here declining role of δ on $\Phi(\xi)$ is witnessed. Features of S_2 on $\Phi(\xi)$ are presented in Fig. 3.24. It is noticed that S_2 reduces the nanoparticle concentration $\Phi(\xi)$. Fig. 3.25 empowers us to decide that growth in \hat{B}_1 leads to decline in concentration $\Phi(\xi)$ curve. It is true because \hat{B}_1 generates heat, as a result, convection phenomenon dominates and hence it reduces concentration $\Phi(\xi)$. Figs. 3.26 and 3.27 are prepared to examine the impact of emerging parameters β_2 and $\hat{\beta}_c$ on skin friction coefficient C_F . For greater estimation of β_2 skin friction coefficient diminishes (see Fig. 3.26) while reverse behaviour is observed for larger $\hat{\beta}_c$ (see Fig. 3.27).

3.6 Graphical outcomes

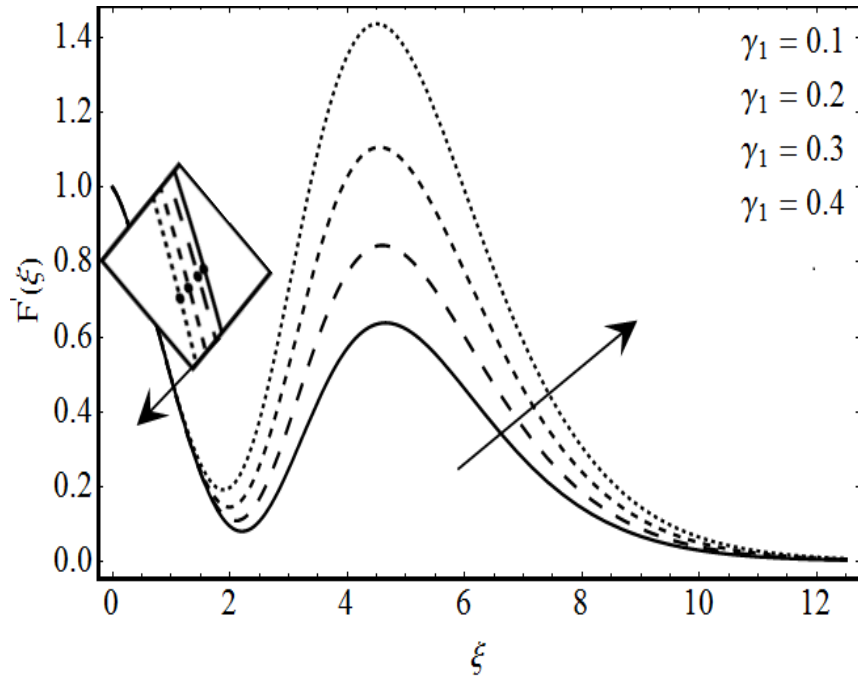


Fig. 3.3: Response of $F'(\xi)$ with γ_1 .

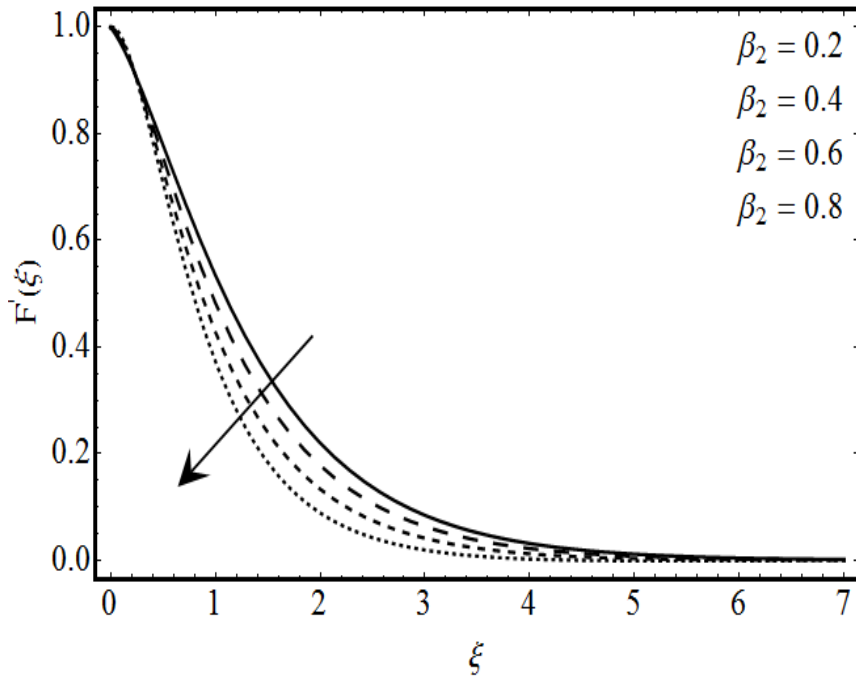


Fig. 3.4: Response of $F'(\xi)$ with β_2 .

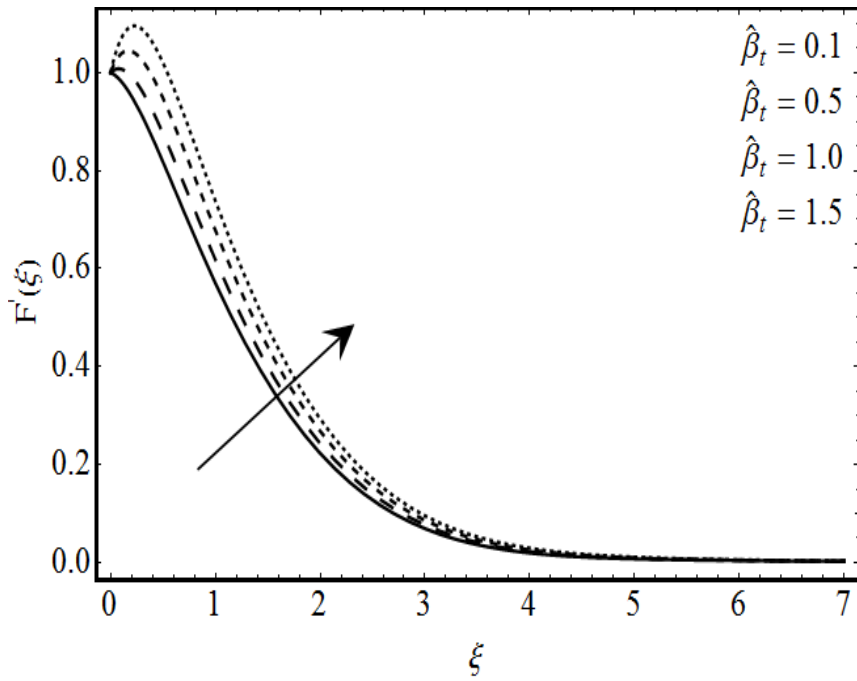


Fig. 3.5: Response of $F'(\xi)$ with $\hat{\beta}_t$.

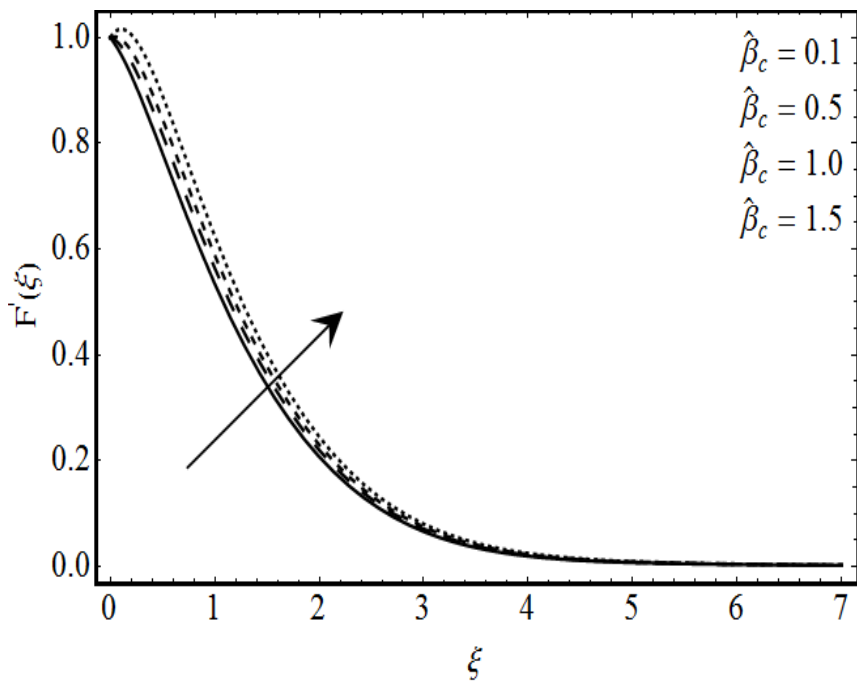


Fig. 3.6: Response of $F'(\xi)$ with $\hat{\beta}_c$.

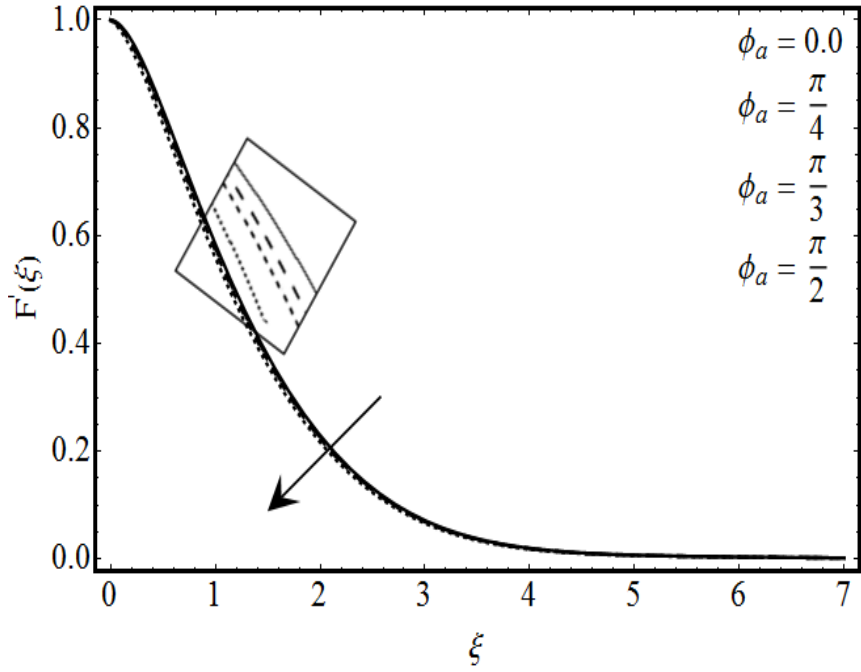


Fig. 3.7: Response of $F'(\xi)$ with ϕ_α .

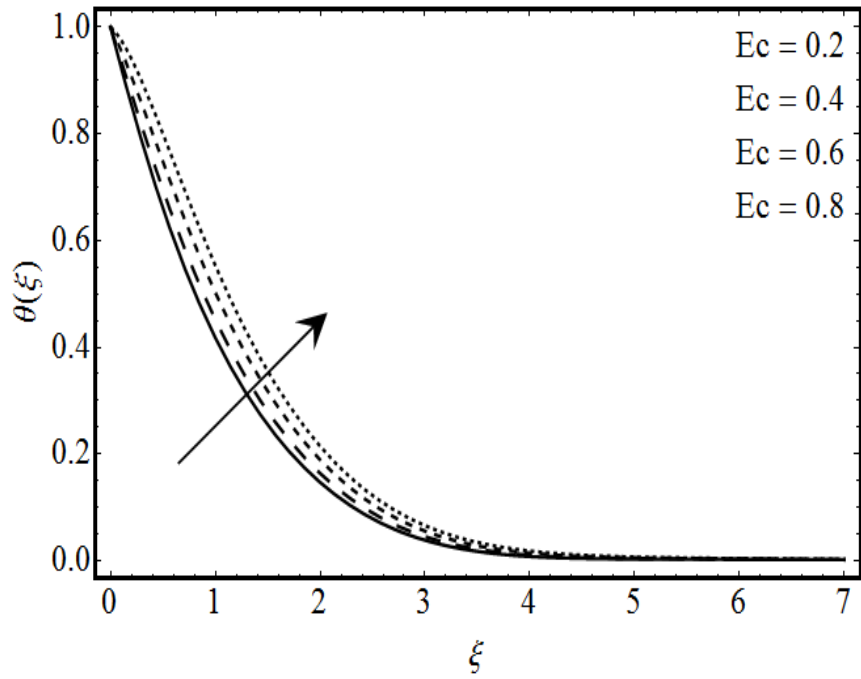


Fig. 3.8: Response of $\theta(\xi)$ with Ec .

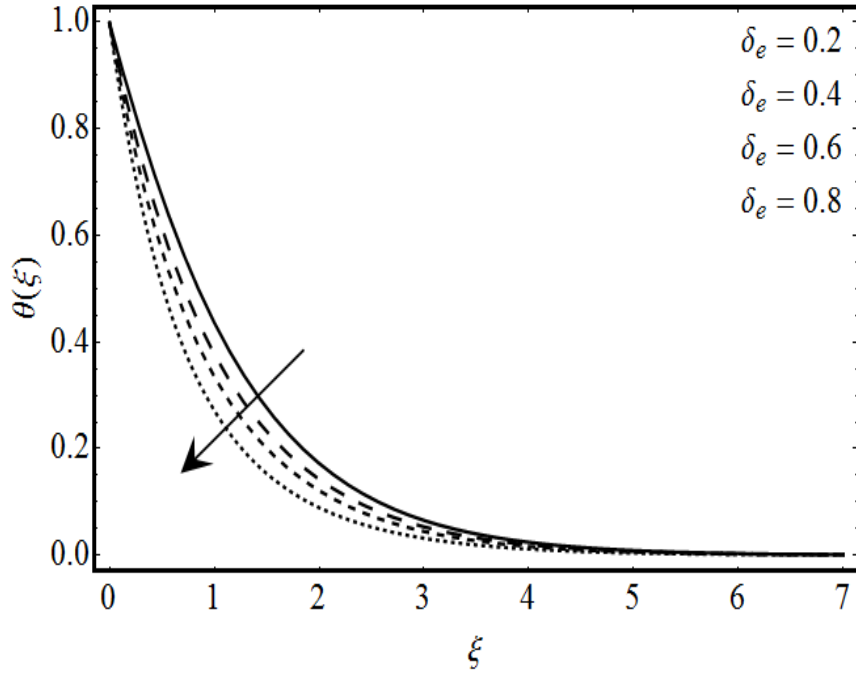


Fig. 3.9: Response of $\theta(\xi)$ with δ_e .

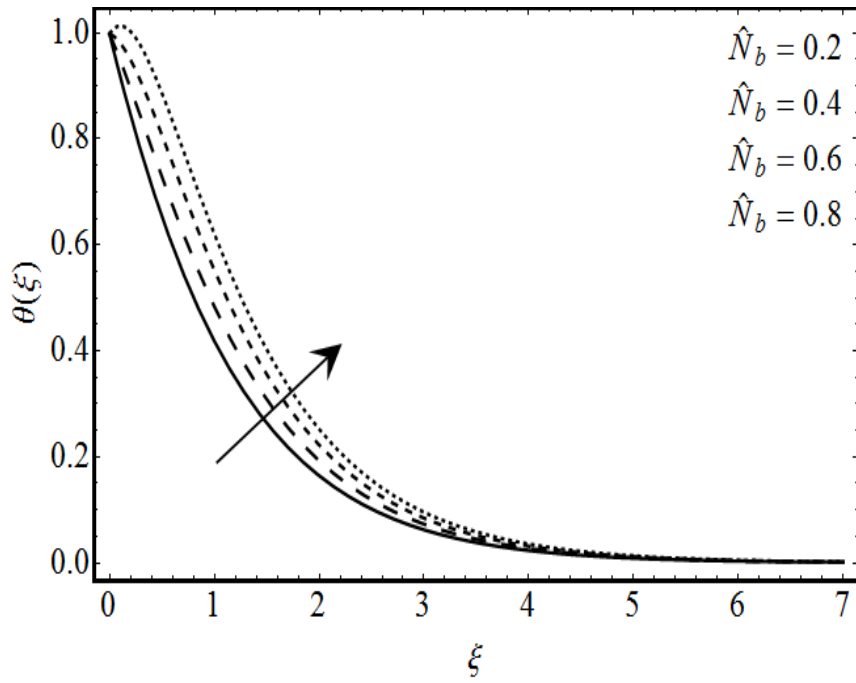


Fig. 3.10: Response of $\theta(\xi)$ with \hat{N}_b .

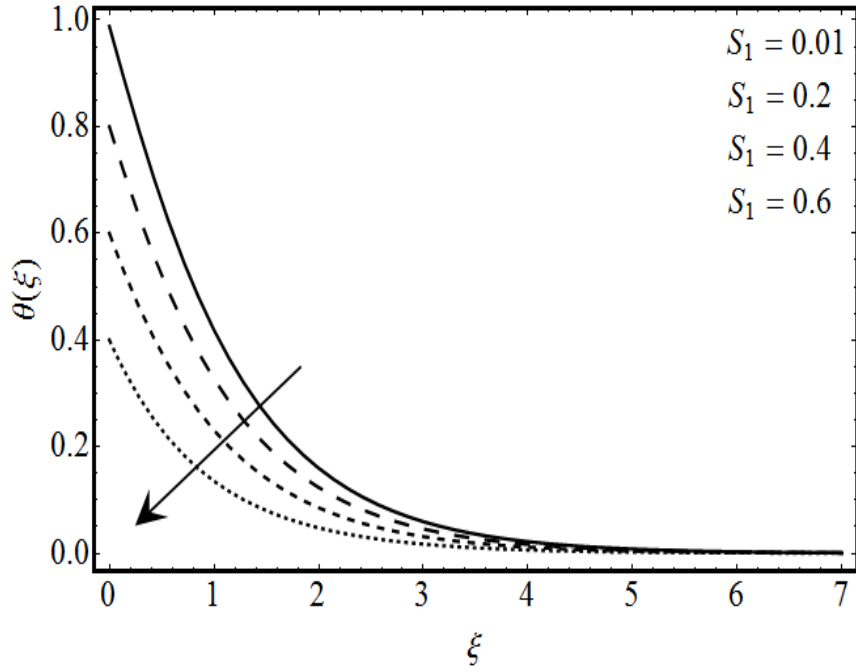


Fig. 3.11: Response of $\theta(\xi)$ with S_1 .

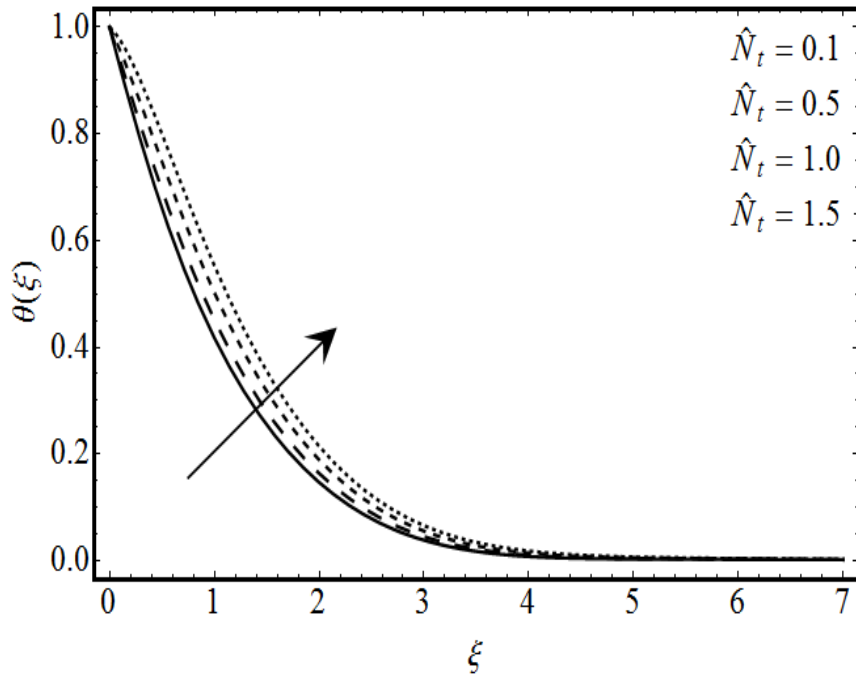


Fig. 3.12: Response of $\theta(\xi)$ with \hat{N}_t .

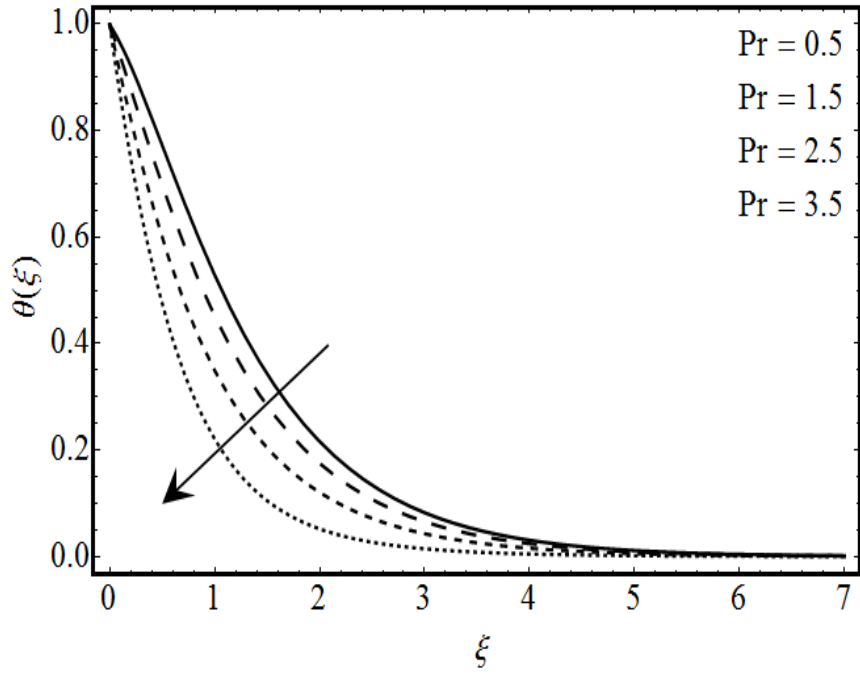


Fig. 3.13: Response of $\theta(\xi)$ with Pr .

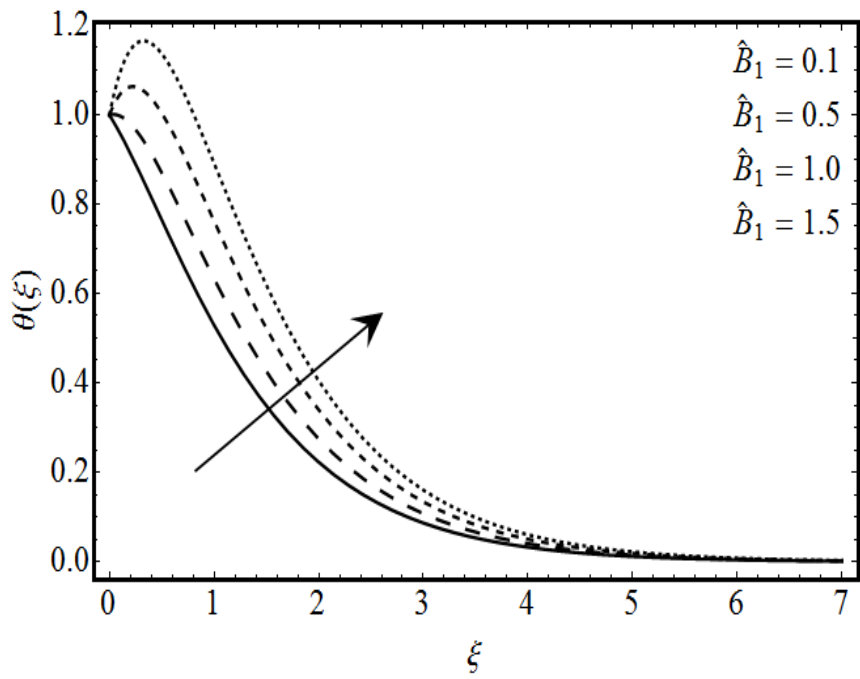


Fig. 3.14: Response of $\theta(\xi)$ with \hat{B}_1 .

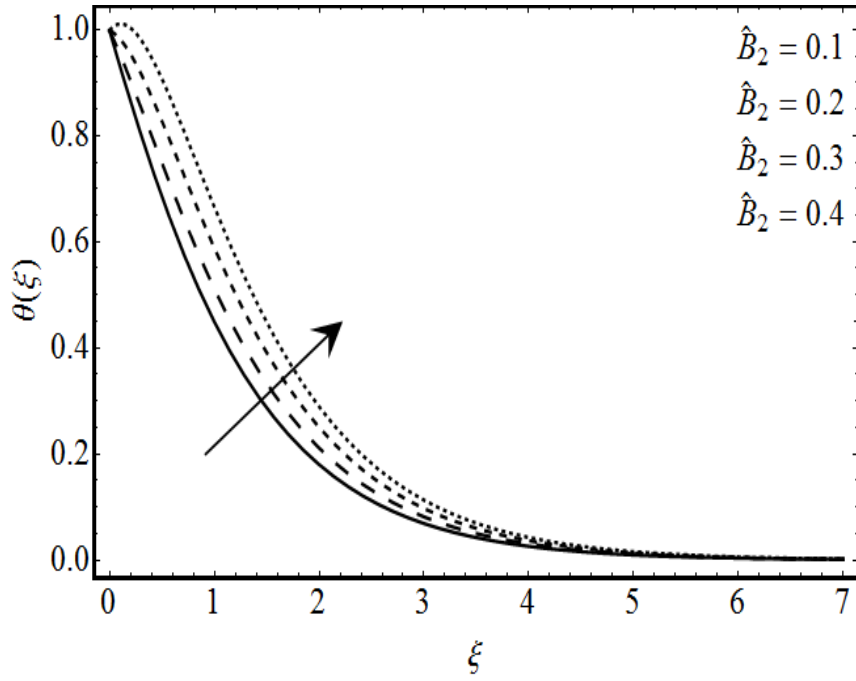


Fig. 3.15: Response of $\theta(\xi)$ with \hat{B}_2 .

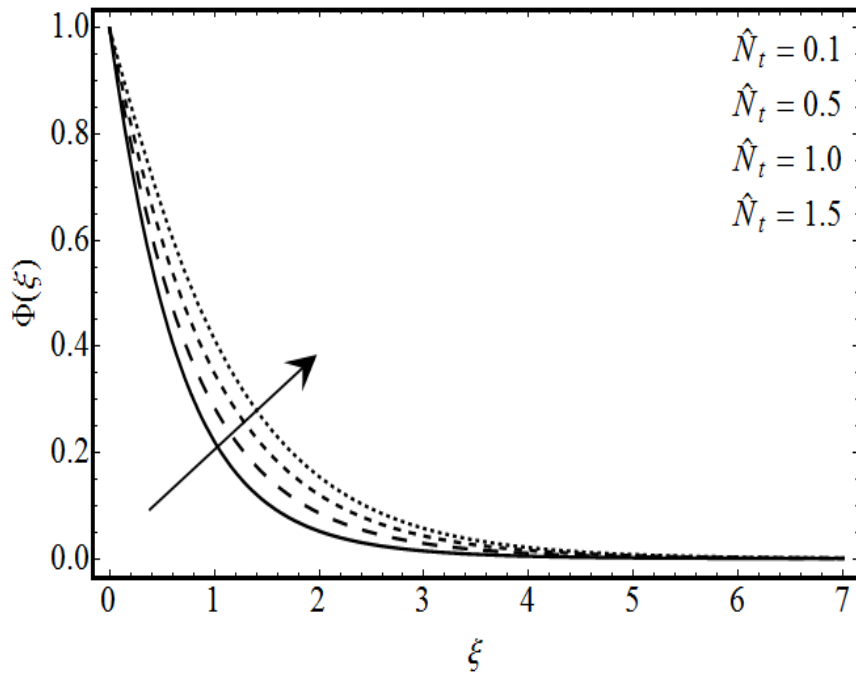


Fig. 3.16: Response of $\Phi(\xi)$ with \hat{N}_t .

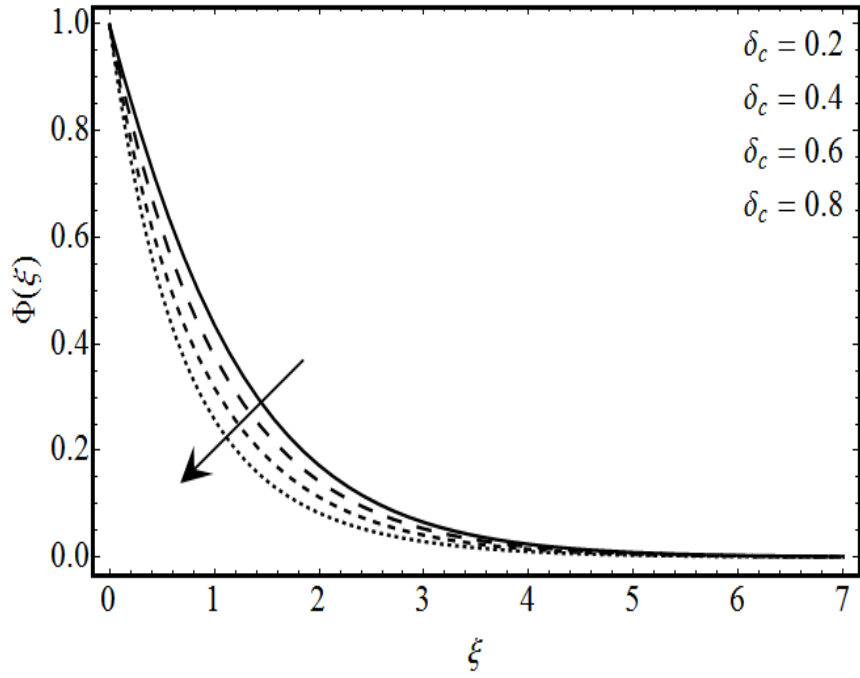


Fig. 3.17: Response of $\Phi(\xi)$ with δ_c .

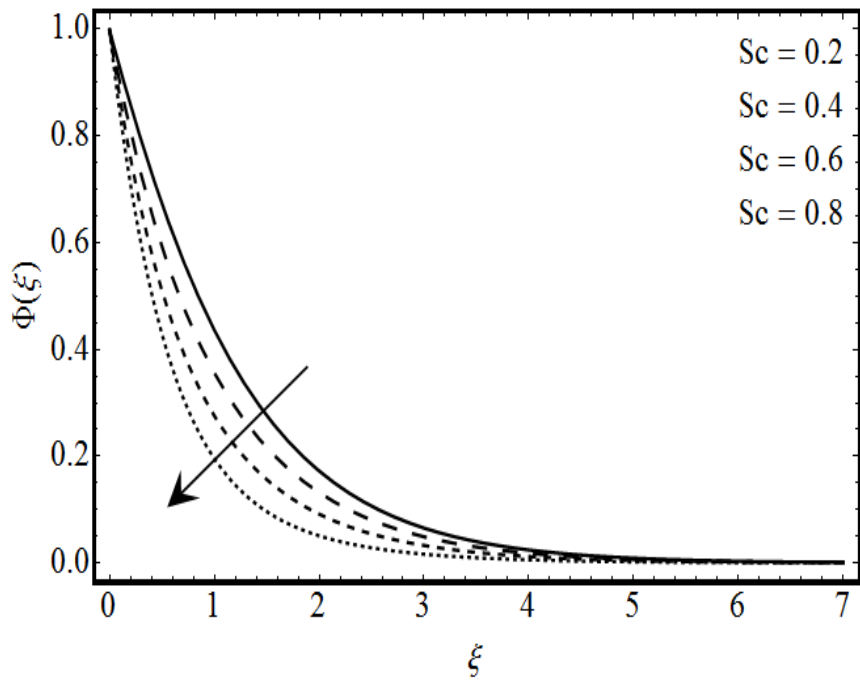


Fig. 3.18: Response of $\Phi(\xi)$ with Sc .

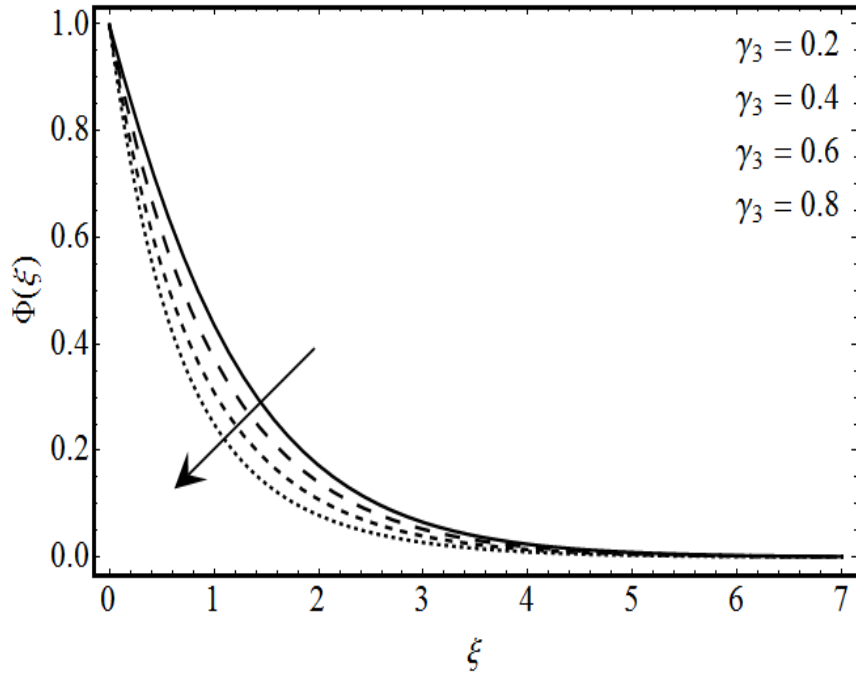


Fig. 3.19: Response of $\Phi(\xi)$ with γ_3 .

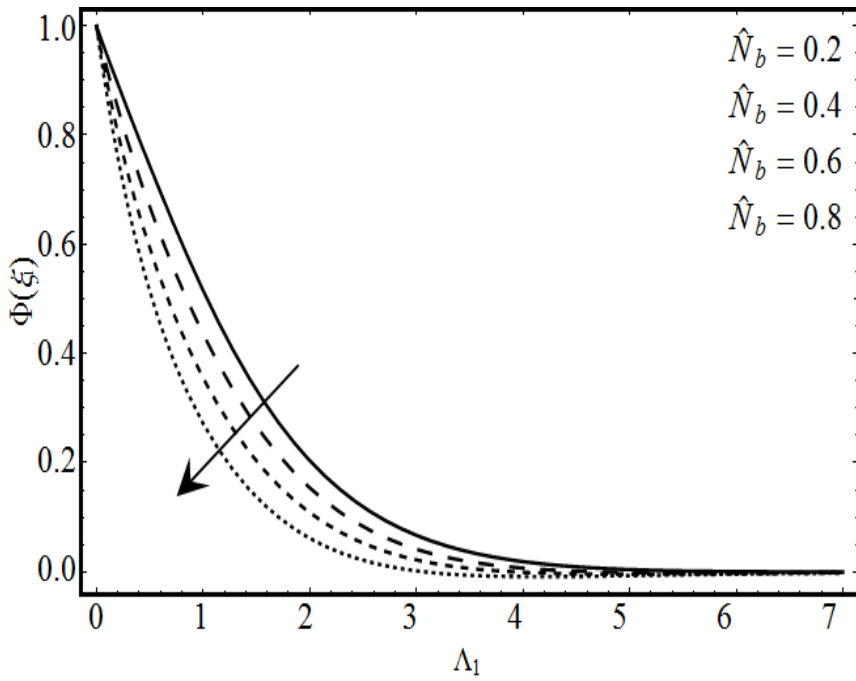


Fig. 3.20: Response of $\Phi(\xi)$ with \hat{N}_b .

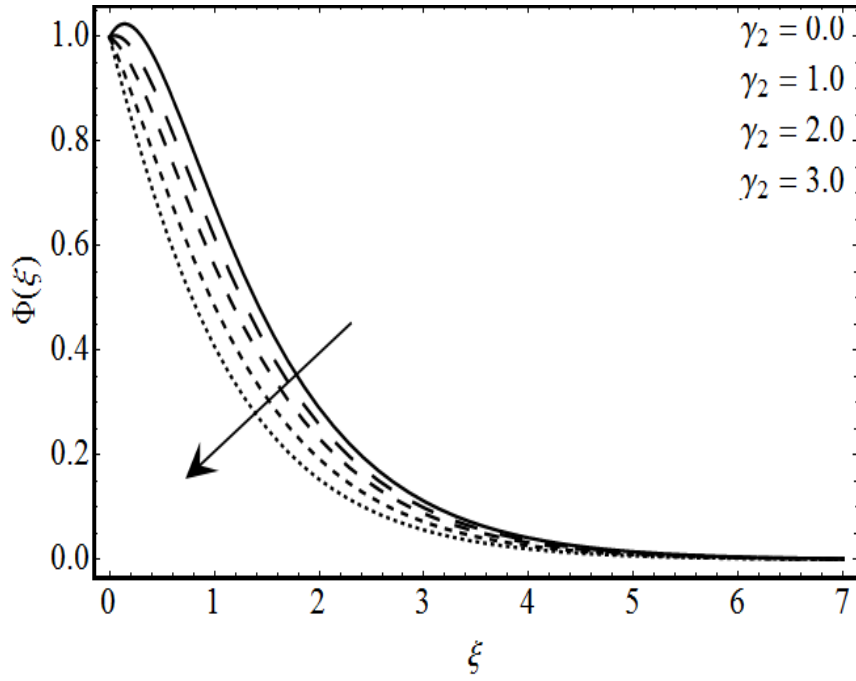


Fig. 3.21: Response of $\Phi(\xi)$ with γ_2 .

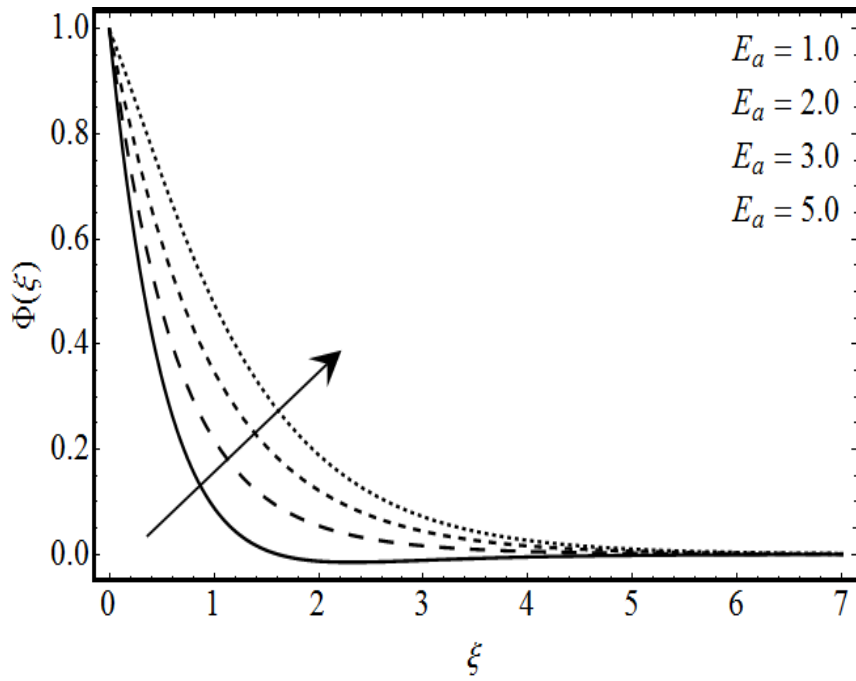


Fig. 3.22: Response of $\Phi(\xi)$ with E_a .

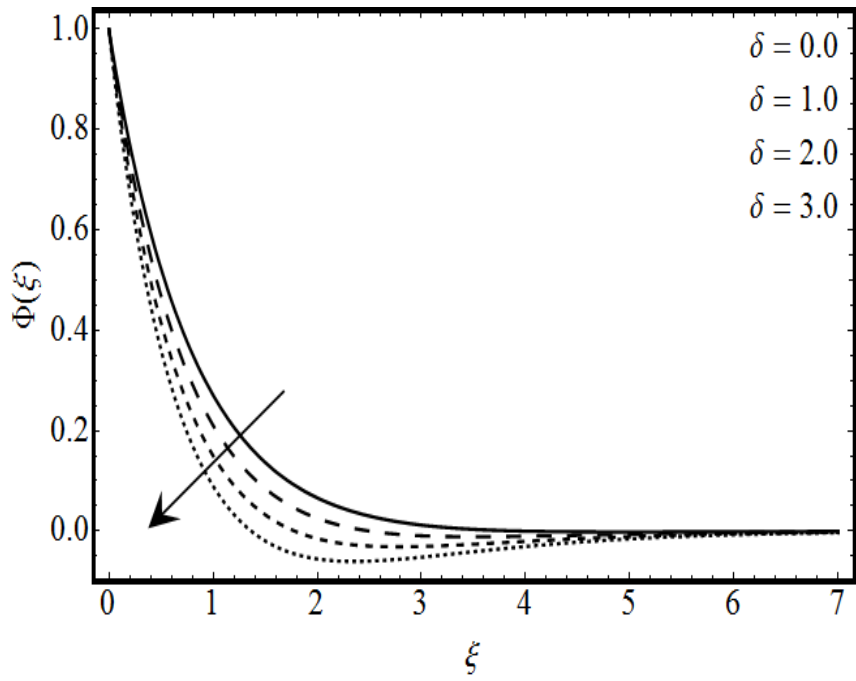


Fig. 3.23: Response of $\Phi(\xi)$ with δ .

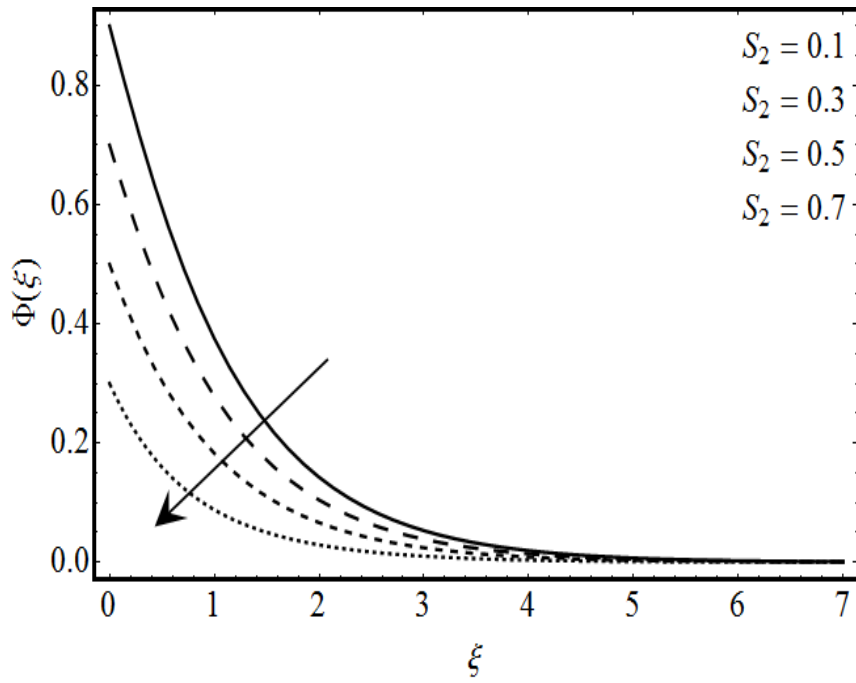


Fig. 3.24: Response of $\Phi(\xi)$ with S_2 .

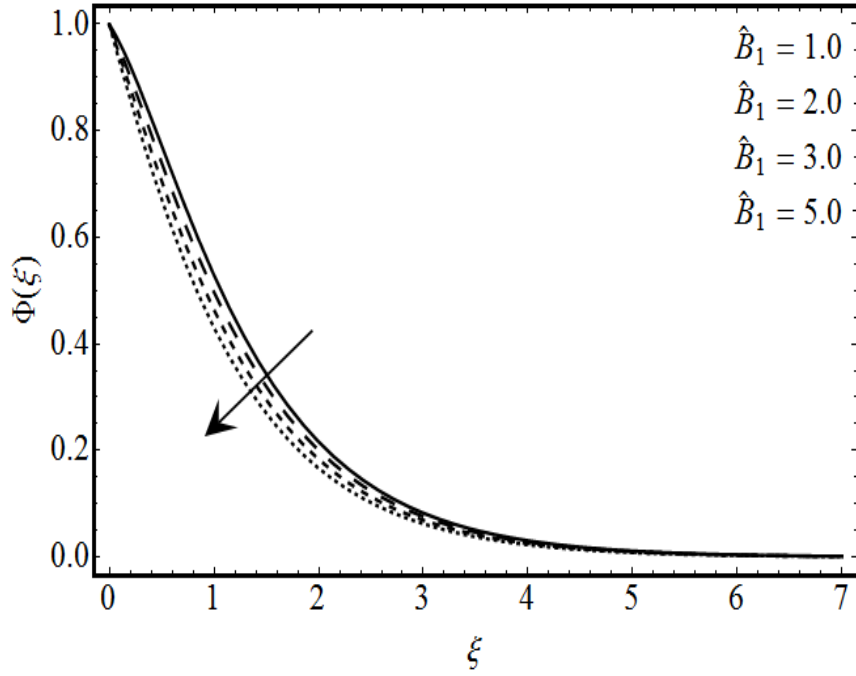


Fig. 3.25: Response of $\Phi(\xi)$ with \hat{B}_1 .

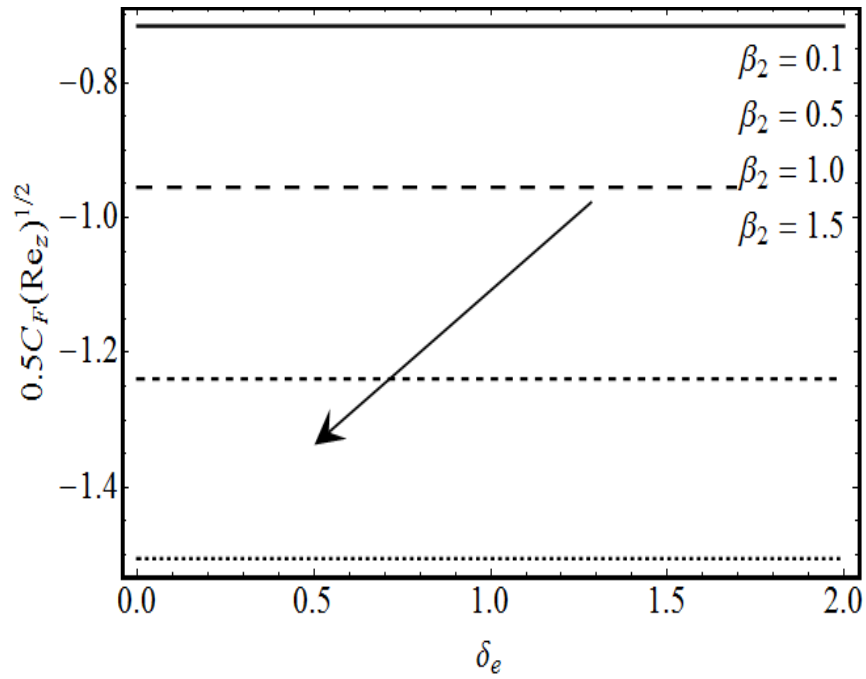


Fig. 3.26: Response of $C_F(Re_z)^{\frac{1}{2}}$ with β_2 .

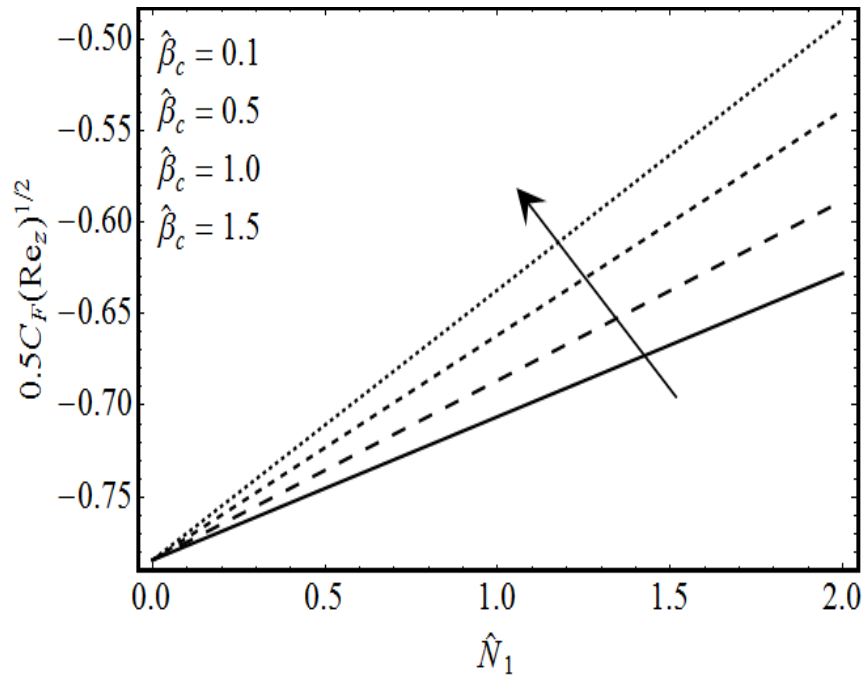


Fig. 3.27: Response of $C_F(Re_z)^{\frac{1}{2}}$ with $\hat{\beta}_c$.

3.7 Conclusions

The main findings are summarized as follows:

- $F'(\xi)$ decays for higher estimation of β_2 and ϕ_a while it boosts up for γ_1 , $\hat{\beta}_t$ and $\hat{\beta}_c$.
- Temperature distribution declines for thermal relaxation time δ_e and thermal stratification parameter S_1 .
- Stratification variables (S_1, S_2) diminishes the temperature and concentration distributions.
- Concentration profile $\Phi(\xi)$ has opposite behaviour versus \hat{N}_b and \hat{N}_t .
- Prandtl number Pr reduces temperature $\theta(\xi)$ while it enhances wall heat flux.
- Nanoparticle concentration $\Phi(\xi)$ is directly proportional to the chemical reaction with activation energy.

CHAPTER 4

Thermally stratified flow of Jeffrey fluid with homogeneous-heterogeneous reactions and non-Fourier heat flux model

4.1 Introduction

This chapter concentrates on Jeffrey fluid flow near the axisymmetric stagnation point over an inclined permeable stretched cylinder with mixed convection effects. Analysis subjected to Cattaneo-Christov heat flux, thermal stratification and homogeneous-heterogeneous reactions are accounted. The governing equations are transmuted into ordinary differential system with suitable transformations. Non-dimensional system of ordinary differential equations is computed by Homotopy technique. Convergence analysis is achieved and suitable values are determined by plotting the h – curves. Effects of physical quantities of interest are studied through graphs and tables. The formulation and interpretation of skin friction coefficient is deliberated.

4.2 Mathematical formulation

We examine the steady two-dimensional stagnation-point flow of an incompressible Jeffrey fluid model subject to Cattaneo-Christov heat flux theory on an inclined permeable stretching cylinder of radius R_0 that makes an angle ϕ_a with vertical position.

Homogeneous/heterogeneous reaction is presented. Here (u_z, u_r) denote axial and radial velocities (see Fig. 4.1). The surface of inclined cylinder is being stretched with the velocity $U_w(z) = \frac{U_0 z}{L}$. The effect of external forces and pressure gradient is supposed to be negligible. For cubic autocatalysis the homogeneous reaction [85-88] is expressed as follows:

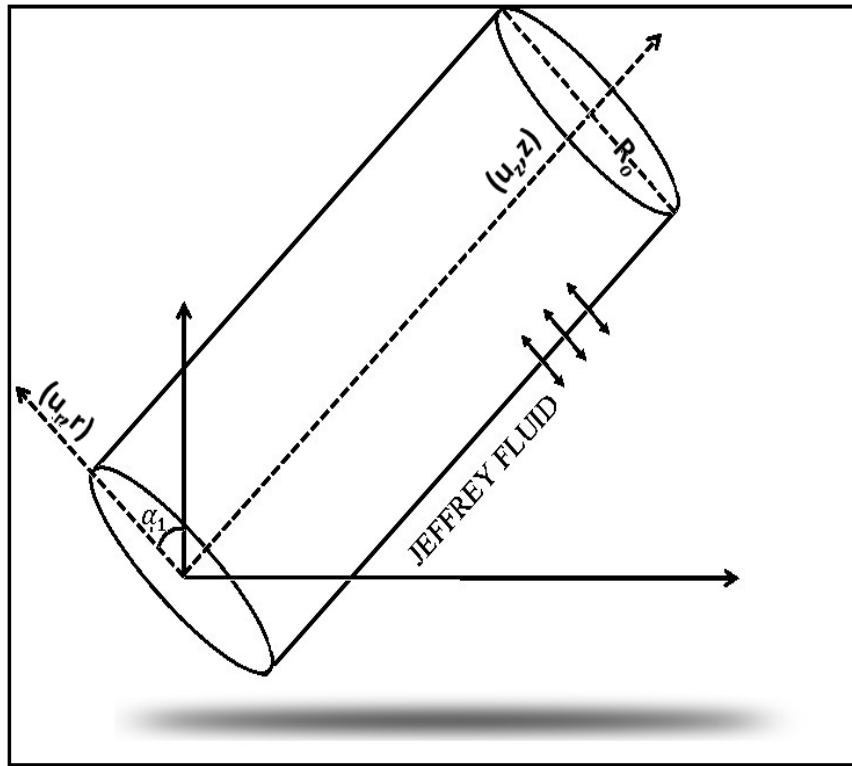
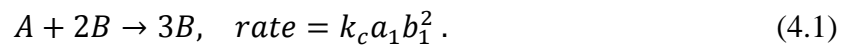


Fig. 4.1: Physical model.



Isothermal reaction of first order on catalyst surface is

$$A \rightarrow B, \quad \text{rate} = k_s a_1. \quad (4.2)$$

Utilizing both the reactions of isothermal nature, the related flow expressions satisfy:

$$\frac{\partial}{\partial r}(ru_r) + \frac{\partial}{\partial z}(ru_z) = 0, \quad (4.3)$$

$$\begin{aligned} u_z \frac{\partial u_z}{\partial z} + u_r \frac{\partial u_z}{\partial r} = U_1 \frac{dU_1}{dz} + \frac{v_1}{(1 + \lambda_1)} \left(\frac{\partial^2 u_z}{\partial r^2} + \frac{1}{r} \frac{\partial u_z}{\partial r} \right) + \frac{\hat{g}_1}{\rho_f} \Gamma_1 (T - T_\infty) \cos \phi_a \\ \frac{v_1 \lambda_2}{(1 + \lambda_1)} \left(u_r \frac{\partial^3 u_z}{\partial r^3} + \frac{\partial u_r}{\partial r} \frac{\partial^2 u_z}{\partial r^2} + u_z \frac{\partial^3 u_z}{\partial z \partial r^2} + \frac{\partial u_z}{\partial r} \frac{\partial^2 u_z}{\partial r \partial z} + \frac{u_r}{r} \frac{\partial^2 u_z}{\partial r^2} + \frac{u_z}{r} \frac{\partial^2 u_z}{\partial r \partial z} \right) \end{aligned} \quad (4.4)$$

In view of Cattaneo-Christov heat flux theory [89,90], \mathbf{q}_1 satisfies the relation

$$\mathbf{q}_1 + \hat{\Gamma}_e \left[\frac{\partial \mathbf{q}_1}{\partial t} + \mathbf{V}_1 \cdot \nabla \mathbf{q}_1 - (\mathbf{q}_1 \cdot \nabla) \mathbf{V}_1 + (\nabla \cdot \mathbf{V}_1) \mathbf{q}_1 \right] = -k_f \nabla T. \quad (4.5)$$

For $\hat{\Gamma}_e = 0$ the above expression reduces to classical Fourier's law. Now by considering incompressible fluid situation one has

$$\mathbf{q}_1 + \hat{\Gamma}_e [\mathbf{V}_1 \cdot \nabla \mathbf{q}_1 - (\mathbf{q}_1 \cdot \nabla) \mathbf{V}_1] = -\hat{k}_f \nabla T. \quad (4.6)$$

The heat and mass conservation equations are

$$u_r \frac{\partial T}{\partial r} + u_z \frac{\partial T}{\partial z} + \hat{\Gamma}_e \Pi_e = \frac{\hat{k}_f}{(\rho C_p)_f} \frac{1}{r} \frac{\partial}{\partial r} \left(r \frac{\partial T}{\partial r} \right), \quad (4.7)$$

$$u_r \frac{\partial a_1}{\partial r} + u_z \frac{\partial a_1}{\partial z} = D_A \left(\frac{\partial^2 a_1}{\partial r^2} + \frac{1}{r} \frac{\partial a_1}{\partial r} \right) - k_c a_1 b_1^2, \quad (4.8)$$

$$u_r \frac{\partial b_1}{\partial r} + u_z \frac{\partial b_1}{\partial z} = D_A \left(\frac{\partial^2 b_1}{\partial r^2} + \frac{1}{r} \frac{\partial b_1}{\partial r} \right) + k_c a_1 b_1^2, \quad (4.9)$$

along with boundary conditions

$$\left. \begin{aligned} u_z &= \frac{U_0 z}{L}, \quad u_r = V_1, \quad T = T_w = T_0 + \frac{d_1 z}{L}, \\ D_A \frac{\partial a_1}{\partial r} &= k_s a_1, \quad D_b \frac{\partial b_1}{\partial r} = -k_s a_1, \end{aligned} \right| \text{at } r = R_0, \quad (4.10)$$

$$\left. \begin{aligned} u_z &\rightarrow U_1 = \frac{U_\infty z}{L}, \quad T \rightarrow T_\infty = T_0 + \frac{d_2 z}{L}, \\ a_1 &\rightarrow a_0, \quad b_1 \rightarrow 0. \end{aligned} \right| \text{when } r \rightarrow \infty, \quad (4.11)$$

with

$$\begin{aligned} \Pi_e &= u_r^2 \frac{\partial^2 T}{\partial r^2} + u_z^2 \frac{\partial^2 T}{\partial z^2} + \frac{\partial T}{\partial r} \left(u_z \frac{\partial u_r}{\partial z} + u_r \frac{\partial u_z}{\partial r} \right) + 2u_z u_r \frac{\partial^2 C}{\partial r \partial z} \\ &\quad + \frac{\partial T}{\partial z} \left(u_z \frac{\partial u_z}{\partial z} + u_r \frac{\partial u_r}{\partial r} \right). \end{aligned} \quad (4.12)$$

Considering suitable transformations for present problem are [90]

$$\begin{aligned} \xi &= \sqrt{\frac{U_0}{Lv_1}} \left(\frac{r^2 - R_0^2}{2R_0} \right), \quad \Psi_1(\xi) = \sqrt{\frac{v_1 U_0 z^2}{L}} F(\xi), \quad u_z(\xi) = \frac{U_0 z}{L} F'(\xi), \\ u_r(\xi) &= -\frac{R_0}{r} \sqrt{\frac{v_1 U_0}{L}} F(\xi), \quad \theta(\xi) = \frac{T - T_\infty}{T_w - T_0}, \quad a_1 = a_0 \Phi(\xi), \quad b_1 = a_0 H(z). \end{aligned} \quad (4.13)$$

The flow expressions under above transformations take the form

$$\begin{aligned} (1 + 2\gamma_1 \xi)[F'''' + \beta_2(F''^2 - FF^4)] + \gamma_1 \beta_2(F'F'' - 3FF''') + 2\gamma_1 F'' \\ + (1 + \lambda_1)(FF'' - F'^2 + A^2) - (1 + \lambda_1)\beta_1 \theta \cos \phi_a = 0, \end{aligned} \quad (4.14)$$

$$\begin{aligned} (1 + 2\gamma_1 \xi)\theta'' + 2\gamma_1 \theta' - Pr(\theta + S_1)F' + PrF\theta' \\ + Pr\delta_e[FF'\theta' - F^2\theta'' + (\theta + S_1)(FF'' - F'^2)] = 0, \end{aligned} \quad (4.15)$$

$$(1 + 2\gamma_1 \xi)G'' + 2\gamma_1 G' + ScFG' - ScK_m GH^2 = 0, \quad (4.16)$$

$$(1 + 2\gamma_1\xi)H'' + 2\gamma_1H' + \frac{Sc}{\delta^*}FH' + \frac{Sc}{\delta^*}K_mGH^2 = 0. \quad (4.17)$$

The transformed boundary conditions are

$$F'(\xi) = 1, F(\xi) = V_p, \theta(\xi) = 1 - S_1, G'(\xi) = K_t G(\xi), \delta^* H'(\xi) = -K_t G(\xi) \text{ at } \xi = 0,$$

$$F'(\xi) = A, \theta(\xi) = 0, G(\xi) = 0 \text{ as } \xi \rightarrow \infty. \quad (4.18)$$

Definitions of involved variables are listed below:

$$\begin{aligned} \gamma_1 &= \sqrt{\frac{\nu_1 L}{U_0 R_0^2}}, & \beta_2 &= \frac{\lambda_2 U_0}{L}, & \delta_e &= \frac{\hat{\Gamma}_e U_0}{L}, \\ K_m &= \frac{k_c a_0^2 L}{U_0}, & Pr &= \frac{(\mu C_p)_f}{\hat{k}_f}, & Sc &= \frac{\nu_1}{D_B}, \\ K_t &= \frac{k_s}{D_A} \sqrt{\frac{\nu_1 L}{U_0}}, & \delta^* &= \frac{D_B}{D_A}. \end{aligned} \quad (4.19)$$

The size of A and B are considered to be comparable so that we further assume the equality of diffusion coefficients as special case i.e., $D_A = D_B$ ($\delta^* = 1$). Thus, we have

$$G(\xi) + H(\xi) = 1. \quad (4.20)$$

Invoking Eq. (4.20) into Eqs. (4.16) and (4.17), we get

$$(1 + 2\gamma_1\xi)G'' + 2\gamma_1G' + ScFG' - ScK_cG(1 - G)^2 = 0. \quad (4.21)$$

The local skin friction coefficient C_f (surface drag) and the local Nusselt number Nu_z (rate of heat transfer) are defined as

$$\begin{aligned} C_f &= \frac{2\tau_w}{\rho_1 U_w^2}, \\ Nu_z &= \frac{zq_w}{k(T_w - T_0)}. \end{aligned} \quad (4.22)$$

Shear stress (τ_w) and heat flux (q_w) are defined as

$$\tau_w = \frac{\mu}{(1 + \lambda_1)} \frac{\partial u_z}{\partial r} + \frac{\mu\lambda_2}{(1 + \lambda_1)} \left(u_r \frac{\partial^2 u_z}{\partial r^2} + u_z \frac{\partial^2 u_z}{\partial r \partial z} \right) \Big|_{r=R_0}, \quad (4.23)$$

$$q_w = -k \frac{\partial T}{\partial r} \Big|_{r=R_0}. \quad (4.24)$$

Above physical quantities in dimensionless form are

$$\frac{1}{2} C_F (Re_z)^{\frac{1}{2}} = \frac{1}{(1 + \lambda_1)} [(1 - \gamma_1 \beta_2 F(0) + \beta_2 F'(0)) F''(0) - \beta_2 F(0) F'''(0)], \quad (4.25)$$

$$Nu_z (Re_z)^{-1/2} = -\theta'(0), \quad (4.26)$$

in which $Re_z \left(= \frac{U_0 z^2}{\nu_1 L} \right)$ is the local Reynolds number.

4.3 Methodology

The initial guesses ($F^0(\xi), \theta^0(\xi), G^0(\xi)$) and auxiliary linear operators ($\mathcal{E}_F, \mathcal{E}_\theta, \mathcal{E}_G$) are:

$$\begin{aligned} F^0(\xi) &= 1 + V_p + A(\xi - 1) + (A - 1) \exp(-\xi), \\ \theta^0(\xi) &= (1 - S_1) \exp(-\xi), \\ G^0(\xi) &= 1 - \frac{1}{2} \exp(-K_t \xi), \end{aligned} \quad (4.27)$$

$$\mathcal{E}_F[F] = F''' - F', \quad \mathcal{E}_\theta[\theta] = \theta'' - \theta, \quad \mathcal{E}_G[G] = G'' - G. \quad (4.28)$$

The above mentioned operators $\mathcal{E}_F, \mathcal{E}_\theta$ and \mathcal{E}_G satisfy the following properties

$$\begin{aligned} \mathcal{E}_F[\omega_2 \exp(-\xi) + \omega_1 + \omega_3 \exp(\xi)] &= 0, \\ \mathcal{E}_\theta[\omega_4 \exp(-\xi) + \omega_5 \exp(\xi)] &= 0, \\ \mathcal{E}_G[\omega_6 \exp(-\xi) + \omega_7 \exp(\xi)] &= 0, \end{aligned} \quad (4.29)$$

where $\omega_j (j = 1 - 7)$ notify the arbitrary constants.

4.3.1 Zeroth-order systems

The zeroth-order deformation expressions are constructed as follows:

$$(1 - \hat{q})\mathcal{E}_F[\hat{F}(\xi; \hat{q}) - F^0(\xi)] = \hat{q}h_F\hat{N}_F[\hat{F}(\xi; \hat{q}), \hat{\theta}(\xi; \hat{q}), \hat{G}(\xi; \hat{q})], \quad (4.30)$$

$$(1 - \hat{q})\mathcal{E}_\theta[\hat{\theta}(\xi; \hat{q}) - \theta^0(\xi)] = \hat{q}h_\theta\hat{N}_\theta[\hat{F}(\xi; \hat{q}), \hat{\theta}(\xi; \hat{q}), \hat{G}(\xi; \hat{q})], \quad (4.31)$$

$$(1 - \hat{q})\mathcal{E}_G[\hat{G}(\xi; \hat{q}) - G^0(\xi)] = \hat{q}h_G\hat{N}_G[\hat{F}(\xi; \hat{q}), \hat{\theta}(\xi; \hat{q}), \hat{G}(\xi; \hat{q})], \quad (4.32)$$

$$\hat{F}'(0; \hat{q}) = 1, \quad \hat{F}(0; \hat{q}) = V_p, \quad \hat{\theta}(0; \hat{q}) = 1 - S_1, \quad \hat{G}'(0; \hat{q}) = K_t\hat{G}(0; \hat{q}),$$

$$\hat{F}'(\xi; \hat{q}) = 0, \quad \hat{\theta}(\xi; \hat{q}) = 0, \quad \hat{G}(\xi; \hat{q}) = 1, \quad as \xi \rightarrow \infty, \quad (4.33)$$

$$\hat{N}_F[\hat{F}(\xi; \hat{q}), \hat{\theta}(\xi; \hat{q}), \hat{G}(\xi; \hat{q})]$$

$$= \gamma_1\beta_2 \left(\frac{\partial \hat{F}(\xi; \hat{q})}{\partial \xi} \frac{\partial^2 \hat{F}(\xi; \hat{q})}{\partial \xi^2} - 3\hat{F}(\xi; \hat{q}) \frac{\partial^3 \hat{F}(\xi; \hat{q})}{\partial \xi^3} \right) + 2\gamma_1 \frac{\partial^2 \hat{F}(\xi; \hat{q})}{\partial \xi^2}$$

$$+ (1 + 2\gamma_1\xi)\beta_2 \left(\frac{\partial^2 \hat{F}(\xi; \hat{q})}{\partial \xi^2} \frac{\partial^2 \hat{F}(\xi; \hat{q})}{\partial \xi^2} - \hat{F}(\xi; \hat{q}) \frac{\partial^4 \hat{F}(\xi; \hat{q})}{\partial \xi^4} \right)$$

$$+ (1 + \lambda_1) \left(\hat{F}(\xi; \hat{q}) \frac{\partial^2 \hat{F}(\xi; \hat{q})}{\partial \xi^2} - \frac{\partial \hat{F}(\xi; \hat{q})}{\partial \xi} \frac{\partial \hat{F}(\xi; \hat{q})}{\partial \xi} \right) +$$

$$(1 + 2\gamma_1\xi) \frac{\partial^3 \hat{F}(\xi; \hat{q})}{\partial \xi^3} + (1 + \lambda_1) \left(A^2(1 - \chi_m) - \beta_1\hat{\theta}(\xi; \hat{q}) \right) \cos\phi_a, \quad (4.34)$$

$$\begin{aligned}
& \hat{N}_\theta[\hat{F}(\xi; \hat{q}), \hat{\theta}(\xi; \hat{q}), \hat{G}(\xi; \hat{q})] \\
&= (1 + 2\gamma_1\xi) \frac{\partial^2 \hat{\theta}(\xi; \hat{q})}{\partial \xi^2} + 2\gamma_1 \frac{\partial \hat{\theta}(\xi; \hat{q})}{\partial \xi} + Pr\hat{F}(\xi; \hat{q}) \frac{\partial \hat{\theta}(\xi; \hat{q})}{\partial \xi} \\
&- Pr\delta_e(\hat{\theta}(\xi; \hat{q}) + S_1) \left(\hat{F}(\xi; \hat{q}) \frac{\partial^2 \hat{F}(\xi; \hat{q})}{\partial \xi^2} - \frac{\partial \hat{F}(\xi; \hat{q})}{\partial \xi} \frac{\partial \hat{F}(\xi; \hat{q})}{\partial \xi} \right) \\
&- Pr\delta_e \left(\hat{F}(\xi; \hat{q}) \frac{\partial \hat{F}(\xi; \hat{q})}{\partial \xi} \frac{\partial \hat{\theta}(\xi; \hat{q})}{\partial \xi} - \hat{F}(\xi; \hat{q}) \hat{F}(\xi; \hat{q}) \frac{\partial^2 \hat{\theta}(\xi; \hat{q})}{\partial \xi^2} \right) \\
&- Pr(\hat{\theta}(\xi; \hat{q}) + S_1) \frac{\partial \hat{F}(\xi; \hat{q})}{\partial \xi}, \tag{4.35}
\end{aligned}$$

$$\begin{aligned}
\hat{N}_G[\hat{F}(\xi; \hat{q}), \hat{\theta}(\xi; \hat{q}), \hat{G}(\xi; \hat{q})] &= (1 + 2\gamma_1\xi) \frac{\partial^2 \hat{G}(\xi; \hat{q})}{\partial \xi^2} + (2\gamma_1 + c\hat{F}(\xi; \hat{q})) \frac{\partial \hat{G}(\xi; \hat{q})}{\partial \xi} \\
&- ScK_c \hat{G}(\xi; \hat{q}) (1 - \hat{G}(\xi; \hat{q}))^2. \tag{4.36}
\end{aligned}$$

The values of $\hat{q} \in [0,1]$ and for $\hat{q} = 0$ and $\hat{q} = 1$, we have

$$\begin{aligned}
\hat{F}(\xi; 0) &= F^0(\xi) & \hat{F}(\xi; 1) &= F(\xi), \\
\hat{\theta}(\xi; 0) &= \theta^0(\xi) & \hat{\theta}(\xi; 1) &= \theta(\xi), \\
\hat{G}(\xi; 0) &= G^0(\xi) & \hat{G}(\xi; 1) &= G(\xi). \tag{4.37}
\end{aligned}$$

4.3.2 m^{th} -order systems

Here problem statements are

$$E_F[F_m(\xi) - \chi_m F_{m-1}(\xi)] = h_F R_m^F(\xi), \tag{4.38}$$

$$E_\theta[\theta_m(\xi) - \chi_m \theta_{m-1}(\xi)] = h_\theta R_m^\theta(\xi), \tag{4.39}$$

$$E_G[G_m(\xi) - \chi_m G_{m-1}(\xi)] = h_G R_m^G(\xi), \tag{4.40}$$

$$\begin{aligned}
F_m(\xi) = 0, \quad F'_m(\xi) = 0, \quad \theta_m(\xi) = 0, \quad G'_m(\xi) = 0, \quad \text{at } \xi = 0, \\
F'_m(\xi) = 0, \quad \theta_m(\xi) = 0, \quad G_m(\xi) = 0, \quad \text{as } \xi \rightarrow \infty,
\end{aligned} \tag{4.41}$$

$$\begin{aligned}
R_m^F(\xi) = (1 + 2\gamma_1\xi) & \left(F'''_{m-1} + \beta_2 \sum_{k=0}^{m-1} (F''_{m-1-k}F''_k - F_{m-1-k}F_k^{iv}) \right) \\
& + \gamma_1 \sum_{k=0}^{m-1} (\beta_2(F'_{m-1-k}F''_k - 3F_{m-1-k}F_k''') + 2F''_{m-1}) + A^2(1 - \chi_m) \\
& + (1 + \lambda_1) \left(\sum_{k=0}^{m-1} (F_{m-1-k}F''_k - F'_{m-1-k}F'_k) + \beta_1\theta_{m-1}\cos\phi_a \right),
\end{aligned} \tag{4.42}$$

$$\begin{aligned}
R_m^\theta(\xi) = (1 + 2\gamma_1\xi)\theta''_{m-1} + 2\gamma_1\theta'_{m-1} - PrS_1F'_{m-1} + Pr \sum_{k=0}^{m-1} (F_{m-1-k}\theta'_k) \\
- Pr \sum_{k=0}^{m-1} (\theta_{m-1-k}F'_k + S_1\delta_e(F'_{m-1-k}F'_k - F_{m-1-k}F_k'')) + \\
Pr\delta_e \sum_{k=0}^{m-1} \left(\theta_{m-1-k} \sum_{l=0}^k (F_{k-l}F_l'' - F'_{k-l}F'_l) + F_{m-1-k} \sum_{l=0}^k (F'_{k-l}\theta'_l - F_{k-l}\theta_l'') \right),
\end{aligned} \tag{4.43}$$

$$\begin{aligned}
R_m^G(\xi) = (1 + 2\gamma_1\xi)G''_{m-1} + 2\gamma_1G'_{m-1} - ScK_cG_{m-1} - K_cG_{m-1-k} \sum_{l=0}^k G_{k-l}G_l \\
+ Sc \sum_{k=0}^m (F_{m-1-k} + 2K_cG_{m-1-k})G_k,
\end{aligned} \tag{4.44}$$

we have

$$\begin{aligned}
\hat{F}(\xi; 0) = F^0(\xi), \quad \hat{\theta}(\xi; 0) = \theta^0(\xi), \quad \hat{G}(\xi; 0) = G^0(\xi), \\
\hat{F}(\xi; 1) = F(\xi), \quad \hat{\theta}(\xi; 1) = \theta(\xi), \quad \hat{G}(\xi; 1) = G(\xi).
\end{aligned} \tag{4.45}$$

Here we observed that when \hat{q} varies from 0 to 1 then functions $\hat{F}(\xi; \hat{q})$, $\hat{\theta}(\xi; \hat{q})$ and $\hat{G}(\xi; \hat{q})$ changes from initial approximations $(F^0(\xi), \theta^0(\xi), G^0(\xi))$ to the desired solutions $(F(\xi), \theta(\xi), G(\xi))$. Through Taylor's series expansion we have

$$\begin{aligned}\hat{F}(\xi; \hat{q}) &= F^0(\xi) + \sum_{m=1}^{\infty} F_m(\xi) \hat{q}^m, \\ F_m(\xi) &= \frac{1}{m!} \frac{\partial^m}{\partial \hat{q}^m} \hat{F}(\xi; \hat{q}) \Big|_{\hat{q}=0},\end{aligned}\tag{4.46}$$

$$\begin{aligned}\hat{\theta}(\xi; \hat{q}) &= \theta^0(\xi) + \sum_{m=1}^{\infty} \theta_m(\xi) \hat{q}^m, \\ \theta_m(\xi) &= \frac{1}{m!} \frac{\partial^m}{\partial \hat{q}^m} \hat{\theta}(\xi; \hat{q}) \Big|_{\hat{q}=0},\end{aligned}\tag{4.47}$$

$$\begin{aligned}\hat{G}(\xi; \hat{q}) &= G^0(\xi) + \sum_{m=1}^{\infty} G_m(\xi) \hat{q}^m, \\ G_m(\xi) &= \frac{1}{m!} \frac{\partial^m}{\partial \hat{q}^m} \hat{G}(\xi; \hat{q}) \Big|_{\hat{q}=0}.\end{aligned}\tag{4.48}$$

The general solutions $(F_m(\xi), \theta_m(\xi), G_m(\xi))$ of Eqs. (4.38) – (4.40) in view of special solutions $(F_m^*(\xi), \theta_m^*(\xi), G_m^*(\xi))$ are

$$F_m(\xi) = F_m^*(\xi) + \omega_1 + \omega_2 \exp(-\xi) + \omega_3 \exp(\xi),\tag{4.49}$$

$$\theta_m(\xi) = \theta_m^*(\xi) + \omega_5 \exp(\xi) + \omega_4 \exp(-\xi),\tag{4.50}$$

$$G_m(\xi) = G_m^*(\xi) + \omega_7 \exp(\xi) + \omega_6 \exp(-\xi),\tag{4.51}$$

Invoking Eq. (4.41), the values of ω_j ($j = 1 - 7$) are as follows

$$\begin{aligned}
\omega_1 &= -F_m^*(0) + \left. \frac{\partial F_m^*(\xi)}{\partial \xi} \right|_{\xi=0}, & \omega_2 &= \left. \frac{\partial F_m^*(\xi)}{\partial \xi} \right|_{\xi=0}, & \omega_4 &= -\theta_m^*(\xi)|_{\xi=0}, \\
\omega_6 &= -G_m^*(\xi)|_{\xi=0} & \omega_3 &= \omega_5 = \omega_7 = 0.
\end{aligned} \tag{4.52}$$

4.4 Convergence analysis

HAM provides great freedom to control rate of convergence of solution by taking appropriate values of auxiliary parameters. The accurate auxiliary parameters h_f, h_θ and h_G are selected from relevant range of plotted h –curves at 25th iteration. In this study, numerical computations are restricted thoroughly with practical range of non-dimensional parameters [91] as $(0.2 \leq \gamma_1 \leq 0.8), (0.1 \leq \beta_1 \leq 0.5), (0.4 \leq \lambda_1 \leq 1.5), (0.2 \leq \hat{\beta}_c \leq 0.6), (0.1 \leq \delta_e \leq 0.5), (0.2 \leq S_1 \leq 0.6), (0.1 \leq K_t \leq 0.5), (0.5 \leq Pr \leq 2.5), (0.1 \leq K_m \leq 0.5)$ and $(0.1 \leq V_p \leq 0.4)$. Fig. 4.2 portrays the acceptable range of auxiliary parameters h_F, h_θ and h_G as $(-1.3 \leq h_F \leq -0.4), (-1.5 \leq h_\theta \leq -0.5)$ and $(-1.2 \leq h_G \leq -0.4)$. Table 4.1 shows that 35th order of approximations is enough to obtain the convergent solution computed to demonstrate the convergence analysis of homotopic expressions. Table 4.2 is built to validate the present consequences with previously published results by Acharya [92], Khan and Pop [93] and Hsiao [94]. This table represents the comparison of present results with the previous literature which gives good agreement.

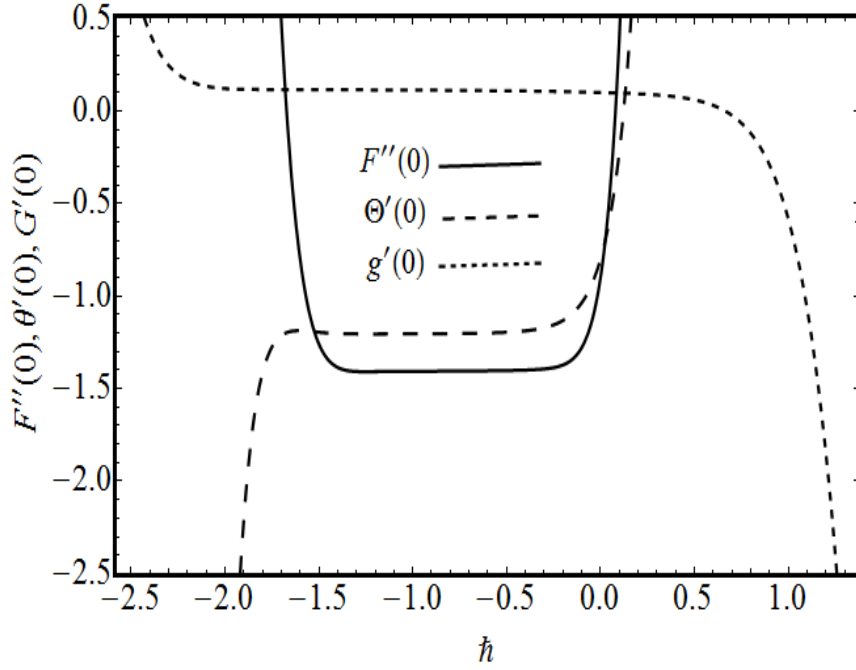


Fig. 4.2: h -curves.

Table 4.1: Convergence analysis when $\gamma_1 = A = K_t = 0.1, \lambda_1 = 0.5, \beta_2 = 0.3, \delta_e = S_1 = V_p = 0.2, K_m = 0.1, \beta_1 = 1.0, Pr = 1.2$ and $Sc = 1.5$.

Approx. order	$-F''(0)$	$-\theta'(0)$	$-\Phi'(0)$
1	0.8587	0.6985	0.1382
7	0.8524	0.7322	0.1345
14	0.8554	0.7524	0.1360
20	0.8582	0.7959	0.1371
25	0.8607	0.7934	0.1450
30	0.8612	0.7668	0.1429
35	0.8624	0.7743	0.1408
40	0.8624	0.7743	0.1408
46	0.8624	0.7743	0.1408

Table 4.2: Numerical comparison of $-\theta(0)$ when $\gamma_1 = \hat{\beta}_t = \lambda_1 = \hat{\beta}_c = A = \beta_1 = S_1 = K_m = 0.0$ and $Pr = 5.0$.

δ_e	Acharya et al. [92]	Khan & Pop [93]	Hsiao et al. [94]	Present HAM
0.1	0.9524	0.9524	0.952432	1.00124
0.2	0.6932	0.6932	0.693211	0.69582
0.3	0.5201	0.5201	0.520147	0.51596
0.4	0.4026	0.4026	0.402631	0.40236
0.5	0.3211	0.3211	0.321149	0.32340

4.5 Results and discussion

In this section, the fluctuations in interested quantities like curvature parameter γ_1 , Deborah number β_2 , velocities ratio parameter A, strength of homogeneous reaction parameter K_m , strength of heterogeneous reaction parameter K_t , mass diffusion ratio δ^* , Schmidt number Sc , thermal relaxation parameter δ_e , Prandtl number Pr, mixed convection parameter β_1 and thermal stratification parameter S_1 on velocity $F'(\xi)$, temperature $\theta(\xi)$ and concentration $G(\xi)$ is displayed in Figs. (4.3 – 4.15). Fig. 4.3 demonstrates curvature parameter γ_1 influences on $F'(\xi)$. As increment in curvature causes decrease in cylinder radius that causes low resistance in flow field. As a result, $F'(\xi)$ shows increasing behavior. Deborah number β_2 consequences upon $F'(\xi)$ are illustrated via Fig. 4.4. The velocity $F'(\xi)$ profile and related momentum boundary layer thickness are diminished with the rise of β_2 . It holds because increase of β_2 describes the growth in the elasticity of fluid material. Fig. 4.5 shows the influences of λ_1 on $F'(\xi)$.

As expected, the velocity profile $F'(\xi)$ declines against λ_1 . It is true because λ_1 is ratio of relaxation to retardation time i.e. its higher values enlarge the relaxation time (resistance in flow). Noticeable features of β_1 are shown in Fig. 4.6. Physically increase of β_1 is responsible for intensification of buoyancy forces. That results in increase of $F'(\xi)$. Fig. 4.7 is revealed to study the features of velocities ratio parameter A on $F'(\xi)$. This figure suggests that in both cases ($A > 1$ and $A < 1$) fluid velocity enhances. The increase of A upsurges free stream velocity that eventually results in the enhancement of $F'(\xi)$. This developing behavior of $F'(\xi)$ remained same when either free stream velocity dominates or followed. Thickness of boundary layer has reverse effects. Fig. 4.8 portrays the inclination ϕ_a effects on $F'(\xi)$. The decaying nature of $F'(\xi)$ is observed for greater estimation of ϕ_a . Since, impact of gravity forces decreases for higher altitude. That causes reduction in velocity profile. Fig. 4.9 elaborates the consequences of thermal relaxation parameter δ_e on temperature $\theta(\xi)$. It can be seen that δ_e causes reduction in temperature $\theta(\xi)$. Physically it holds because increment in thermal relaxation slows down heat transfer between particles, as a result, temperature decreases. Fig. 4.10 depicts fluctuation in fluid temperature against thermal stratification parameter S_1 . As temperature difference $(T_w - T_\infty)$ gradually decreases for higher approximation of S_1 that eventually declines the temperature curve $\theta(\xi)$. Fig. 4.11 elucidates that temperature and thermal boundary layer thickness are decreased significantly when the values of Prandtl number Pr are greater. Since, Prandtl number is the ratio of momentum to thermal diffusivities. Increase in Prandtl number corresponds to stronger momentum diffusivity and weaker thermal diffusivity. Here weaker thermal diffusivity dominant over the stronger momentum diffusivity due to which lesser temperature is noticed. The influence

of the homogeneous reaction parameter K_m on $G(\xi)$ is illustrated through Fig. 4.12. Since during the homogeneous reaction, reactants are consumed and as a result, the fluid concentration denigrates which is apparently seen from this figure. Fig. 4.13 explained the heterogeneous reaction parameter K_t impacts on the concentration profile $G(\xi)$. The concentration boundary layer thickness upsurges with increasing K_t which agrees with the common physical behavior of the homogeneous and heterogeneous reactions parameters. Variation of concentration profile $G(\xi)$ against various values of the Schmidt number Sc is displayed in Fig. 4.14. As Schmidt number varies inversely as mass diffusivity which consequently, declines the concentration. Wall friction coefficient C_F , for emerging parameters $\hat{\beta}_c$ and A are presented in Figs. 4.15 and 4.16. The dwindling influence of wall friction is observed for both $\hat{\beta}_c$ and A .

4.6 Graphical outcomes

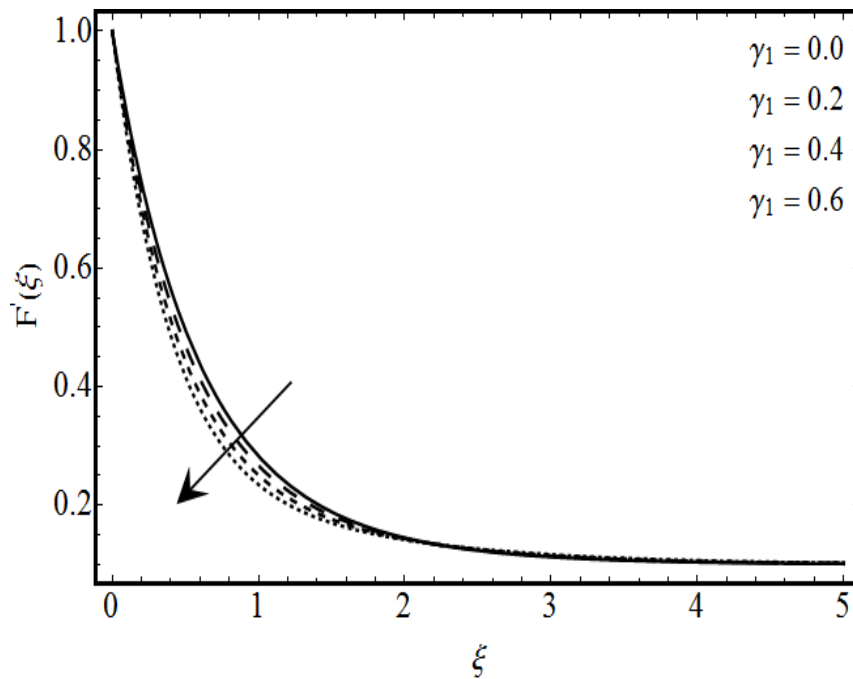


Fig. 4.3: Variation of γ_1 on $F'(\xi)$.

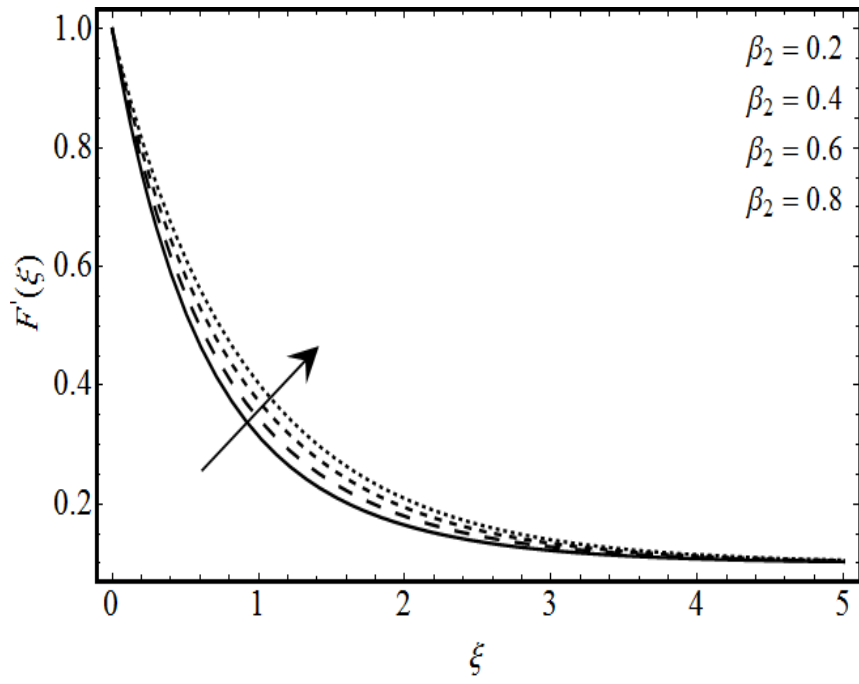


Fig. 4.4: Variation of β_2 on $F'(\xi)$.

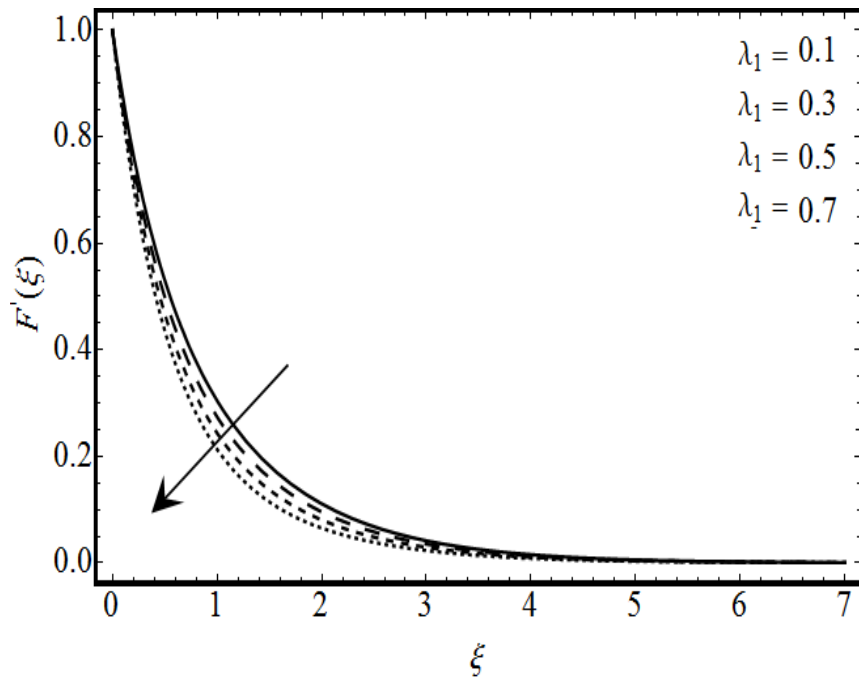


Fig. 4.5: Variation of λ_1 on $F'(\xi)$.

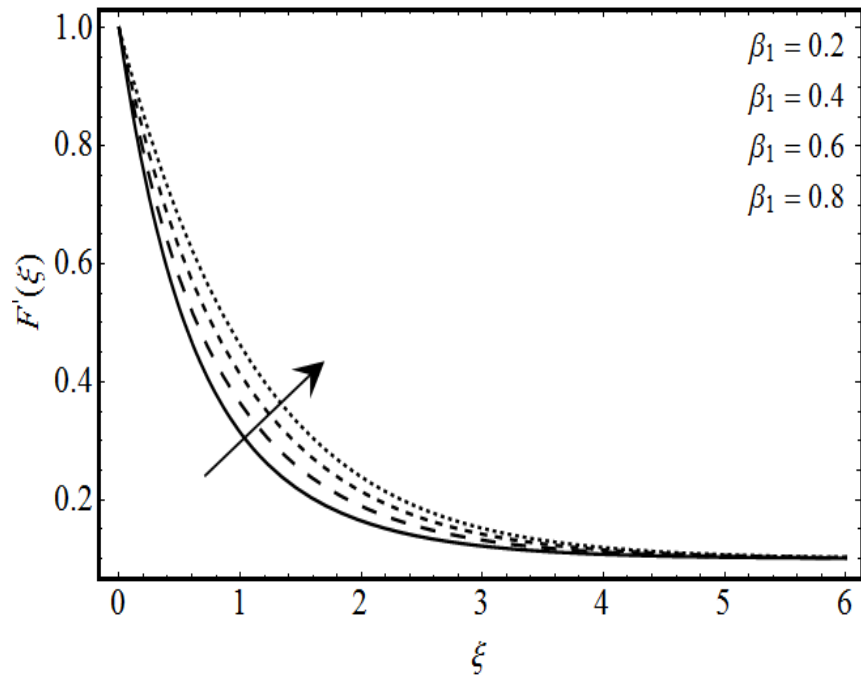


Fig. 4.6: Variation of β_1 on $F'(\xi)$.

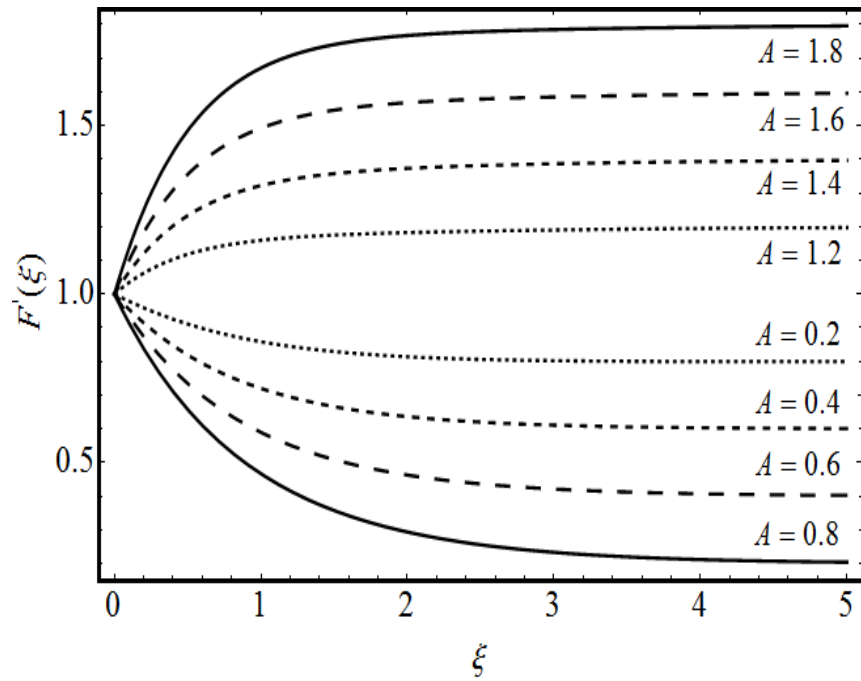


Fig. 4.7: Variation of A on $F'(\xi)$.

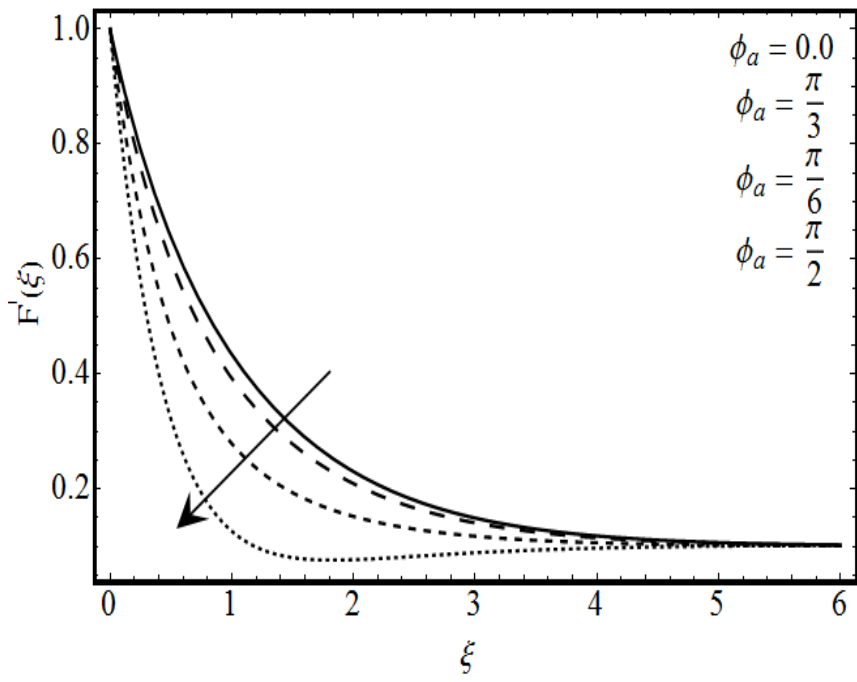


Fig. 4.8: Variation of ϕ_a on $F'(\xi)$.

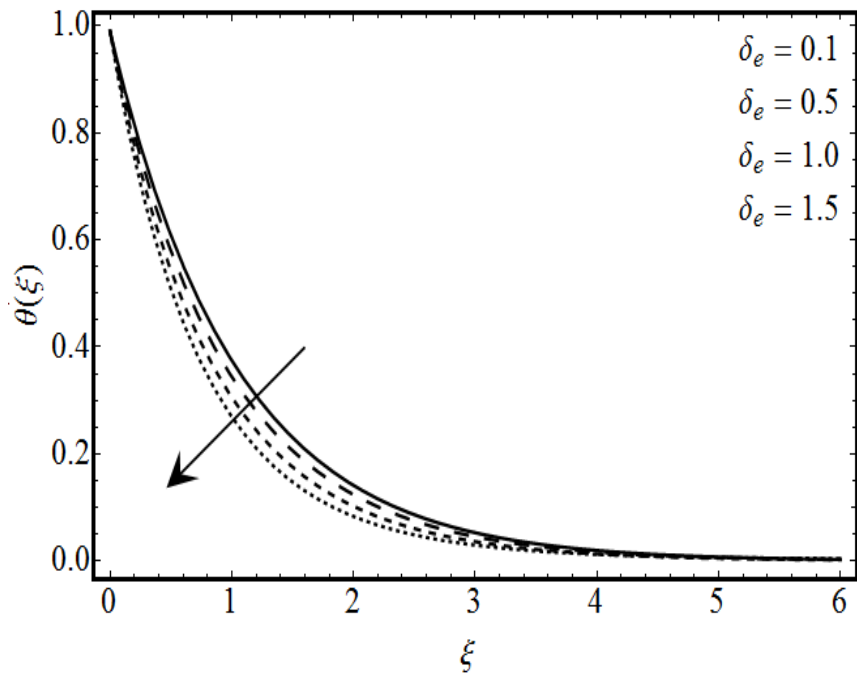


Fig. 4.9: Variation of δ_e on $\theta(\xi)$.

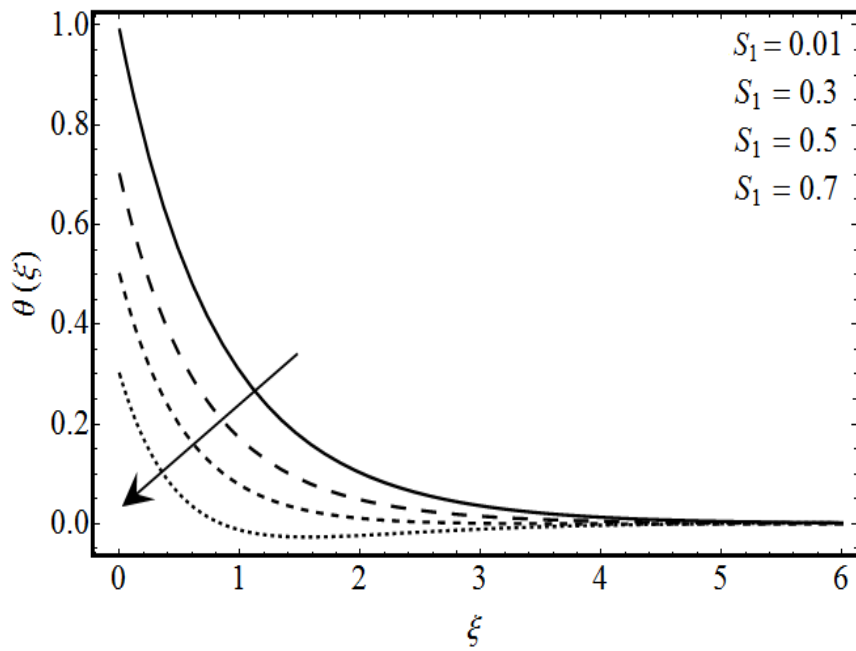


Fig. 4.10: Variation of S_1 on $\theta(\xi)$.

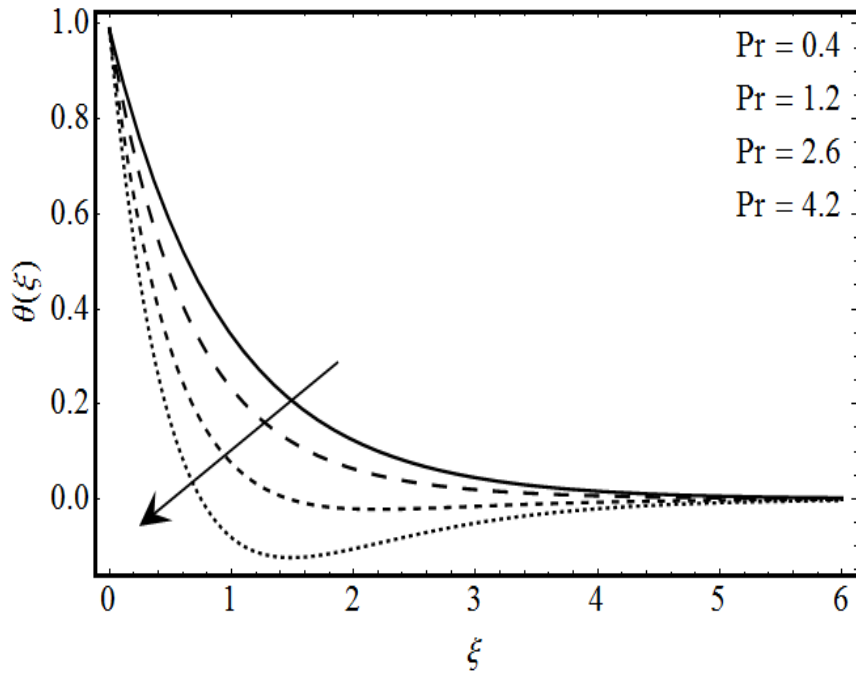


Fig. 4.11: Variation of Pr on $\theta(\xi)$.

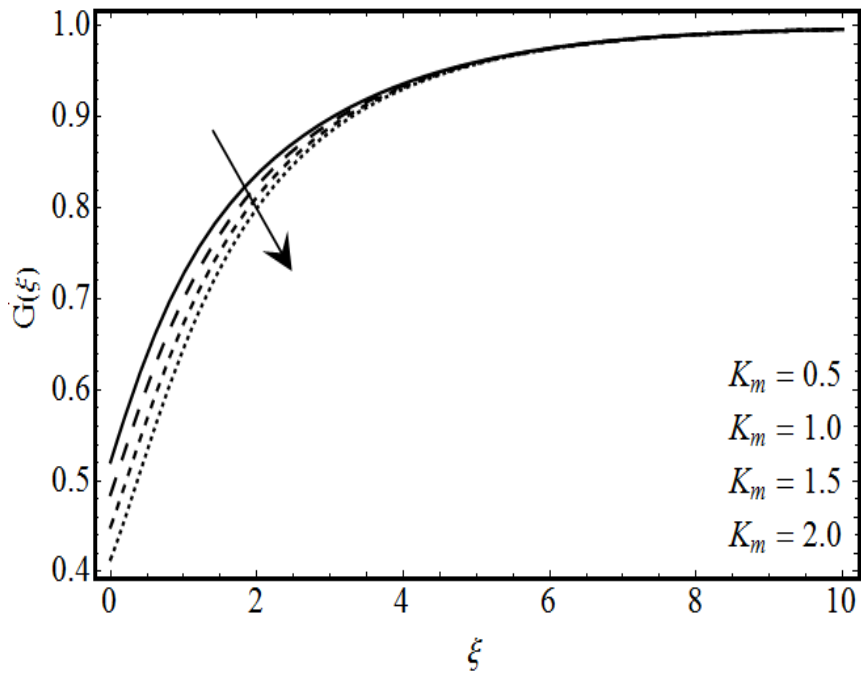


Fig. 4.12: Variation of K_m on $G(\xi)$.

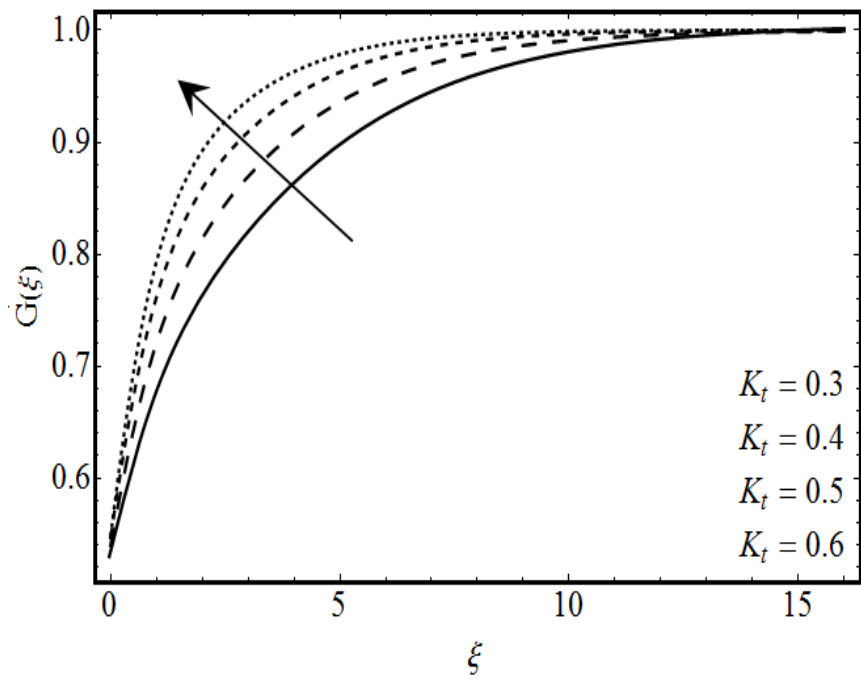


Fig. 4.13: Variation of K_t on $G(\xi)$.

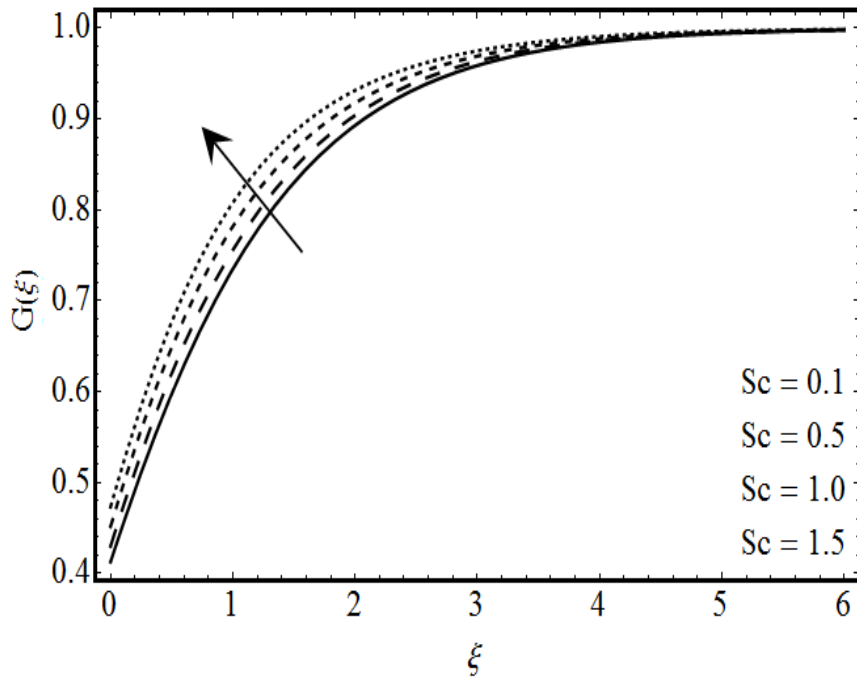


Fig. 4.14: Variation of Sc on $G(\xi)$.

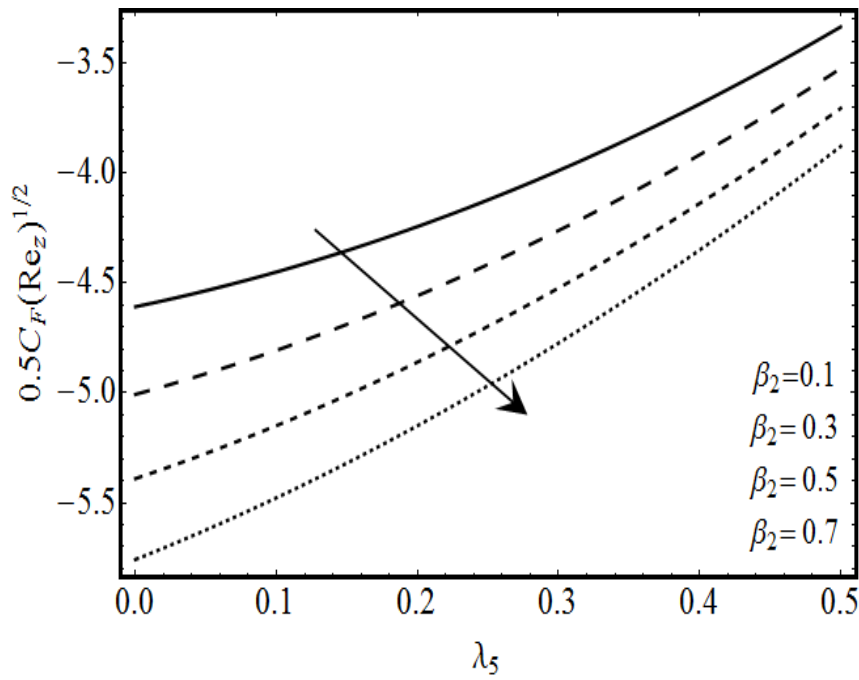


Fig. 4.15: Variation of $C_F(Re_z)^{\frac{1}{2}}$ on β_2 .

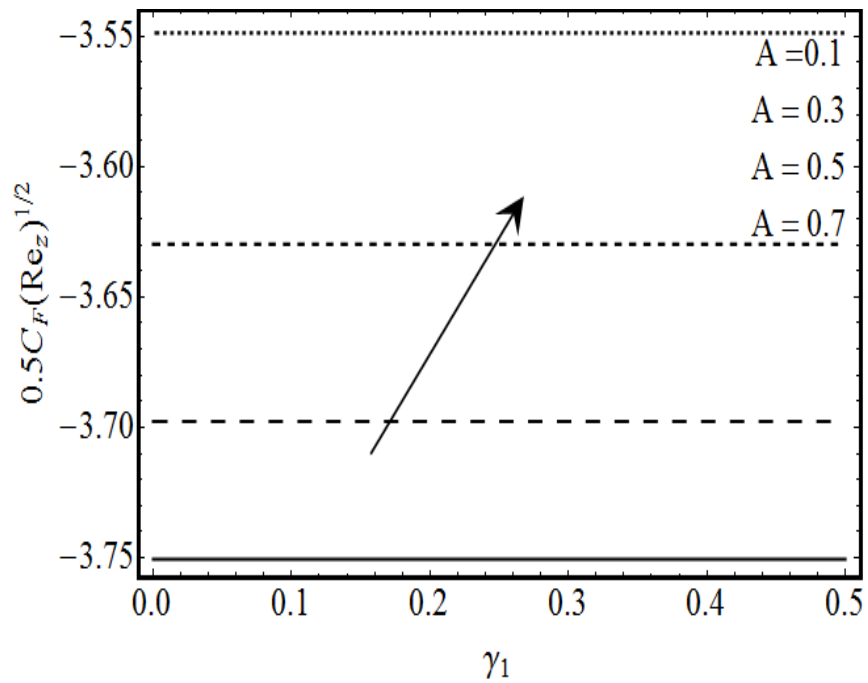


Fig. 4.16: Variation of $C_F(Re_z)^{\frac{1}{2}}$ on A .

4.5 Conclusions

Here we analyze the homogeneous/heterogeneous reactions for Jeffery fluid model induced by an inclined stretching cylinder. Heat transfer analysis has been accomplished within frame of Cattaneo-Christove heat flux model. Major key points are summarized as follows:

- Deborah number β_2 deaccelerates the linear momentum.
- Homogeneous parameter K_m is responsible to decrease in concentration while heterogeneous parameter K_t has opposite effect.
- Thermal stratification parameters reduce the temperature distribution.
- Prandtl number Pr and thermal stratification parameter declines fluid temperature significantly.

CHAPTER 5

Aspects of activation energy for Jeffrey nanofluid with Cattaneo-Christov double diffusion model

5.1 Introduction

In this chapter, nonlinear convective flow of Jeffrey nanofluid within the frame of Cattaneo-Christov double diffusion over an inclined permeable stretched cylinder is addressed. Analysis subjected to Arrhenius activation energy, chemical reaction, double stratification and non-uniform heat generation/absorption are assumed. For activation energy, a novel binary chemical reaction model is used. Cattaneo-Christov double diffusion model are employed to configure heat and mass transfer. Apposite similarity transformations are engaged to attain nonlinear ordinary differential system. Non-dimensional system of governing equations is solved analytically to obtain the series solution by Homotopy technique. Expressions of skin friction and Nusselt number are calculated through numerical values. Graphs and tables are created to analyze the impact of governing parameters on interested physical entities.

5.2 Mathematical formulation

Consider 2D, nonlinear convective flow of Jeffrey nanofluid subjected to Arrhenius activation energy, generalized Fourier and Fick's models by an inclined permeable stretching cylinder of radius R_0 . Non-uniform heat generation/absorption, binary chemical reaction, nonlinear mixed convection, thermal and solutal stratification are accounted for present flow framework. The problem is considered in cylindrical polar coordinates (r, θ, z) with velocity components (u_r, u_θ, u_z) . The flow is generated with the linear stretching velocity of the form $U_w \left(= \frac{U_0 z}{L} \right)$. Flow geometry is given in Fig. 5.1. The cylindrical surface is thermally and solutally stratified by maintaining (T_w, C_w) in the form $\left(T_0 + \frac{d_1 z}{L}, C_0 + \frac{d_3 z}{L} \right)$, while ambient temperature and concentration (T_∞, C_∞) are

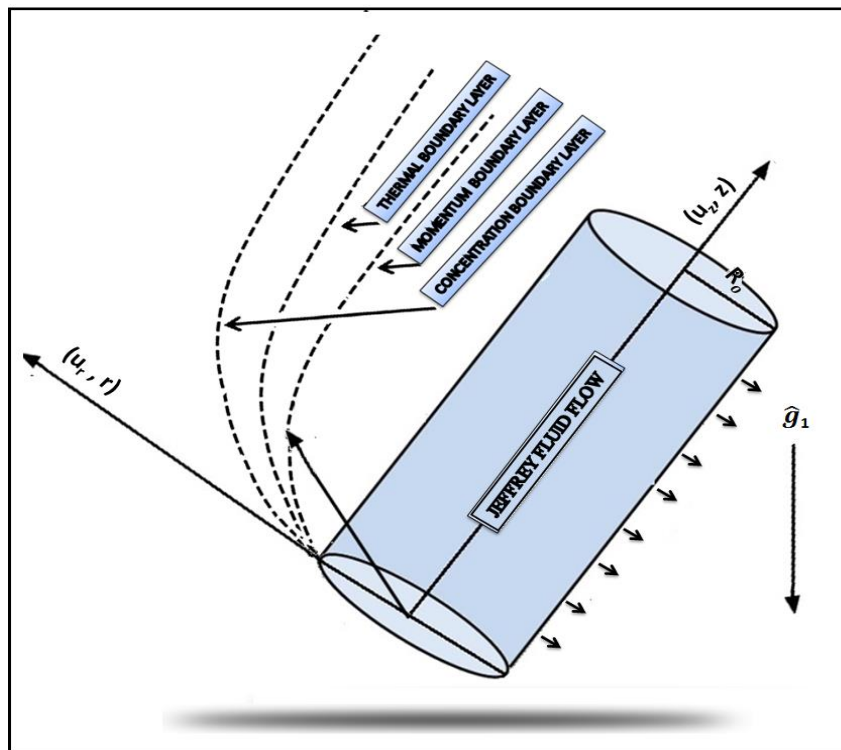


Fig. 5.1: Physical model.

measured in the form $(T_0 + \frac{d_2 z}{L}, C_0 + \frac{d_4 z}{L})$. The effect of external forces and pressure gradient is supposed to be negligible. The conservation laws under above supposition after using the boundary layer approximations are [95,96]

$$\frac{\partial}{\partial r}(ru_r) + \frac{\partial}{\partial z}(ru_z) = 0, \quad (5.1)$$

$$\begin{aligned} u_z \frac{\partial u_z}{\partial z} + u \frac{\partial u_z}{\partial r} &= \frac{\nu_1}{(1 + \lambda_1)} \left(\frac{\partial^2 u_z}{\partial r^2} + \frac{1}{r} \frac{\partial u_z}{\partial r} \right) + \frac{\sigma B_0^2 u_z}{\rho_f} \\ &+ \frac{\nu_1 \lambda_2}{(1 + \lambda_1)} \left(u_r \frac{\partial^3 u_z}{\partial r^3} + \frac{\partial u_r}{\partial r} \frac{\partial^2 u_z}{\partial r^2} + u_z \frac{\partial^3 u_z}{\partial z \partial r^2} \frac{\partial u_z}{\partial r} \frac{\partial^2 u_z}{\partial r \partial z} + \frac{u_r}{r} \frac{\partial^2 u_z}{\partial r^2} + \frac{u_z}{r} \frac{\partial^2 u_z}{\partial r \partial z} \right) \\ &+ \frac{\hat{g}_1}{\rho_f} (\Gamma_1 (T - T_\infty) + \Gamma_2 (T - T_\infty)^2 + \Gamma_3 (C - C_\infty) + \Gamma_4 (C - C_\infty)^2) \cos \phi_a. \end{aligned} \quad (5.2)$$

Heat and mass fluxes $(\mathbf{q}_1, \mathbf{J}_1)$ within the frame of Cattaneo-Christov double diffusive model [97] are

$$\mathbf{q}_1 + \hat{\Gamma}_e \left[\frac{\partial \mathbf{q}_1}{\partial t} + \mathbf{V}_1 \cdot \nabla \mathbf{q}_1 - (\mathbf{q}_1 \cdot \nabla) \mathbf{V}_1 + (\nabla \cdot \mathbf{V}_1) \mathbf{q}_1 \right] = -k_f \nabla T, \quad (5.3)$$

$$\mathbf{J}_1 + \hat{\Gamma}_c \left[\frac{\partial \mathbf{J}_1}{\partial t} + \mathbf{V}_1 \cdot \nabla \mathbf{J}_1 - (\mathbf{J}_1 \cdot \nabla) \mathbf{V}_1 + (\nabla \cdot \mathbf{V}_1) \mathbf{J}_1 \right] = -D_B \nabla C. \quad (5.4)$$

Classical Fourier's and Fick's laws are deduced by inserting $\hat{\Gamma}_e = \hat{\Gamma}_c = 0$ in Eqs. (5.3) and (5.4). After employing the steady and incompressibility conditions, the models reduce to:

$$\mathbf{q}_1 + \hat{\Gamma}_e [\mathbf{V}_1 \cdot \nabla \mathbf{q}_1 - (\mathbf{q}_1 \cdot \nabla) \mathbf{V}_1] = -\hat{k}_f \nabla T, \quad (5.5)$$

$$\mathbf{J}_1 + \hat{\Gamma}_c [\mathbf{V}_1 \cdot \nabla \mathbf{J}_1 - (\mathbf{J}_1 \cdot \nabla) \mathbf{V}_1] = -D_B \nabla C. \quad (5.6)$$

Then two-dimensional energy and concentration expressions yields

$$\begin{aligned}
u_r \frac{\partial T}{\partial r} + u_z \frac{\partial T}{\partial z} + \hat{\Gamma}_e \Pi_e &= \frac{\hat{k}_f}{(\rho C_p)_f} \frac{1}{r} \frac{\partial}{\partial r} \left(r \frac{\partial T}{\partial r} \right) + \frac{\hat{Q}_m}{(\rho C_p)_f} \\
&+ \tau_1 D_B \frac{\partial C}{\partial r} \frac{\partial T}{\partial r} + \frac{\tau_1 D_T}{T_\infty} \left(\frac{\partial T}{\partial r} \right)^2,
\end{aligned} \tag{5.7}$$

$$\begin{aligned}
u_r \frac{\partial C}{\partial r} + u_z \frac{\partial C}{\partial z} + \hat{\Gamma}_c \Pi_c &= D_B \frac{\partial}{\partial r} \left(r \frac{\partial C}{\partial r} \right) + \frac{D_T}{T_\infty} \frac{1}{r} \frac{\partial}{\partial r} \left(r \frac{\partial T}{\partial r} \right) - \hat{K}_1 (C - C_\infty) \\
&- \hat{K}_r^2 (C_w - C_0) \left(\frac{T}{T_\infty} \right)^p \exp \left[-\frac{E_1}{T k^*} \right],
\end{aligned} \tag{5.8}$$

with

$$\begin{aligned}
u_z = \frac{U_0 z}{L}, \quad T = T_w = T_0 + \frac{d_1 z}{L}, \\
u_r = V_1, \quad C = C_w = C_0 + \frac{d_3 z}{L}
\end{aligned} \Bigg|_{\text{at } r = R_0}, \tag{5.9}$$

$$\begin{aligned}
u_z \rightarrow 0, \quad T \rightarrow T_\infty = T_0 + \frac{d_2 x}{L}, \\
u_r \rightarrow 0, \quad C \rightarrow C_\infty = C_0 + \frac{d_4 x}{L}.
\end{aligned} \Bigg|_{\text{when } r \rightarrow \infty}, \tag{5.10}$$

$$\begin{aligned}
\Pi_e &= u_r^2 \frac{\partial^2 T}{\partial r^2} + u_z^2 \frac{\partial^2 T}{\partial z^2} + \frac{\partial T}{\partial r} \left(u_z \frac{\partial u_r}{\partial z} + u_r \frac{\partial u_r}{\partial r} \right) + 2u_z u_r \frac{\partial^2 C}{\partial r \partial z} \\
&+ \frac{\partial T}{\partial z} \left(u_z \frac{\partial u_z}{\partial z} + u_r \frac{\partial u_r}{\partial r} \right),
\end{aligned} \tag{5.11}$$

$$\begin{aligned}
\Pi_c &= u_r^2 \frac{\partial^2 C}{\partial r^2} + u_z^2 \frac{\partial^2 C}{\partial z^2} + \frac{\partial C}{\partial r} \left(u_z \frac{\partial u_r}{\partial z} + u_r \frac{\partial u_r}{\partial r} \right) + 2u_r u_z \frac{\partial^2 C}{\partial r \partial z} \\
&+ \frac{\partial C}{\partial z} \left(u_z \frac{\partial u_z}{\partial z} + u_r \frac{\partial u_r}{\partial r} \right).
\end{aligned} \tag{5.12}$$

The non-uniform heat source/sink \hat{Q}_m [98] is expressed as

$$\hat{Q}_m = \frac{U_w \hat{k}_f}{z\nu_1} \left[\hat{B}_1 (T_w - T_0) \frac{\partial F}{\partial \xi} + \hat{B}_2 (T - T_\infty) \right], \quad (5.13)$$

where \hat{B}_1 and \hat{B}_2 are the coefficients of space and temperature dependent heat generation/absorption, respectively. The case $\hat{B}_1 > 0$ and $\hat{B}_2 > 0$ denote internal heat generation while $\hat{B}_1 < 0$ and $\hat{B}_2 < 0$ represent internal heat absorption.

Considering

$$\begin{aligned} \xi &= \sqrt{\frac{U_0}{Lv_1}} \left(\frac{r^2 - R_0^2}{2R_0} \right), & \Psi_1(\xi) &= \sqrt{\frac{\nu_1 U_0 z^2}{L}} F(\xi), \\ u_z(\xi) &= \frac{U_0 z}{L} F'(\xi), & u_r(\xi) &= -\frac{R_0}{r} \sqrt{\frac{\nu_1 U_0}{L}} F(\xi), \\ \theta(\xi) &= \frac{T - T_\infty}{T_w - T_0}, & \Phi(\xi) &= \frac{C - C_\infty}{C_w - C_0}. \end{aligned} \quad (5.14)$$

Now flow problem under above transformations become

$$\begin{aligned} &(1 + 2\gamma_1 \xi) [F'''' + \beta_2 (F''^2 - FF^4)] + 2\gamma_1 F'' - M_1 F' + \gamma_1 \beta_2 (F'F'' - 3FF''') \\ &+ (1 + \lambda_1) \left[(FF'' - F'^2) - \beta_1 \left((1 + \hat{\beta}_t \theta) \theta + \hat{N}_1 (1 + \hat{\beta}_c \Phi) \Phi \right) \cos \phi_a \right] = 0, \end{aligned} \quad (5.15)$$

$$\begin{aligned} &(1 + 2\gamma_1 \xi) \left[\theta'' + Pr \hat{N}_b \left(\Phi' \theta' + \frac{\hat{N}_t}{\hat{N}_b} \theta'^2 + Ec F''^2 \right) \right] + Pr F \theta' + (\hat{B}_1 F' + \hat{B}_2 \theta) \\ &- Pr \delta_e [F^2 \theta'' + (F'^2 - FF'')(\theta + S_1) - FF' \theta'] + 2\gamma_1 \theta' - Pr(\theta + S_1) F' = 0, \end{aligned} \quad (5.16)$$

$$\begin{aligned} &(1 + 2\gamma_1 \xi) \left[\Phi'' + \frac{\hat{N}_t}{\hat{N}_b} \theta'' \right] + 2\gamma_1 \left(\Phi' + \frac{\hat{N}_t}{\hat{N}_b} \theta' \right) + Sc(\Phi + S_2) [F' - \delta_c (F'^2 - FF'')] \\ &Sc(F\Phi' - \gamma_2 \Phi - \delta_c (F^2 \Phi'' - FF' \Phi')) - Sc\gamma_3 (1 + \delta\theta)^p \exp \left[-\frac{E_a}{1 + \delta\theta} \right] = 0, \end{aligned} \quad (5.17)$$

with endpoint conditions

$$\begin{aligned} F'(\xi) = 1, \quad F(\xi) = V_p, \quad \theta(\xi) = 1 - S_1, \quad \Phi(\xi) = 1 - S_2, \quad \text{at } \xi = 0, \\ F'(\xi) = 0, \quad \theta(\xi) = 0, \quad \Phi(\xi) = 0, \quad \text{as } \xi \rightarrow \infty. \end{aligned} \quad (5.18)$$

The dimensionless variables [99-101] appeared are expressed as follows:

$$\begin{aligned} \hat{\beta}_c &= \frac{\Gamma_4(C_w - C_0)}{\Gamma_3}, \gamma_1 = \sqrt{\frac{\nu_1 L}{U_0 R_0^2}}, \hat{N}_1 = \frac{\Gamma_3(C_w - C_0)}{\Gamma_1(T_w - T_0)}, \alpha_1 = \frac{\lambda_2}{\nu_1 L}, \delta = \frac{T_w - T_0}{T_\infty}, \\ Gr^* &= \frac{\hat{g}_1 \Gamma_3 (C_w - C_0) z^3}{\nu_1^2}, \hat{N}_t = \frac{\tau_1 D_T (T_w - T_0)}{T_\infty \nu_1}, \hat{\beta}_t = \frac{\Gamma_2 (T_w - T_0)}{\Gamma_1}, Sc = \frac{\nu_1}{D_B}, \\ \beta_1 &= \frac{L^2 (T_w - T_0) \hat{g}_1 \Gamma_1}{U_0^2 z^2}, \hat{N}_b = \frac{\tau_1 D_B (C_w - C_0)}{\nu_1}, \beta_2 = \frac{\lambda_2 U_0}{L}, \gamma_3 = \frac{\hat{K}_r^2 L}{U_0}, \\ \delta_c &= \frac{\hat{\Gamma}_c U_0}{L}, Pr = \frac{(\mu C_p)_f}{\hat{k}_f}, \gamma_2 = \frac{\hat{K}_1 L}{U_0}, Ec = \frac{U_w^2}{C_p (T_w - T_0)}, \delta_e = \frac{\hat{\Gamma}_e U_0}{L}. \end{aligned} \quad (5.19)$$

The skin friction coefficient C_F , local Nusselt Nu_z and Sherwood Sh_z numbers are

$$C_F = \frac{2\tau_w}{\rho_f U_w^2}, \quad Nu_z = \frac{zq_w}{\hat{k}_f (T_w - T_0)}, \quad Sh_z = \frac{zj_w}{D_B (C_w - C_0)}, \quad (5.20)$$

with

$$\tau_w = \frac{\mu}{(1 + \lambda_1)} \frac{\partial u_z}{\partial r} + \frac{\mu \lambda_2}{(1 + \lambda_1)} \left(u_r \frac{\partial^2 u_z}{\partial r^2} + u_z \frac{\partial^2 u_z}{\partial r \partial z} \right) \Big|_{r=R_0}, \quad (5.21)$$

$$q_w = -\hat{k}_f \frac{\partial T}{\partial r} \Big|_{r=R_0}, \quad (5.22)$$

$$j_w = -D_B \frac{\partial C}{\partial r} \Big|_{r=R_0}. \quad (5.23)$$

The dimensionless forms of these quantities are

$$\frac{1}{2}C_F(Re_z)^{\frac{1}{2}} = \frac{1}{(1 + \lambda_1)} [(1 - \gamma_1\beta_2F(0) + \beta_2F'(0))F''(0) - \beta_2F(0)F'''(0)], \quad (5.24)$$

$$Nu_z(Re_z)^{-\frac{1}{2}} = -\theta'(0), \quad (5.25)$$

$$Sh_z(Re_z)^{-\frac{1}{2}} = -\Phi'(0), \quad (5.26)$$

in which $Re_z \left(= \frac{U_0 z^2}{\nu_1 L} \right)$ is the local Reynolds number.

5.3 Methodology

The selected initial guesses $(F^0(\xi), \theta^0(\xi), \Phi^0(\xi))$ and auxiliary linear operators $(\mathcal{E}_F, \mathcal{E}_\theta, \mathcal{E}_\Phi)$ are of the form:

$$\begin{aligned} F^0(\xi) &= 1 + V_p - \exp(-\xi), \\ \theta^0(\xi) &= (1 - S_1) \exp(-\xi), \\ \Phi^0(\xi) &= (1 - S_2) \exp(-\xi), \end{aligned} \quad (5.27)$$

$$\mathcal{E}_F[F] = F''' - F', \quad \mathcal{E}_\theta[\theta] = \theta'' - \theta, \quad \mathcal{E}_\Phi[\Phi] = \Phi'' - \Phi, \quad (5.28)$$

the following properties holds (see Ref. [102])

$$\begin{aligned} \mathcal{E}_F[\omega_2 \exp(-\xi) + \omega_1 + \omega_3 \exp(\xi)] &= 0, \\ \mathcal{E}_\theta[\omega_4 \exp(-\xi) + \omega_5 \exp(\xi)] &= 0, \\ \mathcal{E}_\Phi[\omega_6 \exp(-\xi) + \omega_7 \exp(\xi)] &= 0, \end{aligned} \quad (5.29)$$

in which ω_j with $(j = 1 - 5)$ are arbitrary constants.

5.3.1 Zeroth-order systems

The zeroth-order deformation problems are constructed as follows:

$$(1 - \hat{q})\mathcal{E}_F[\hat{F}(\xi; \hat{q}) - F^0(\xi)] = \hat{q}h_F\hat{N}_F[\hat{F}(\xi; \hat{q}), \hat{\theta}(\xi; \hat{q}), \hat{\Phi}(\xi; \hat{q})], \quad (5.30)$$

$$(1 - \hat{q})\mathcal{E}_\theta[\hat{\theta}(\xi; \hat{q}) - \theta^0(\xi)] = \hat{q}h_\theta\hat{N}_\theta[\hat{F}(\xi; \hat{q}), \hat{\theta}(\xi; \hat{q}), \hat{\Phi}(\xi; \hat{q})], \quad (5.31)$$

$$(1 - \hat{q})\mathcal{E}_\Phi[\hat{\Phi}(\xi; \hat{q}) - \Phi^0(\xi)] = \hat{q}h_\Phi\hat{N}_\Phi[\hat{F}(\xi; \hat{q}), \hat{\theta}(\xi; \hat{q}), \hat{\Phi}(\xi; \hat{q})], \quad (5.32)$$

with

$$\begin{aligned} \hat{F}'(0; \hat{q}) &= 1, \quad \hat{F}(0; \hat{q}) = V_p, \quad \hat{\theta}(0; \hat{q}) = 1 - S_1, \quad \hat{\Phi}(0; \hat{q}) = 1 - S_2, \\ \hat{F}'(\xi; \hat{q}) &= 0, \quad \hat{\theta}(\xi; \hat{q}) = 0, \quad \hat{\Phi}(\xi; \hat{q}) = 0, \quad \text{as } \xi \rightarrow \infty. \end{aligned} \quad (5.33)$$

Nonlinear operators \hat{N}_F , \hat{N}_θ and \hat{N}_Φ are

$$\begin{aligned} &\hat{N}_F[\hat{F}(\xi; \hat{q}), \hat{\theta}(\xi; \hat{q}), \hat{\Phi}(\xi; \hat{q})] \\ &= \gamma_1\beta_2 \left(\frac{\partial \hat{F}(\xi; \hat{q})}{\partial \xi} \frac{\partial^2 \hat{F}(\xi; \hat{q})}{\partial \xi^2} - 3\hat{F}(\xi; \hat{q}) \frac{\partial^3 \hat{F}(\xi; \hat{q})}{\partial \xi^3} \right) - M_1 \frac{\partial \hat{F}(\xi; \hat{q})}{\partial \xi} \\ &+ (1 + 2\gamma_1\xi) \left(\frac{\partial^3 \hat{F}(\xi; \hat{q})}{\partial \xi^3} + \beta_2 \left(\left(\frac{\partial^2 \hat{F}(\xi; \hat{q})}{\partial \xi^2} \right)^2 - \hat{F}(\xi; \hat{q}) \frac{\partial^4 \hat{F}(\xi; \hat{q})}{\partial \xi^4} \right) \right) \\ &+ 2\gamma_1 \frac{\partial^2 \hat{F}(\xi; \hat{q})}{\partial \xi^2} + (1 + \lambda_1) \left(\hat{F}(\xi; \hat{q}) \frac{\partial^2 \hat{F}(\xi; \hat{q})}{\partial \xi^2} - \frac{\partial \hat{F}(\xi; \hat{q})}{\partial \xi} \frac{\partial \hat{F}(\xi; \hat{q})}{\partial \xi} \right) \\ &- (1 + \lambda_1)\beta_1 \left(\frac{(1 + \hat{\beta}_t \hat{\theta}(\xi; \hat{q})) \hat{\theta}(\xi; \hat{q}) + \hat{N}_1 (1 + \hat{\beta}_c \hat{\Phi}(\xi; \hat{q})) \hat{\Phi}(\xi; \hat{q})}{\hat{N}_1 (1 + \hat{\beta}_c \hat{\Phi}(\xi; \hat{q})) \hat{\Phi}(\xi; \hat{q})} \right) \cos \phi_a, \end{aligned} \quad (5.34)$$

$$\begin{aligned}
& \hat{N}_\theta [\hat{F}(\xi; \hat{q}), \hat{\theta}(\xi; \hat{q}), \hat{\Phi}(\xi; \hat{q})] \\
&= (1 + 2\gamma_1 \xi) \frac{\partial^2 \hat{\theta}(\xi; \hat{q})}{\partial \xi^2} + 2\gamma_1 \frac{\partial \hat{\theta}(\xi; \hat{q})}{\partial \xi} + \hat{B}_1 \frac{\partial F(\xi; q)}{\partial \xi} + \hat{B}_2 \\
&+ (1 + 2\gamma_1 \xi) Pr \left(\hat{N}_b \frac{\partial \hat{\theta}(\xi; \hat{q})}{\partial \xi} \frac{\partial \hat{\Phi}(\xi; \hat{q})}{\partial \xi} + \hat{N}_t \left(\frac{\partial \hat{\theta}(\xi; \hat{q})}{\partial \xi} \right)^2 + Ec \left(\frac{\partial^2 \hat{F}(\xi; \hat{q})}{\partial \xi^2} \right)^2 \right) \\
&- Pr(\hat{\theta}(\xi; \hat{q}) + S_1) \left(\delta_e \left(\frac{\partial \hat{F}(\xi; \hat{q})}{\partial \xi} \frac{\partial \hat{F}(\xi; \hat{q})}{\partial \xi} - \hat{F}(\xi; \hat{q}) \frac{\partial^2 \hat{F}(\xi; \hat{q})}{\partial \xi^2} \right) + \frac{\partial \hat{F}(\xi; \hat{q})}{\partial \xi} \right) \\
&- Pr \left(\delta_e \left(\left(\hat{F}(\xi; \hat{q}) \right)^2 \frac{\partial^2 \hat{F}(\xi; \hat{q})}{\partial \xi^2} - \hat{F}(\xi; \hat{q}) \frac{\partial \hat{F}(\xi; \hat{q})}{\partial \xi} \frac{\partial \hat{\theta}(\xi; \hat{q})}{\partial \xi} \right) - \hat{F} \frac{\partial \hat{\theta}(\xi; \hat{q})}{\partial \xi} \right),
\end{aligned} \tag{5.35}$$

$$\begin{aligned}
& \hat{N}_\Phi [\hat{F}(\xi; \hat{q}), \hat{\theta}(\xi; \hat{q}), \hat{\Phi}(\xi; \hat{q})] \\
&= (1 + 2\gamma_1 \xi) \left(\frac{\partial^2 \hat{\Phi}(\xi; \hat{q})}{\partial \xi^2} + \frac{\hat{N}_t}{\hat{N}_b} \frac{\partial^2 \hat{\theta}(\xi; \hat{q})}{\partial \xi^2} \right) + Sc \hat{F}(\xi; \hat{q}) \frac{\partial \hat{\Phi}(\xi; \hat{q})}{\partial \xi} \\
&+ 2\gamma_1 \left(\frac{\hat{N}_t}{\hat{N}_b} \frac{\partial \hat{\theta}(\xi; \hat{q})}{\partial \xi} + \frac{\partial \hat{\Phi}(\xi; \hat{q})}{\partial \xi} \right) - \delta_c Sc \hat{F}(\xi; \hat{q}) \hat{F}(\xi; \hat{q}) \frac{\partial^2 \hat{\Phi}(\xi; \hat{q})}{\partial \xi^2} \\
&- Sc(\hat{\Phi}(\xi; \hat{q}) + S_2) \left(\delta_c \left(\frac{\partial \hat{F}(\xi; \hat{q})}{\partial \xi} \frac{\partial \hat{F}(\xi; \hat{q})}{\partial \xi} - \hat{F}(\xi; \hat{q}) \frac{\partial^2 \hat{F}(\xi; \hat{q})}{\partial \xi^2} \right) \right. \\
&\left. - \frac{\partial \hat{F}(\xi; \hat{q})}{\partial \xi} \right) + \delta_c Sc \hat{F}(\xi; \hat{q}) \frac{\partial \hat{F}(\xi; \hat{q})}{\partial \xi} \frac{\partial \hat{\Phi}(\xi; \hat{q})}{\partial \xi} - Sc \gamma_2 \hat{\Phi}(\xi; \hat{q}) \\
&- Sc \gamma_3 \left(1 + \delta \hat{\theta}(\xi; \hat{q}) \right)^p \exp \left[- \frac{E_a}{1 + \delta \hat{\theta}(\xi; \hat{q})} \right],
\end{aligned} \tag{5.36}$$

where $\hat{q} \in [0,1]$ is the embedding variable and when \hat{q} varies from 0 to 1 then we have

$$\begin{aligned}
F(\xi; 0) &= F^0(\xi) & F(\xi; 1) &= F(\xi), \\
\theta(\xi; 0) &= \theta^0(\xi) & \theta(\xi; 1) &= \theta(\xi), \\
\Phi(\xi; 0) &= \Phi^0(\xi) & \Phi(\xi; 1) &= \Phi(\xi).
\end{aligned} \tag{5.37}$$

5.3.2 m^{th} -order systems

The m^{th} order system is

$$\mathcal{E}_F[F_m(\xi) - \chi_m F_{m-1}(\xi)] = h_F R_m^F(\xi), \tag{5.38}$$

$$\mathcal{E}_\theta[\theta_m(\xi) - \chi_m \theta_{m-1}(\xi)] = h_\theta R_m^\theta(\xi), \tag{5.39}$$

$$\mathcal{E}_\Phi[\Phi_m(\xi) - \chi_m \Phi_{m-1}(\xi)] = h_\Phi R_m^\Phi(\xi), \tag{5.40}$$

$$F_m(0) = 0, \quad F'_m(0) = 0, \quad \theta_m(0) = 0, \quad \Phi_m(0) = 0,$$

$$F'_m(\xi) = 0, \quad \theta_m(\xi) = 0, \quad \Phi_m(\xi) = 0, \quad \text{when } \xi \rightarrow \infty. \tag{5.41}$$

where the nonlinear functions $R_m^F(\xi)$, $R_m^\theta(\xi)$ and $R_m^\Phi(\xi)$ have the following forms:

$$\begin{aligned}
R_m^F(\xi) &= (1 + 2\gamma_1 \xi) F_{m-1}''' + 2\gamma_1 F_{m-1}'' - M_1 F_{m-1}' - (1 + \lambda_1) \beta_1 \theta_{m-1} \cos \phi_a \\
&\quad + (1 + 2\gamma_1 \xi) \beta_2 \sum_{k=0}^m (F_{m-1-k}'' F_k'' - F_{m-1-k} F_k^4) - \hat{N}_1 \Phi_{m-1} \cos \phi_a \\
&\quad - (1 + \lambda_1) \beta_1 \left(\sum_{k=0}^m (\hat{\beta}_t \theta_{m-1-k} \theta_k + \hat{N}_1 \hat{\beta}_c \Phi_{m-1-k} \Phi_k) \right) \cos \phi_a \\
&\quad + (1 + \lambda_1) (1 + 2\gamma_1 \xi) \sum_{k=0}^m (F_{m-1-k} F_k'' - F_{m-1-k}' F_k'),
\end{aligned} \tag{5.42}$$

$$\begin{aligned}
R_m^\theta(\xi) &= (1 + 2\gamma_1\xi)\theta''_{m-1} + 2\gamma_1\theta'_{m-1} - Pr S_1 F'_{m-1} + \hat{B}_1 F'_{m-1} + \hat{B}_2 \theta_{m-1} \\
&+ (1 + 2\gamma_1\xi)Pr\hat{N}_b \sum_{k=0}^m \left(\Phi'_{m-1-k}\theta'_k + \frac{\hat{N}_t}{\hat{N}_b}\theta'_{m-1-k}\theta'_k + EcF''_{m-1-k}F'_k \right) \\
&+ Pr \sum_{k=0}^m (F_{m-1-k}\theta'_k - \theta_{m-1-k}F'_k - \delta_e S_1 (F'_{m-1-k}F'_k - F_{m-1-k}F''_k)) \\
&+ Pr\delta_e \sum_{k=0}^{m-1} \left(F_{m-1-k} \sum_{l=0}^k (F'_{k-l}\theta'_l - F_{k-l}\theta''_l) \right) \\
&+ Pr\delta_e \sum_{k=0}^{m-1} \left(\theta_{m-1-k} \sum_{l=0}^k (F_{k-l}F''_l - F'_{k-l}F'_l) \right), \tag{5.43}
\end{aligned}$$

$$\begin{aligned}
R_m^\Phi(\xi) &= (1 + 2\gamma_1\xi) \left(\Phi''_{m-1} + \frac{\hat{N}_t}{\hat{N}_b}\theta''_{m-1} \right) + 2\gamma_1 \left(\frac{\hat{N}_t}{\hat{N}_b}\theta'_{m-1} + \Phi'_{m-1} \right) - Sc\gamma_2\Phi_{m-1} \\
&+ Sc \sum_{k=0}^m (F_{m-1-k}\Phi'_k + \Phi_{m-1-k}F'_k + p\gamma_3 E_\alpha \delta^2 \theta_{m-1-k}\theta_k) + ScS_2 F'_{m-1} \\
&- Sc\delta_c S_2 \sum_{k=0}^m (F'_{m-1-k}F'_k - F_{m-1-k}F''_k) - Sc\gamma_3(1 - E_\alpha)(1 - \chi_m) \\
&+ Sc\delta_c \sum_{k=0}^{m-1} \left(F_{m-1-k} \sum_{l=0}^k (F'_{k-l}\Phi'_l - F_{k-l}\Phi''_l) \right) - Sc\gamma_3((1-p)E_\alpha\delta) \\
&+ Sc\delta_c \sum_{k=0}^{m-1} \left(\Phi_{m-1-k} \left(\sum_{l=0}^k (F_{k-l}F''_l - F'_{k-l}F'_l) \right) \right), \tag{5.44}
\end{aligned}$$

we have

$$\begin{aligned}
\hat{F}(\xi; 0) &= F^0(\xi), & \hat{\theta}(\xi; 0) &= \theta^0(\xi), & \hat{\Phi}(\xi; 0) &= \Phi^0(\xi), \\
\hat{F}(\xi; 1) &= F(\xi), & \hat{\theta}(\xi; 1) &= \theta(\xi), & \hat{\Phi}(\xi; 1) &= \Phi(\xi).
\end{aligned} \tag{5.45}$$

The solutions through Taylor's series are reduced to

$$\begin{aligned}\hat{F}(\xi; \hat{q}) &= F^0(\xi) + \sum_{m=1}^{\infty} F_m(\xi) \hat{q}^m, \\ F_m(\xi) &= \frac{1}{m!} \frac{\partial^m}{\partial \hat{q}^m} \hat{F}(\xi; \hat{q}) \Big|_{\hat{q}=0},\end{aligned}\tag{5.46}$$

$$\begin{aligned}\hat{\theta}(\xi; \hat{q}) &= \theta^0(\xi) + \sum_{m=1}^{\infty} \theta_m(\xi) \hat{q}^m, \\ \theta_m(\xi) &= \frac{1}{m!} \frac{\partial^m}{\partial \hat{q}^m} \hat{\theta}(\xi; \hat{q}) \Big|_{\hat{q}=0},\end{aligned}\tag{5.47}$$

$$\begin{aligned}\hat{\Phi}(\xi; \hat{q}) &= \Phi^0(\xi) + \sum_{m=1}^{\infty} \Phi_m(\xi) \hat{q}^m, \\ \Phi_m(\xi) &= \frac{1}{m!} \frac{\partial^m}{\partial \hat{q}^m} \hat{\Phi}(\xi; \hat{q}) \Big|_{\hat{q}=0}.\end{aligned}\tag{5.48}$$

The F, θ and Φ through Taylor's series are chosen convergent for $\hat{q} = 1$ and thus

$$\begin{aligned}F(\xi) &= F^0(\xi) + \sum_{m=1}^{\infty} F_m(\xi), \\ \theta(\xi) &= \theta^0(\xi) + \sum_{m=1}^{\infty} \theta_m(\xi), \\ \Phi(\xi) &= \Phi^0(\xi) + \sum_{m=1}^{\infty} \Phi_m(\xi).\end{aligned}\tag{5.49}$$

In terms of special functions ($F_m^*(\xi), \theta_m^*(\xi), \Phi_m^*(\xi)$), the general solutions ($F_m(\xi), \theta_m(\xi), \Phi_m(\xi)$) of Eqs. (5.38 – 5.40) are

$$F_m(\xi) = \hat{F}_m(\xi) + \omega_1 + \omega_2 \exp(-\xi) + \omega_3 \exp(\xi),\tag{5.50}$$

$$\theta_m(\xi) = \hat{\theta}_m(\xi) + \omega_5 \exp(\xi) + \omega_4 \exp(-\xi), \quad (5.51)$$

$$\Phi_m(\xi) = \hat{\Phi}_m(\xi) + \omega_7 \exp(\xi) + \omega_6 \exp(-\xi), \quad (5.52)$$

in which

$$\begin{aligned} \omega_1 &= -\hat{F}'_m(0) + \left. \frac{\partial \hat{F}_m(\xi)}{\partial \xi} \right|_{\xi=0}, & \omega_2 &= \left. \frac{\partial \hat{F}_m(\xi)}{\partial \xi} \right|_{\xi=0}, & \omega_4 &= -\hat{\theta}_m(\xi) \Big|_{\xi=0}, \\ \omega_6 &= -\hat{\Phi}_m(\xi) \Big|_{\xi=0} & \omega_3 &= \omega_5 = \omega_7 = 0. \end{aligned} \quad (5.53)$$

5.4 Convergence analysis

The accurate auxiliary parameters h_F, h_θ and h_Φ are selected from relevant range of plotted h –curves at 25th iteration. For present analysis, numerical computations are restricted thoroughly with specific range of non-dimensional parameters as $(0.2 \leq \gamma_1 \leq 0.6)$, $(0.2 \leq \beta_1 \leq 0.6)$, $(0.4 \leq \lambda_1 \leq 1.4)$, $(0.2 \leq \hat{\beta}_c \leq 0.6)$, $(0.1 \leq \beta_2 \leq 0.5)$, $(0.2 \leq \delta_e \leq 0.4)$, $(0.2 \leq \hat{N}_t \leq 0.6)$, $(0.1 \leq S_1 \leq 0.6)$, $(0.1 \leq \hat{\beta}_t \leq 0.5)$, $(0.1 \leq M_1 \leq 0.3)$, $(0.1 \leq S_2 \leq 0.6)$, $(0.2 \leq \hat{B}_1 \leq 0.4)$, $(0.2 \leq \hat{N}_b \leq 0.4)$, $(0.5 \leq Pr \leq 2.5)$, $(0.2 \leq \hat{B}_2 \leq 0.5)$, $(0.1 \leq \gamma_2 \leq 0.3)$, $(0.5 \leq \gamma_3 \leq 1.4)$, $(0.5 \leq E_a \leq 1.0)$, $(0.1 \leq V_p \leq 0.3)$ and $(0.1 \leq \hat{N}_1 \leq 1.2)$. Fig. 5.2, provides the the ranges $(-1.5 \leq h_F \leq -0.7)$, $(-1.6 \leq h_\theta \leq -0.4)$ and $(-1.6 \leq h_\Phi \leq -0.5)$ of convergence controlling parameters. Table 5.1 proved that 25th, 20th and 30th order of approximation are sufficient for convergent solutions of $F''(0)$, $\theta'(0)$ and $\Phi'(0)$, respectively. Table 5.2 shows fluctuations in wall friction coefficient versus governing parameters. Results presented in Table 5.3 are compared with previously reported data (Abbasi et al. [103]). From this table a great agreement has been observed with the previous literature.

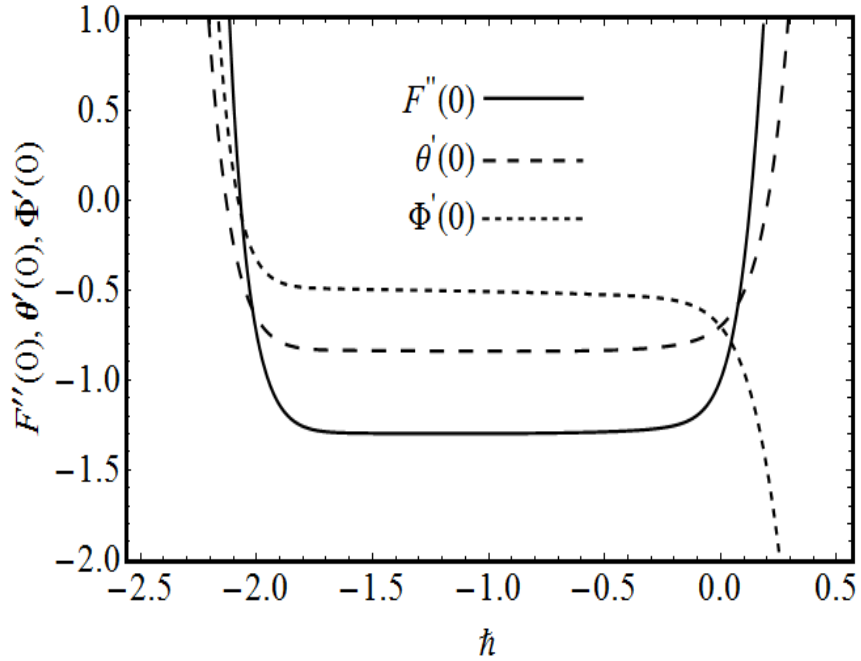


Fig. 5.2: h -curves.

Table 5.1: Convergence analysis when $\gamma_1 = 0.2$, $\beta_1 = \lambda_1 = 0.4$, $\hat{N}_t = \beta_2 = 0.3$, $\gamma_3 = E_a = \hat{N}_1 = 1.0$, $\hat{\beta}_t = M_1 = S_2 = \hat{B}_1 = \gamma_2 = 0.1$, $\hat{\beta}_c = S_1 = \hat{N}_b = \hat{B}_2 = 0.2$, $Pr = 1.2$, $Sc = 1.5$ and $\phi_a = \frac{\pi}{4}$.

Approximation Order	$-F''(0)$	$-\theta'(0)$	$-\Phi'(0)$
1	1.3543	0.9744	0.2869
8	1.4015	0.8675	0.4875
12	1.4033	0.8461	0.5126
20	1.4046	0.8453	0.5133
25	1.4048	0.8453	0.5144
30	1.4048	0.8453	0.5147
35	1.4048	0.8453	0.5147
40	1.4048	0.8453	0.5147

Table 5.2: Numerical values of $C_F(Re_z)^{\frac{1}{2}}$ when $\widehat{N}_t = 0.3, Pr = 1.2, \gamma_1 = \widehat{B}_2 = 0.2,$
 $\widehat{\beta}_t = S_2 = \widehat{B}_1 = \gamma_2 = 0.1, \delta_e = \widehat{\beta}_c = S_1 = V_p = \widehat{N}_b = 0.2, \gamma_3 = \widehat{N}_1 = E_a = 1.0,$
 $Sc = 1.5$ and $\phi_a = \frac{\pi}{4}.$

γ_1	M_1	λ_1	β_1	β_2	$C_F(Re_z)^{\frac{1}{2}}$
0.2					0.8466
0.4					0.8647
0.6					0.8854
	0.1				0.8466
	0.2				0.8542
	0.3				0.8639
		0.4			0.8466
		0.8			0.8035
		1.2			0.7463
			0.2		0.8152
			0.4		0.8466
			0.6		0.8734
				0.1	0.7857
				0.3	0.8466
				0.5	0.8792

Table 5.3: Comparative analysis of $C_F(Re_z)^{\frac{1}{2}}$ when $\hat{B}_1 = \phi_a = \gamma_2 = E_a = \hat{\beta}_c = V_p = \hat{B}_2 = \hat{\beta}_t = 0, Pr = 1.2, S_1 = S_2 = 0.2, \hat{N}_b = \hat{N}_t = 0.2$ and $\hat{N}_1 = 0.3$.

β_2	λ_1	M_1	β_1	Ref. [103]	Present
0.0				0.91586	0.91586
0.3				1.05963	1.05963
0.5				1.14651	1.14651
	0.1			1.11097	1.11097
	0.4			0.97340	0.97340
	0.7			0.87539	0.87539
		0.0		0.79447	0.79447
		0.3		0.91104	0.91104
		0.7		1.20901	1.20901
			0.0	1.17277	1.17277
			0.5	0.91683	0.91683
			1.0	0.69008	0.69008

5.5 Results and discussion

Here the effects of various flow variables on the velocity $F'(\xi)$, temperature $\theta(\xi)$ and concentration fields $\Phi(\xi)$ are discussed in detail. Figs. (5.3 – 5.6) are sketched to analyze the influence of $\gamma_1, \beta_2, \lambda_1$ and ϕ_a on velocity profile $F'(\xi)$ versus increment in curvature parameter γ_1 near the cylindrical surface while opposite behaviour has been

observed far away from surface. It holds because enhancement in curvature reduces surface area (i.e contact area). As a result, less resistance is offered to fluid movement. Fig. 5.4 illustrates the behavior of $F'(\xi)$ for distinct variation of Deborah number β_2 . As larger values of β_2 enhances the retardation time that ultimately boosts the elasticity of the material which is accountable for upsurge in velocity field. Fig. 5.5 expresses the behavior of $F'(\xi)$ against ratio of relaxation to retardation times λ_1 . It is noticed that velocity profile $F'(\xi)$ is decreasing function of λ_1 . Since, relaxation time of fluid enhances for higher approximation of λ_1 that develops a declining trend in the magnitude of $F'(\xi)$. Fig. 5.6, demonstrates the impact of inclination of cylinder on the velocity profile $F'(\xi)$, when inclined cylinder's angle ϕ_a enhances, fluid velocity diminishes. Figs. (5.7 – 5.13) exposes the temperature profile $\theta(\xi)$ variations against δ_e , S_1 , \widehat{N}_b , \widehat{N}_t , Pr , \widehat{B}_1 and Ec . The consequences of δ_e on fluid temperature $\theta(\xi)$ are presented in Fig. 5.7. One can see that δ_e falls down temperature because material particle takes some extra time to transfer heat due to thermal relaxation enhancement. Hence, temperature $\theta(\xi)$ decreases. Figs. 5.8 and 5.9 displayed the effect of thermal stratification parameter S_1 and Prandtl number Pr on temperature distribution $\theta(\xi)$. Similar type of behavior for both parameters has been observed in temperature. In fact, temperature difference between cylindrical surface and ambient fluid i.e. $(T_w - T_\infty)$ gradually falls for higher S_1 . As a result, $\theta(\xi)$ declines. Also, higher Prandtl number corresponds to fluids with low thermal conductivity i.e. capacity of heat transfer. Such weaker thermal diffusivity becomes a source of decrease in the temperature and thermal boundary layer thickness (see Fig.5.9). Impacts of \widehat{N}_b and \widehat{N}_t for temperature $\theta(\xi)$ is exposed in Figs. 5.10 and 5.11. Similar enhancing is observed on temperature against both parameters. As Brownian motion randomly disperses

the fluid particles, so this dispersion causes increment in thermal energy. As thermophoresis transports fluid particles from hot to cold regions which consequently rises fluid temperature $\theta(\xi)$. Fig. 5.12 reveals the features of \hat{B}_1 on $\theta(\xi)$. Scientifically, higher approximation of \hat{B}_1 generates heat and hence temperature enlarges. The temperature distributions $\theta(\xi)$ are portrayed against different values of Ec in Fig. 5.13. Since larger values of Ec leads to increase in kinetic energy i.e. fluid particles collides more rapidly with each other and converts its mechanical energy into thermal energy, as a result, temperature increases. Fig. 5.14 is adorned to analyse the impact of chemical reaction parameter γ_2 on $\Phi(\xi)$. It discloses that the concentration $\Phi(\xi)$ declines with a rise in the destructive chemical reaction ($\gamma_2 > 0$), whereas the reverse trend is observed in the case of generative ($\gamma_2 < 0$) chemical reaction. Fig. 5.15 predicts the consequences of solutal relaxation time δ_c on concentration profile $\Phi(\xi)$. The concentration profile decreases versus greater values of δ_c (see Fig. 5.15). Variation of $\Phi(\xi)$ against the Schmidt number Sc is displayed in Fig. 5.16. Since higher values of Sc corresponds to decrease in the mass diffusivity and hence in concentration. Fig. 5.17, captured the fluctuations in concentration $\Phi(\xi)$ for different values of \hat{N}_b . It is noticed that concentration decreases for larger \hat{N}_b . Fig. 5.18 displays the thermophoresis parameter \hat{N}_t effects on concentration $\Phi(\xi)$. This figure provides the information that \hat{N}_t enhances the concentration field $\Phi(\xi)$. Fig. 5.19 is sketched to investigate the relationship between activation energy E_a and nanoparticle concentration for definite values of other flow parameters. The modified Arrhenius function decays as activation energy E_a increases. This finally endorses the generative chemical reaction due to which nanoparticle concentration upsurges. Figs. 5.20 and 5.21 elucidate the variations of reaction rate

constant γ_3 and solutal stratification parameter S_2 on concentration distribution $\Phi(\xi)$. A drop in concentration profile $\Phi(\xi)$ is detected while the destructive chemical reaction parameter $\gamma_3 (> 0)$ is amplified (see Fig. 5.20). Fig. 5.21 portrays the effect of S_2 on $\Phi(\xi)$. Here decreasing trend of $\Phi(\xi)$ is found against S_2 . It is due to the fact that difference between the surface concentration and ambient concentration lessens for greater S_2 . Thus, concentration field $\Phi(\xi)$ decreases. Figs. 5.22 and 5.23 show the impacts of various flow parameters on wall heat flux coefficient. It is analyzed that wall heat flux coefficient decays for larger values of \hat{B}_1 and S_1 . Moreover, wall mass flux coefficient declines versus S_2 while it enhances against γ_3 (Figs. 5.24 and 5.25).

5.6 Graphical outcomes

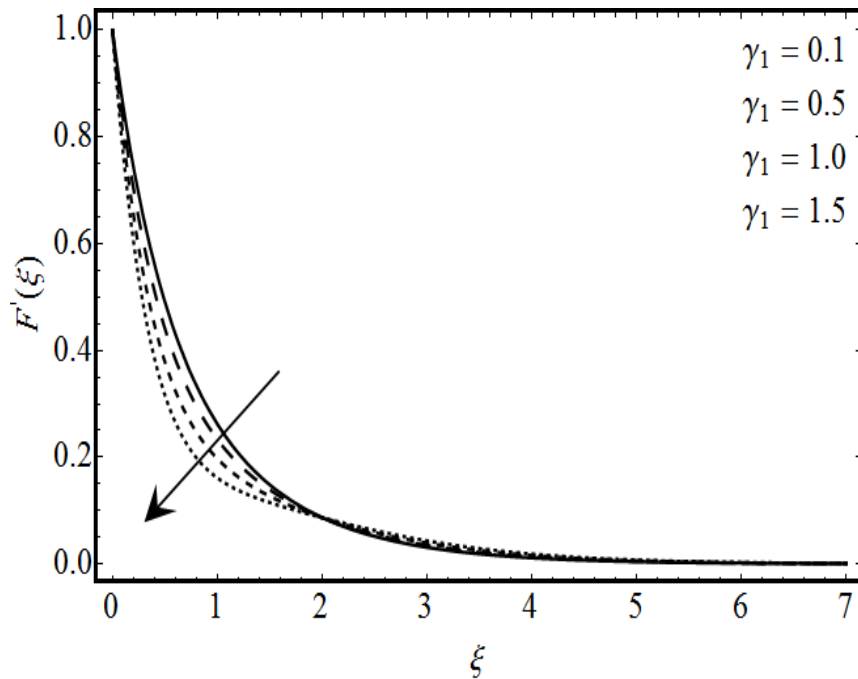


Fig. 5.3: Response of $F'(\xi)$ with γ_1 .

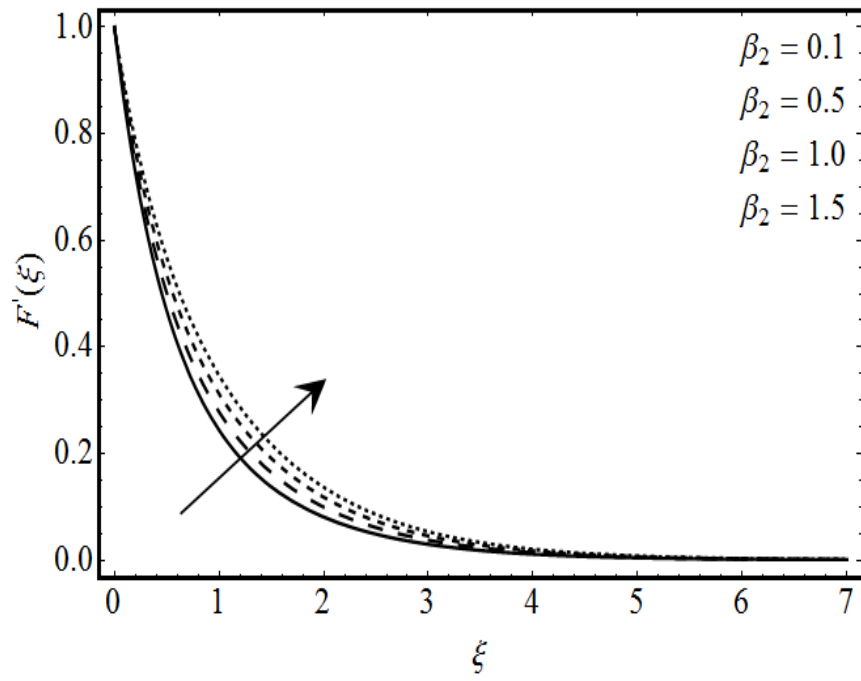


Fig. 5.4: Response of $F'(\xi)$ with β_2 .

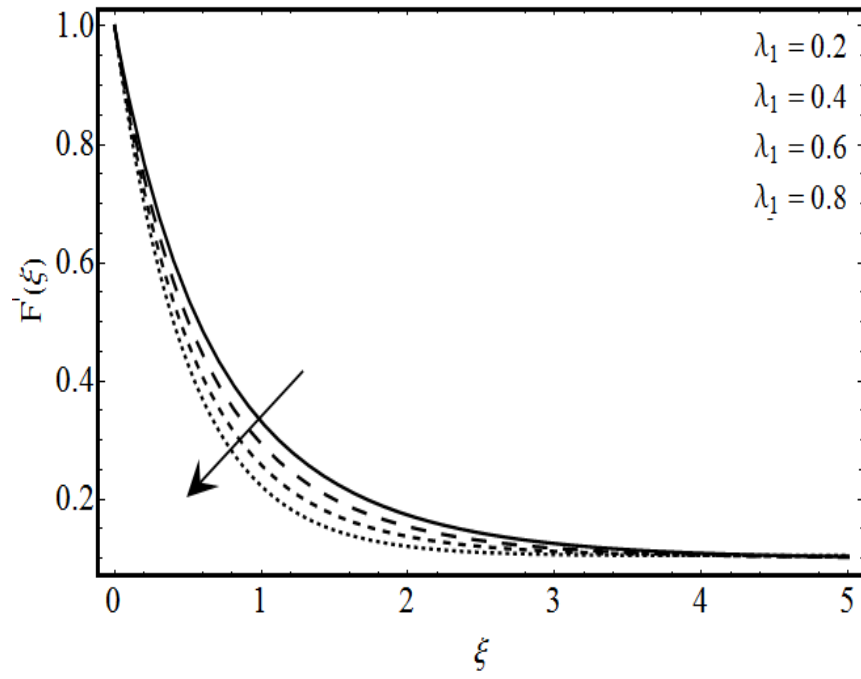


Fig. 5.5: Response of $F'(\xi)$ with λ_1 .

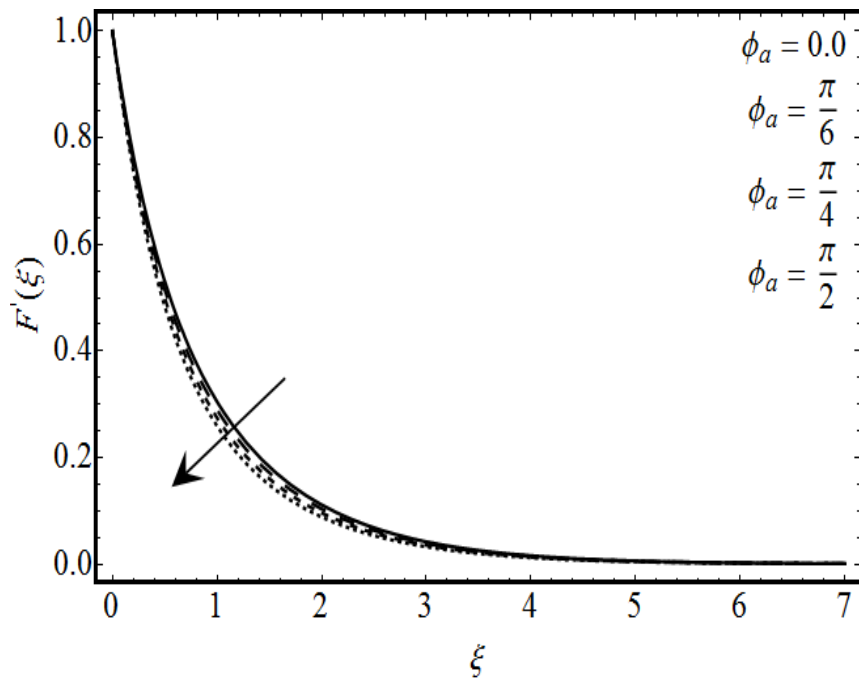


Fig. 5.6: Response of $F'(\xi)$ with ϕ_a .

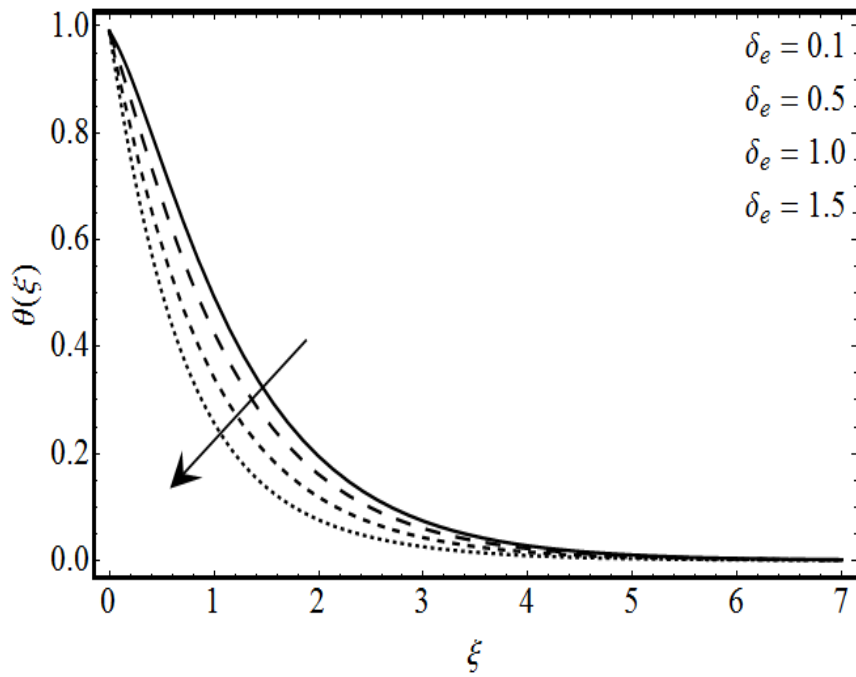


Fig. 5.7: Response of $\theta(\xi)$ with δ_e .

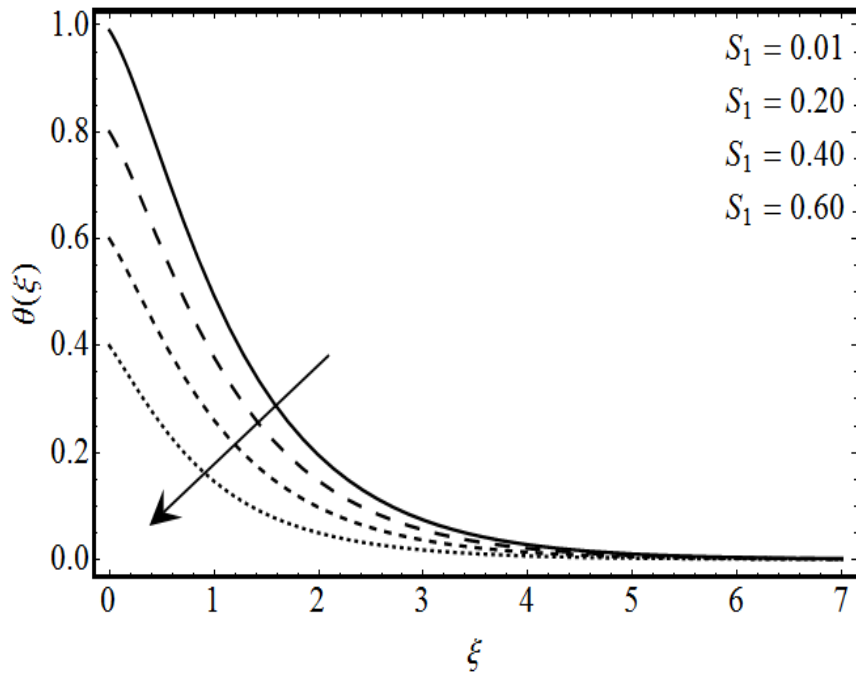


Fig. 5.8: Response of $\theta(\xi)$ with S_1 .

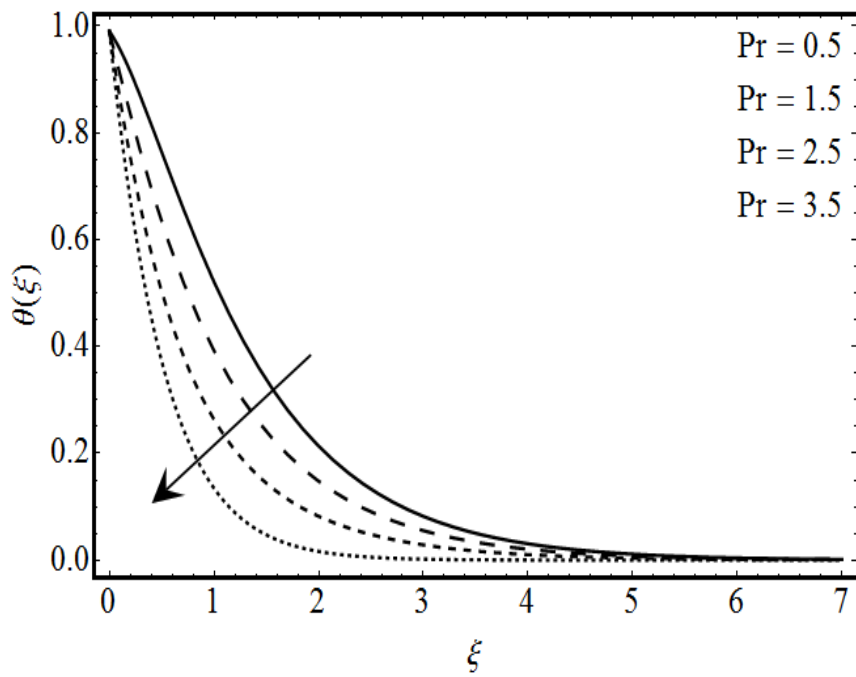


Fig. 5.9: Response of $\theta(\xi)$ with Pr .

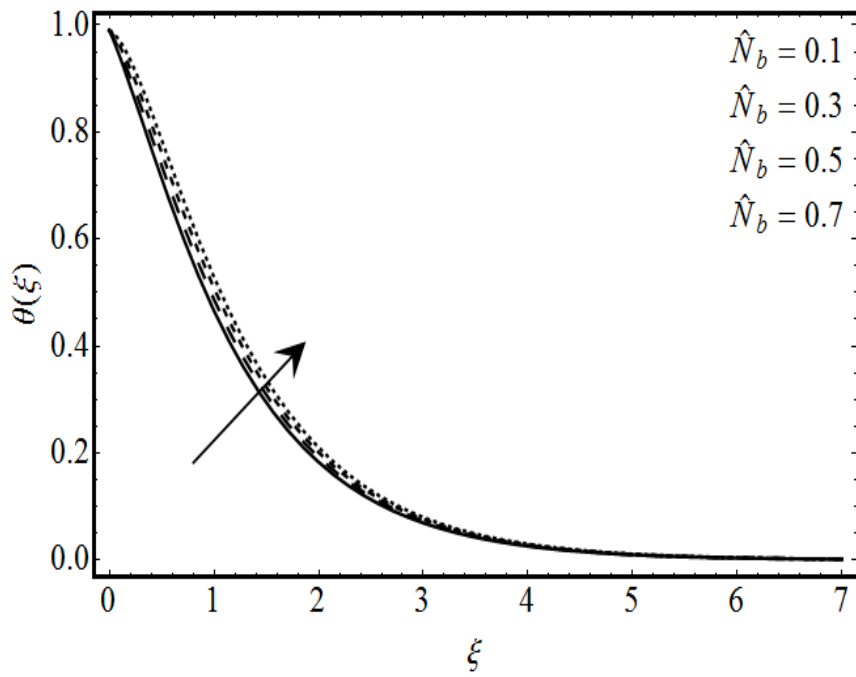


Fig. 5.10: Response of $\theta(\xi)$ with \hat{N}_b .

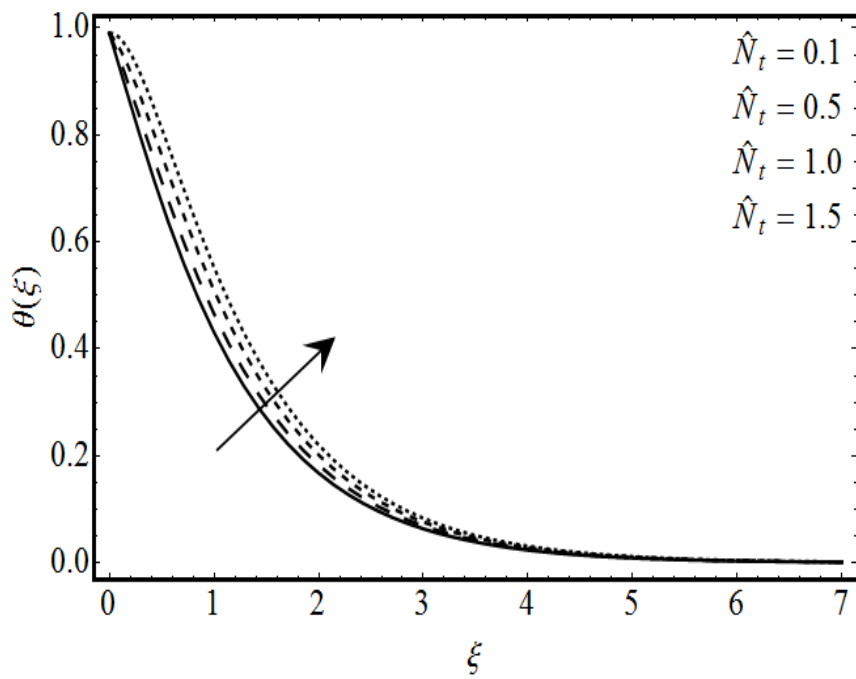


Fig. 5.11: Response of $\theta(\xi)$ with \hat{N}_t .

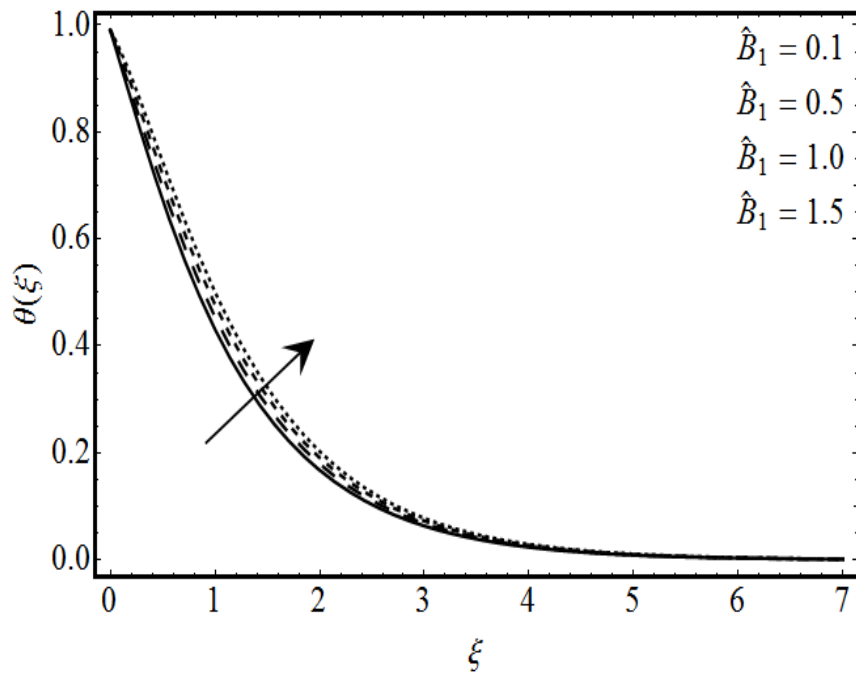


Fig. 5.12: Response of $\theta(\xi)$ with \hat{B}_1 .

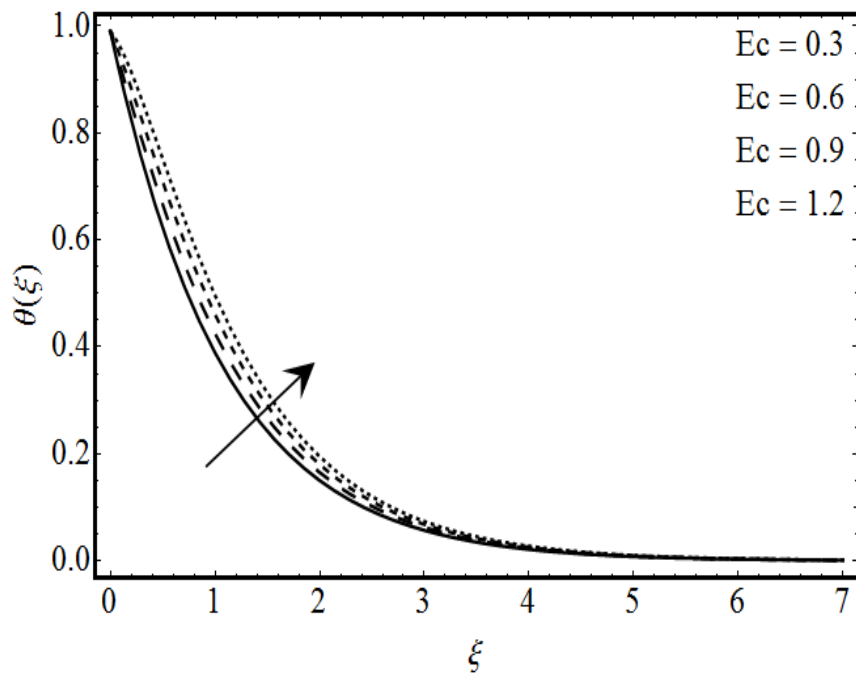


Fig. 5.13: Response of $\theta(\xi)$ with Ec .

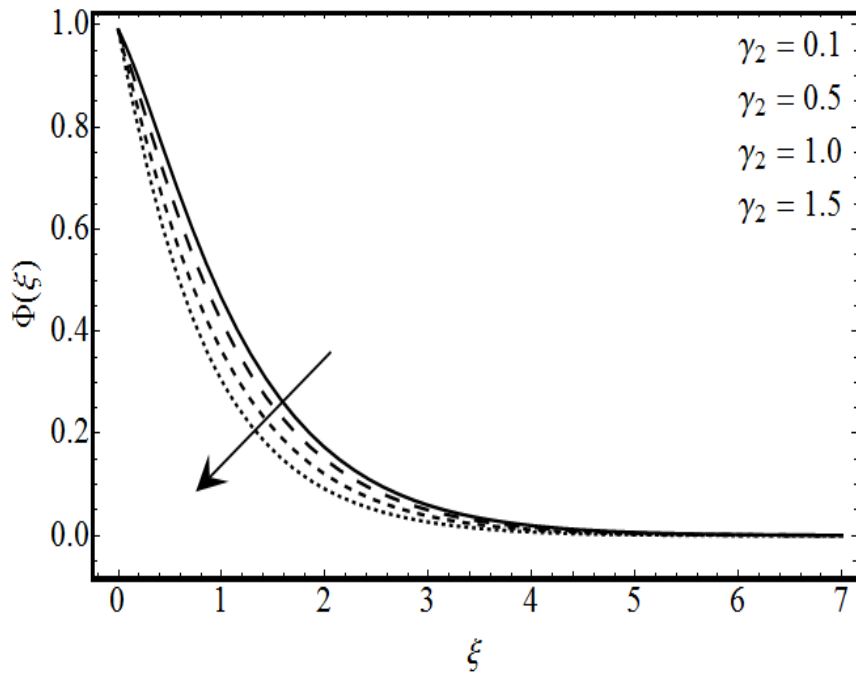


Fig. 5.14: Response of $\Phi(\xi)$ with γ_2 .

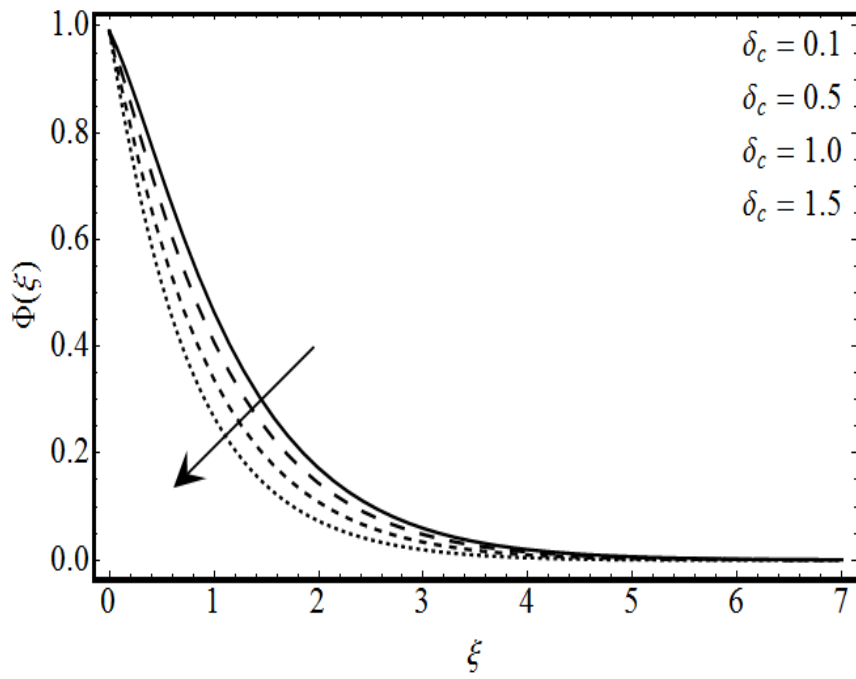


Fig. 5.15: Response of $\Phi(\xi)$ with δ_c .

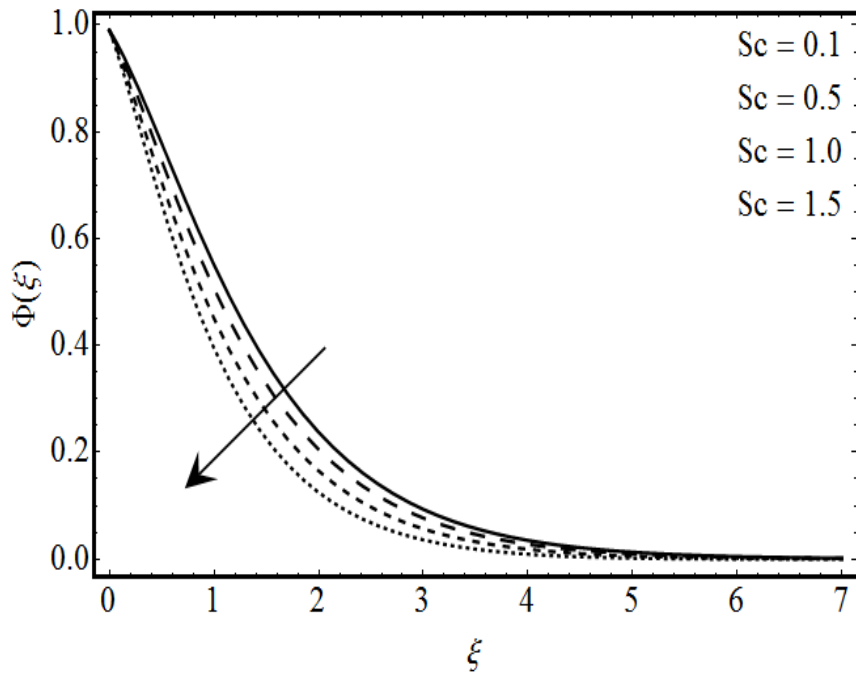


Fig. 5.16: Response of $\Phi(\xi)$ with Sc .

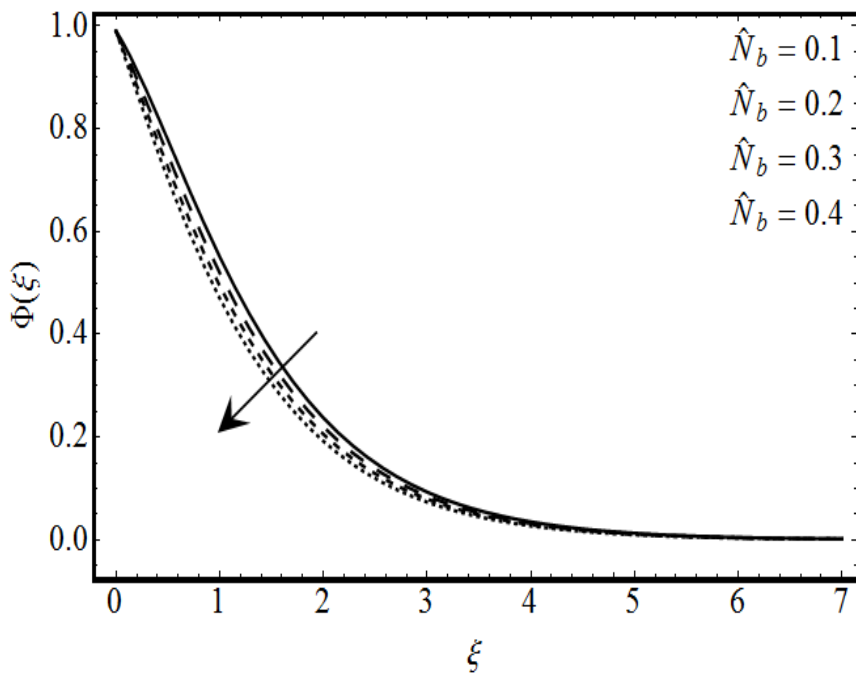


Fig. 5.17: Response of $\Phi(\xi)$ with \hat{N}_b .

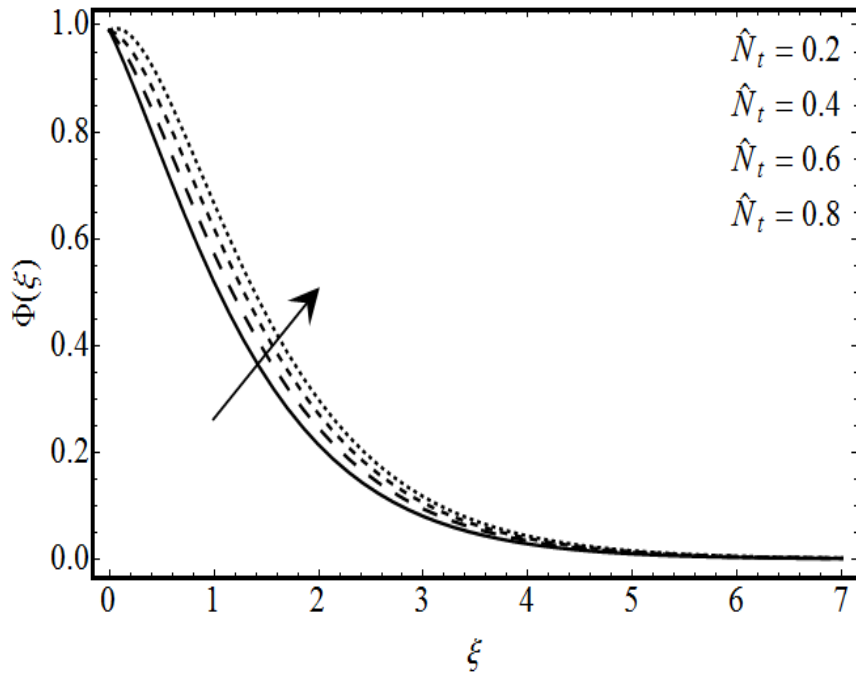


Fig. 5.18: Response of $\Phi(\xi)$ with \hat{N}_t .

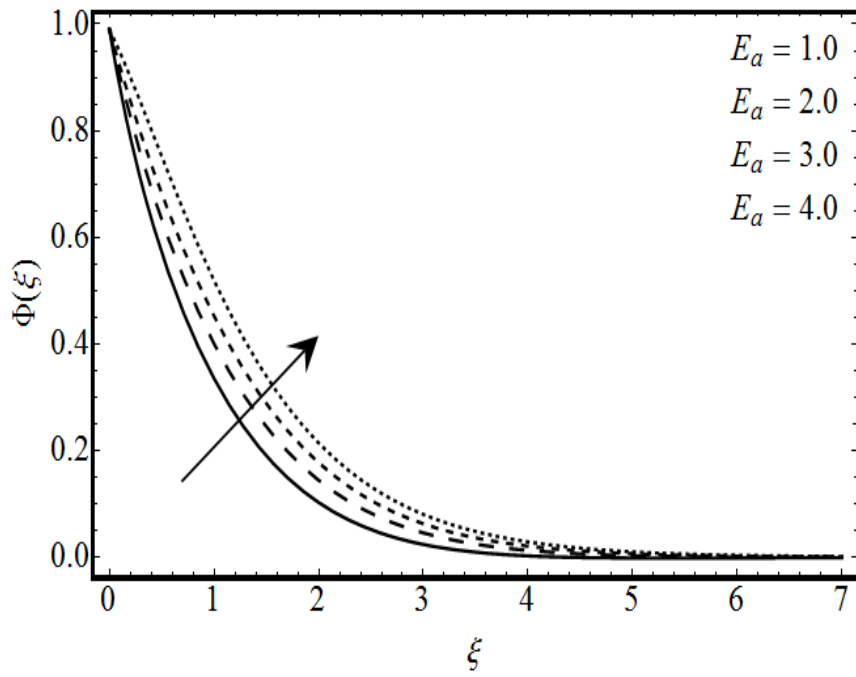


Fig. 5.19: Response of $\Phi(\xi)$ with E_α .

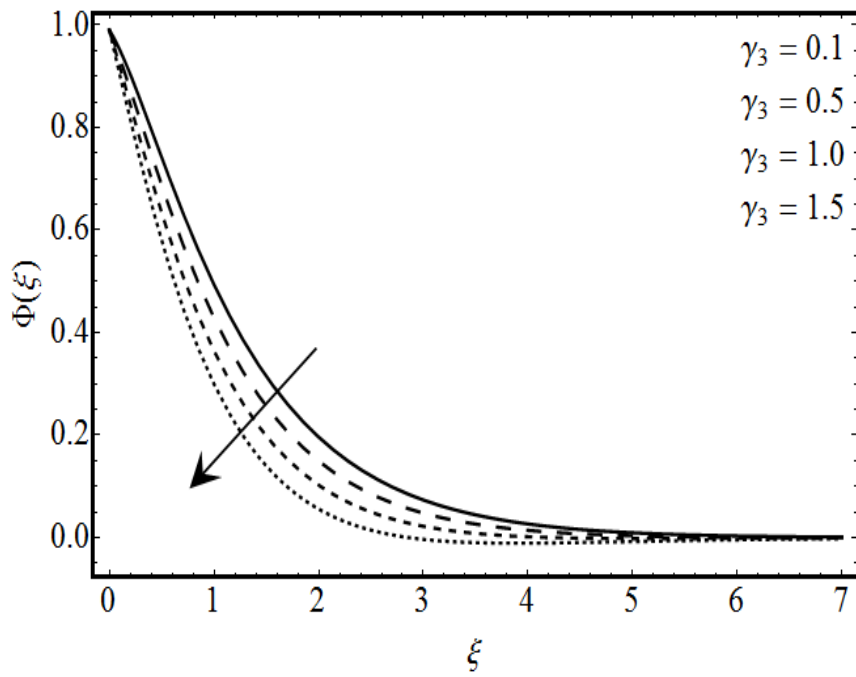


Fig. 5.20: Response of $\Phi(\xi)$ with γ_3 .

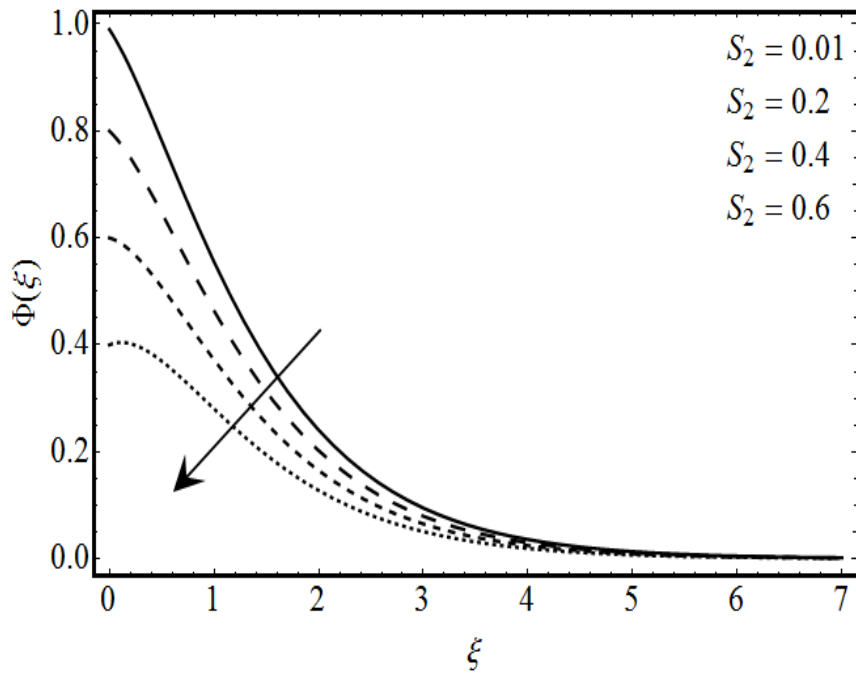


Fig. 5.21: Response of $\Phi(\xi)$ with S_2 .

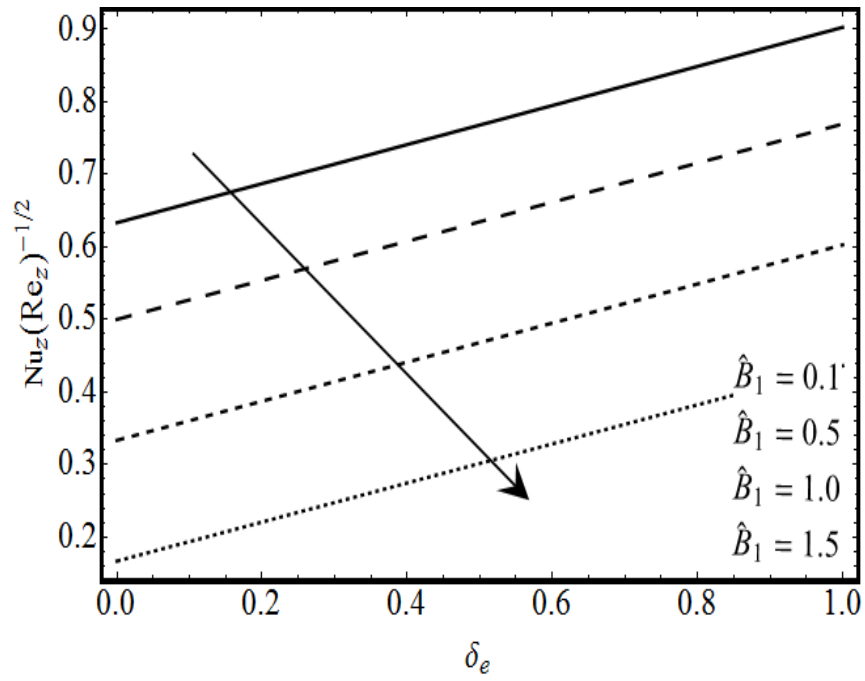


Fig. 5.22: Response of $Nu_z(Re_z)^{-1/2}$ with \hat{B}_1 .

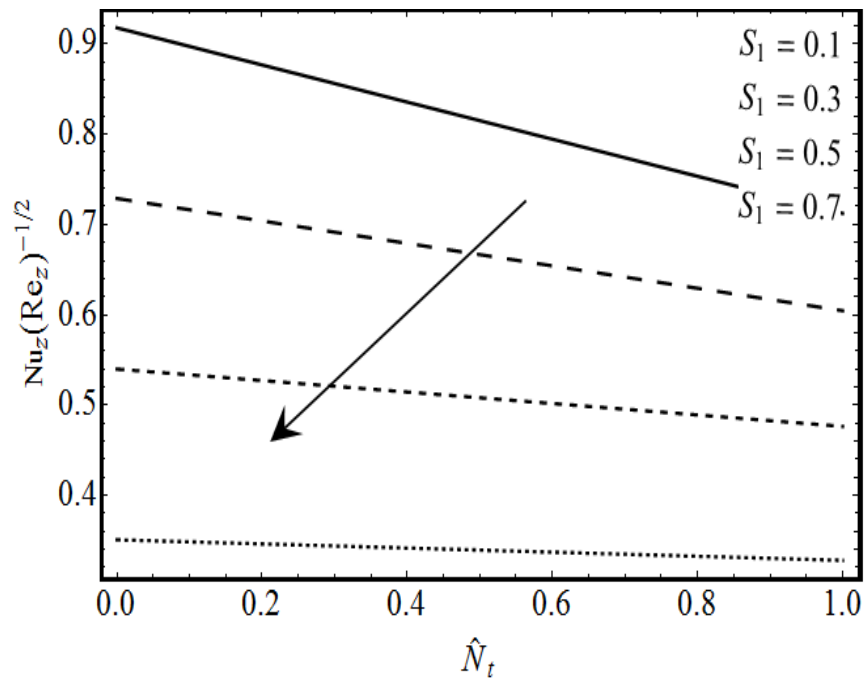


Fig. 5.23: Response of $Nu_z(Re_z)^{-1/2}$ with S_1 .

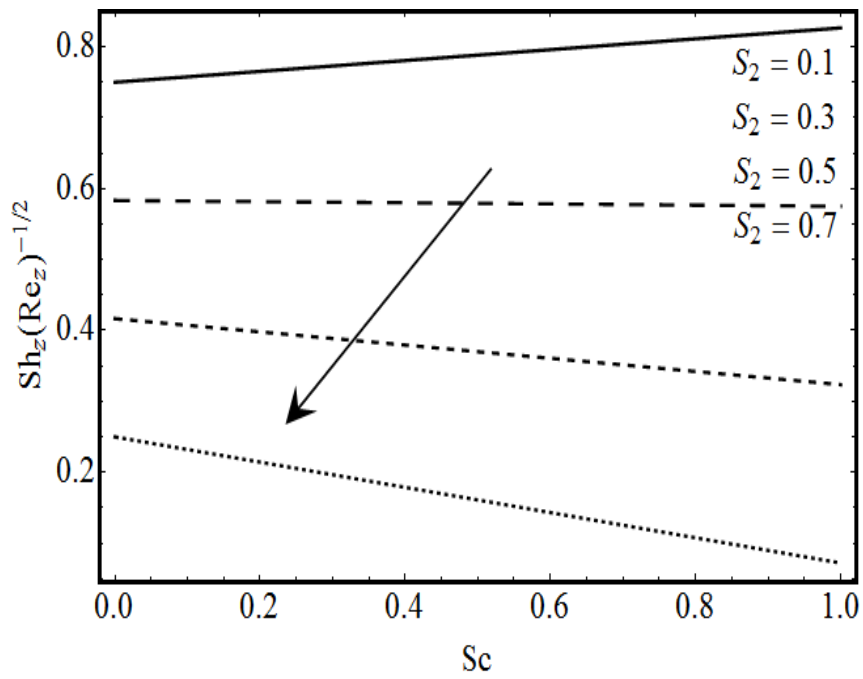


Fig. 5.24: Response of $Sh_z(Re_z)^{-\frac{1}{2}}$ with S_2 .

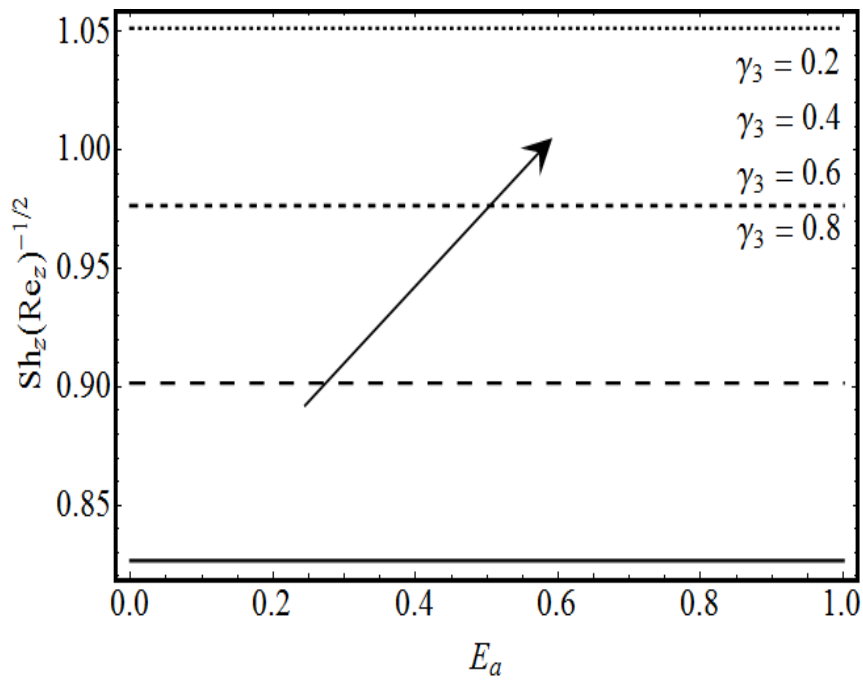


Fig. 5.25: Response of $Sh_z(Re_z)^{-\frac{1}{2}}$ with γ_3 .

5.7 Conclusions

Major highlights of presented flow analysis are:

- Higher estimations of Deborah number (β_2) result in the reduction of velocity and momentum boundary layer thickness.
- Thermal and solutal stratification (S_1, S_2) decays the temperature and concentration distribution respectively.
- Both temperature field and thermal boundary layer thickness reduce by enhancing thermal relaxation parameter (δ_e).
- Larger solutal relaxation parameter (δ_c) show decay in the concentration field and associated concentration layer thickness.
- Skin friction coefficient increases for higher values of (β_2) and (γ_1).

CHAPTER 6

Dual stratification effects for Walter-B fluid flow in view of Cattaneo–Christov double diffusion

6.1 Introduction

Present chapter focuses on activation energy and dual stratification impacts on Walter-B nanofluid over a permeable stretched sheet. Heat and mass diffusion are delineated with the aid of Cattaneo – Christov models. Thermophoresis and Brownian motion effects are also taken into account. Influence of heat generation/absorption and chemical reaction is also measured. Modified Arrhenius formula for activation energy is implemented carefully. The resulting nonlinear differential system is tackled with homotopy analysis method. Effects of emanating variables are examined through graphs and tables.

6.2 Mathematical formulation

Present study has explored the novel features of activation energy for unsteady and nonlinear convective flow of Walter-B nanofluid [104] with generalized Fourier's and Fick's models. Non-uniform heat generation/absorption, dual stratification, nonlinear mixed convection, chemical reaction and activation energy are considered. Due to

variations in the temperature and concentration, thermal and concentration buoyancy forces are applied to the fluid with double stratification effect. Walter-B fluid occupies the semi-infinite region $y > 0$ over the surface with stretching velocity $U_w(x) = \frac{U_0 x}{L}$ (see Fig. 6.1). Temperature and the nanoparticle fraction at surface of the sheet are T_w and C_w respectively. While the ambient temperature and nanoparticles volume fraction is specified by T_∞ and C_∞ , respectively. Walter-B nanomaterial model is engaged which defines the important slip mechanism namely Brownian and thermophoresis diffusions. The boundary layer approximation reduces the continuity, momentum, heat and mass equations [105-107] to

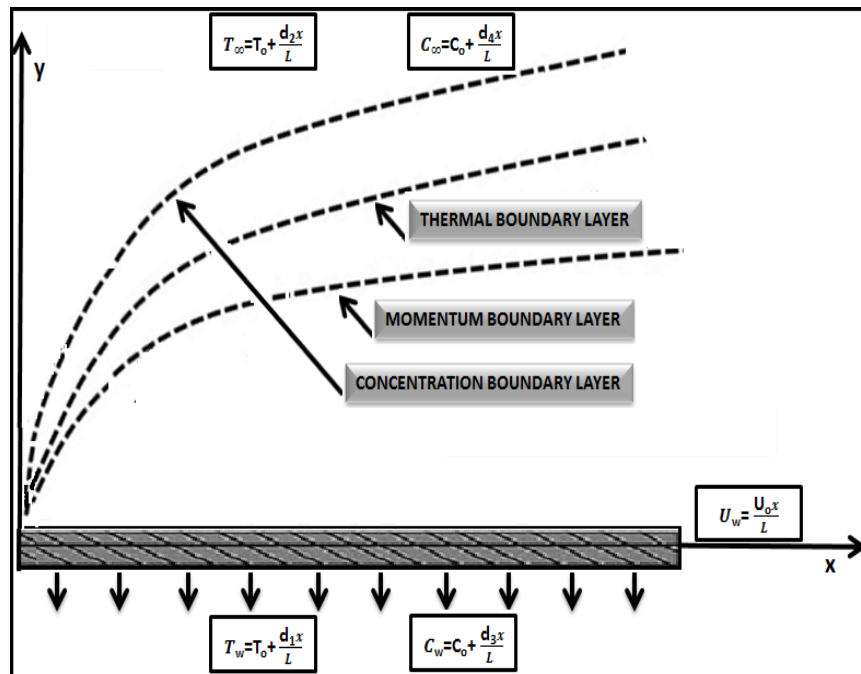


Fig. 6.1: Physical model.

$$\frac{\partial u}{\partial x} + \frac{\partial v}{\partial y} = 0, \quad (6.1)$$

$$u \frac{\partial u}{\partial x} + v \frac{\partial u}{\partial y} = v_1 \frac{\partial^2 u}{\partial y^2} - \lambda_3 \left(u \frac{\partial^3 u}{\partial x \partial y^2} + v \frac{\partial^3 u}{\partial y^3} + \frac{\partial u}{\partial x} \frac{\partial^2 u}{\partial y^2} - \frac{\partial u}{\partial y} \frac{\partial^2 u}{\partial x \partial y} \right) + \frac{\hat{g}_1}{\rho_f} [\Gamma_1 (T - T_\infty) + \Gamma_2 (T - T_\infty)^2 + \Gamma_3 (C - C_\infty) + \Gamma_4 (C - C_\infty)^2]. \quad (6.2)$$

Within the frame of Cattaneo – Christove double diffusive scheme [108]

$$\mathbf{q}_1 + \hat{\Gamma}_e \left[\frac{\partial \mathbf{q}_1}{\partial t} + \mathbf{V}_1 \cdot \nabla \mathbf{q}_1 - (\mathbf{q}_1 \cdot \nabla) \mathbf{V}_1 + (\nabla \cdot \mathbf{V}_1) \mathbf{q}_1 \right] = -k_f \nabla T, \quad (6.3)$$

$$\mathbf{J}_1 + \hat{\Gamma}_e \left[\frac{\partial \mathbf{J}_1}{\partial t} + \mathbf{V}_1 \cdot \nabla \mathbf{J}_1 - (\mathbf{J}_1 \cdot \nabla) \mathbf{V}_1 + (\nabla \cdot \mathbf{V}_1) \mathbf{J}_1 \right] = -D_B \nabla C. \quad (6.4)$$

By imposing steady and incompressibility conditions, we get

$$\mathbf{q}_1 + \hat{\Gamma}_e [\mathbf{V}_1 \cdot \nabla \mathbf{q}_1 - (\mathbf{q}_1 \cdot \nabla) \mathbf{V}_1] = -\hat{k}_f \nabla T, \quad (6.5)$$

$$\mathbf{J}_1 + \hat{\Gamma}_e [\mathbf{V}_1 \cdot \nabla \mathbf{J}_1 - (\mathbf{J}_1 \cdot \nabla) \mathbf{V}_1] = -D_B \nabla C. \quad (6.6)$$

Two-dimensional governing energy and concentration expressions are

$$u \frac{\partial T}{\partial x} + v \frac{\partial T}{\partial y} + \hat{\Gamma}_e \Pi_e = \frac{\hat{k}_f}{(\rho C_p)_f} \frac{\partial^2 T}{\partial y^2} + \frac{\hat{Q}_m}{(\rho C_p)_f} + \tau_1 D_B \frac{\partial C}{\partial y} \frac{\partial T}{\partial y} + \frac{\tau_1 D_T}{T_\infty} \left(\frac{\partial T}{\partial y} \right)^2, \quad (6.7)$$

$$u \frac{\partial C}{\partial x} + v \frac{\partial C}{\partial y} + \hat{\Gamma}_c \Pi_c = D_B \frac{\partial^2 C}{\partial y^2} + \frac{D_T}{T_\infty} \left(\frac{\partial^2 T}{\partial y^2} \right) - K_1 (C - C_\infty) - \hat{K}_r^2 (C_w - C_0) \left(\frac{T}{T_\infty} \right)^p \exp \left[-\frac{E_1}{T k^*} \right], \quad (6.8)$$

with

$$\left. \begin{aligned} u &= \frac{U_0 x}{L}, & T &= T_w = T_0 + \frac{d_1 x}{L}, \\ v &= V_1, & C &= C_w = C_0 + \frac{d_3 x}{L} \end{aligned} \right| \text{at } y = 0, \quad (6.9)$$

$$\left. \begin{aligned} u &\rightarrow 0, & T &\rightarrow T_\infty = T_0 + \frac{d_2 x}{L}, \\ v &\rightarrow 0, & C &\rightarrow C_\infty = C_0 + \frac{d_4 x}{L}. \end{aligned} \right| \text{when } y \rightarrow \infty, \quad (6.10)$$

$$\begin{aligned} \Pi_e &= u^2 \frac{\partial^2 T}{\partial x^2} + v^2 \frac{\partial^2 T}{\partial y^2} + \frac{\partial T}{\partial y} \left(u \frac{\partial v}{\partial x} + v \frac{\partial v}{\partial y} \right) + \frac{\partial T}{\partial x} \left(u \frac{\partial u}{\partial x} + v \frac{\partial u}{\partial y} \right) \\ &+ 2uv \frac{\partial^2 T}{\partial y \partial x}, \end{aligned} \quad (6.11)$$

$$\begin{aligned} \Pi_c &= u^2 \frac{\partial^2 C}{\partial x^2} + v^2 \frac{\partial^2 C}{\partial y^2} + \frac{\partial C}{\partial y} \left(u \frac{\partial v}{\partial x} + v \frac{\partial v}{\partial y} \right) + \frac{\partial C}{\partial x} \left(u \frac{\partial u}{\partial x} + v \frac{\partial u}{\partial y} \right) \\ &+ 2uv \frac{\partial^2 C}{\partial y \partial x}. \end{aligned} \quad (6.12)$$

The expression of non-uniform heat generation/absorption \hat{Q}_m [109] is

$$\hat{Q}_m = \frac{U_w(x) \hat{k}_f}{x v_1} \left[\hat{B}_1 (T_w - T_0) \frac{\partial F}{\partial \xi} + \hat{B}_2 (T - T_\infty) \right]. \quad (6.13)$$

Here, $\hat{B}_1 > 0$ and $\hat{B}_2 > 0$ corresponds to heat generation case while $\hat{B}_1 < 0$ and $\hat{B}_2 <$

0) resembles to the heat absorption.

Introducing the following similarity transformations

$$\begin{aligned} \xi &= \sqrt{\frac{U_0}{L v_1}} y, & u(\xi) &= \frac{U_0 x}{L} F'(\xi), & v(\xi) &= \sqrt{\frac{v_1 U_0}{L}} F(\xi), & \Psi_1(\xi) &= \sqrt{\frac{v_1 U_0 x^2}{L}} F(\xi), \\ \theta(\xi) &= \frac{T - T_\infty}{T_w - T_0}, & \Phi(\xi) &= \frac{C - C_\infty}{C_w - C_0}. \end{aligned} \quad (6.14)$$

Introducing Eq. (6.14) into Eqs. (6.2), (6.7) and (6.8), we get the following system of ordinary differential equations

$$F''' - F'^2 + FF'' + \alpha_2[F''^2 - 2F'F''' + FF^4] + \beta_1[(1 + \hat{\beta}_t\theta)\theta + \hat{N}_1(1 + \hat{\beta}_c\Phi)\Phi] = 0, \quad (6.15)$$

$$\theta'' + Pr[F\theta' + \hat{N}_b\Phi'\theta' + \hat{N}_t\theta'^2 - (\theta + S_1)F'] + (\hat{B}_1F' + \hat{B}_2) - Pr\delta_e[F^2\theta'' + (F'^2 - FF'')(\theta + S_1) - FF'\theta'] = 0, \quad (6.16)$$

$$\Phi'' + ScF\Phi' + \frac{\hat{N}_t}{\hat{N}_b}\theta'' - \delta_cSc[F^2\Phi'' + (F'^2 - FF'')(\Phi + S_2) - FF'\Phi'] - Sc\left(\gamma_2\Phi + (\Phi + S_2)F' + \gamma_3(1 + \delta\theta)^p \exp\left[-\frac{E_a}{1 + \delta\theta}\right]\right) = 0. \quad (6.17)$$

Transformed boundary conditions for present flow problem are

$$F'(0) = 1, \quad F(0) = V_p, \quad \theta(0) = 1 - S_1, \quad \Phi(0) = 1 - S_2, \\ F'(\xi) = 0, \quad \theta(\xi) = 0, \quad \Phi(\xi) = 0, \quad \xi \rightarrow \infty. \quad (6.18)$$

The dimensionless parameters used in Eqs. (6.15) – (6.18) are as follows:

$$\hat{\beta}_t = \frac{\Gamma_2(T_w - T_0)}{\Gamma_1}, \quad E_a = \frac{E_1}{T_\infty k^*}, \quad \delta = \frac{T_w - T_0}{T_\infty}, \\ \hat{N}_1 = \frac{\Gamma_3(C_w - C_0)}{\Gamma_1(T_w - T_0)}, \quad \delta_e = \frac{\hat{\Gamma}_e U_0}{L}, \quad \alpha_2 = \frac{\lambda_3}{\nu_1 L}, \\ \hat{\beta}_c = \frac{\Gamma_4(C_w - C_0)}{\Gamma_3}, \quad \gamma_3 = \frac{\hat{K}_r^2 L}{U_0}, \quad \gamma_2 = \frac{\hat{K}_1 L}{U_0}, \\ \beta_1 = \frac{L^2(T_w - T_0)\hat{g}_1\Gamma_1}{U_0^2 x^2}, \quad \hat{N}_t = \frac{\tau_1 D_T(T_w - T_0)}{T_\infty \nu_1}, \quad A = \frac{U_\infty}{U_0}. \quad (6.19)$$

The interested quantities (C_F, Nu_x, Sh_x) in the wall vicinity are given as

$$C_F = \frac{2\tau_w}{\rho_f U_w^2}, \quad Nu_x = \frac{xq_w}{\hat{k}_f(T_w - T_0)}, \quad Sh_x = \frac{xj_w}{D_B(C_w - C_0)}, \quad (6.20)$$

with

$$\tau_w = \nu_1 \frac{\partial u}{\partial y} - \lambda_3 \left(u \frac{\partial^2 u}{\partial y \partial x} - 2 \frac{\partial u}{\partial x} \frac{\partial u}{\partial y} \right) \Big|_{y=0}, \quad (6.21)$$

$$q_w = -\hat{k}_f \frac{\partial T}{\partial y} \Big|_{y=0}, \quad (6.22)$$

$$j_w = -D_B \frac{\partial C}{\partial y} \Big|_{y=0}. \quad (6.23)$$

In dimensionless form, skin friction coefficient C_F , local Nusselt Nu_x and Sherwood Sh_x numbers are

$$\frac{1}{2} C_F (Re_x)^{\frac{1}{2}} = [(1 + \alpha_2)F'(0)]F''(0), \quad (6.24)$$

$$Nu_x (Re_x)^{-\frac{1}{2}} = -\theta'(0), \quad (6.25)$$

$$Sh_x (Re_x)^{-\frac{1}{2}} = -\Phi'(0), \quad (6.26)$$

in which $Re_x \left(= \frac{U_0 x^2}{\nu_1 L} \right)$ is the local Reynolds number.

6.3 Methodology

The flow governing system (6.15 – 6.17) along with boundary conditions (6.18) is solved with HAM [110]. For this, first we have to choose initial approximations $(F^0(\xi), \theta^0(\xi), \Phi^0(\xi))$ and auxiliary linear operators $(\mathcal{L}_F, \mathcal{L}_\theta, \mathcal{L}_\Phi)$ in the form:

$$\begin{aligned}
F^0(\xi) &= 1 + V_p - \exp(-\xi), \\
\theta^0(\xi) &= (1 - S_1) \exp(-\xi), \\
\Phi^0(\xi) &= (1 - S_2) \exp(-\xi),
\end{aligned} \tag{6.27}$$

$$\mathcal{E}_F[F] = F''' - F', \quad \mathcal{E}_\theta[\theta] = \theta'' - \theta, \quad \mathcal{E}_\Phi[\Phi] = \Phi'' - \Phi, \tag{6.28}$$

with the following properties

$$\begin{aligned}
\mathcal{E}_F[\omega_2 \exp(-\xi) + \omega_1 + \omega_3 \exp(\xi)] &= 0, \\
\mathcal{E}_\theta[\omega_4 \exp(-\xi) + \omega_5 \exp(\xi)] &= 0, \\
\mathcal{E}_\Phi[\omega_6 \exp(-\xi) + \omega_7 \exp(\xi)] &= 0.
\end{aligned} \tag{6.29}$$

According to the procedure (see Ref. [111]), we have

$$\begin{aligned}
F_m(\xi) &= F_m^*(\xi) + \omega_2 \exp(-\xi) + \omega_1 + \omega_3 \exp(\xi), \\
\theta_m(\xi) &= \theta_m^*(\xi) + \omega_4 \exp(-\xi) + \omega_5 \exp(\xi), \\
\Phi_m(\xi) &= \Phi_m^*(\xi) + \omega_6 \exp(-\xi) + \omega_7 \exp(\xi),
\end{aligned} \tag{6.30}$$

where $(F_m^*(\xi), \theta_m^*(\xi), \Phi_m^*(\xi))$ are the special solutions and ω_j ($j = 1 - 7$) are the arbitrary constants that are defined as follows

$$\begin{aligned}
\omega_1 &= \left. \frac{\partial F_m^*}{\partial \xi} \right|_{\xi=0} - F_m^*(0), & \omega_2 &= \left. \frac{\partial F_m^*}{\partial \xi} \right|_{\xi=0}, & \omega_4 &= -\theta_m^*(\xi)|_{\xi=0} \\
\omega_6 &= -\Phi_m^*(\xi)|_{\xi=0}, & \omega_3 &= 0, & \omega_5 &= \omega_7 = 0.
\end{aligned} \tag{6.31}$$

6.4 Convergence analysis

The nonlinear problem is analyzed through homotopy technique to get convergent solutions. Here h –curves are sketched in Fig. 6.2 to see the appropriate ranges of h_F , h_θ and h_ϕ . The admissible convergent regions parallel to h –axis are $(-1.0 \leq h_F \leq -0.5)$, $(-1.3 \leq h_\theta \leq -0.5)$ and $(-1.4 \leq h_\phi \leq -1.1)$, respectively. Convergence of velocity $F''(0)$, temperature $\theta'(0)$ and concentration $\Phi'(0)$ is attained at 18th, 26th and 30th order of approximation, respectively (see Table 6.1).

Table 6.1: Convergence analysis when $\gamma_2 = 0.9$, $\hat{N}_b = \hat{N}_t = 0.5$, $Sc = 1.5$, $S_2 = 0.1$, $\hat{\beta}_t = \alpha_2 = \hat{B}_1 = \delta_e = 0.2$, $\hat{B}_2 = \delta_c = S_1 = 0.3$, $\gamma_3 = \hat{N}_1 = E_a = \delta = 1.0$ and $Pr = 1.2$.

Approximation Order	$-F''(0)$	$-\theta'(0)$	$-\Phi'(0)$
1	0.6253	0.2014	2.4943
8	0.6545	0.2386	2.5761
12	0.7138	0.3495	2.6874
18	0.7957	0.3828	2.7136
26	0.7957	0.4395	2.7250
30	0.7957	0.4395	2.7544
36	0.7957	0.4395	2.7544
40	0.7957	0.4395	2.7544
42	0.7957	0.4395	2.7544

6.4 Results and discussion

In this section we will discuss in detail the behavior of velocity $F'(\xi)$, temperature $\theta(\xi)$ and concentration $\Phi(\xi)$, heat transfer and mass transfer rate for various flow parameters in graphical and tabulated form. Fig. 6.3 presents the declining trend of $F'(\xi)$ for greater α_2 . Physically, higher α_2 correspond to the enhancement in viscoelasticity through tensile stress. That develops resistance in boundary layer and hence velocity $F'(\xi)$ profile declines. Fig. 6.4 elaborates behavior of β_1 for velocity $F'(\xi)$ curve. Here $F'(\xi)$ enriches for higher estimation of β_1 . Since higher values of β_1 corresponds due to the dominant role of thermal buoyancy force which helps to heighten $F'(\xi)$. Impact of \widehat{N}_b and \widehat{N}_t on temperature $\theta(\xi)$ is presented in Figs. 6.5 and 6.6 respectively. Increase in temperature $\theta(\xi)$ and apposite boundary layer thickness is found for greater marks of \widehat{N}_b (see Fig. 6.5). In fact, additional heat is generated due to random motion of liquid molecules within the frame of greater \widehat{N}_b . Hence, temperature $\theta(\xi)$ curve upsurges. Fig. 6.6 depicts same enhancing behaviour of $\theta(\xi)$ against increasing values of \widehat{N}_t . For higher approximation of \widehat{N}_t , fluid particles drag out from hotter region to colder region of medium which subsequently boost up temperature profile $\theta(\xi)$. Fig. 6.7 reveals the declining effect of temperature $\theta(\xi)$ for greater values of Pr . In fact, rise in Pr corresponds to weaker thermal diffusivity over the stronger momentum diffusivity due to which reduction in $\theta(\xi)$ is observed. Fig. 6.8 examines the declining trend of $\theta(\xi)$ for higher values of S_1 . Infact, temperature difference $(T_w - T_\infty)$ gradually decreases for higher approximation of S_1 that result in decrease of temperature. In Fig. 6.9 variation of $\theta(\xi)$ due to sundry values of δ_e is displayed. Temperature is found to be decline in nature through greater value of δ_e . Physically, material particles take more time to transfigure

heat due rise in thermal relaxation time. Fig. 6.10 reveals the impact of \hat{B}_1 on $\theta(\xi)$ profile. One can noticed that $\theta(\xi)$ is increasing function of \hat{B}_1 . Because \hat{B}_1 increases the thickness of thermal boundary layer that performs as an agent to produce more heat. Due to this fact, an increase in $\theta(\xi)$ is observed for greater estimation of \hat{B}_1 . Impact of Sc on $\Phi(\xi)$ is deliberated in Fig. 6.11. Concentration outline reduces for larger values of Sc . Since higher values of Sc resembles to the lower mass diffusivity which reduces concentration $\Phi(\xi)$ profile. Fig. 6.12 displays the role of \hat{N}_b on concentration $\Phi(\xi)$. This figure predicts that the nanoparticles concentration become low versus Brownian motion. This assertive response produces more collision among fluid particles due to which $\Phi(\xi)$ diminishes. Fig. 6.13 elaborates the character of \hat{N}_t on $\Phi(\xi)$. For greater estimation of \hat{N}_t fluid thermal conductivity develops promptly. Such extra thermal conductivity corresponds due to rise in $\Phi(\xi)$. Fig. 6.14 displays the variation of $\Phi(\xi)$ due to temperature change parameter δ . Here declining role of $\Phi(\xi)$ is analyzed for greater value of δ . Physically, it indicates that concentration in boundary thickness $\Phi(\xi)$ upsurges for higher temperature difference $(T_w - T_\infty)$. Fig. 6.15 investigates the activation energy parameter E_a effects on concentration $\Phi(\xi)$. One can observe that increasing behavior of concentration $\Phi(\xi)$ exists for higher marks of E_a . Physically greater E_a decreases the modified Arrhenius function which eventually endorses the generative chemical reaction. Therefore $\Phi(\xi)$ enriches. Higher variation of γ_3 corresponds to increase in rate of destructive chemical reaction which terminates/dissolves the fluid species more effectively (see Fig. 6.16). Hence, concentration $\Phi(\xi)$ decays. Fig. 6.17 interprets the impact of fitted rate constant p on $\Phi(\xi)$. Here $\Phi(\xi)$ is found to be decreasing function of p . The role of skin friction coefficient C_F , Nusselt number Nu_x

and Sherwood Number Sh_x for emerging parameters \hat{N}_b , \hat{B}_2 , Pr , γ_3 and β_1 are presented in Figs. (6.18) – (6.23) respectively. It is depicted from Figs. 6.18 and 6.19 that skin friction coefficient C_F enhances for larger values of both parameters \hat{N}_b and β_1 , respectively. While behavior of Nusselt number $Nu_x(Re_x)^{\frac{1}{2}}$ for \hat{B}_2 and Pr are perceived in Figs. 6.20 and 6.21. Fig. 6.20 depicts the decline role of Nu_x for greater values of \hat{B}_2 whereas reverse impact is identified for fixed values of \hat{B}_2 (see Fig.6.22). Impact of local Sherwood number $Sh_x(Re_x)^{-\frac{1}{2}}$ for γ_3 and β_1 are displayed in Figs. 6.22 and 6.23. Here we revealed that $Sh_x(Re_x)^{-\frac{1}{2}}$ enhances via γ_3 and it diminishes for fixed values of β_1 .

6.5 Graphical outcomes

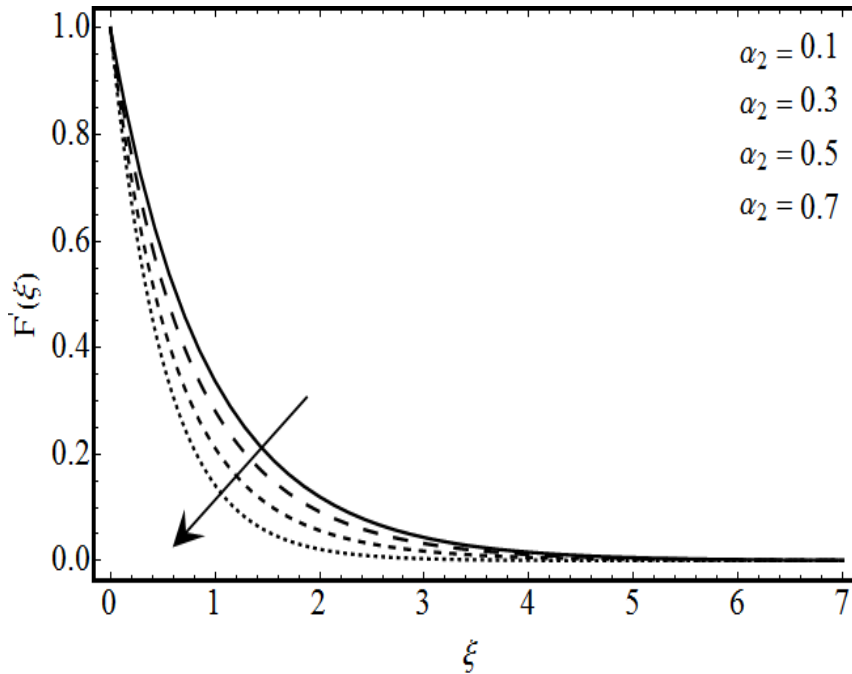


Fig. 6.3: Response of $F'(\xi)$ with α_2 .

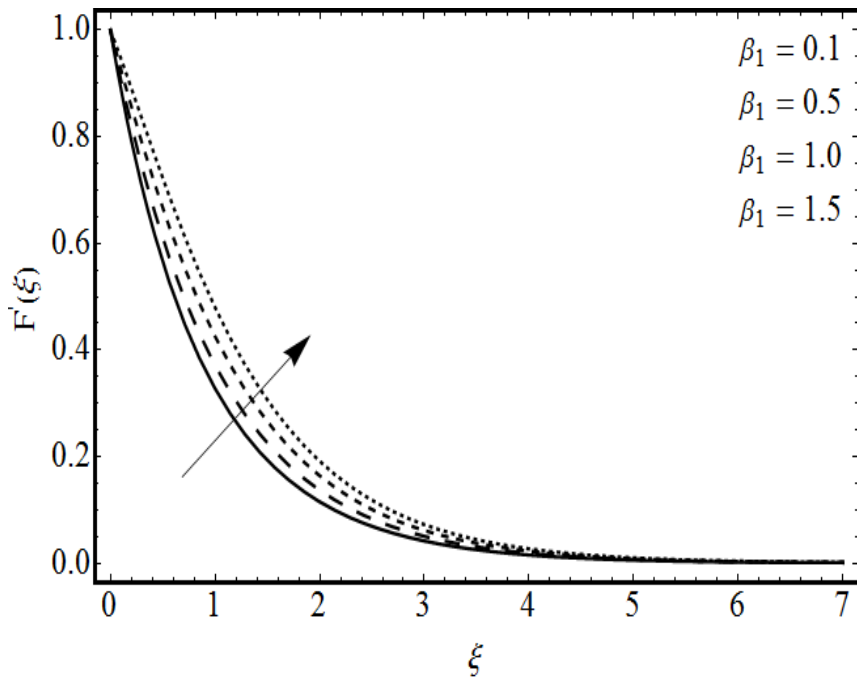


Fig. 6.4: Response of $F'(\xi)$ with β_1 .

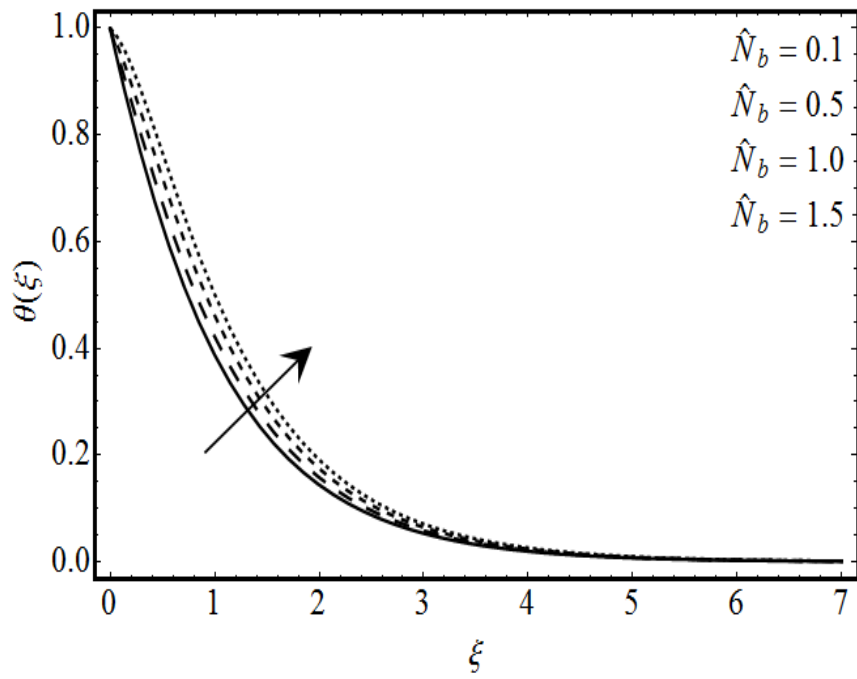


Fig. 6.5: Response of $\theta(\xi)$ with \hat{N}_b .

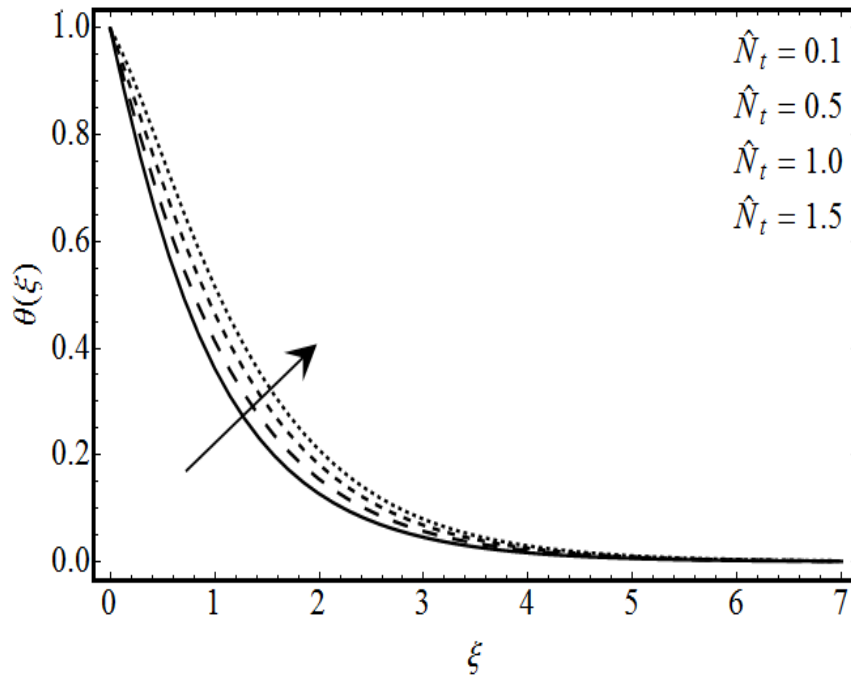


Fig. 6.6: Response of $\theta(\xi)$ with \hat{N}_t .

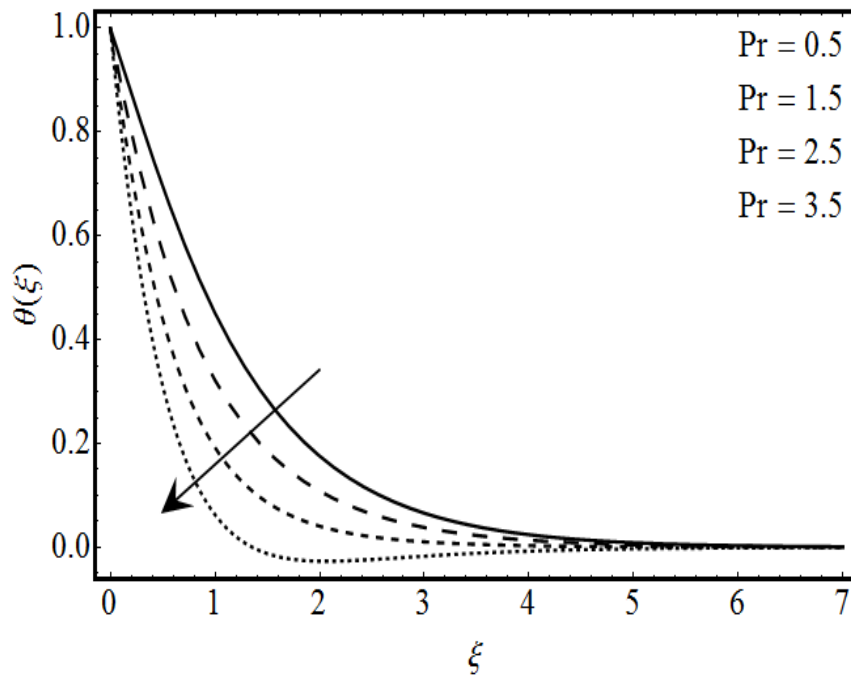


Fig. 6.7: Response of $\theta(\xi)$ with Pr .

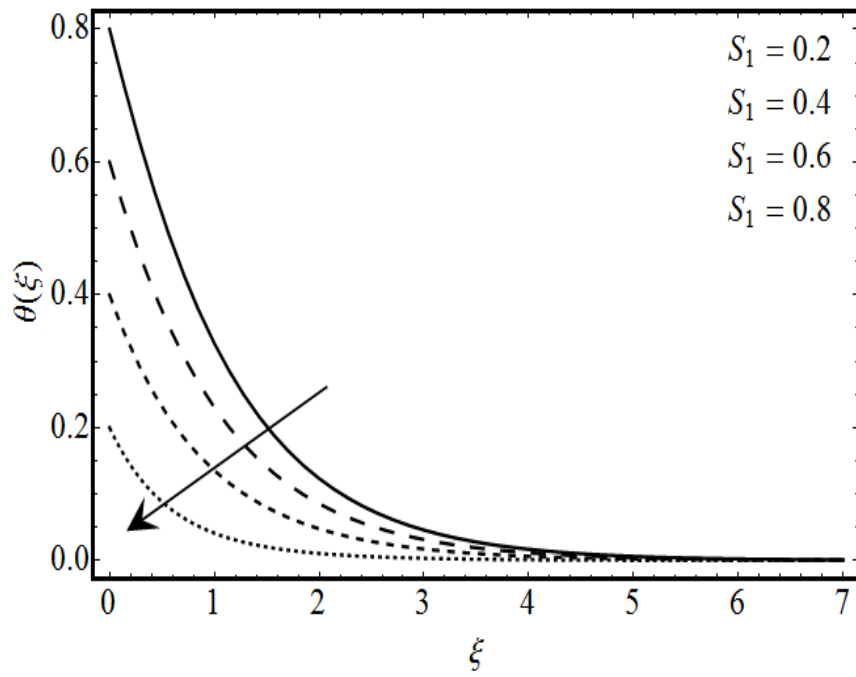


Fig. 6.8: Response of $\theta(\xi)$ with S_1 .

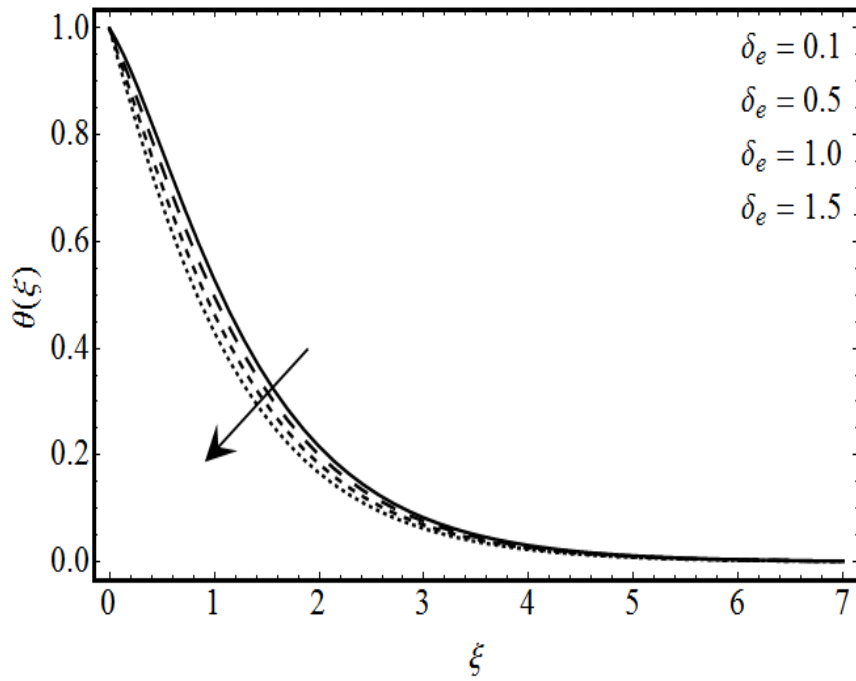


Fig. 6.9: Response of $\theta(\xi)$ with δ_e .

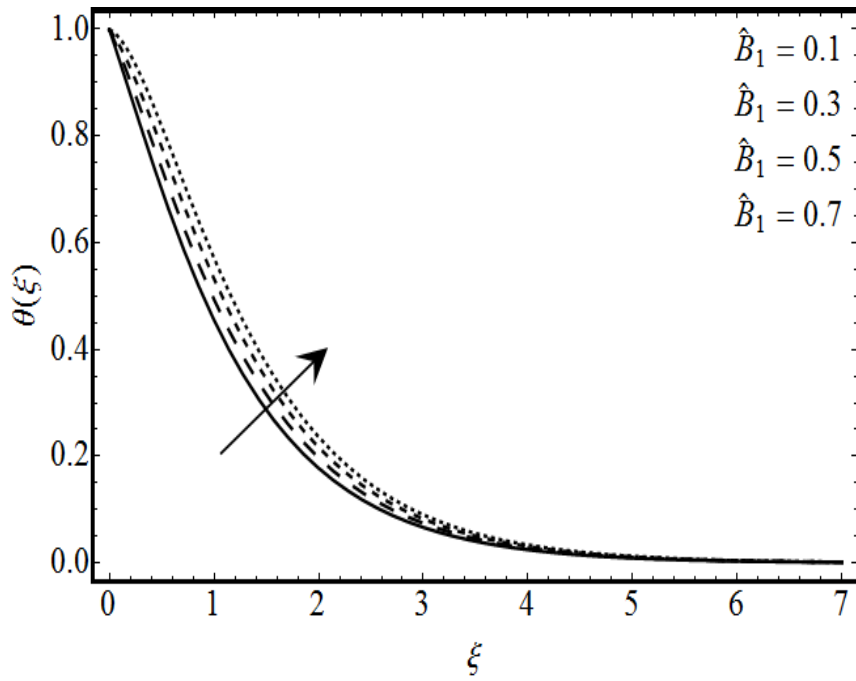


Fig. 6.10: Response of $\theta(\xi)$ with \hat{B}_1 .

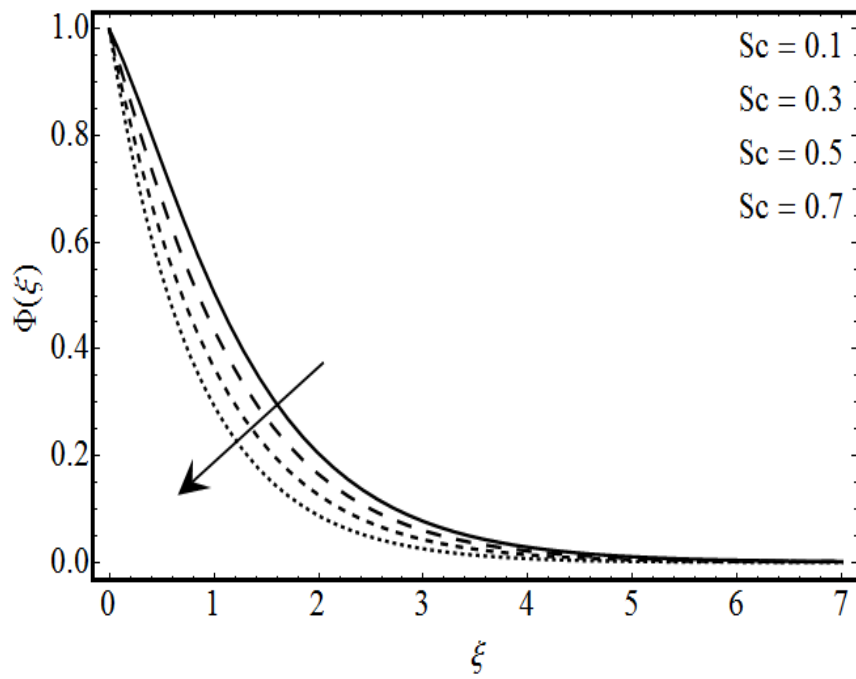


Fig. 6.11: Response of $\Phi(\xi)$ with Sc .

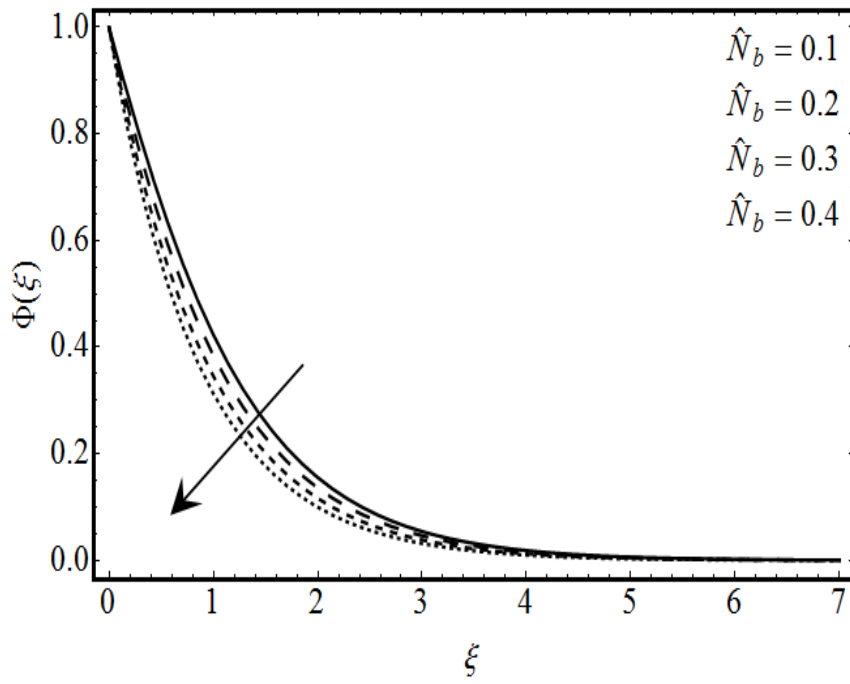


Fig. 6.12: Response of $\Phi(\xi)$ with \hat{N}_b .

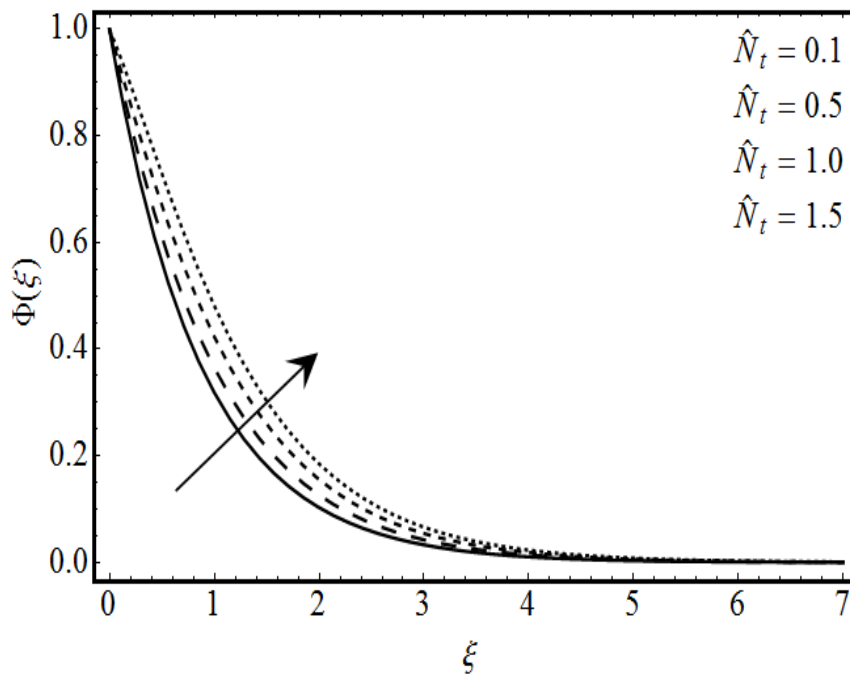


Fig. 6.13: Response of $\Phi(\xi)$ with \hat{N}_t .

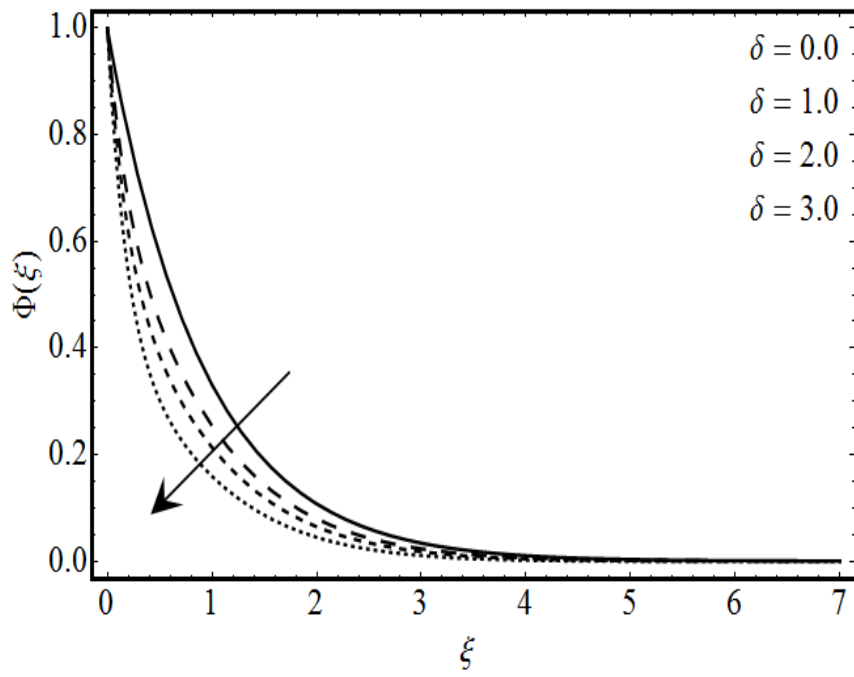


Fig. 6.14: Response of $\Phi(\xi)$ with δ .

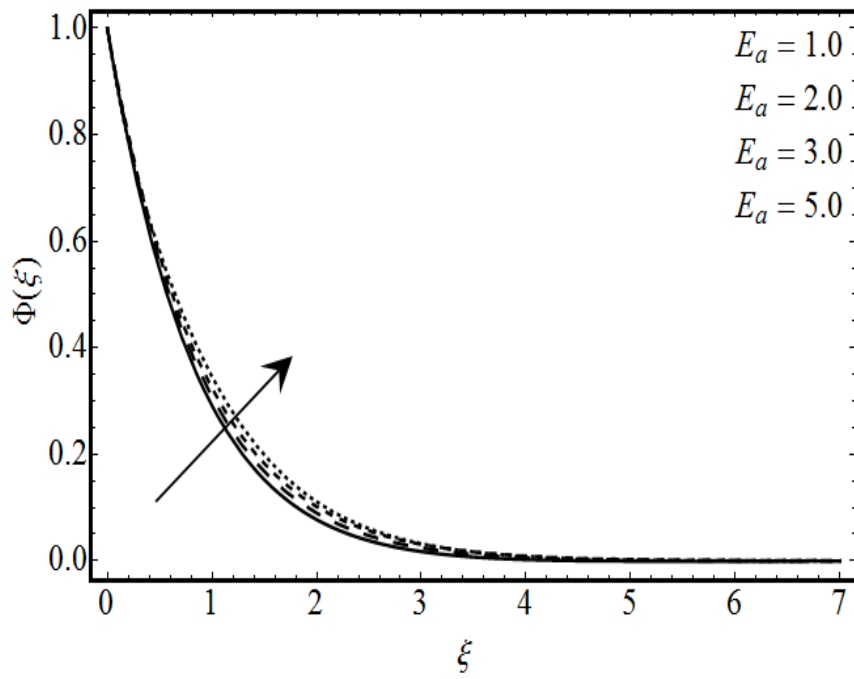


Fig. 6.15: Response of $\Phi(\xi)$ with E_a .

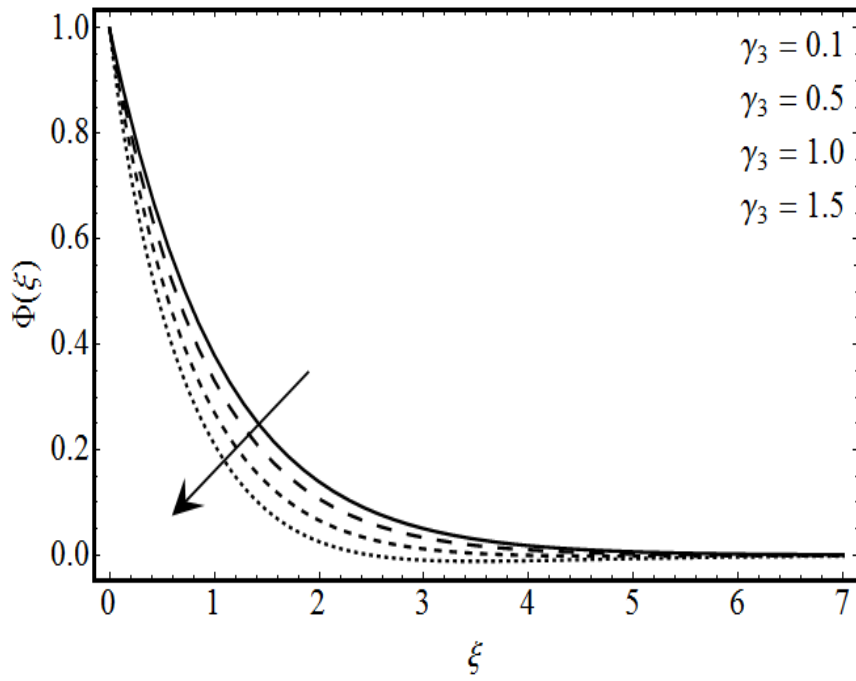


Fig. 6.16: Response of $\Phi(\xi)$ with γ_3 .

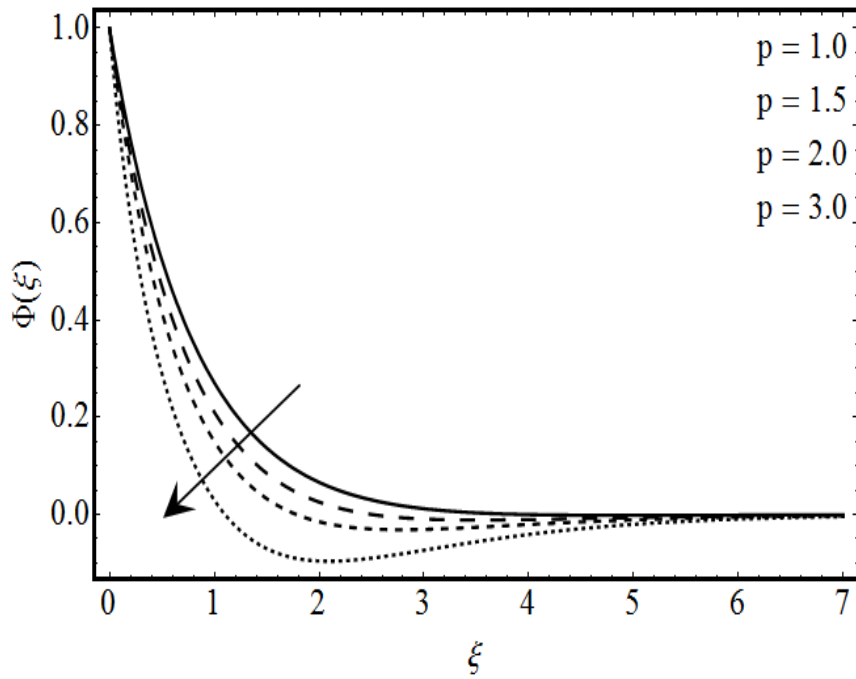


Fig. 6.17: Response of $\Phi(\xi)$ with p .

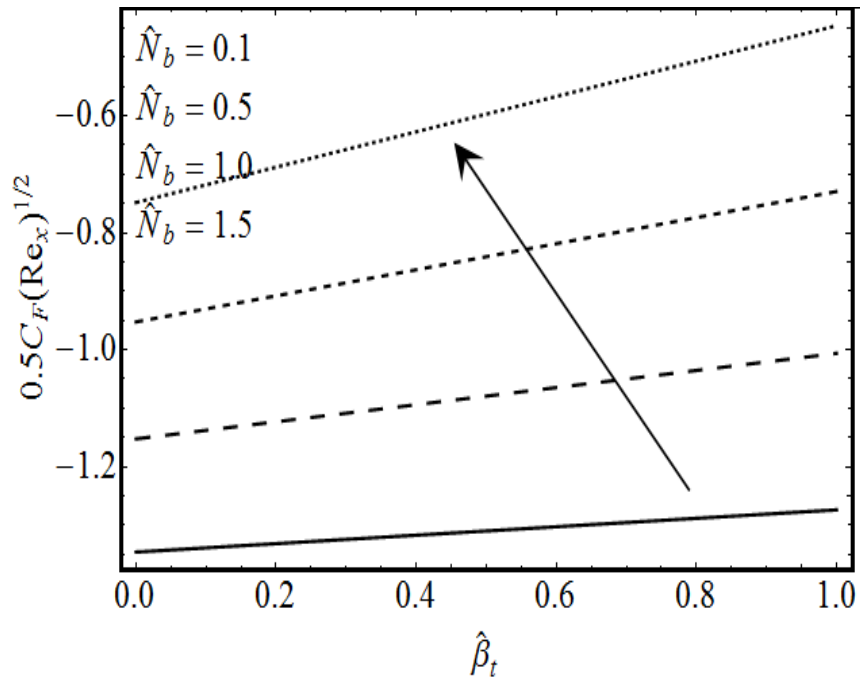


Fig. 6.18: Response of $\frac{1}{2}C_F(Re_x)^{\frac{1}{2}}$ with \hat{N}_b .

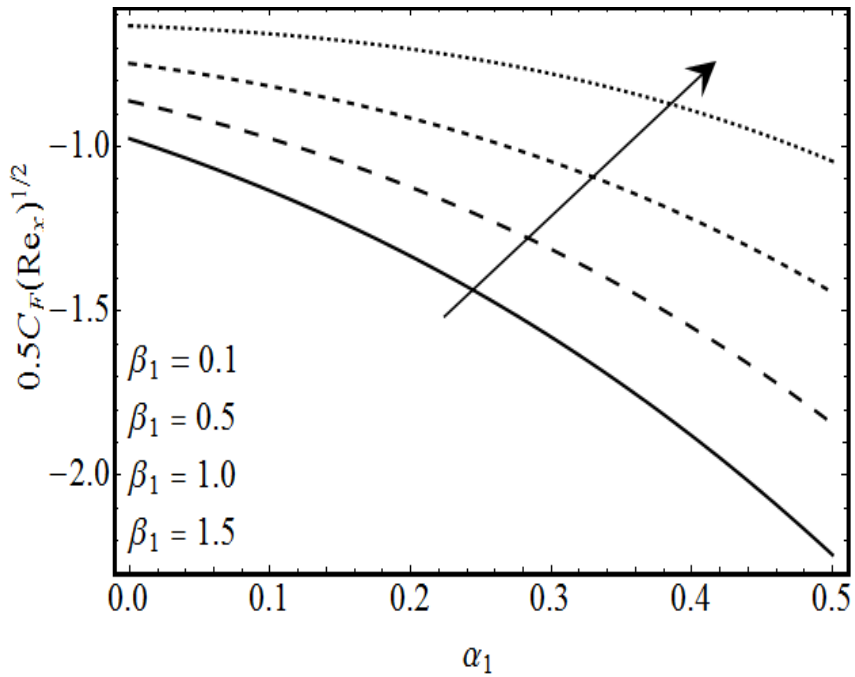


Fig. 6.19: Response of $\frac{1}{2}C_F(Re_x)^{\frac{1}{2}}$ with β_1 .

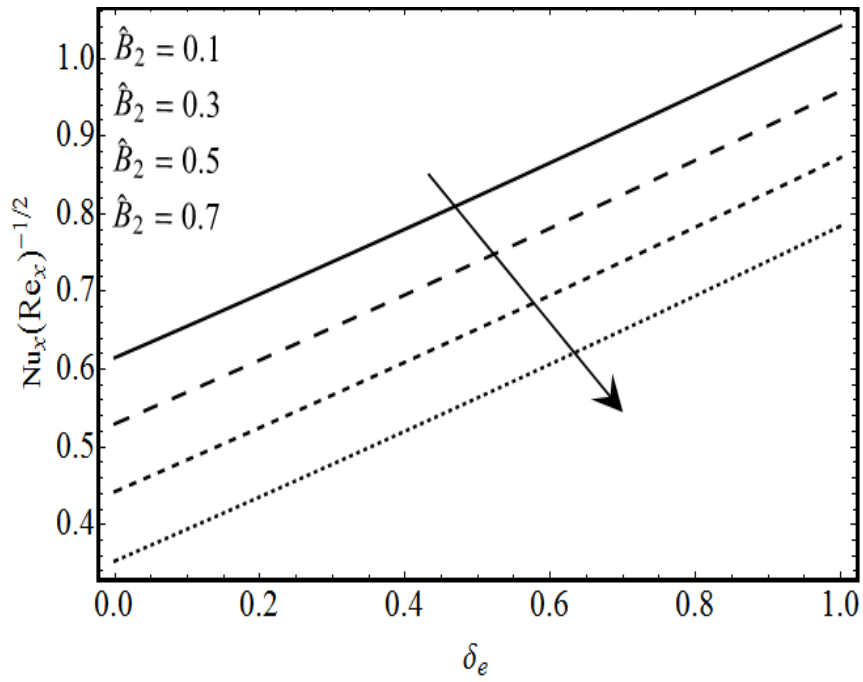


Fig. 6.20: Response of $Nu_x(Re_x)^{-1/2}$ with \hat{B}_2 .

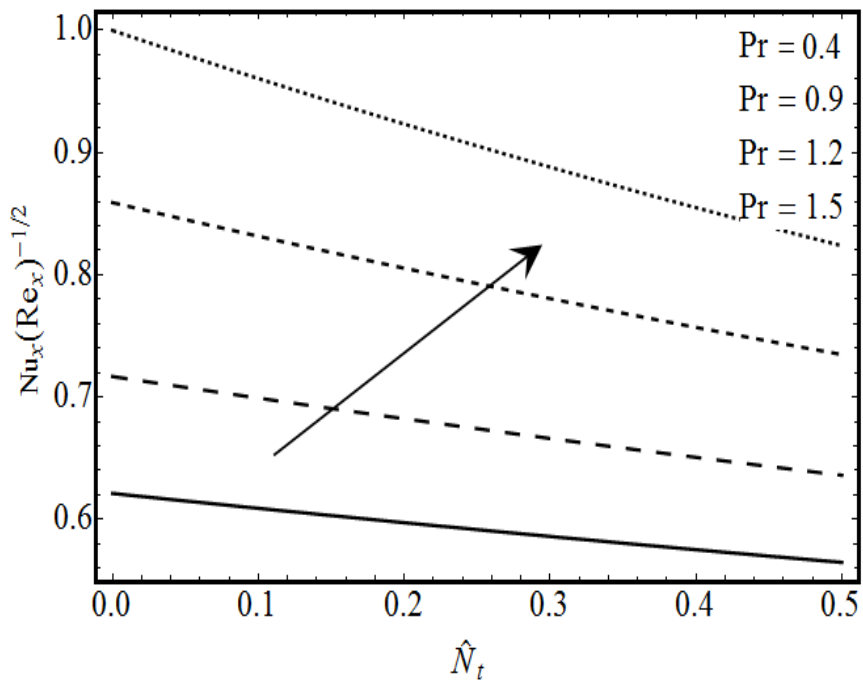


Fig. 6.21: Response of $Nu_x(Re_x)^{-1/2}$ with Pr .

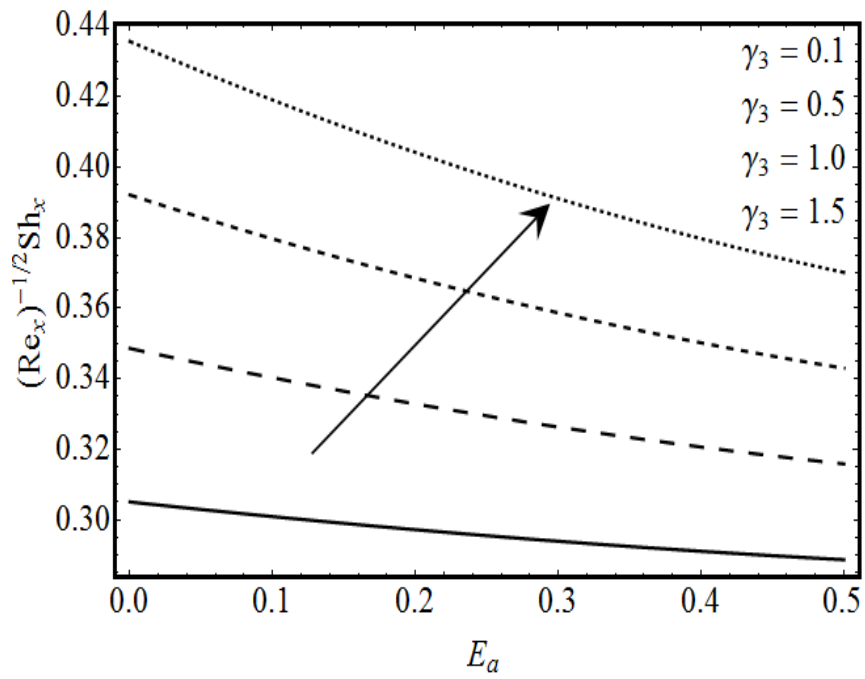


Fig. 6.22: Response of $Sh_x(Re_x)^{-1/2}$ with γ_3 .

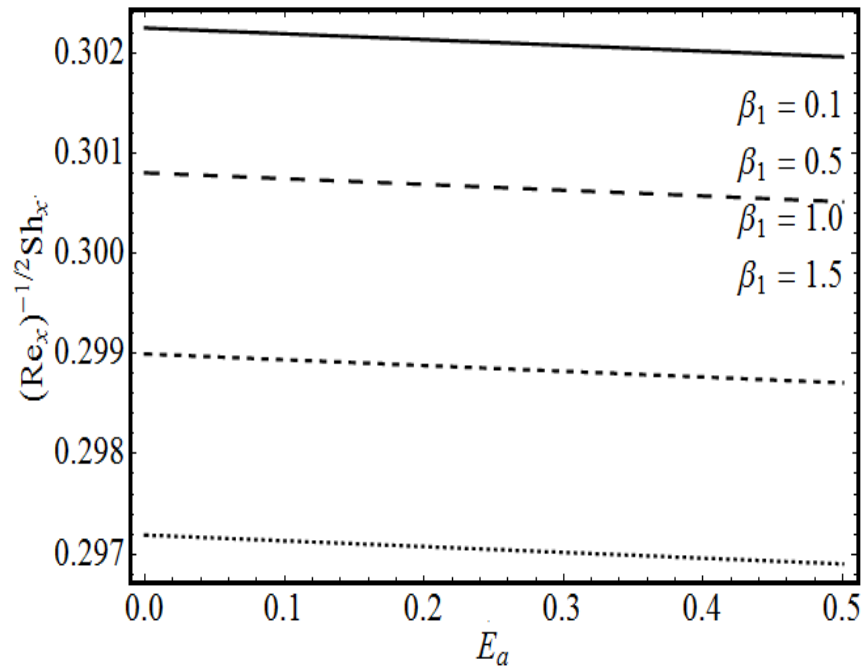


Fig. 6.23: Response of $Sh_x(Re_x)^{-1/2}$ with β_1 .

6.6 Conclusions

Main findings of the study are listed below:

- Velocity profile $F'(\xi)$ declines for higher values of viscoelastic factor α_2 while it boosts up for larger estimation of mixed convection parameter β_1 .
- Temperature field $\theta(\xi)$ enhances for greater values of flow parameters \widehat{N}_b , \widehat{N}_t and \widehat{B}_1 .
- For greater estimations of activation energy parameter E_a , concentration profile $\Phi(\xi)$ enhances while reverse impact is noticed for reaction rate constant γ_3 .
- Reverse behavior of concentration field $\Phi(\xi)$ is remarked in view of \widehat{N}_b and \widehat{N}_t .
- Skin friction coefficient is amplified via Brownian parameter \widehat{N}_b .

CHAPTER 7

Numerical simulation of nonlinear radiative flow of Casson nanofluid with Cattaneo-Christov heat flux model

7.1 Introduction

This chapter investigates Cattaneo-Christov heat flux model for nonlinear radiative flow of Casson nanofluid over an inclined permeable stretched cylinder with slip mechanism. The novel characteristics of activation energy are studied in the presence of non-uniform heat generation/absorption, dual stratification, nonlinear mixed convection and binary chemical reaction. Casson fluid nanomaterial model is measured that refers to the significant slip mechanism such as Brownian and thermophoresis diffusions. The governing dimensional system is transformed into dimensionless system by implementing similarity variables. The developed nonlinear system is unravelled through shooting technique along with Runge–Kutta–Fehlberg (RK–45) approach. Physical quantities of interest are investigated through graphs and tables. A validation of the work is offered by comparing the current results with published literature.

7.2 Mathematical formulation

Consider two dimensional, incompressible, nonlinear radiative flow of Casson nanofluid [112-114] over an inclined stretched cylinder of radius R_0 . Fluid flow is maintained due to linear stretching velocity of the form $U_w \left(= \frac{U_0 z}{L} \right)$. Present analysis has been accomplished with nonlinear thermal radiation, non-uniform heat source/sink, thermal and solutal stratification, nonlinear mixed convection, binary chemical reaction and Arrhenius activation energy. The velocity and thermal slip are also inspected for present flow problem. The uniform magnetic field of strength B_0 is applied in normal radial direction (see Fig. 7.1). Cattaneo–Christov heat flux theory is used for heat transfer. The governing expression of problem are

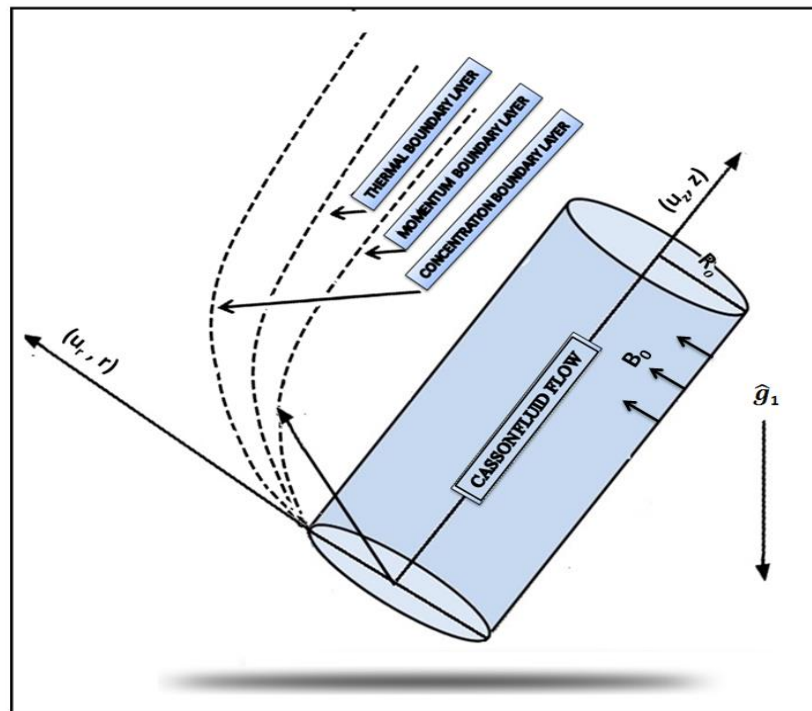


Fig. 7.1: Physical model.

$$\frac{\partial}{\partial r}(ru_r) + \frac{\partial}{\partial z}(ru_z) = 0, \quad (7.1)$$

$$u_z \frac{\partial u_z}{\partial z} + u_r \frac{\partial u_z}{\partial r} = v_1 \left(1 + \frac{1}{\lambda_c}\right) \left(\frac{\partial^2 u_z}{\partial r^2} + \frac{1}{r} \frac{\partial u_z}{\partial r}\right) - \frac{\sigma B_0^2 u_z}{\rho_f} + \frac{\hat{g}_1}{\rho_f} [\Gamma_1(T - T_\infty) + \Gamma_2(T - T_\infty)^2 + \Gamma_3(C - C_\infty) + \Gamma_4(C - C_\infty)^2] \cos \phi_a. \quad (7.2)$$

Cattaneo–Christov heat flux model is defined as

$$\mathbf{q}_1 + \hat{\Gamma}_e \left[\frac{\partial \mathbf{q}_1}{\partial t} + \mathbf{V}_1 \cdot \nabla \mathbf{q}_1 - (\mathbf{q}_1 \cdot \nabla) \mathbf{V}_1 + (\nabla \cdot \mathbf{V}_1) \mathbf{q}_1 \right] = -k_f \nabla T. \quad (7.3)$$

Utilizing the condition of steady incompressible flow i.e., $\frac{\partial}{\partial t} = 0$ and $\nabla \cdot \mathbf{V}_1 = 0$, Eq. (7.3)

reduces to

$$\mathbf{q}_1 + \hat{\Gamma}_e [\mathbf{V}_1 \cdot \nabla \mathbf{q}_1 - (\mathbf{q}_1 \cdot \nabla) \mathbf{V}_1] = -\hat{k}_f \nabla T. \quad (7.4)$$

The heat and mass conservation laws are

$$u_r \frac{\partial T}{\partial r} + u_z \frac{\partial T}{\partial z} + \hat{\Gamma}_e \Pi_e = \frac{\hat{k}_f}{(\rho C_p)_f} \frac{1}{r} \frac{\partial}{\partial r} \left(r \frac{\partial T}{\partial r} \right) + \frac{\hat{Q}_m}{(\rho C_p)_f} + \frac{1}{(\rho C_p)_f} \frac{1}{r} \frac{\partial}{\partial r} \left(\frac{16\sigma_2 T^3}{3\hat{K}_3} r \frac{\partial T}{\partial r} \right) + \tau_1 D_B \frac{\partial C}{\partial r} \frac{\partial T}{\partial r} + \frac{\tau_1 D_T}{T_\infty} \left(\frac{\partial T}{\partial r} \right)^2, \quad (7.5)$$

$$u_r \frac{\partial C}{\partial r} + u_z \frac{\partial C}{\partial z} = D_B \frac{\partial}{\partial r} \left(r \frac{\partial C}{\partial r} \right) + \frac{D_T}{T_\infty} \frac{1}{r} \frac{\partial}{\partial r} \left(r \frac{\partial T}{\partial r} \right) - \hat{K}_1 (C - C_\infty) - \hat{K}_r^2 (C_w - C_0) \left(\frac{T}{T_\infty} \right)^p \exp \left[-\frac{E_1}{T k^*} \right]. \quad (7.6)$$

The corresponding boundary conditions are

$$\left. \begin{aligned} u_z &= \frac{U_0 z}{L} + V_2 \left(1 + \frac{1}{\lambda_c}\right) \frac{\partial u_z}{\partial r}, & T &= T_w = T_0 + \frac{d_1 z}{L}, \\ u_r &= V_1, & C &= C_w = C_0 + \frac{d_3 z}{L} \end{aligned} \right| \text{at } r = R_0, \quad (7.7)$$

$$\left. \begin{aligned} u_z &\rightarrow 0, & T &\rightarrow T_\infty = T_0 + \frac{d_2 x}{L}, \\ u_r &\rightarrow 0, & C &\rightarrow C_\infty = C_0 + \frac{d_4 x}{L}. \end{aligned} \right| \text{when } r \rightarrow \infty, \quad (7.8)$$

with

$$\begin{aligned} \Pi_e &= u_r^2 \frac{\partial^2 T}{\partial r^2} + u_z^2 \frac{\partial^2 T}{\partial z^2} + \frac{\partial T}{\partial r} \left(u_z \frac{\partial u_r}{\partial z} + u_r \frac{\partial u_r}{\partial r} \right) + 2u_z u_r \frac{\partial^2 C}{\partial r \partial z} \\ &+ \frac{\partial T}{\partial z} \left(u_z \frac{\partial u_z}{\partial z} + u_r \frac{\partial u_r}{\partial r} \right). \end{aligned} \quad (7.9)$$

The mathematical expression of non-uniform heat generation/absorption \hat{Q}_m [115] is

$$\hat{Q}_m = \frac{U_w \hat{k}_f}{z \nu_1} \left[\hat{B}_1 (T_w - T_0) \frac{\partial F}{\partial \xi} + \hat{B}_2 (T - T_\infty) \right]. \quad (7.10)$$

Here, $(\hat{B}_1, \hat{B}_2) > 0$ corresponds to heat generation state while $(\hat{B}_1, \hat{B}_2) < 0$ resembles to the heat absorption.

Apposite transformations for present flow are [116]

$$\begin{aligned} \xi &= \sqrt{\frac{U_0}{L \nu_1}} \left(\frac{r^2 - R_0^2}{2R_0} \right), & \Psi_1(\xi) &= \sqrt{\frac{\nu_1 U_0 z^2}{L}} F(\xi), \\ u_z(\xi) &= \frac{U_0 z}{L} F'(\xi), & u_r(\xi) &= -\frac{R_0}{r} \sqrt{\frac{\nu_1 U_0}{L}} F(\xi), \\ \theta(\xi) &= \frac{T - T_\infty}{T_w - T_0}, & \Phi(\xi) &= \frac{C - C_\infty}{C_w - C_0}. \end{aligned} \quad (7.11)$$

The resulting ordinary differential equations are

$$(1 + 2\gamma_1\xi) \left(1 + \frac{1}{\lambda_c}\right) F''' + 2\gamma_1 \left(1 + \frac{1}{\lambda_c}\right) F'' + FF'' - F'^2 + \beta_1[(1 + \hat{\beta}_t\theta)\theta + \hat{N}_1(1 + \hat{\beta}_c\Phi)\Phi] \cos \phi_a - M_1F' = 0, \quad (7.12)$$

$$(1 + 2\gamma_1\xi) \left(\theta'' + \text{Pr} \hat{N}_b \left(\theta'\Phi' + \frac{\hat{N}_t}{\hat{N}_b} \theta'^2 + Ec \left(1 + \frac{1}{\lambda_c}\right) F''^2 \right) \right) + 2\gamma_1\theta' + (1 + \hat{N}_r(1 + (\theta_w - 1)\theta)^3\theta')' + \text{Pr}F\theta' + \text{Pr}\delta_e(FF'\theta' - \theta''F^2) + \hat{B}_1F' + \hat{B}_2\theta + \text{Pr}(S_1 + \theta)(\delta_e(FF'' - F'^2) - F') = 0, \quad (7.13)$$

$$(1 + 2\gamma_1\xi) \left(\Phi'' + \frac{\hat{N}_t}{\hat{N}_b} \theta'' \right) + 2\gamma_1 \left(\Phi' + \frac{\hat{N}_t}{\hat{N}_b} \theta' \right) + ScF\Phi' - Sc(S_2 + \Phi)F' + \gamma_2\Phi - Sc\gamma_3(1 + \delta\theta)^p \exp \left[-\frac{E_a}{(1 + \delta\theta)} \right] = 0, \quad (7.14)$$

with

$$F'(0) = 1 + S_v \left(1 + \frac{1}{\lambda_c}\right) F''(0), \quad F(0) = V_p, \quad \theta(0) = 1 - S_1, \quad \Phi(0) = 1 - S_2, \\ F'(\xi) = 0, \quad \theta(\xi) = 0, \quad \Phi(\xi) = 0, \quad \text{when } \xi \rightarrow \infty. \quad (7.15)$$

Emerging flow parameters are listed below:

$$\begin{aligned}
\hat{N}_b &= \frac{\tau_1 D_B (C_w - C_0)}{\nu_1}, & \hat{\beta}_c &= \frac{\Gamma_4 (C_w - C_0)}{\Gamma_3}, & \delta_e &= \frac{U_0 \hat{\Gamma}_e}{L}, \\
\hat{N}_1 &= \frac{\Gamma_3 (C_w - C_0)}{\Gamma_1 (T_w - T_0)}, & \delta &= \frac{(T_w - T_0)}{T_\infty}, & \gamma_3 &= \frac{L \hat{K}_r^2}{U_0}, \\
Gr &= \frac{\hat{g}_1 \Gamma_1 (T_w - T_0) z^3}{\nu_1^2}, & \hat{\beta}_t &= \frac{\Gamma_2 (T_w - T_0)}{\Gamma_1}, & \gamma_2 &= \frac{K_1 L}{U_0}, \\
\hat{N}_t &= \frac{\tau_1 D_T (T_w - T_0)}{T_\infty \nu_1}, & \gamma_1 &= \sqrt{\frac{L \nu_1}{R_0^2 U_0}}, & E_a &= \frac{E_1}{T_\infty k^*}, \\
Gr^* &= \frac{\hat{g}_1 \Gamma_3 (C_w - C_0) z^3}{\nu_1^2}, & S_v &= \frac{V_2 r}{R_0} \sqrt{\frac{U_0}{\nu_1 L}}, & Pr &= \frac{(\mu C_p)_f}{\hat{k}_f}, \\
Ec &= \frac{U_w^2}{C_p (T_w - T_0)}, & S_1 &= \frac{d_2}{d_1}, & Sc &= \frac{\nu_1}{D_B}.
\end{aligned} \tag{7.16}$$

The interested physical quantities (C_F, Nu_z, Sh_z) near surface are

$$C_F = \frac{2\tau_w}{\rho_f U_w^2}, \quad Nu_z = \frac{z q_w}{\hat{k}_f (T_w - T_0)}, \quad Sh_z = \frac{z j_w}{D_B (C_w - C_0)}, \tag{7.17}$$

with

$$\tau_w = \mu \left(1 + \frac{1}{\lambda_c} \right) \frac{\partial u_z}{\partial r} \Big|_{r=R_0}, \tag{7.18}$$

$$q_w = -\hat{k}_f \frac{\partial T}{\partial r} \Big|_{r=R_0} + q_r|_w, \tag{7.19}$$

$$q_m = -D_B \frac{\partial C}{\partial r} \Big|_{r=R_0}, \tag{7.20}$$

where $q_r|_w$ is defined as

$$(q_r)_w = -\frac{16\sigma_2 T^3}{3\hat{k}_f \hat{K}_3} \left(\frac{\partial T}{\partial r} \right)_{r=R_0}. \tag{7.21}$$

From above equations, one can write

$$\begin{aligned}\frac{1}{2} C_F(Re_z)^{\frac{1}{2}} &= \left(1 + \frac{1}{\lambda_c}\right) F''(0), \\ Nu_z(Re_z)^{-\frac{1}{2}} &= -\left(1 + \hat{N}_r(1 + (\theta_w - 1)\theta(0))^3\right) \theta'(0), \\ Sh_z(Re_z)^{-\frac{1}{2}} &= -\Phi'(0).\end{aligned}\tag{7.22}$$

7.3 Methodology

The numerical solution of resulting system of coupled non-linear Eqs. (7.12) – (7.14) along with boundary conditions Eq. (7.15) is computed through shooting technique along with fifth order Runge–Kutta–Fehlberg method with $\xi = 0.001$. Newton method is applied for the modification of initial guesses U_1, U_2 and U_3 subjected to the tolerance of $\varepsilon = 10^{-7}$. For present study, the domain of the problem is considered as $[0 - 15]$ instead of $[0 - \infty)$. To proceed with this technique, we have to reduce higher order coupled system into the first order equivalent system by defining new variables:

$$(Z_1, Z_2, Z_3, Z_4, Z_5, Z_6, Z_7) = (F, F', F'', \theta, \theta', \Phi, \Phi').$$

The first order equivalent system in term of Z_i for $(i = 1, 2, 3, 4, 5, 6, 7)$ is

$$Z'_1 = Z_2, \tag{7.23}$$

$$Z'_2 = Z_3, \tag{7.24}$$

$$Z'_3 = \frac{\begin{pmatrix} -2\gamma_1 \left(1 + \frac{1}{\lambda_c}\right) Z_3 - Z_1 Z_3 + Z_2^2 + M_1 Z_2 - \\ \beta_1 \left((1 + \hat{\beta}_t Z_4) Z_4 + \hat{N}_1 (1 + \hat{\beta}_c Z_6) Z_6 \right) \cos \phi_a \end{pmatrix}}{(1 + 2\gamma_1 \xi) \left(1 + \frac{1}{\lambda_c}\right)}, \tag{7.25}$$

$$Z'_4 = Z_5, \quad (7.26)$$

$$Z'_5 = \frac{\left(\begin{aligned} &-(1 + 2\gamma_1\xi)Pr \left(\widehat{N}_b Z_5 Z_7 + \widehat{N}_t Z_5^2 + Ec \left(1 + \frac{1}{\lambda_c} \right) Z_3^2 \right) - 2\gamma_1 Z_5 \\ &+ Pr(S_1 + Z_4)Z_2 - PrZ_1 Z_5 - (1 + \widehat{N}_r(1 + (\theta_w - 1)Z_4)^3 Z_5)' \\ &- Pr\delta_e((S_1 + Z_4)(Z_1 Z_3 - Z_2^2) + Z_1 Z_2 Z_5) - (\widehat{B}_1 Z_2 + \widehat{B}_2 Z_4) \end{aligned} \right)}{(1 + 2\gamma_1\xi - Pr\delta_e Z_1^2)}, \quad (7.27)$$

$$Z'_6 = Z_7, \quad (7.28)$$

$$Z'_7 = \frac{\left(\begin{aligned} &-\frac{\widehat{N}_t}{\widehat{N}_b} \left((1 + 2\gamma_1\xi)\theta'' + 2\gamma_1 Z_5 \right) - \gamma_2 Z_6 - ScZ_1 Z_7 - 2\gamma_1 Z_7 \\ &+ Sc(S_2 + Z_6)Z_2 + Sc\gamma_3(1 + \delta Z_4)^p \exp \left[-\frac{E_a}{(1 + \delta Z_4)} \right] \end{aligned} \right)}{(1 + 2\gamma_1\xi)}, \quad (7.29)$$

with

$$\begin{aligned} Z_1(0) &= V_p, & Z_2(0) &= S_v \left(1 + \frac{1}{\lambda_c} \right) U_1, & Z_3(0) &= U_1, \\ Z_4(0) &= 1 - S_1, & Z_5(0) &= U_2, & Z_6(0) &= 1 - S_2, \\ Z_7(0) &= U_3, \end{aligned} \quad (7.30)$$

The terminating benchmarks for the iterative process is set as

$$\max(|Z_2(15) - 0|, |Z_4(15) - 0|, |Z_6(15) - 0|) < \varepsilon,$$

7.4 Results and discussion

The computed results are explained for interested physical entities by restricting physical parameters as $(0.2 \leq \gamma_1 \leq 0.8)$, $(0.5 \leq \lambda_c \leq \infty)$, $(0.1 \leq \beta_1 \leq 0.5)$, $(0.3 \leq \widehat{N}_b \leq 1.5)$, $(0.2 \leq \widehat{N}_t \leq 1.5)$, $(1 \leq \widehat{N}_1 \leq 1.5)$, $(0.2 \leq \gamma_2 \leq 0.8)$, $(0.5 \leq Pr \leq 2.5)$, $(0.2 \leq S_v \leq 0.8)$, $(0.5 \leq \widehat{N}_r \leq 3)$, $(0.2 \leq \widehat{M} \leq 0.6)$, $(0.2 \leq E_a \leq 1.5)$, $(0.1 \leq \gamma_3 \leq 1.0)$,

$(0.1 \leq Sc \leq 1.0)$, $(0.1 \leq S_1 \leq 0.5)$ and $(0.1 \leq \beta_t \leq 0.5)$. Tables (7.1 – 7.3) are constructed to notice the behavior of skin friction coefficient, local Nusselt and Sherwood number towards various flow controlling parameters such as γ_1 curvature parameter, λ_c Casson fluid parameter, M_1 Hartman number, Sc Schmidt number, β_1 mixed convection parameter, \widehat{N}_r radiation parameter, \widehat{N}_b Brownian motion parameter, \widehat{N}_t thermophoresis parameter (S_1, S_2) thermal stratification and solutal stratification parameters, respectively. Specifically, Tables 7.1 and 7.2 provide a comparison of the skin friction coefficient and local Nusselt number with the previously published results. Table 7.1 portrays the skin friction coefficient for numerous values of λ_c and M_1 and match these values with Ref. [117] when all other parameters remains unchanged. Without emphasis of Eq. (7.13), the present outcomes for Nusselt number using a number of values of Prandtl number are compared with existing values through Table 7.2. An excellent agreement of results has been noticed that confirms the validity of our present endeavor. (see Tables (7.1 and 7.2)). Table 7.3 is presented to study the sound effects of parameters like γ_1 , λ_c , β_1 , M_1 , S_1 , E_a and S_2 on skin friction coefficient. It is noticed that wall friction in the absolute sense, displays a provoking nature towards thermal stratification parameter S_1 , curvature parameter γ_1 , Casson fluid parameter λ_c and magnetic parameter M_1 while opposite approach is viewed for positive values of mixed convection parameter β_1 , activation energy parameter E_a and solutal stratification parameter S_2 respectively. Table 7.4 spectacles the impact of curvature parameter γ_1 , fluid parameter λ_c , thermal radiation parameter \widehat{N}_r , activation energy parameter E_a , thermal relaxation parameter δ_e , thermal stratification parameter S_1 , and \widehat{B}_1 on local wall heat flux. Here, wall heat flux inclines versus γ_1 and E_a while it declines for higher

marks of λ_c , \widehat{N}_r , \widehat{B}_1 , δ_e and S_1 . From Table 7.5, it is detected that an enhancement in curvature parameter γ_1 Schmidt number Sc , Brownian motion parameter \widehat{N}_b corresponds to rise in Sherwood number while \widehat{N}_t , E_a reduces it. The MATLAB built-in function (bvp4c) is employed for the verification of the present results attained from the shooting code.

Figs. (7.2 – 7.7) are portrayed to explore the velocity profile $F'(\xi)$, for distinct values of λ_c , γ_1 , M_1 , $\widehat{\beta}_t$ and S_v . Fig. 7.2 depict the behavior of $F'(\xi)$ on variation of Casson parameter λ_c . As stress of the Casson fluid causes a decrease in rheological characteristics. When λ_c approaches to its maximum value or infinity, the flow behavior resemble to the Newtonian fluid model and the fluid is able to shear faster along the surface. Fig. 7.3 captured fluctuations in velocity $F'(\xi)$ by varying curvature parameter γ_1 . One can see from graph that velocity distribution $F'(\xi)$ upsurges within the frame of larger curvature parameter γ_1 . Fig. 7.4 reveals the effect of an inclination ϕ_a on velocity profile. It is observed that for greater values of ϕ_a , the velocity profile decreases. Behavior of $F'(\xi)$ for higher approximation of nonlinear thermal convection parameter $\widehat{\beta}_t$ is presented in Fig. 7.5. Motion of fluid particles boosts up for higher marks of nonlinear thermal convection parameter $\widehat{\beta}_t$. For greater approximation of $\widehat{\beta}_t$, the temperature difference $(T_w - T_\infty)$ intensifies which is responsible for upsurge in velocity distribution. Impact of velocity slip parameter S_v on $F'(\xi)$ is delineated through Fig. 7.6. Here the velocity $F'(\xi)$ decelerates versus velocity slip parameter S_v . In fact, the stretching of the sheet becomes a source of decrease in fluid flow that weaken the velocity field $F'(\xi)$ against velocity slip parameter S_v . Figs. (7.7 – 7.15) elaborates the influence of physical parameters such as S_1 , \widehat{N}_b , \widehat{N}_t , Pr , δ_e , \widehat{B}_1 and \widehat{B}_1 on temperature distribution $\theta(\xi)$. The

effect of thermal stratification parameter S_1 on fluid temperature $\theta(\xi)$ is identified in Fig. 7.7. This figure displays a decreasing fashion of temperature field for positive values of thermal stratification parameter. This tendency of curve is due to the existence of potential drop between cylindrical surface and ambient fluid. Enhancing trend of $\theta(\xi)$ is remarked for larger nonlinear thermal radiation parameter \widehat{N}_r (see Fig. 7.8). It strengthens the fact that radiation is a heat transfer mode that transmits the thermal energy through fluid particles. Figs. 7.9 and 7.10 are adorned to study the influence of Brownian motion \widehat{N}_b and thermophoresis parameter \widehat{N}_t on temperature $\theta(\xi)$. It can be seen that both parameters give rise in temperature $\theta(\xi)$. It holds because Brownian motion accelerates random motion i.e. fluid particles collision becomes rapid and hence these collisions produce more thermal energy. Also, as fluid particles rush from hot to cold region for higher thermophoresis parameter \widehat{N}_t due to increase in thermophoresis force (see Fig. 7.10). Influences of temperature ratio parameter θ_w on temperature $\theta(\xi)$ are examined through Fig. 7.11. This figure shows that fluid temperature rises by increasing θ_w . This is due to higher thermal state of liquid when compared with ambient temperature. Fig. 7.12 elucidates the effect of Pr on temperature distribution $\theta(\xi)$. One can observe that temperature $\theta(\xi)$ is a diminishing function of Pr. This response of temperature $\theta(\xi)$ against Pr is in line for weaker thermal diffusivity as compared to momentum diffusivity. Fig. 7.13 revealed the thermal relaxation time δ_e effects on fluid temperature. It is observed that temperature falls down versus δ_e . Due to rise in thermal relaxation time, particles require additional time for heat transmission to its adjacent particles. Figs. 7.14 and 7.15 portraits deviations in temperature against space dependent and temperature dependent heat source/sink parameters $(\widehat{B}_1, \widehat{B}_2)$. It is noticed that temperature $\theta(\xi)$ rises

for $\hat{B}_1 > 0$ and $\hat{B}_2 > 0$ while opposite behaviour is captured in case of $\hat{B}_1 < 0$ and $\hat{B}_2 < 0$. Figs. (7.16 – 7.22) are revealed to show the impact of γ_2 , S_2 , \hat{N}_b , \hat{N}_t , Sc , E_a and γ_3 on $\Phi(\xi)$. Impact of destructive chemical reaction variable $\gamma_2 > 0$ on concentration $\Phi(\xi)$ is pointed out in Fig. 7.16. Here $\Phi(\xi)$ and relevant boundary layer thickness are reduced for larger destructive chemical reaction variable $\gamma_2 > 0$. From Fig. 7.17, it is detected that $\Phi(\xi)$ is a decreasing function of solutal stratification parameter S_2 . In reality, reduction in concentration potential between ambient fluid and the cylindrical surface is identified hence, it reduces the concentration $\Phi(\xi)$ respectively. In Fig. 7.18 features of Brownian parameter \hat{N}_b on $\Phi(\xi)$ is presented. It is observed that concentration profile is a falling function of \hat{N}_b . Since fluid particles are pushed in opposite direction to the concentration gradient to make more homogeneous nanoparticle solution. Therefore, small concentration gradient value is noticed for greater values of \hat{N}_b . That eventually drops the concentration $\Phi(\xi)$. Decreasing features of concentration profile is found against larger Sc (see Fig. 7.19). This tendency is expected because larger Sc values leads to diminish the mass diffusivity. Increase in \hat{N}_t contributes higher fluid thermal conductivity which spectacles the higher concentration $\Phi(\xi)$ as seen in Fig. 7.20. The relationship between activation energy E_a and nanoparticle concentration for particular values of parameters is analyzed in Fig. 7.21. The modified Arrhenius function dwindles as activation energy E_a enlarges. This lastly endorses the generative chemical reaction due to which nanoparticle concentration $\Phi(\xi)$ upswings. Decreasing tend of $\Phi(\xi)$ is comprehended for larger γ_3 (see Fig. 7.22). Physically, as we enhance the values of γ_3 , the destructive rate of chemical reaction also grows which is used to terminate/dissolve the liquid species more effectively.

Table 7.1: Comparison of $\left(1 + \frac{1}{\lambda_c}\right)F''(0)$ with [117] for limiting case.

λ_c	M_1	$-\left(1 + \frac{1}{\lambda_c}\right)F''(0)$	
		Ref. [117]	Present
∞	0	1.0042	1.00001
5		-1.0954	-1.09545
1		-1.4142	-1.41426
∞	10	-3.3165	-3.31664
5		-3.6331	-3.63318
1		-4.6904	-4.69042
∞	100	-10.049	-10.04987
5		-11.0091	-11.00909
1		-14.2127	-14.21267

Table 7.2: Comparison of $Nu_z(Re_z)^{-\frac{1}{2}}$ with Refs. [118] and [119] in the limiting cases.

Pr.	Ref. [118]	Ref. [119]	Present
	(St = S ₁ = M ₁)	(E _a = γ_1 = 0)	$\left(\lambda_c \rightarrow \infty, \gamma_1 = S_1 = M_1 = \beta_1\right)$ $\left(= \hat{B}_1 = \hat{B}_2 = \hat{N}_r = 0\right)$
1.0	0.9547	0.9547	0.9547
2.0	1.4714	1.4714	1.4714
3.0	1.8961	1.8961	1.8962

Table 7.3: Numerical values of $\frac{1}{2}C_F(\text{Re}_{z_1})^{\frac{1}{2}}$ for various physical parameters.

γ_1	λ_c	β_1	M_1	S_1	E_a	S_2	$-\left(1 + \frac{1}{\lambda_c}\right)F''(0)$	
							Shooting	Bvp4c
0.2							2.1046	2.1046
0.4							3.0086	3.0086
0.6							4.0524	4.0524
	1.1						1.7580	1.7580
	1.3						1.7846	1.7846
	1.5						1.8077	1.8077
		0.1					1.6649	1.6649
		0.3					1.5278	1.5278
		0.5					1.3884	1.3884
			0.2				1.5675	1.5675
			0.4				1.7968	1.7968
			0.6				1.9654	1.9654
				0.1			1.7456	1.7456
				0.3			1.7698	1.7698
				0.5			1.7864	1.7864
					0.4		1.9789	1.9789
					0.8		1.4876	1.4876
					1.2		1.0754	1.0754
						0.2	1.7487	1.7487
						0.4	1.7356	1.7356
						0.6	1.7245	1.7245

Table 7.4: Numerical values of $Nu_z(Re_z)^{-\frac{1}{2}}$ for various physical parameters.

γ_1	λ_c	\hat{N}_r	δ_e	S_1	E_a	\hat{B}_1	$-Nu_z(Re_z)^{-\frac{1}{2}}$	
							Shooting	Bvp4c
0.2							0.6254	0.6254
0.4							0.7367	0.7367
0.6							0.8498	0.8498
	1.1						0.7568	0.7568
	1.3						0.7365	0.7365
	1.5						0.7149	0.7149
		1.0					0.7857	0.7857
		2.0					0.7286	0.7286
		3.0					0.6394	0.6394
			0.3				0.7465	0.7465
			0.5				0.7389	0.7389
			0.7				0.7266	0.7266
				0.2			0.7465	0.7465
				0.4			0.7387	0.7387
				0.6			0.7259	0.7259
					0		0.8854	0.8854
					1		1.0657	1.0657
					2		1.8784	1.8784
						0.1	0.7593	0.7593
						0.3	0.7048	0.7048
						0.5	0.6532	0.6532

Table 7.5: Numerical values of $Sh_z(Re_z)^{-\frac{1}{2}}$ for various physical parameters.

γ_1	Sc	\hat{N}_b	\hat{N}_t	S_2	E_a	γ_3	$-Sh_z(Re_z)^{-\frac{1}{2}}$	
							Shooting	Bvp4c
0.2							0.5473	0.5473
0.4							0.6537	0.6537
0.6							0.7265	0.7264
	0.1						0.4872	0.4872
	0.5						0.5438	0.5438
	1.0						0.6679	0.6678
		0.3					0.6278	0.6278
		0.5					0.7256	0.7256
		0.7					0.7483	0.7482
			0.3				0.5867	0.5866
			0.5				0.4259	0.4259
			0.7				0.3765	0.3764
				0.2			0.4573	0.4573
				0.4			0.5246	0.5246
				0.6			0.6375	0.6375
					0.4		0.7854	0.7853
					0.6		0.7736	0.7736
					1.2		0.7523	0.7522
						0.1	0.7871	0.7871
						0.5	0.8534	0.8534
						1.0	0.9657	0.9656

7.5 Graphical outcomes

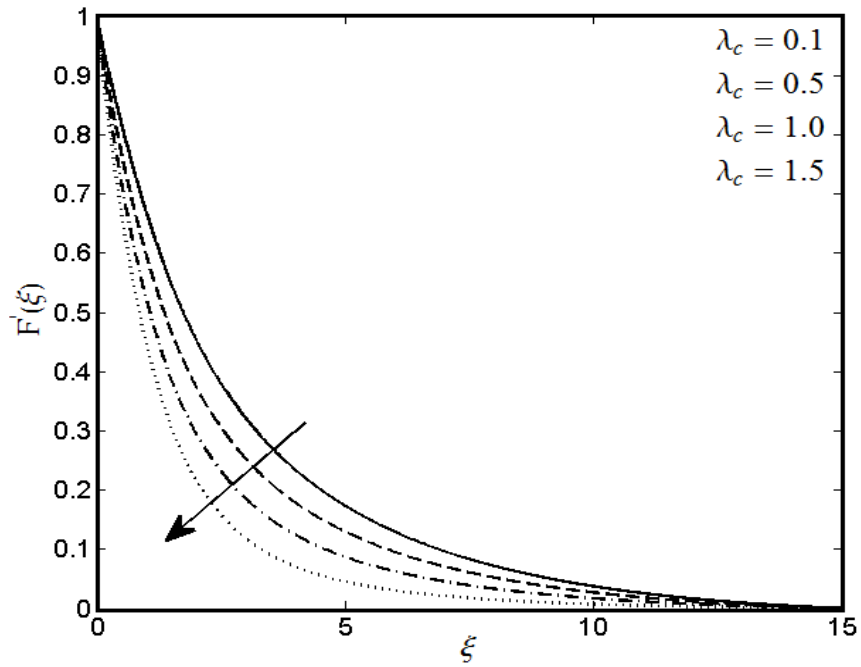


Fig. 7.2: Response of $F'(\xi)$ with λ_c .

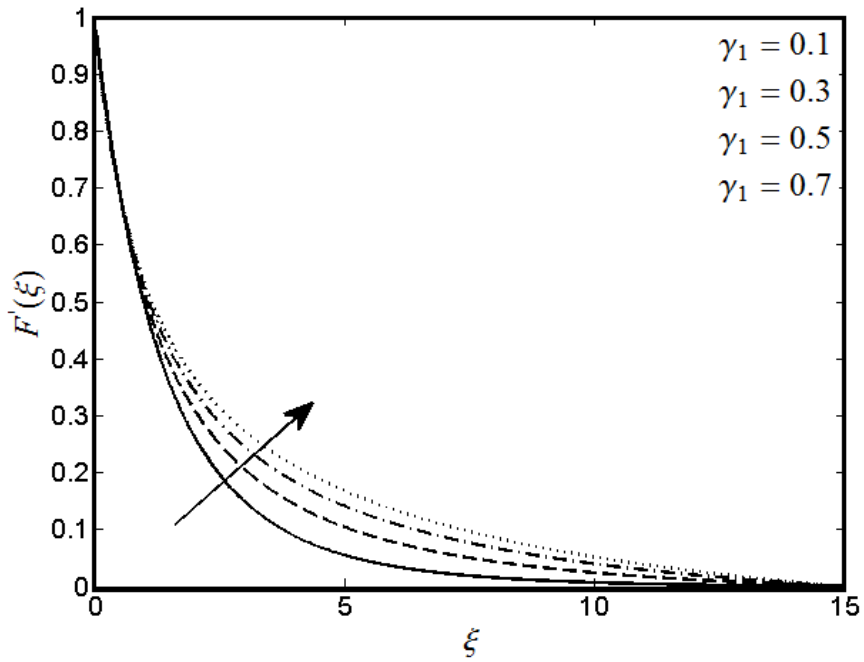


Fig. 7.3: Response of $F'(\xi)$ with γ_1 .

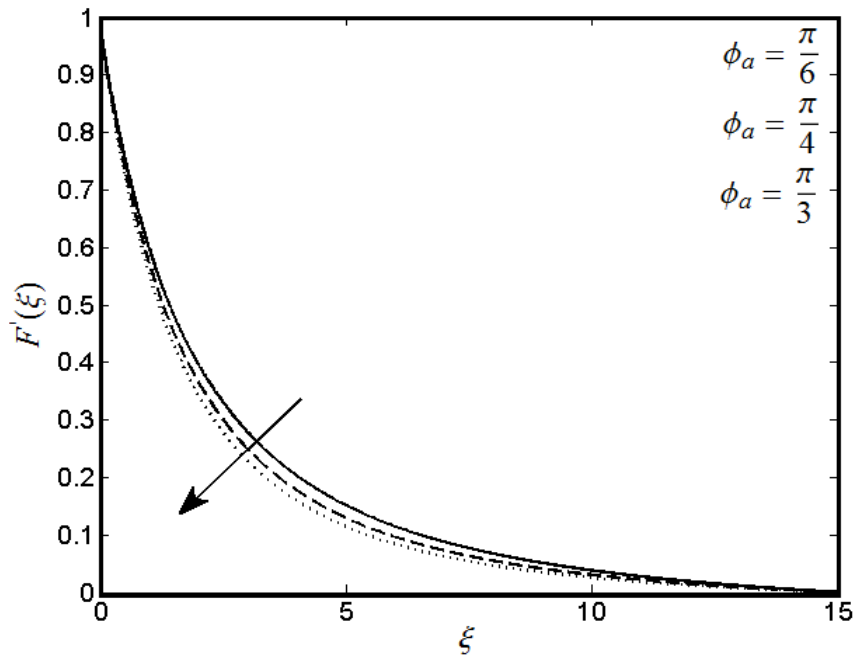


Fig. 7.4: Response of $F'(\xi)$ with ϕ_α .

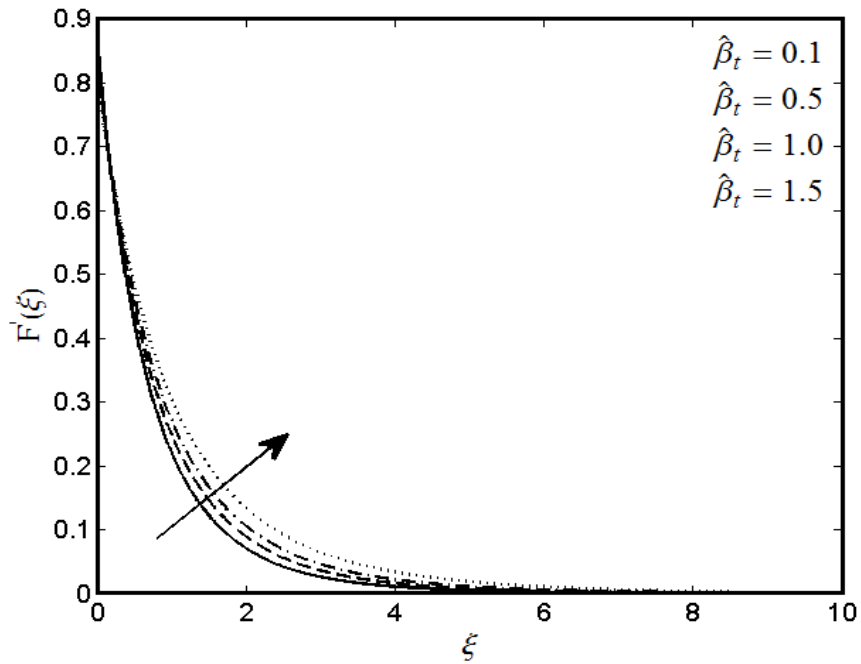


Fig. 7.5: Response of $F'(\xi)$ with $\hat{\beta}_t$.

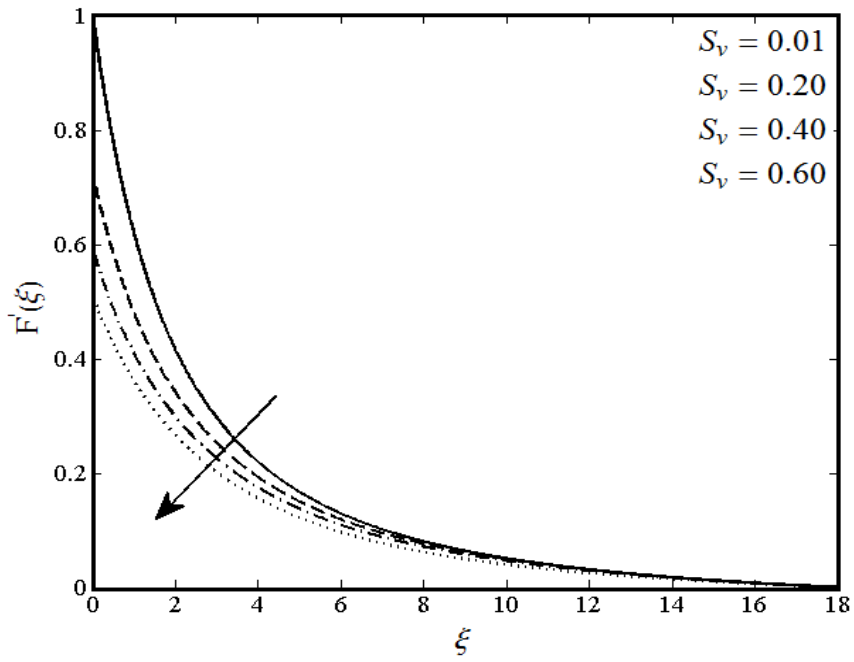


Fig. 7.6: Response of $F'(\xi)$ with S_v .

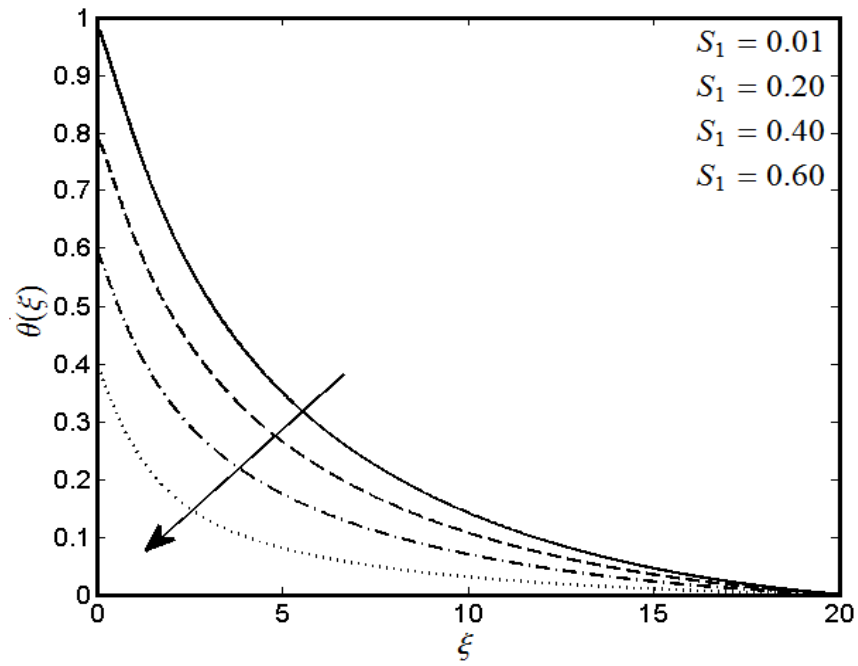


Fig. 7.7: Response of $\theta(\xi)$ with S_1 .

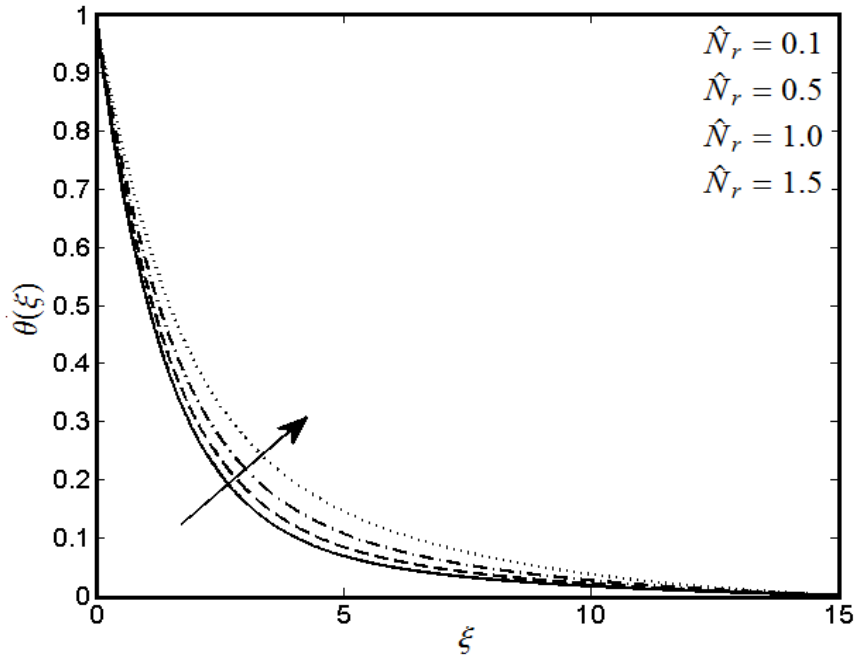


Fig. 7.8: Response of $\theta(\xi)$ with \hat{N}_r .

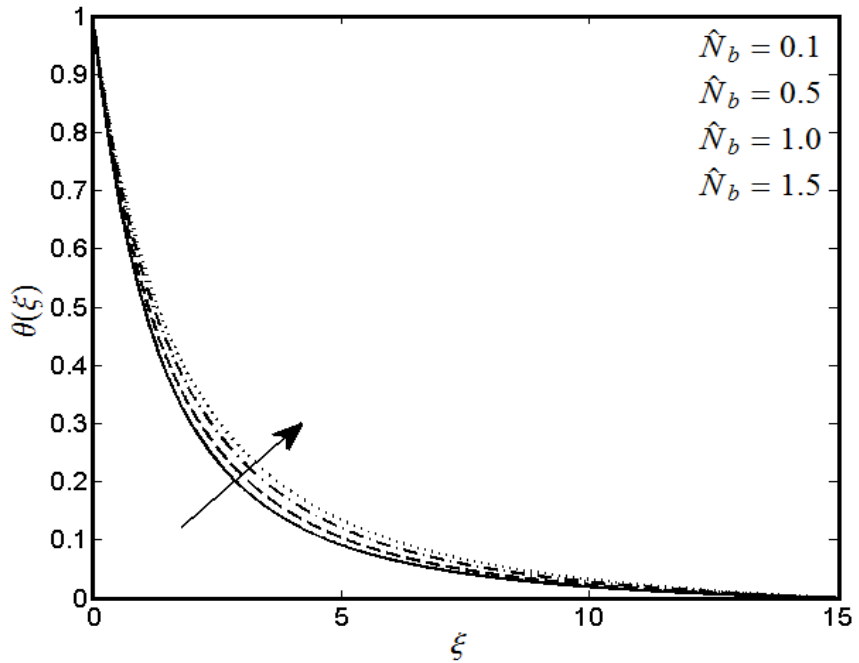


Fig. 7.9: Response of $\theta(\xi)$ with \hat{N}_b .

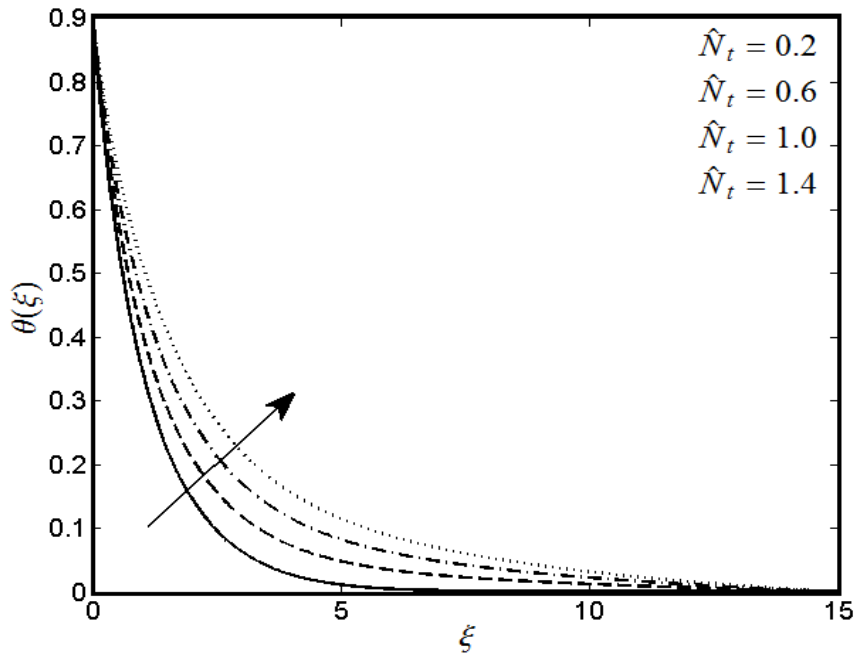


Fig. 7.10: Response of $\theta(\xi)$ with \hat{N}_t .

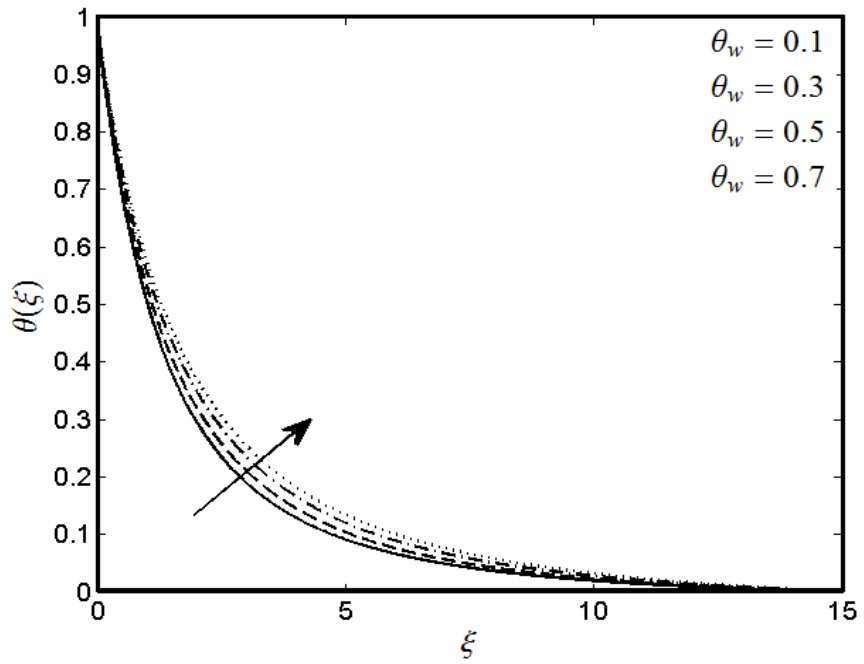


Fig. 7.11: Response of $\theta(\xi)$ with θ_w .

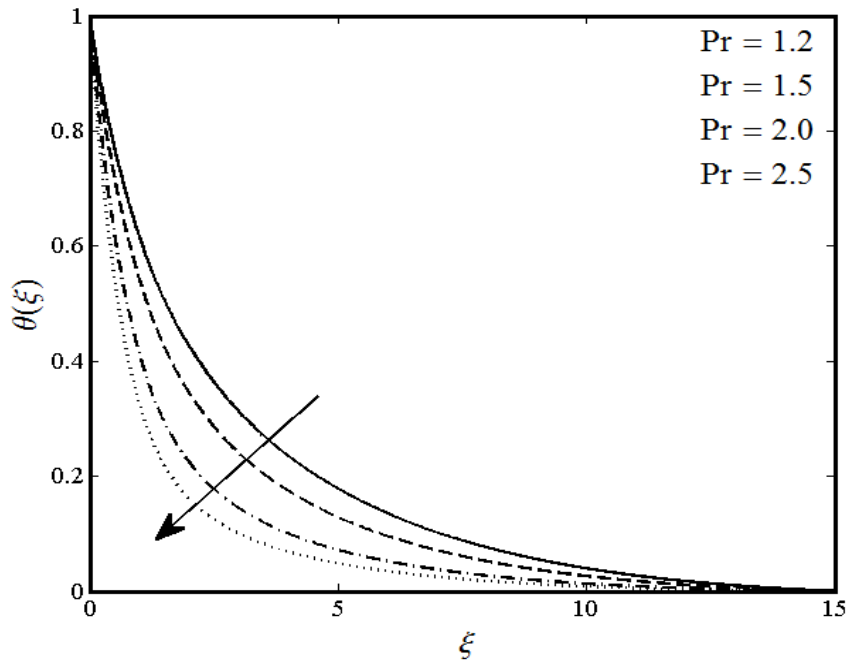


Fig. 7.12: Response of $\theta(\xi)$ with Pr .

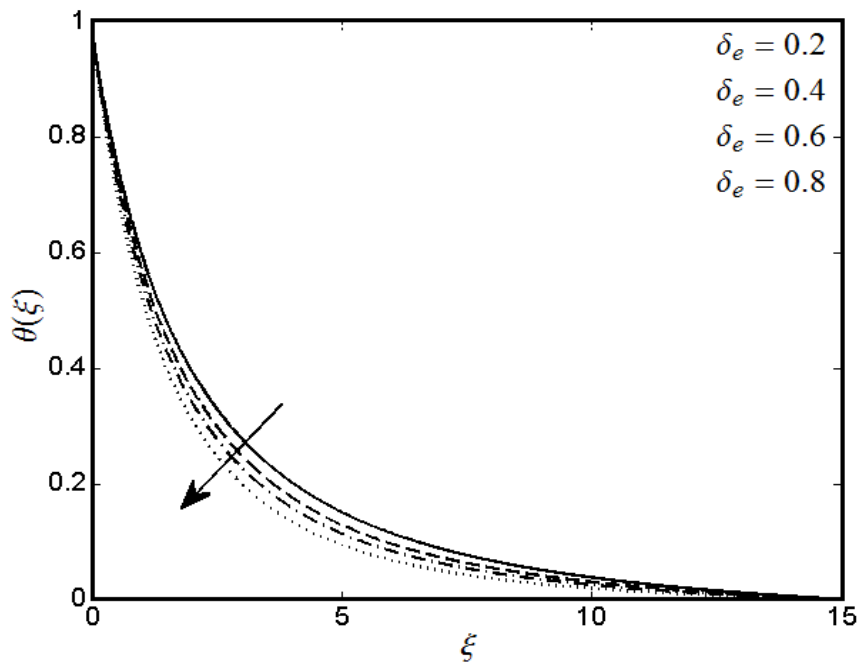


Fig. 7.13: Response of $\theta(\xi)$ with δ_e .

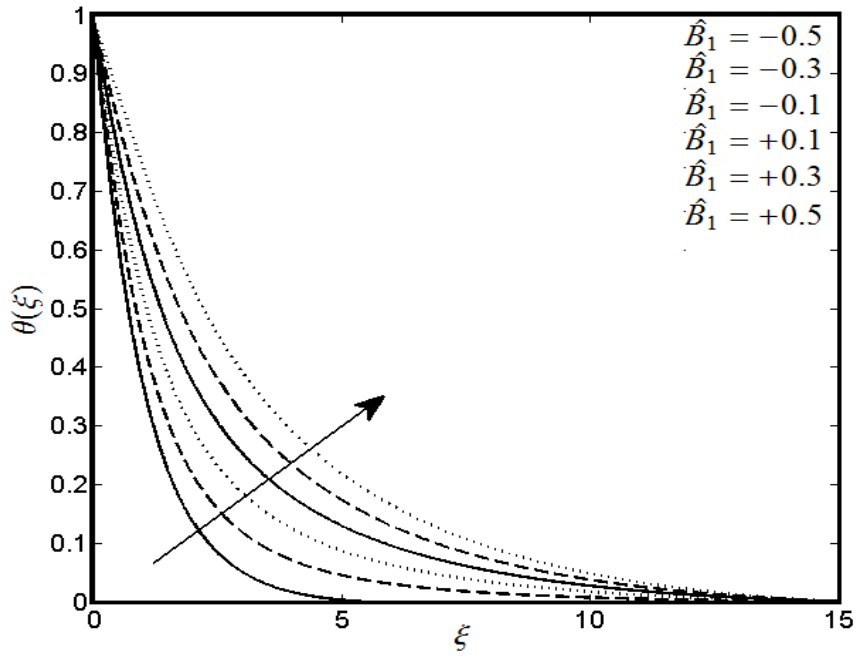


Fig. 7.14: Response of $\theta(\xi)$ with \hat{B}_1 .

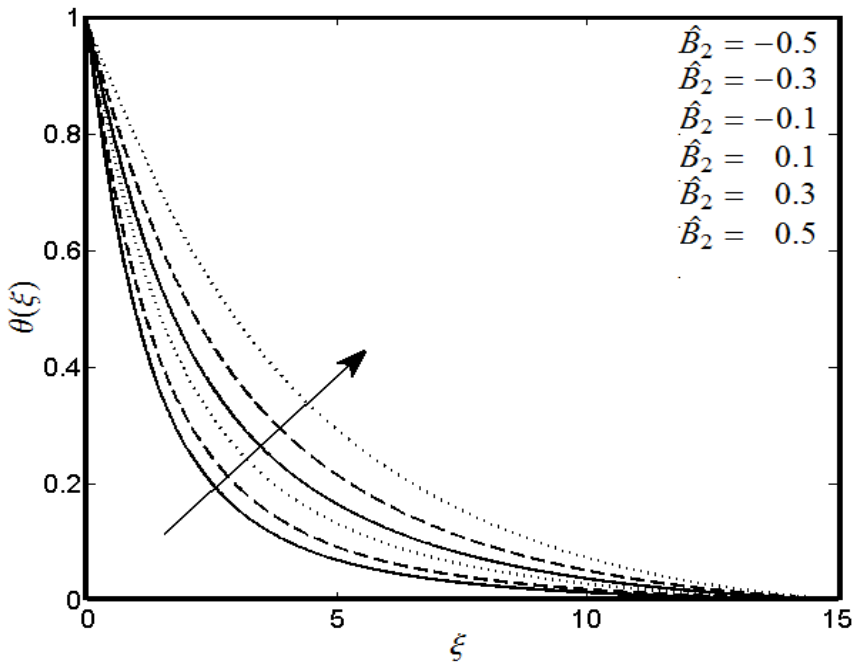


Fig. 7.15: Response of $\theta(\xi)$ with \hat{B}_2 .

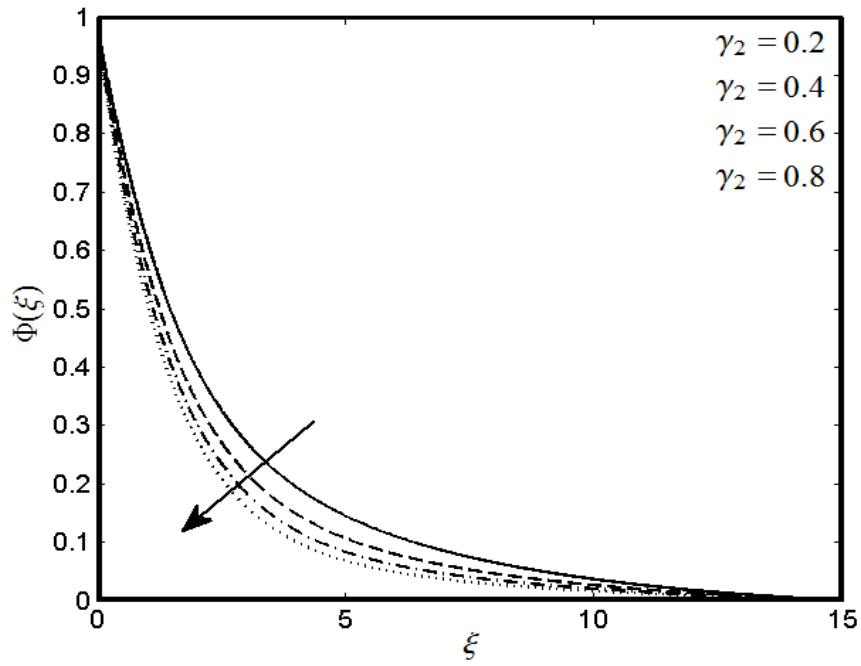


Fig. 7.16: Response of $\Phi(\xi)$ with γ_2 .

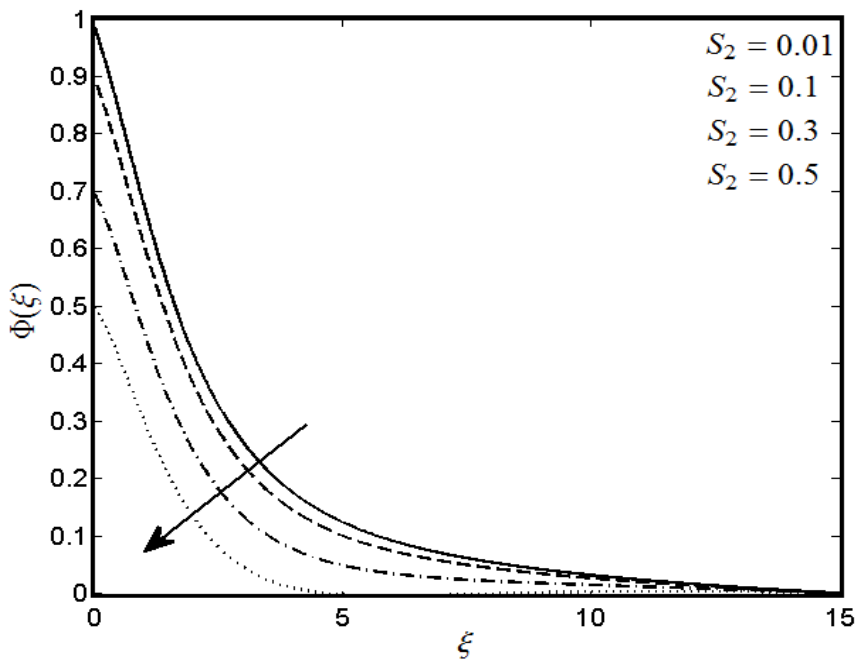


Fig. 7.17: Response of $\Phi(\xi)$ with S_2 .

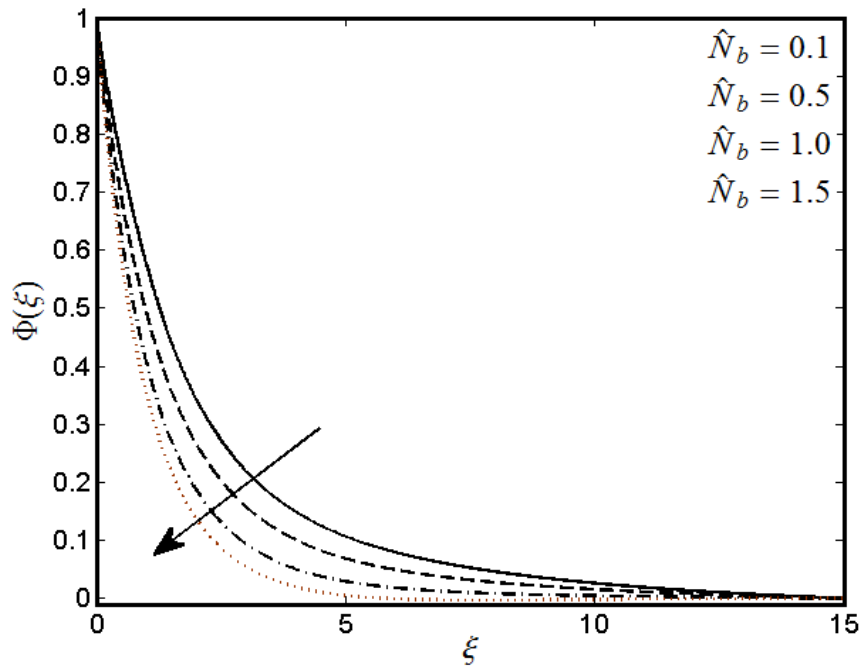


Fig. 7.18: Response of $\Phi(\xi)$ with \hat{N}_b .

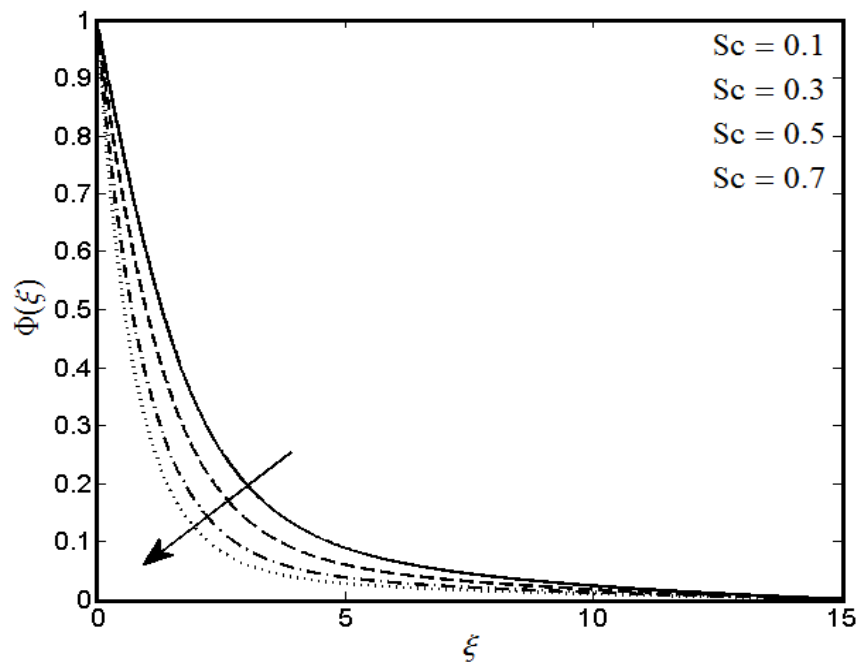


Fig. 7.19: Response of $\Phi(\xi)$ with Sc .

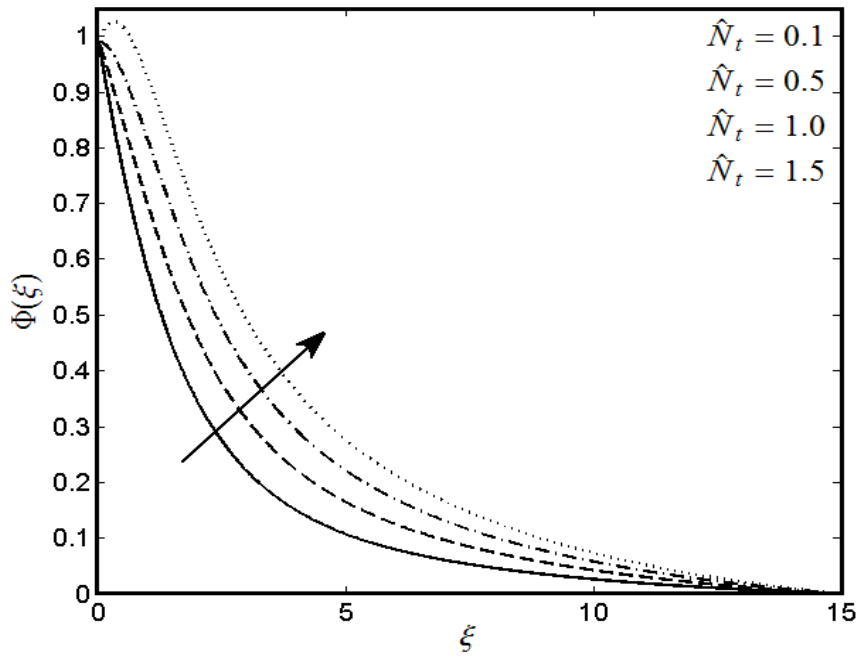


Fig. 7.20: Response of $\Phi(\xi)$ with \hat{N}_t .

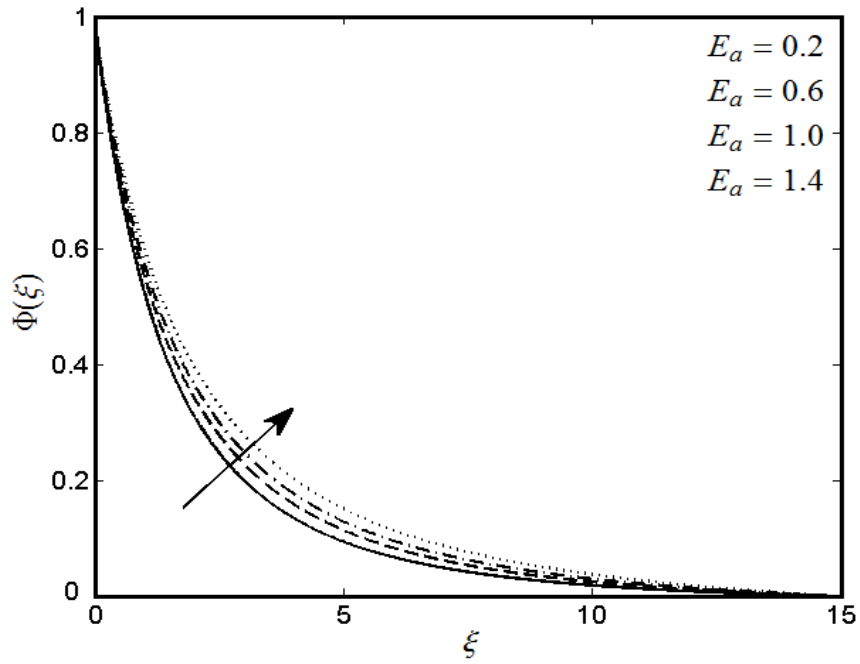


Fig. 7.21: Response of $\Phi(\xi)$ with E_a .

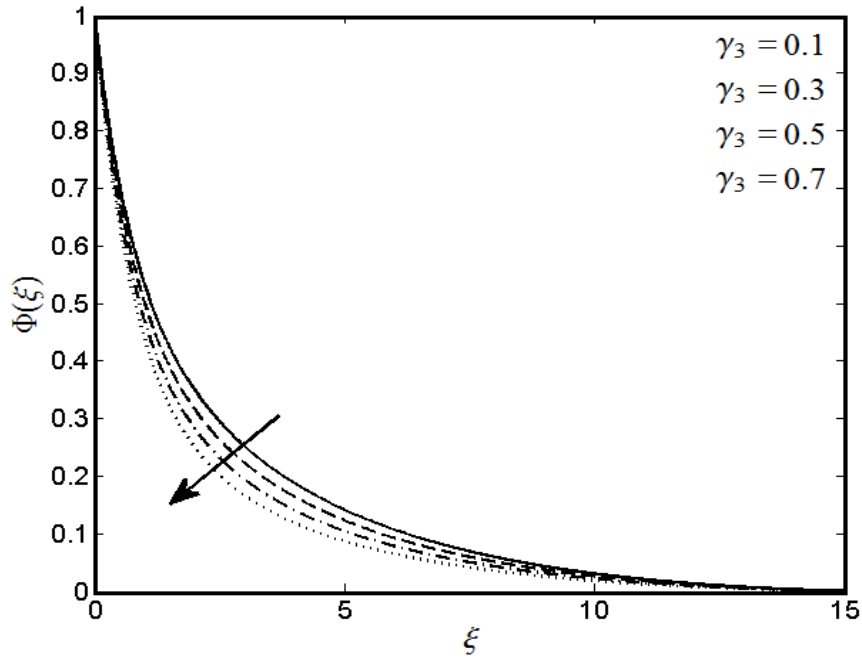


Fig. 7.22: Response of $\Phi(\xi)$ with γ_3 .

7.6 Conclusions

A numerical analysis is presented to investigate the influence of slip boundary conditions on a nonlinearly radiative flow of Casson nanofluid with novel impacts of activation energy, non-uniform heat generation/absorption and binary chemical reaction. Heat transfer for current problem is investigated through Cattaneo-Christove heat flux model with thermal and solutal stratification phenomena. Numerical solution of transformed system is achieved by using shooting technique. The key observations are summarized as follows:

- Nanoparticle concentration is an enhancing function of activation energy E_a for chemical reaction and thermophoresis parameter \widehat{N}_t . Additionally, the response of chemical reaction parameter γ_3 is qualitatively opposite to that of E_a

- An enhancement in non-uniform heat generation/absorption parameters (\hat{B}_1, \hat{B}_2) , Brownian motion and thermophoresis parameters (\hat{N}_b, \hat{N}_t) become a source of rise in temperature distribution while greater approximation of Prandlt number Pr and thermal relaxation parameter δ_e generates fall in temperature field.
- Temperature and concentration fields are dwindling functions of thermal and solutal stratification parameters (S_1, S_2) , respectively.
- Heat transfer rate at the cylindrical surface and thermal boundary layer thickness enhances in presence of thermal radiation \hat{N}_r .
- Sherwood number has contrary behavior for larger E_a and γ_3 .

CHAPTER 8

Stratified flow of ferromagnetic nanofluid with heat generation/absorption

8.1 Introduction

The objective of existing article is to analyze the effects of non-uniform heat source/sink and magnetic dipole in flow of ferromagnetic Maxwell liquid over a stretched sheet. Highlights of Brownian movement and thermophoresis are explored within the sight of magnetic dipole. Effects of thermal and concentration stratification are additionally considered. Apposite transformations are employed to obtain the nonlinear differential system. The procured nonlinear framework is locked in numerically with the assistance of shooting technique. Velocity and temperature gradients are discussed and analysed in detail through graphs and tables.

8.2 Mathematical formulation

Consider an incompressible Maxwell ferromagnetic fluid with dual stratification phenomena over a linearly stretched sheet. The stretching of sheet is directly proportional to the distance from the origin. Heat transfer analysis is examined through viscous dissipation. The present investigation is carried out in addition to Brownian motion,

thermophoresis and viscous dissipation. Further, magnetic dipole of adequate strength is positioned at some distance (a) below the x -axis and centered at y -axis (see Fig. 8.1). The direction of magnetic field is taken along positive x -direction. Here Curie temperature T_c is taken to be greater than the temperature at stretched surface T_w , otherwise, $T = T_c$ is temperature far from surface that follows $T_w < T < T_c$. The liquid above T_c is inadequate of being magnetized. Here variable temperature $T_w = T_0 + d_1x$ and $T_c = T_0 + d_2x$ are scrutinized at the sheet distant from the surface. The boundary layer equations in a ferrofluid flow and heat transfer rate are as follow:

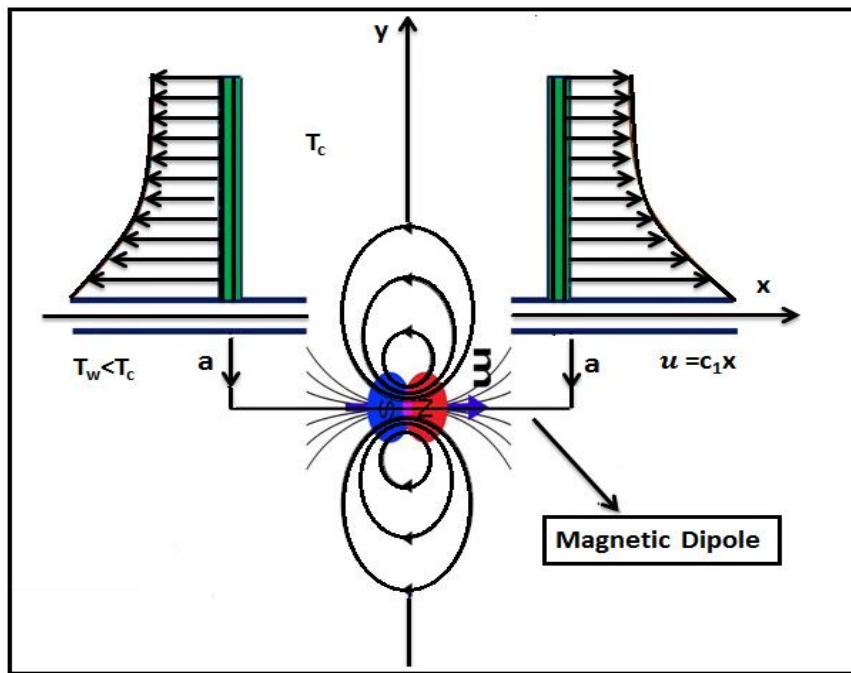


Fig. 8.1: Physical model.

$$\frac{\partial u}{\partial x} + \frac{\partial v}{\partial y} = 0, \quad (8.1)$$

$$u \frac{\partial u}{\partial x} + v \frac{\partial u}{\partial y} = \nu_1 \frac{\partial^2 u}{\partial y^2} + \frac{\lambda_m}{\rho_f} \left(u^2 \frac{\partial^2 u}{\partial x^2} + 2uv \frac{\partial^2 u}{\partial x \partial y} + v^2 \frac{\partial^2 u}{\partial y^2} \right) + \frac{\zeta_0 M_1}{\rho_f} \frac{\partial \mathbf{H}}{\partial x}, \quad (8.2)$$

$$u \frac{\partial T}{\partial x} + v \frac{\partial T}{\partial y} + \left(u \frac{\partial \mathbf{H}}{\partial x} + v \frac{\partial \mathbf{H}}{\partial y} \right) \frac{\zeta_0 T}{\rho_f} \frac{\partial M_1}{\partial T} = \alpha^* \frac{\partial^2 T}{\partial y^2} + \frac{\hat{Q}_m}{(\rho C_p)_f} + \hat{\tau}_1 \left(D_B \frac{\partial C}{\partial y} \frac{\partial T}{\partial y} + \frac{D_T}{T_c} \left(\frac{\partial T}{\partial y} \right)^2 \right) + \frac{\mu}{(\rho C_p)_f} \left(\frac{\partial u}{\partial y} \right)^2, \quad (8.3)$$

$$u \frac{\partial C}{\partial x} + v \frac{\partial C}{\partial y} = D_B \frac{\partial^2 C}{\partial y^2} + \frac{D_T}{T_c} \frac{\partial^2 T}{\partial y^2}. \quad (8.4)$$

The boundary conditions are

$$u = U_w = c_1 x, v = 0, \quad T = T_w = T_0 + d_1 x, \quad C = C_w = C_0 + d_3 x \quad \text{at } y = 0, \quad (8.5)$$

$$u \rightarrow 0, \quad v \rightarrow 0, \quad T \rightarrow T_c = T_0 + d_2 x, \quad C \rightarrow C_c = C_0 + d_4 x. \quad \text{when } y \rightarrow \infty. \quad (8.6)$$

The time dependent non-uniform heat source/sink \hat{Q}_m [120] is considered as

$$\hat{Q}_m = \frac{U_w(x) \hat{k}_1}{x \nu_1} \left[\hat{B}_1 (T_w - T_0) \frac{\partial F}{\partial \xi} + \hat{B}_2 (T - T_c) \right], \quad (8.7)$$

in the above equation positive values ($\hat{B}_1 > 0$ and $\hat{B}_2 > 0$) corresponds to heat generation and negative values ($\hat{B}_1 < 0$ and $\hat{B}_2 < 0$) resembles to the heat absorption.

8.3 Magnetic Potential

The features of magnetic field influence the ferrofluid flow due to a magnetic dipole. Such impacts of magnetic dipole are pronounced by a magnetic scalar potential Ω_1 , which is demonstrated as [121]

$$\Omega_1 = \frac{\alpha}{2\pi} \frac{x}{[x^2 + (y + a)^2]} \quad (8.8)$$

The components of scalar potential of magnetic dipole are

$$\frac{\partial H}{\partial x} = -\frac{\partial \Omega_1}{\partial x} = \frac{\alpha}{2\pi} \frac{x^2 - (y + a)^2}{[x^2 + (y + a)^2]^2}, \quad (8.9)$$

$$\frac{\partial H}{\partial y} = -\frac{\partial \Omega_1}{\partial y} = \frac{\alpha}{2\pi} \frac{2x(y + a)}{[x^2 + (y + a)^2]^2}. \quad (8.10)$$

Since the magnetic body force is (generally) proportional to the gradient of the magnetic of H , we thus have

$$H = \sqrt{\left(\frac{\partial \Omega_1}{\partial x}\right)^2 + \left(\frac{\partial \Omega_1}{\partial y}\right)^2}, \quad (8.11)$$

by utilizing Eqs. (8.9) and (8.10) in Eq. (8.11), we obtain the following equations, after expanded in powers of x and retained terms up to order x^2

$$\frac{\partial H}{\partial x} = -\frac{\alpha}{2\pi} \frac{2x}{(y + a)^4}, \quad (8.12)$$

$$\frac{\partial H}{\partial y} = \frac{\alpha}{2\pi} \left[-\frac{2}{(y + a)^3} + \frac{4x^2}{(y + a)^5} \right]. \quad (8.13)$$

The approximation of magnetization M_1 through temperature T is estimated by

$$M_1 = \widehat{K}_2(T - T_c). \quad (8.14)$$

Here, \widehat{K}_2 identifies as pyromagnetic coefficient.

8.4 Methodology

By invoking following transformations [122]

$$\begin{aligned} u &= c_1 x F'(\xi), \quad v = -\sqrt{\frac{c_1 \mu}{\rho}} F(\xi), \quad \Psi_1 = \frac{\mu \xi_1 F(\xi)}{\rho}, \\ \xi &= \sqrt{\frac{c_1 \mu}{\rho}} y, \quad \theta(\xi_1, \xi) = \frac{T_c - T}{T_c - T_w} = \theta_1(\xi) + \xi_1^2 \theta_2(\xi), \\ \xi_1 &= \sqrt{\frac{c_1 \mu}{\rho}} x, \quad \Phi(\xi_1, \xi) = \frac{C_c - C}{C_c - C_w} = \Phi_1(\xi) + \xi_1^2 \Phi_2(\xi). \end{aligned} \quad (8.15)$$

Employing the boundary layer approximation and utilizing similarity variables given in Eq. (8.15), the Eqs. (8.2) – (8.4) along with stated boundary conditions given in Eq. (8.5) reduces to the following system of equations

$$F''' + FF'' - F'^2 + M_e(F'''F^2 - 2FF'F'') - \frac{2\lambda_f \theta_1}{(\xi + \alpha_1)^4} = 0, \quad (8.16)$$

$$\begin{aligned} \theta_1'' + Pr(F\theta_1' - 2F'\theta_1) + (\widehat{B}_1 F' + \widehat{B}_2 \theta_1) + \frac{2\lambda_f \lambda_v F(\theta_1 - \varepsilon_1)}{(\xi + \alpha_1)^3} \\ + Pr \widehat{N}_b \left(\theta_1' \Phi_1' + \frac{\widehat{N}_t}{\widehat{N}_b} \theta_1'^2 \right) - Pr S_1 F' - 4\lambda_v F'^2 = 0, \end{aligned} \quad (8.17)$$

$$\begin{aligned} \theta_2'' - Pr(4F'\theta_2 - F\theta_2') + Pr \widehat{N}_b (\theta_2' \Phi_1' + \theta_1' \Phi_2') - \lambda_v F''^2 + \frac{2\lambda_f \lambda_v F \theta_2}{(\xi + \alpha_1)^3} \\ + \widehat{B}_2 \theta_2 + 2Pr \widehat{N}_t \theta_1' \theta_2' - \lambda_f \lambda_v (\theta_1 - \varepsilon_1) \left(\frac{2F'}{(\xi + \alpha_1)^4} + \frac{4F}{(\xi + \alpha_1)^5} \right) = 0, \end{aligned} \quad (8.18)$$

$$\Phi_1'' + \frac{\hat{N}_t}{\hat{N}_b} \theta_1'' - PrLeF'\Phi_1 + ScF\Phi_1' - PrLeS_2F' = 0, \quad (8.19)$$

$$\Phi_2'' + \frac{\hat{N}_t}{\hat{N}_b} \theta_2'' - 3PrLeF'\Phi_2 + ScF\Phi_2' = 0, \quad (8.20)$$

with

$$\begin{aligned} F(0) = 0, \quad F'(0) = 1, \quad \theta_1(0) = 1 - S_1, \\ \theta_2(0) = 0, \quad \Phi_2(0) = 0, \quad \Phi_1(0) = 1 - S_2, \end{aligned} \quad (8.21)$$

$$F'(\infty) = 0, \quad \theta_1(\infty) = 0, \quad \theta_2(\infty) = 0, \quad \Phi_1(\infty) = 0, \quad \Phi_2(\infty) = 0. \quad (8.22)$$

Mathematically, the non-dimensional governing parameters are defined as follows:

$$\begin{aligned} \lambda_f &= \frac{\alpha \zeta_0 \hat{K}_2 \rho (T_0 - T_w)}{2\pi \mu^2}, & \lambda_v &= \frac{c_1 \mu^2}{\rho \hat{k}_1 (T_0 - T_w)}, & \alpha_1 &= \sqrt{\frac{c_1 \rho a^2}{\mu}} \\ \hat{N}_1 &= \frac{\Gamma_3 (C_w - C_0)}{\Gamma_1 (T_w - T_0)}, & \varepsilon_1 &= \frac{T_c}{T_w - T_0}, & Le &= \frac{\alpha^*}{D_B}, \\ \hat{N}_t &= \frac{\tau_1 D_T (T_w - T_0)}{T_c \nu_1}, & M_e &= \lambda_m c_1, & Pr &= \frac{\mu C_p}{\hat{k}_1}, \\ \hat{N}_b &= \frac{\tau_1 D_B (C_w - C_0)}{\nu_1}, & S_1 &= \frac{d_2}{d_1}, & S_2 &= \frac{d_4}{d_3}. \end{aligned} \quad (8.23)$$

The skin friction coefficient C_F , local Nusselt Nu_x and Sherwood Sh_x numbers are

$$C_F = \frac{2\tau_w}{\rho U_w^2}, \quad Nu_x = \frac{xq_w}{\hat{k}_1 (T_w - T_0)}, \quad Sh_x = \frac{xj_w}{D_B (C_w - C_0)}. \quad (8.24)$$

In dimensionless form, we have

$$\begin{aligned} C_F (Re_x)^{\frac{1}{2}} &= -2F''(0), \\ Nu_x (Re_x)^{-\frac{1}{2}} &= -[\theta_1'(0) + \xi_1^2 \theta_2'(0)], \\ Sh_x (Re_x)^{-\frac{1}{2}} &= -[\Phi_1'(0) + \xi_1^2 \Phi_2'(0)]. \end{aligned} \quad (8.25)$$

8.5 Results and discussion

Here the effects of elasticity parameter M_e , Prandtl number Pr , ferrohydrodynamic interaction parameter λ_f , Brownian parameter \widehat{N}_b , dimensionless temperature ε_1 , Schmidt number Sc , thermophoresis variable \widehat{N}_t , thermal stratification parameter S_1 , space and temperature based source/sink parameters $(\widehat{B}_1, \widehat{B}_2)$ and Lewis number Le on velocity $F'(\xi)$, temperature $\theta(\xi)$ and concentration $\Phi(\xi)$ are studied. Table (8.1) conveys the computational results of Nusselt number against certain physical factors. Here heat transfer rate enriches for greater \widehat{N}_b , λ_f , M_e and Sc while it declines for ε_1 , \widehat{N}_t and α_1 . Table (8.2) provides outcomes of Sherwood number against different physical variables. It is observed that mass transfer rate improves for growing values of α_1 , λ_f and Pr , while it declines for increasing λ_v and \widehat{N}_t . Figs. (8.2 – 8.4) are revealed to display the effect of M_e and λ_f on $F'(\xi)$. Impacts of elasticity parameter M_e are marked in Fig. 8.2. For greater M_e velocity $F'(\xi)$ advances progressively, the outcome designates that velocity and apposite boundary layer becomes thicker with a rise in M_e . It is pondered that response velocity ascends by incrementing elastic force of system. Surface forces ranges to its lowest value for $M_e = 0$. That defines the absence of internal elastic force due to which the fluid moderates to Newtonian fluid. Fig. 8.3 inspects the declining trend of $F'(\xi)$ for higher values of ferromagnetic parameter λ_f . Physically higher values of λ_f provide additional resistance to fluid flow. Hence $F'(\xi)$ reduces. Figs. (8.5 – 8.12) are sketched out to investigate the temperature profile $\theta_1(\xi)$ for various estimations of λ_v , Pr , λ_f , S_1 , \widehat{N}_b and \widehat{N}_t . Fig. 8.5 displays the effect of Eckert number Ec on $\theta_1(\xi)$. For larger value of Ec , temperature $\theta_1(\xi)$ is found to be heightens near the surface. For

greater Ec additional inner energy of liquid produces rise in $\theta_1(\xi)$. Variation of Pr on $\theta_1(\xi)$ is displayed in Fig. 8.6. Here greater appraisal of Pr corresponds to lessen the temperature field. In fact, higher Pr relates to greater momentum diffusion and thinner thermal layer. That results in reduction of $\theta_1(\xi)$. It is notified from Fig. 8.7 that for expanding estimations of λ_f relate to higher temperature field $\theta_1(\xi)$. Physically for bigger λ_f resistive force (Lorentz compel) improves and along these lines $\theta_1(\xi)$ increases. The role of thermal stratified parameter S_1 against $\theta_1(\xi)$ is presented in Fig. 8.8. It is noted that both temperature and thermal boundary layer are diminished for higher S_1 . Due to rise in S_1 , the temperature difference (between sheet, ambient fluid) is reduced that result in weaker temperature profile and apposite thermal boundary thickness. Figs. 8.9 and 8.10 are displayed to know the nature of $\theta_1(\xi)$ for distinct values of heat source/sink parameters \hat{B}_1 and \hat{B}_2 . Enhancing nature of $\theta_1(\xi)$ is noticed for both parameters \hat{B}_1 and \hat{B}_2 . Scientifically, higher estimation of \hat{B}_1 increases the boundary layer thickness and hence it acts as an agent to generate heat. Due to this reason, an amplification in $\theta_1(\xi)$ is perceived for higher \hat{B}_1 (see Fig. 8.9). Impact of \hat{N}_b and \hat{N}_t on $\theta_1(\xi)$ is displayed in Fig. 8.11 and 8.12. Similar conduct of \hat{N}_b and \hat{N}_t is observed for $\theta_1(\xi)$ and related layer thickness. In fact, additional heat is created through the random motion of fluid particles inside the frame of larger Brownian motion parameter \hat{N}_b . Consequently, $\theta_1(\xi)$ increases. Movement of liquid particles ascends from hot to cool locations in the framework for bigger \hat{N}_t . It is expected an expansion in thermophoresis force and therefore the temperature profile builds up (see Fig. 8.12). Figs. (8.13 – 8.16) scrutinize the behavior of concentration $\Phi_1(\xi)$ against Le , Sc , \hat{N}_b and \hat{N}_t . Effect of Lewis number Le on $\Phi_1(\xi)$ is plotted in Fig. 8.13. It is notice that

increase in Lewis number Le leads to decrease in $\Phi_1(\xi)$. Behavior of Sc on $\Phi_1(\xi)$ is exposed in Fig. 8.14. Here $\Phi_1(\xi)$ is decreasing function of Sc . Physically Sc enhances momentum diffusivity and thus concentration curve decreases. Figs. 8.15 and 8.16 are designed to study the concentration $\Phi_1(\xi)$ for larger Brownian parameter \widehat{N}_b and thermophoresis parameter \widehat{N}_t . It is noticed from Fig. 8.15 that concentration $\Phi_1(\xi)$ reduces with rise in Brownian parameter \widehat{N}_b . Physically, \widehat{N}_b improves Brownian diffusion rate and as a result $\Phi_1(\xi)$ diminishes. For greater \widehat{N}_t concentration $\Phi_1(\xi)$ increases (see Fig. 8.16). As higher \widehat{N}_t offer ascent to thermal conductivity of the fluid that ultimately produces enhancement in $\Phi_1(\xi)$. Fig. 8.17 depicts the total averaged squared residual error $E_{m,tot}$ at different orders of approximations m .

Table 8.1: Numerical values of $-C_F(\text{Re}_x)^{\frac{1}{2}}$ for various physical parameters.

λ_f	S_1	M_e	Pr	$-C_F(\text{Re}_x)^{\frac{1}{2}}$
1.0	0.2	0.5	1.2	1.2975
				1.5033
3.0	0.2	0.5	1.2	1.6122
	0.4			1.2975
	0.6			1.3044
1.0	0.2	0.1	1.2	1.3189
		0.5		1.3175
1.0	0.2	1.0	1.2	1.2975
			2.2	1.2747
			3.2	1.2975

Table 8.2: Numerical values of $-Nu_x(\text{Re}_x)^{-\frac{1}{2}}$ for various physical parameters.

λ_f	λ_v	\hat{N}_b	\hat{N}_t	\hat{B}_1	α_1	ε_1	M_e	Pr	$-Nu_x(Re_x)^{-\frac{1}{2}}$
0.2	0.4	0.2	0.2	0.3	0.2	0.1	0.5	1.2	0.690618
	0.4								0.649362
	0.6								0.608331
		0.1							0.684573
		0.3							0.678502
		0.5							0.672406
			0.2						0.710402
			0.3						0.730151
			0.4						0.750126
				0.1					0.704658
				0.2					0.717790
				0.3					0.729936
					0.1				0.689512
					0.3				0.689262
					0.5				0.688432
						0.2			0.706592
						0.4			0.715294
						0.6			0.720367
							0.1		0.693605
							0.2		0.696584
							0.3		0.699562
								0.1	0.696195
								0.5	0.694292
								1.0	0.692434
								0.5	0.726713
								1.0	0.762634
								1.2	0.798277

Table 8.3: Numerical values of $-Sh_x(Re_x)^{-\frac{1}{2}}$ for various physical parameters.

λ_f	λ_v	\hat{N}_b	\hat{N}_t	\hat{B}_1	α_1	ε_1	M_e	Pr	$-Sh_x(Re_x)^{-\frac{1}{2}}$
0.2	0.4	0.2	0.2	0.3	0.2	0.1	0.5	1.2	0.487562
	0.4								0.486294
	0.6								0.484172
	0.1								0.487403
	0.3								0.488204
	0.5								0.488562
		0.2							0.475904
		0.3							0.478485
		0.4							0.480266
			0.1						0.454873
			0.2						0.438595
			0.3						0.421272
				0.1					0.487403
				0.3					0.488200
				0.5					0.488561
					0.2				0.467321
					0.4				0.467307
					0.6				0.467228
						0.1			0.466524
						0.2			0.466281
						0.3			0.466038
							0.1		0.484342
							0.5		0.502060
							1.0		0.519874
								0.5	0.461302
								1.0	0.454521

8.6 Graphical outcomes

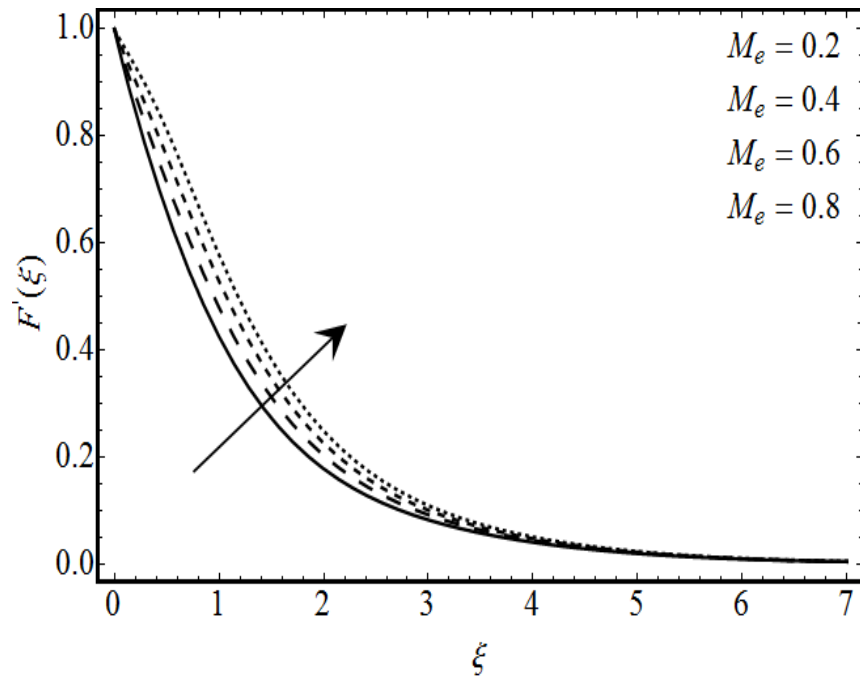


Fig. 8.2: Response of $F'(\xi)$ with M_e .

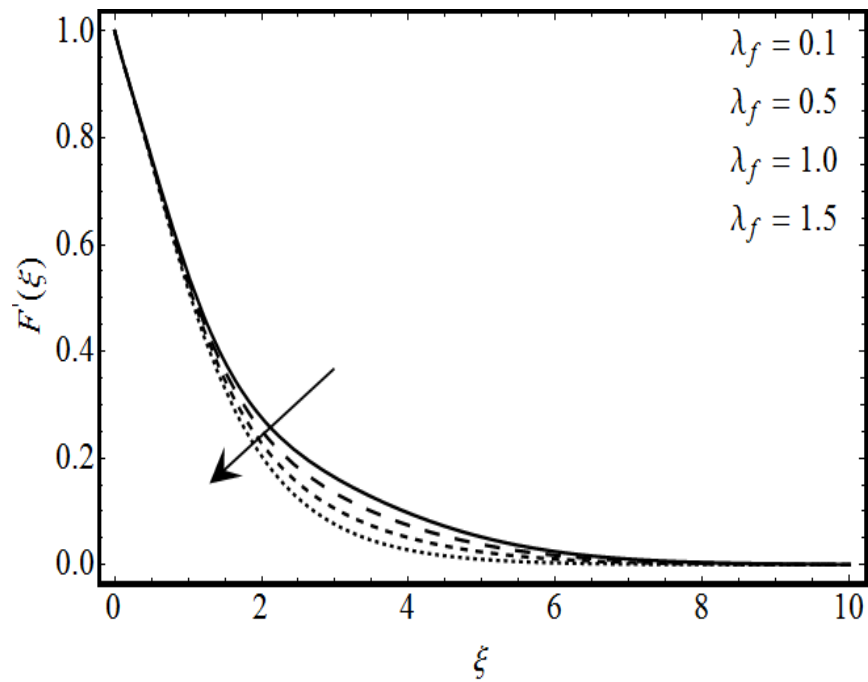


Fig. 8.3: Response of $F'(\xi)$ with λ_f .

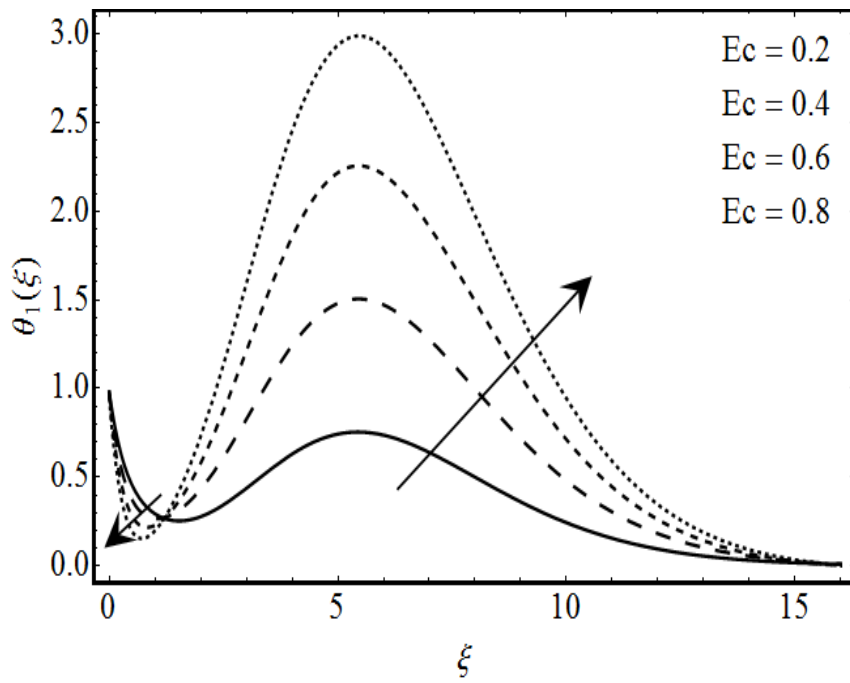


Fig. 8.4: Response of $\theta_1(\xi)$ with Ec .

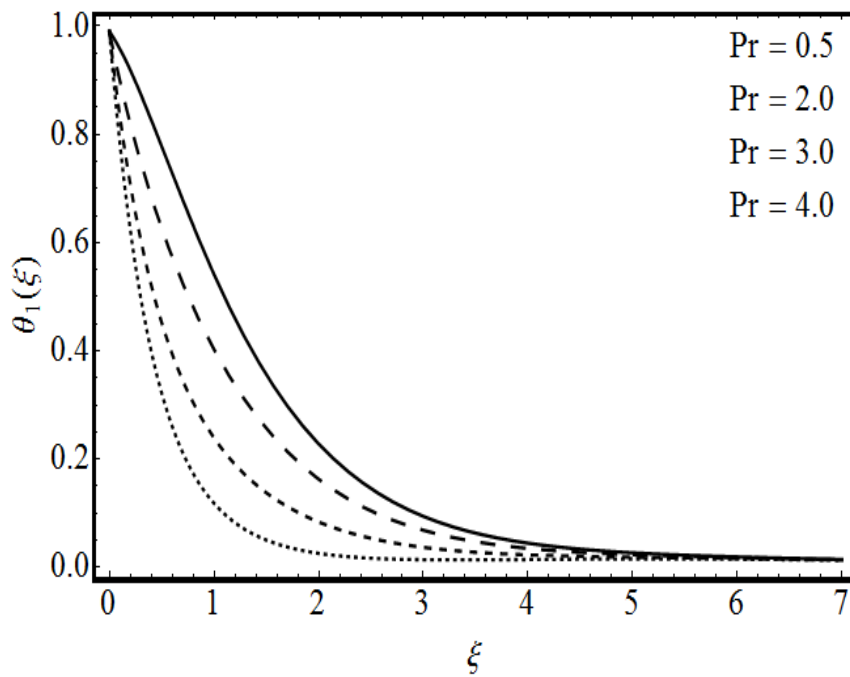


Fig. 8.5: Response of $\theta_1(\xi)$ with Pr .

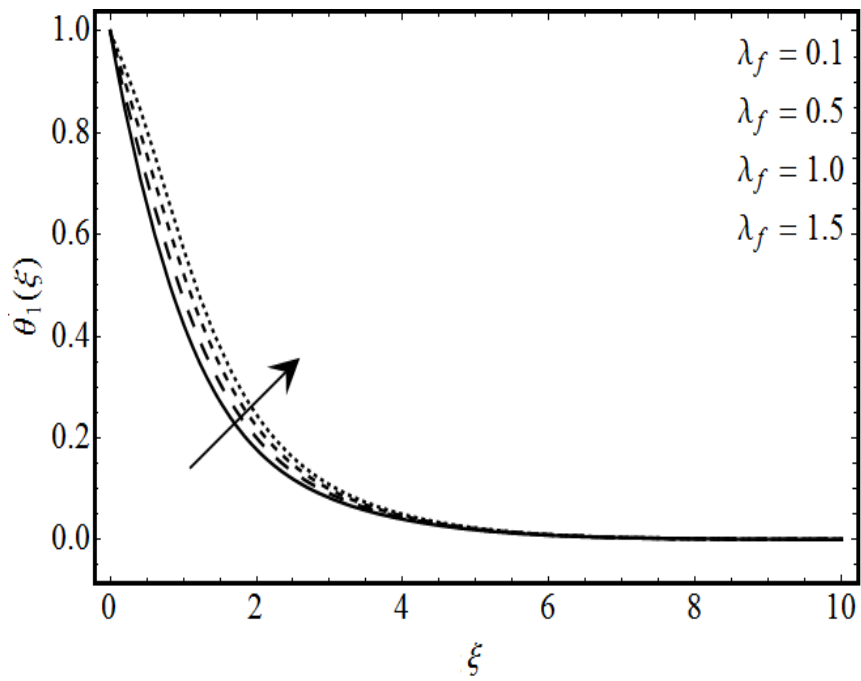


Fig. 8.6: Response of $\theta_1(\xi)$ with λ_f .

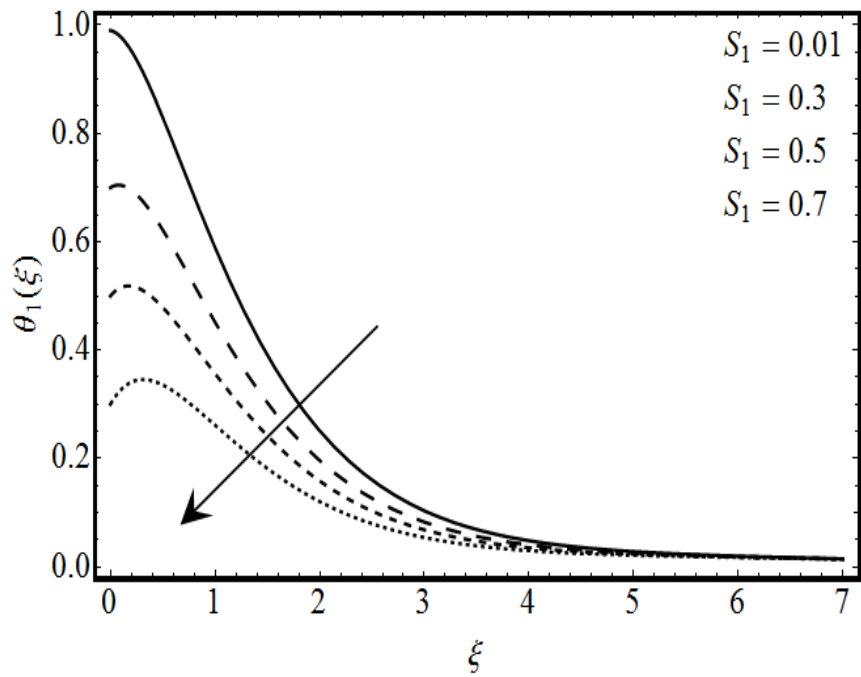


Fig. 8.7: Response of $\theta_1(\xi)$ with λ_f .

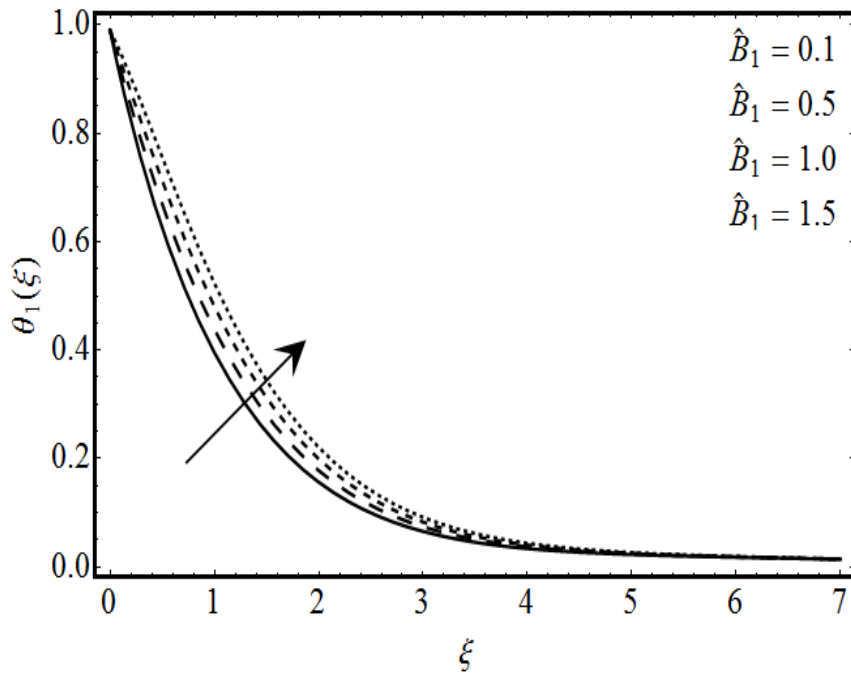


Fig. 8.8: Response of $\theta_1(\xi)$ with \hat{B}_1 .

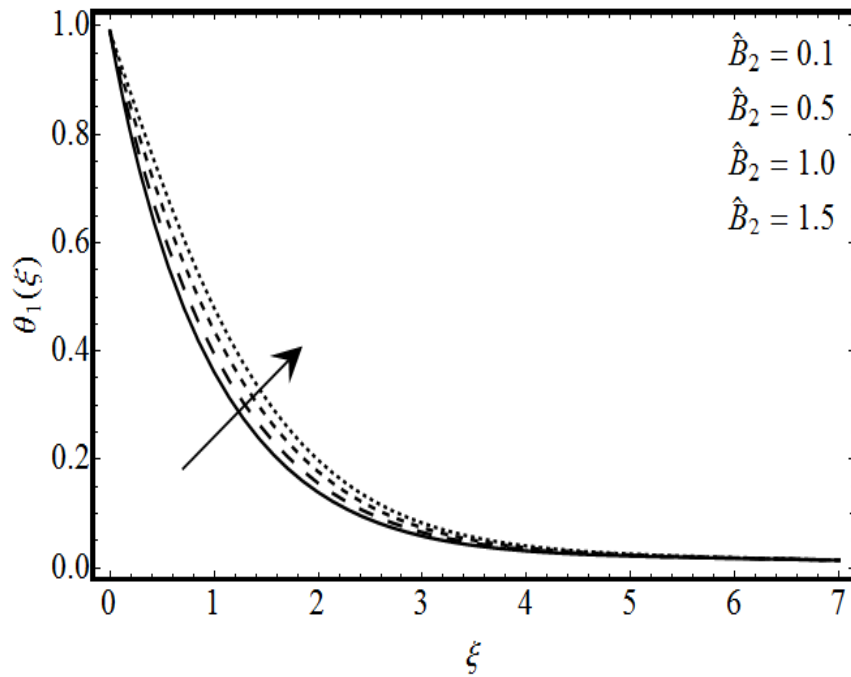


Fig. 8.9: Response of $\theta_1(\xi)$ with \hat{B}_2 .

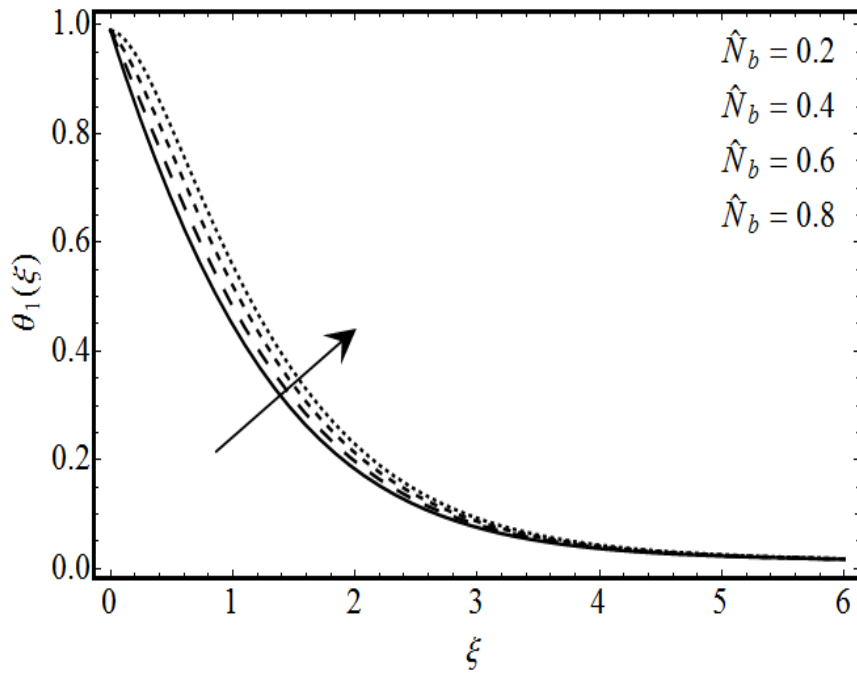


Fig. 8.10: Response of $\theta_1(\xi)$ with \hat{N}_b .

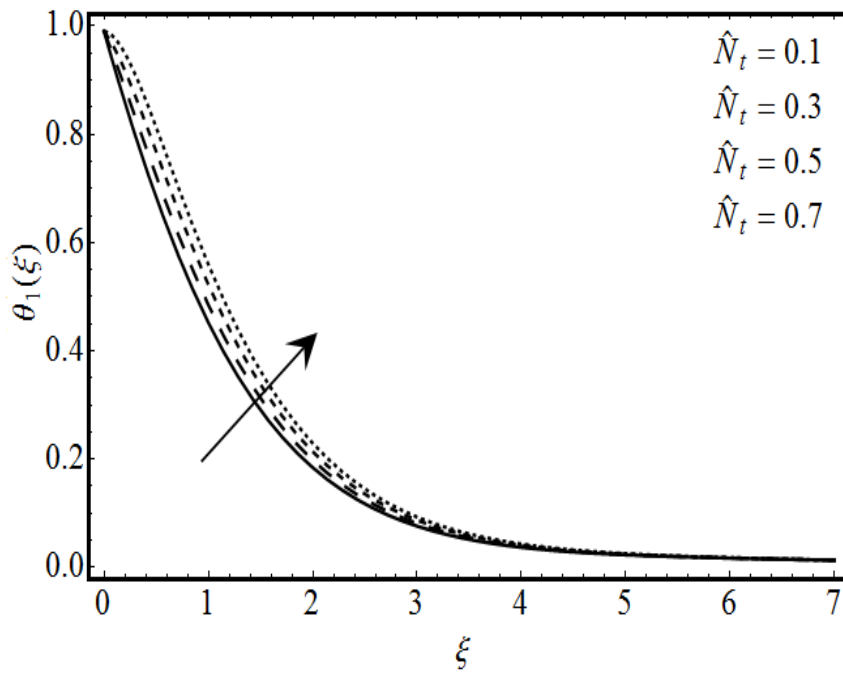


Fig. 8.11: Response of $\theta_1(\xi)$ with \hat{N}_t .

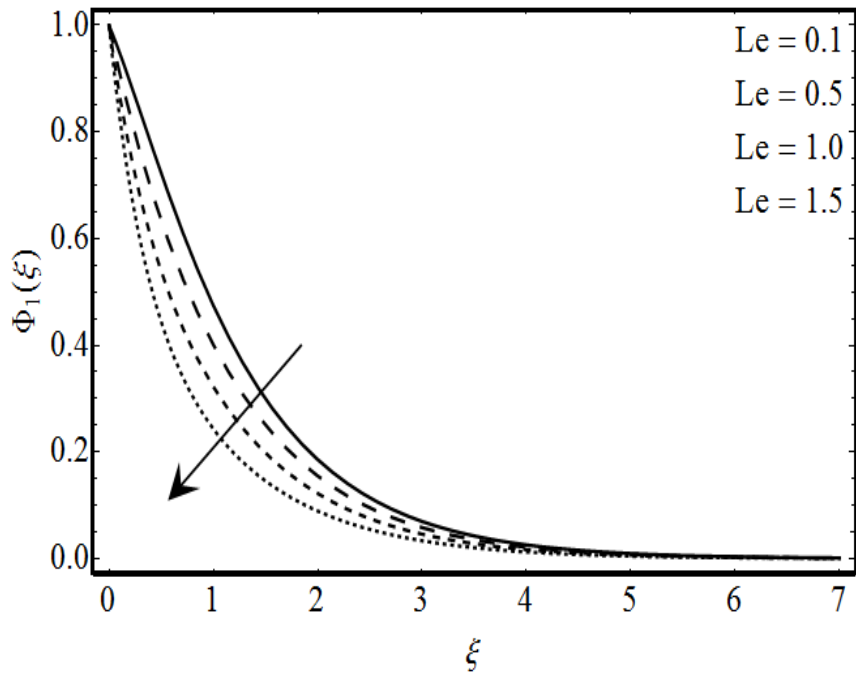


Fig. 8.12: Response of $\Phi_1(\xi)$ with Le .

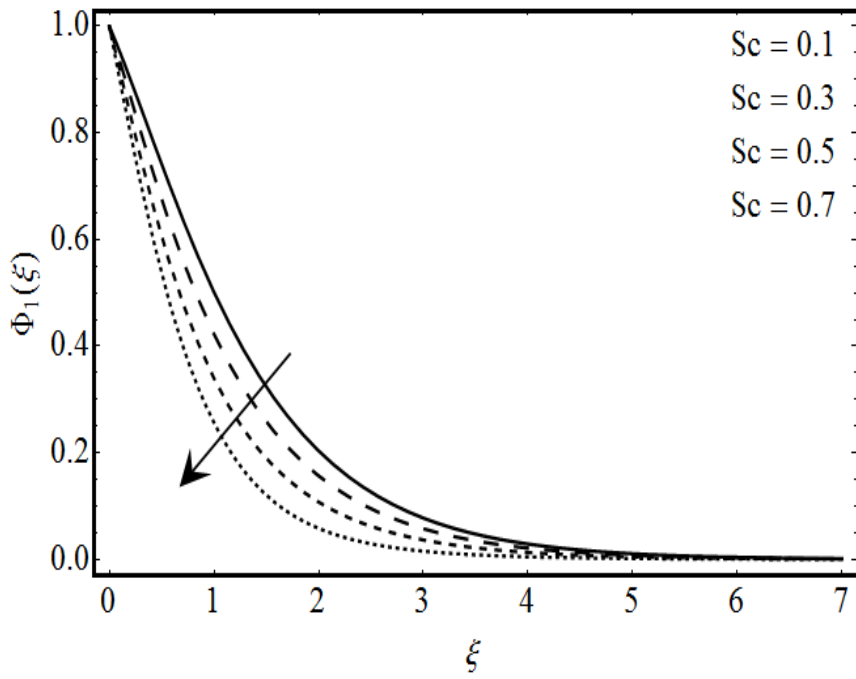


Fig. 8.13: Response of $\Phi_1(\xi)$ with Sc .

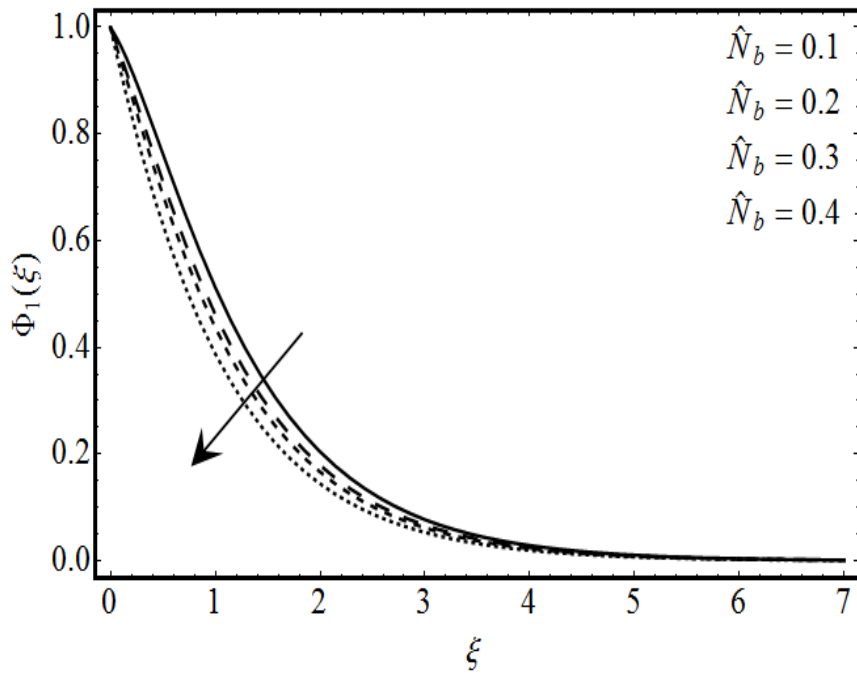


Fig. 8.14: Response of $\Phi_1(\xi)$ with \hat{N}_b .

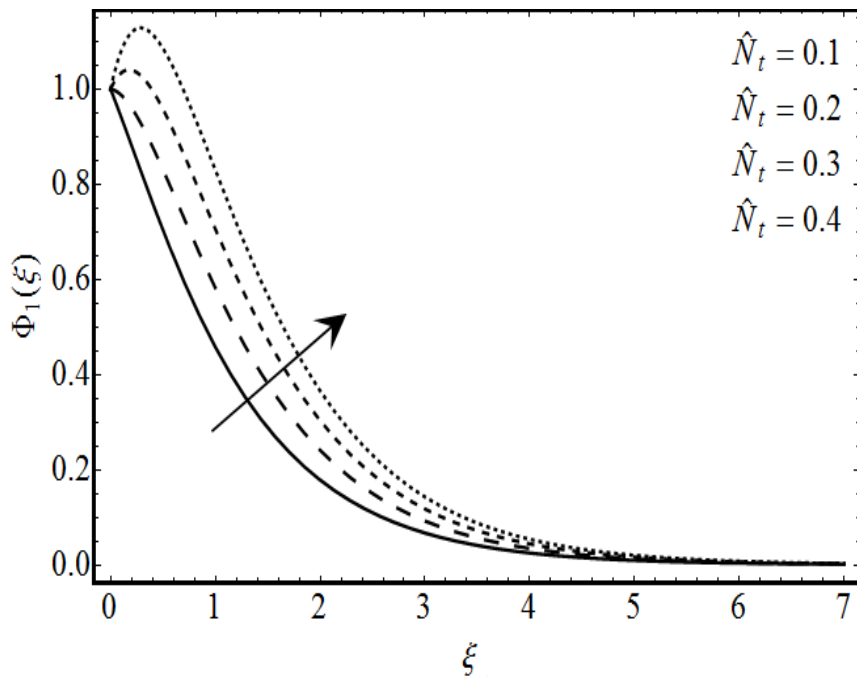


Fig. 8.15: Response of $\Phi_1(\xi)$ with \hat{N}_t .

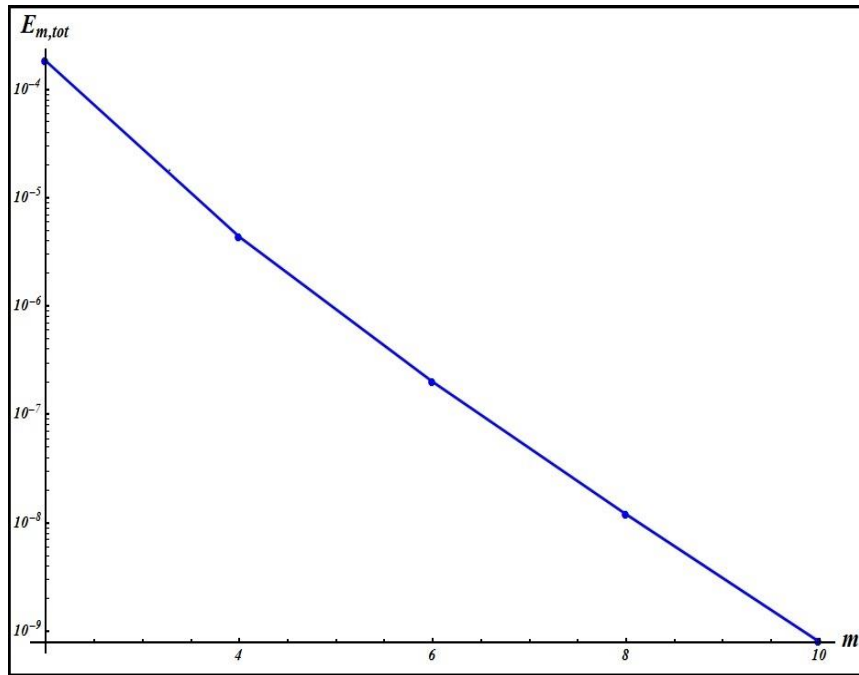


Fig. 8.16: Total averaged squared residual error $E_{m,tot}$ for different m .

8.7 Conclusions

Some of the conclusive remarks for the present work are presented below:

- Temperature $\theta_1(\xi)$ enhances for greater estimations of $\hat{N}_b, \lambda_f, \hat{B}_1, \hat{B}_2$ and \hat{N}_t however it decays for increasing Pr and S_1 .
- Velocity $F'(\xi)$ enhances for M_e while it decays for S_1 and λ_f .
- Larger estimations of \hat{B}_1 and \hat{B}_2 decays temperature $\theta_1(\xi)$ profile.
- Outcomes of \hat{N}_b and \hat{N}_t are reverse on concentration $\Phi_1(\xi)$.

Bibliography

- [1] T. Hayat, M. Zubair, M. Waqas, A. Alsaedi and M. Ayub, Importance of chemical reactions in flow of Walter-B liquid subject to non-Fourier flux modeling. *J. Mol. Liq.* 238 (2017) 229-235.
- [2] M. Waqas, M. I. Khan, T. Hayat and A. Alsaedi, Numerical simulation for magneto Carreau nanofluid model with thermal radiation: A revised model. *Comp. Methods Appl. Mech. Eng.* (2017) doi: 10.1016 / j.cma.2017.06.012.
- [3] T. Hayat, S. Qayyum, M. Imtiaz and A. Alsaedi, Radiative flow due to stretchable rotating disk with variable thickness. *Result Phys.* 7 (2017) 156-165.
- [4] R. Ellahi, M. Hassan and A. Zeeshan, Aggregation effects on water base Al_2O_3 nanofluid over a permeable wedge in mixed convection. *Asia Pacific J. Chem. Eng.* 11 (2016) 179-186.
- [5] M. I. Khan, M. Waqas, T. Hayat, M. I. Khan and A. Alsaedi, Behavior of stratification phenomenon in flow of Maxwell nanomaterial with motile gyrotactic microorganisms in the presence of magnetic field. *Int. J. Mech. Sci.* 131 (2017) 426- 434.
- [6] A. V. Mernone, J. N. Mazumdar and S. K. Lucas, A mathematical study of peristaltic transport of a Casson fluid. *Math. Comp. Model.* 35 (2002) 895-912.
- [7] M. Mustafa, Cattaneo-Christov heat flux model for rotating flow and heat transfer of upper-convected Maxwell fluid. *AIP Adv.* 5 (4) (2015) 047109.

- [8] T. Hayat, M. Mustafa, S. A. Shehzad and S. Obaidat, Melting heat transfer in the stagnation-point flow of an upper-convected Maxwell (UCM) fluid past a stretching sheet, *Int. J. Numer. Methods Fluid.* 68 (2) (2011) 233e243.
- [9] M. Ijaz and M. Ayub, Nonlinear convective stratified flow of Maxwell nanofluid with activation energy. *Heliyon* doi: 10.1016/j.heliyon.2019. e01121.
- [10] T. Hayat, S. A. Shehzad, H. H. Al-Sulami and S. Asghar, Influence of thermal stratification on the radiative flow of Maxwell fluid, *J. Braz. Soc. Mech. Sci. Eng.* 35 (4) (2013) 381e389.
- [11] M. Ijaz, M. Ayub, M. Zubair and A. Riaz, On stratified flow of ferromagnetic nanofluid with heat generation/absorption. *Phys. Scr.* doi.org/10. 1088/1402-4896/aaf6df
- [12] T. Hayat, S.A. Shehzad, M. Qasim and S. Obaidat, Radiative flow of Jeffrey fluid in a porous medium with power law heat flux and heat source. *Nucl. Eng. Des.* 243 (2012) 15 -19.
- [13] T. Hayat, S. Qayyum, M. Imtiaz and A. Alsaedi, Impact of Cattaneo-Christov heat flux in Jeffrey fluid flow with homogeneous-heterogeneous reactions. *PLoS One* 11(2016) 0148662.
- [14] T. Hayat, A. Alsaedi and S. A. Shehzad, Three-dimensional flow of Jeffrey fluid with convective surface boundary conditions. *Int. J. Heat Mass Transf.* 55 (2012) 3971–3976.
- [15] T. Hayat, M. I. Khan, M. Farooq and A. Alsaedi, Thermally stratified stretching flow with Cattaneo-Christov heat flux. *Int. J. Heat Mass Transf.* 106 (2017) 289 – 294.

- [16] T. Hussain, S. A. Shehzad, T. Hayat and A. Alsaedi, Radiative hydromagnetic flow of Jeffrey nanofluid by an exponentially stretching sheet. PLoS One 9 (2014) 103719.
- [17] T. Hayat, S. Qayyum, S. A. Shehzad and A. Alsaedi, Simultaneous effects of heat generation/absorption and thermal radiation in magneto-hydrodynamics (MHD) flow of Maxwell nanofluid towards a stretched surface. Res. Phys.7 (2017) 562 – 573.
- [18] D. Tripathi, N. Ali, T. Hayat, M. K. Chaube and A. A. Hendi, Peristaltic flow of MHD Jeffrey fluid through finite length cylindrical tube. Appl. Math Mech. 32 (2011) 1231-1244.
- [19] N. Ramachandran, T. S. Chen and B. F. Armaly, Mixed convection in stagnation flows adjacent to vertical surfaces. J. Heat Mass Transf. 110(2) (1988) 373-377.
- [20] T. Hayat, M. Ijaz, S. Qayyum, M. Ayub and A. Alsaedi, Mixed convective stagnation point flow of nanofluid with Darcy-Fochheimer relation and partial slip. Results Phys. 9 (2018) 771-778.
- [21] T. Hayat, M. Waqas and S. A. Shehzad, Mixed convection flow of viscoelastic nanofluid by a cylinder with variable thermal conductivity and heat source/sink. Int. J. Numer. Methods Heat Fluid Flow. 26(1) (2016) 214-234.
- [22] S. Mukhopadhyay, Effect of thermal radiation on unsteady mixed convection flow and heat transfer over a porous stretching surface in porous medium. Int. J. Heat Mass Transf. 52 (2009) 3261-3265.
- [23] J. B. J. Fourier, Theorie analytique de la chaleur, Paris, (1822).

- [24] C. Cattaneo, Some aspects of diffusion theory, *Atti Semin. Mat. Fis Univ. Modena Reggio Emilia.* 3 (1948) 83e101.
- [25] C.I. Christov, On frame indifferent formulation of the Maxwell-Cattaneo model of finite speed heat conduction, *Mech. Res. Commun.* 36 (4) (2009) 481e486.
- [26] M. Ciarletta and B. Straughan, Uniqueness and structural stability for the Cattaneo-Christov equations, *Mech. Res. Commun.* 37 (2010) 445-447.
- [27] S. Han, L. Zheng, C. Li and X. Zhang, Coupled flow and heat transfer in viscoelastic fluid with Cattaneo-Christov heat flux model, *Appl. Math. Lett.* 38 (2014) 87-93.
- [28] T. Hayat, S. Qayyum, S. Shehzad, A. Sabir and A. Alsaedi, Cattaneo-Christov double-diffusion model for flow of Jeffrey fluid. *J. Braz. Soc. Mech. Sci. Eng.* 39 (12) (2017) 4965e4971.
- [29] U. Ali, K. U. Rehman and M. Y. Malik, The influence of MHD and heat generation/absorption in a Newtonian flow field manifested with Cattaneo-Christov heat flux model. *Phys. Scr.* (2019) <https://doi.org/10.1088/1402-4896/ab11ff>.
- [30] M. Khan, T. Salahuddin and M. Y. Malik, Impact of enhancing diffusion on Carreau–Yasuda fluid flow over a rotating disk with slip conditions. *J. Braz. Soc. Mech. Sci. Eng.* 41(2019)78.<https://doi.org/10.1007/s40430-018-1492-y>.
- [31] A Hussain, S Ameer, F Javed and M. Y. Malik, Rheological analysis on non-Newtonian wire coating. *J. Braz. Soc. Mech. Sci. Eng.* 41(2019) 115. <https://doi.org/10.1007/s40430-019-1575-4>.

- [32] A. Tahmasebi, M. Mahdavi and M. Ghalambaz, Local thermal nonequilibrium conjugate natural convection heat transfer of nanofluids in a cavity partially filled with porous media using Buongiorno's model. *Numeric. Heat transf. Appl.* 73(2018) 254-276.
- [33] S. Nadeem and N. Muhammad, Impact of stratification and Cattaneo-Christov heat flux in the flow saturated with porous medium. *J. Mol. Liq.* 224 (2016) 423-430.
- [34] M. Bibi, M. Y. Malik and A. Zeeshan, Numerical analysis of unsteady magneto-biphase Williamson fluid flow with time dependent magnetic field. *Commun. Theor. Phys.* 71(2019)143–151.
- [35] H. I. Andersson, O. A. Valnes, Flow of a heated ferrofluid over a stretching sheet in the presence of a magnetic dipole. *Acta Mech.* 128 (1998) 39–47.
- [36] L. S. R. Titus, A. Abraham, Heat transfer in ferrofluid flow over a stretching sheet with radiation. *Int. J. Eng. Res. Tech.* 3 (2014) 2278 0181.
- [37] J. L. Neuringer and R. E. Rosensweig, Ferrohydrodynamics. *Phys. Fluids* 7 (1964) 1927-1937.
- [38] T. Yasmeen, T. Hayat, M. I. Khan, M. Imtiaz and A. Alseadi, Ferrofluid flow by a stretched surface in the presence of magnetic dipole and homogeneous heterogeneous reactions. *J. Mol. Liq.* 223 (2016) 1000-1005.
- [39] A. Majeed, A. Zeeshan, S. Z. Alamri and R. Ellahi, Heat transfer analysis in ferromagnetic viscoelastic fluid flow over a stretching sheet with suction. *Neural Comput. Appl.* 30 (6) (2018) doi:10.1007/s00521-016-2830-6.

- [40] E. D. Vtulkina and E. A. Elfimova, Thermodynamic and magnetic properties of ferrofluids in external uniform magnetic field. *J. Magn. Magn. Mater.* 431 (2017) 218- 221.
- [41] M. Zubair, M. Ijaz, T. Abbas and A. Riaz, Analysis of modified Fourier law in flow of ferromagnetic Powell-Eyring fluid considering two equal magnetic dipoles. *Can. J. Phys.* doi: 10.1139/cjp-2018-0586
- [42] T. Hayat, S. Ahmad, M. I. Khan and A. Alsaedi, Exploring magnetic dipole contribution on radiative flow of ferromagnetic Williamson fluid. *Res. Phy.* 8 (2018) 545–551.
- [43] M. Ijaz and M. Ayub, Simulation of magnetic dipole and dual stratification in radiative flow of ferromagnetic Maxwell fluid, *Heliyon* 5 (2019) e01465.doi: 10.1016/j.heliyon.2019. e01465.
- [44] M. Tencer, J. S. Moss and T. Zapach, Arrhenius average temperature: the effective temperature for non-fatigue wearout and long term reliability in variable thermal conditions and climates. *IEEE T. COMPON. PACK. T.* 27 (3) (2004) 602-607.
- [45] C. Truesdell, *Sulle basi della thermomeccanica*. Accademia Nazionale del Lincei, *Rendiconti della Classe di Scienze Fisiche.* 22(8) (1957) 33-38.
- [46] C. Truesdell, *Sulle basi della thermomeccanica*, Accademia nazionale del lincei, *rendiconti della classe di scienze fisiche*, 22(8) (1957) 158-166.
- [47] N. Mills, Incompressible mixtures of newtonian fluids. *Int. J. Eng. Sci.* 4(2) (1966) 97-112.

- [48] C. E. Beevers and R. E. Craine, On the determination of response functions for a binary mixture of incompressible newtonian fluids. *Int. J. Eng. Sci.* 20(6) (1982) 737-745.
- [49] A. R. Bestman, Natural convection boundary layer with suction and mass transfer in a porous medium. *Int. J. Energy Res.* 14 (4) (1990) 389e396.
- [50] R. Kandasamy, K. Periasamy and K. K. S. Prabhu, Effects of chemical reaction, heat and mass transfer along a wedge with heat source and concentration in the presence of suction or injection. *Int. J. Heat Mass Tran.* 48 (2005) 1388e1394.
- [51] A. R. Bestman, Radiative heat transfer to flow of a combustible mixture in a vertical pipe. *Int. J. Energy Res.* 15(3) (1991) 179-184.
- [52] E. M. Abo-Eldahab, M. A. El-Aziz, Blowing/suction effect on hydromagnetic heat transfer by mixed convection from an inclined continuously stretching surface with internal heat generation/absorption. *Int. J. Therm. Sci.* 43 (2004) 709e719.
- [53] M. S. Abel, P.G. Siddheshwar, M. M. Nandeppanawar, Heat transfer in a viscoelastic boundary layer flow over a stretching sheet with viscous dissipation and non-uniform heat source. *Int. J. Heat Mass Transf.* 50 (2007) 960e966.
- [54] M. S. Abel, N. Mahesha, Heat transfer in MHD viscoelastic fluid flow over a stretching sheet with variable thermal conductivity, non-uniform heat source and radiation, *Appl. Math. Model.* 32 (10) (2008) 1965e1983.
- [55] K.A. Kumar, J. V. R. Reddy, V. Sugunamma and N. Sandeep, Magnetohydrodynamic Cattaneo-Christov flow past a cone and a wedge with variable heat source/sink. *Alex. Eng. J.* 57 (2018) 435e443.

- [56] Dulal Pal and H. Mondal, Effect of variable viscosity on MHD non-Darcy mixed convective heat transfer over a stretching sheet embedded in a porous medium with non-uniform heat source/sink. *Commun. Nonlinear Sci. Numer. Simulat.* 15 (2010) 1553–1564.
- [57] G. Kumaran and N. Sandeep, Thermophoresis and Brownian moment effects on parabolic flow of MHD Casson and Williamson fluids with cross diffusion. *J. Mol. Liq.* 233 (2017) 262e269.
- [58] K. A. Kumar, J. V. R. Reddy, V. Sugunamma and N. Sandeep, MHD flow of chemically reacting Williamson fluid over a curved/flat surface with variable heat source/sink. *Int. J. Fluid Mech. Res.* 46 (2) (2018) 1e19.
- [59] K.A. Kumar, V. Sugunamma, N. Sandeep, J. V. R. Reddy, Impact of Brownian motion and thermophoresis on bioconvective flow of nanoliquids past a variable thickness surface with slip effects. *Heat Transf. Res.* (2018), 025939.
- [60] F. Hussain, R. Ellahi, A. Zeeshan, Mathematical models of electro magnetohydrodynamic multiphase flows synthesis with nano-sized Hafnium particles. *Appl. Sci.* 8 (2) (2018) 8020275.
- [61] E. Magyari and A. Pantokratoras, Note on the effect of thermal radiation in the linearized Rosseland approximation on the heat transfer characteristics of various boundary layer flows. *Int. Comm. Heat Mass Transf.* 38 (2011) 554-556.
- [62] A. Pantokratoras, Natural convection along a vertical isothermal plate with linear and nonlinear Rosseland thermal radiation. *Int. J. Therm. Sci.* 84 (2014) 151-157.
- [63] R. Cortell, Fluid flow and radiative nonlinear heat transfer over a stretching sheet. *J. King Saud Univ. Sci.* 26 (2014) 161-167.

- [64] A. Mushtaq, M. Mustafa, T. Hayat and A. AlSaedi, Nonlinear radiative heat transfer in the flow of nanofluid due to solar energy: A numerical study. *J. Taiwan Inst. Chem. Eng.* 45 (2014) 1176–1183.
- [65] M. Monica and J. Sucharitha, Effects of nonlinear thermal radiation, non-uniform heat source/sink on MHD stagnation point flow of a Casson fluid over a nonlinear stretching sheet with slip conditions. *J. Nanofluids* 6 (2017) 692–701.
- [66] B. Mahanthesh, B. J. Giressha and R. S. R. Gorla, Nonlinear radiative heat transfer in MHD three-dimensional flow of water based nanofluid over a non-linearly stretching sheet with convective boundary condition. *J. Nigerian Math Soc.* 35 (2016) 178–198.
- [67] M. Bhatti, A. Zeeshan, and R. Ellahi, Study of heat transfer with nonlinear thermal radiation on sinusoidal motion of magnetic solid particles in a dusty fluid. *J. Theor. Appl. Mech.* 46 (2016) 75–94.
- [68] N. S. Akbar, S. Nadeem, R. Ul Haq and Z. H. Khan, Radiation effects on MHD stagnation point flow of nanofluid towards a stretching surface with convective boundary condition. *Chin. J. Aeronaut.* 26 (2013) 1389–1397.
- [69] S. K. Parida, S. Panda and B. R. Rout, MHD boundary layer slip flow and radiative nonlinear heat transfer over a flat plate with variable fluid properties and thermophoresis. *Alexandria Eng. J.* 54 (2015) 941-953.
- [70] B. Straughan and F. Franchi, Benard convection and the Cattaneo law of heat conduction. *Proceedings Royal Soci. Edinburgh A.* 96 (1984) 175-178.
- [71] A. Fick, Ueber diffusion, *Annalen der Physik und Chemie.* 170 (1) (1855) 59e86.

- [72] S. J. Liao, *Beyond Perturbation: Introduction to Homotopy Analysis Method*. Chapman and Hall/CRC Press, Boca Raton, (2003).
- [73] M.Y. Malik, A. Hussain, T. Salahuddin and M. Awais, Numerical Solution of MHD Sisko fluid over a stretching cylinder and heat transfer analysis. *Int. J. Numer. Methods Heat Fluid Flow*. 26(6) (2016) 1787-1801.
- [74] R. J. Tiwari, M. K. Das, Heat transfer augmentation in a two-sided lid-driven differentially heated square cavity utilizing nanofluids, *Int. J. Heat Mass Transf.* 50 (2007) 2002–2018.
- [75] T. Mahmood and J. H. Merkin, Similarity solutions in axisymmetric mixed convection boundary-layer flow. *J. Eng. Math.* 22 (1988) 73–92.
- [76] H. F. Oztop and E. Abu-Nada, Numerical study of natural convection in partially heated rectangular enclosures filled with nanofluids. *Int. J. Heat Fluid Flow*. 29 (2008) 1326–1336.
- [77] S. Dinarvand, R. Hosseini and I. Pop, Axisymmetric mixed convective stagnation-point flow of a nanofluid over a vertical permeable cylinder by Tiwari-Das nanofluid model. *Powd. Tech.* 311 (2017) 147–156.
- [78] T. Hayat, A. Aziz, T. Muhammad and A. Alsaedi, Model and comparative study for flow of viscoelastic nanofluids with Cattaneo-Christov double diffusion. *PLoS One* 12 (2017) e0168824.
- [79] F. Mabood, S. M. Ibrahim, M. M. Rashidi, M.S. Shadloo and G. Lorenzini, Non-uniform heat source/sink and Soret effects on MHD non-Darcian convective flow past a stretching sheet in a micropolar fluid with radiation. *Int. J. Heat Mass Transf.* 93 (2016) 674e682.

- [80] T. Hayat, M. Farooq, A. Alsaedi and F. Al-Solamy, Impact of Cattaneo-Christov heat flux in the flow over a stretching sheet with variable thickness. *AIP Adv.* 5 (2015) 087159.
- [81] S. Qayyum, T. Hayat, A. Alsaedi and B. Ahmad, MHD nonlinear convective flow of thixotropic nanofluid with chemical reaction and Newtonian heat and mass conditions. *Results Phys.* 7 (2017) 2124-2133.
- [82] R. Cortell, Viscous flow and heat transfer over a nonlinearly stretching sheet. *Appl. Math. Comp.* 184 (2007) 864-873.
- [83] A. M. Megahed, Variable fluid properties and variable heat flux effects on the flow and heat transfer in a non-Newtonian Maxwell fluid over an unsteady stretching sheet with slip velocity. *Chin. Phys. B.* 22 (2013) 094701. doi: 10.1088/1674-1056/22/9/094701.
- [84] M. S. Abel, J. V. Tawade and M. M. Nandeppanavar, MHD flow and heat transfer for the upper-convected Maxwell fluid over a stretching sheet. *Meccanica* 47 (2012) 385-393.
- [85] R. Malik and M. Khan, Numerical study of homogeneous-heterogeneous reactions in Sisko fluid flow past a stretching cylinder. *Results Phys.* (2018) 64-70.
- [86] M. A. Chaudhary and J. H. Merkin, A simple isothermal model for homogeneous-heterogeneous reactions in boundary-layer flow in Equal diffusivities. *Fluid Dyn. Res.* 16 (3) (1995)11–33.

- [87] M. A. Chaudhary and J. H. Merkin, Homogeneous-heterogeneous reactions in boundary-layer flow: effects of loss of reactant. *Math Comput. Model.* 24(3) (1996) 21-28.
- [88] S. Nadeem, M.Y. Malik and Nadeem Abbas, Heat transfer of three dimensional micropolar fluids on Riga plate. *Can. J. Phys.* (2019). <https://doi.org/10.1139/cjp-2018-0973>.
- [89] S.A.M. Haddad, Thermal instability in Brinkman porous media with Cattaneo-Christov heat flux. *Int. J. Heat Mass Transf.* 68 (2014) 659-668.
- [90] T. Hayat, M. I. Khan, M. Farooq, A. Alsaedi and M. I. Khan, Thermally stratified stretching flow with Cattaneo-Christov heat flux. *Int. J. Heat Mass Transf.* 106 (2017) 289–294.
- [91] M. Turkyilmazoglu, Determination of the correct range of physical parameters in the approximate analytical solutions of nonlinear equations using the adomian decomposition method. *Mediterranean J. Math.* 13 (6) (2016) 4019-4037.
- [92] N. Acharyaa, K. Das and P.K. Kundua, Cattaneo-Christov intensity of magnetised upper-convected Maxwell nanofluid flow over an inclined stretching sheet: A generalised Fourier and Fick's perspective. *Int. J. Mech. Sci.* 130 (2017) 167-173.
- [93] W. A. Khan and I. Pop, Boundary-layer flow of a nanofluid past a stretching sheet. *Int. J. Heat Mass Transf.* 53 (2010) 2477-2483.
- [94] K. L. Hsiao, Stagnation electrical MHD nanofluid Mixed convection with slip boundary on a Stretching Sheet. *Appl. Therm. Eng.* 98 (2016) 850-861.

- [95] S.A. Shehzad, T. Hayat and A. Alsaedi, MHD flow of Jeffrey nanofluid with convective boundary conditions. *J. Braz. Soci. Mech. Sci. Eng.* 37 (2015) 873-883.
- [96] M. Farooq, N. Gull, A. Alsaedi, T. Hayat, MHD flow of a Jeffrey fluid with Newtonian heating. *J. Mech.* 33 (03) (2015) 1–11.
- [97] M. Ijaz and M. Ayub, Activation energy and dual stratification effects for Walter-B fluid flow in view of Cattaneo-Christov double diffusion. *Heliyon.* 5 (2019) e01815. doi.org/10.1016/j.heliyon.2019.e01815.
- [98] K. Mehmood, S. Hussain and M. Sagheer, Mixed convection flow with nonuniform heat source/sink in a doubly stratified magnetonanofluid. *AIP Adv.* 6 (2016) 065126.
- [99] R. Ellahi, M. M. Bhatti and I. Pop, Effects of hall and ion slip on MHD peristaltic flow of Jeffrey fluid in a non-uniform rectangular duct. *Int. J. Numer. Methods Heat Fluid Flow.* 26 (2016) 1802 - 1820.
- [100] S. U. Rahman, R. Ellahi, S. Nadeem and Q. M. Z. Zia, Simultaneous effects of nanoparticles and slip on Jeffrey fluid through tapered artery with mild stenosis. *J. Mol. Liqs.* 218 (2016) 484-493.
- [101] K. Ahmad, Z. Hanouf and A. Ishak, Mixed convection Jeffrey fluid flow over an exponentially stretching sheet with magnetohydrodynamic effect. *AIP Adv.* 6 (2016) 035024.
- [102] M. Ijaz, M. Ayub and H. Khan, Entropy generation and activation energy mechanism in nonlinear radiative flow of Sisko nanofluid: rotating disk. *Heliyon.* doi.org/10.1016/j.heliyon.2019.e01863.

- [103]F. M. Abbasi, S. A. Shehzad, T. Hayat and M. S. Althuthali, Mixed convection flow of Jeffrey nanofluid with thermal radiation and double stratification. *J. Hydrody.* 28(5) (2016) 840-849.
- [104]W. D. Beard, K. Walters, Elasto-viscous boundary layer flow. *Proc. Camb. Phil. Soc.* 60 (1964) 667.
- [105]T. Hayat, S. Asad, M. Mustafa, H. H. Alsulami, Heat transfer analysis in the flow of Walters' B fluid with a convective boundary condition. *Chin. Phys. B* 23(2014) 084701.
- [106]S. Nadeem, R. Mehmood, S. S. Motsa, Numerical investigation on MHD oblique flow of Walter's B type nano fluid over a convective surface. *Int. J. Therm. Sci.* 92 (2015) 162–172.
- [107]F. Ali, M. Saquib, I. Khan, N. A. Sheikh, Application of Caputo-Fabrizio derivatives to MHD free convection flow of generalized Walters'-B fluid model. *Eur. Phys. J. Plus.* 131 (2016). doi:10.1140/epjp/i2016-16377-x
- [108]J. Sui, L. Zheng and X. Zhang, Boundary layer heat and mass transfer with Cattaneo-Christov double-diffusion in upper-convected Maxwell nanofluid past a stretching sheet with slip velocity. *Int. J. Therm. Sci.* 104(2016) 461-468.
- [109]K. Mehmood, S. Hussain, and M. Sagheer, Mixed convection flow with non-uniform heat source/sink in a doubly stratified magnetonanofluid. *AIP Adv.* 6, 065126 (2016). doi: 10.1063/1.4955157.
- [110]R. Ellahi, M. Hassan and A. Zeeshan, Shape effects of nanosize particles in Cu – H₂O nanofluid on entropy generation. *Int. J. Heat Mass Transf.* 81 (2015) 449-456.

- [111]M. Turkyilmazoglu, Some issues on HPM and HAM methods: a convergence scheme. *Math. Comput. Model.* 53 (2011) 1929-1936.
- [112]S. Nadeem, R. U. Haq, N. S. Akbar and Z. H. Khan, MHD three-dimensional Casson fluid flow past a porous linearly stretch sheet. *Alex. Eng. J.* 52(4) (2013) 577-582.
- [113]R. K. Dash, K. N. Mehta and G. Jayaraman, Effect of yield stress on the flow of a Casson fluid in a homogeneous porous medium bounded by a circular tube. *Appl. Sci. Res.* 57(2) (1996) 133-149.
- [114]C. S. K. Raju, M. M. Hoque and T. Sivasankar, Radiative flow of Casson fluid over a moving wedge filled with gyrotactic microorganisms. *Adv. Powder Tech.* 28(2) (2017) 575-583.
- [115]M. Y. Malik, S. Bilal and M. Bibi, Numerical analysis for MHD thermal and solutal stratified stagnation point flow of Powell-Eyring fluid induced by cylindrical surface with dual convection and heat generation effects. *Results Phys.* 7 (2017) 482-492.
- [116]K. U. Rehman, A. Qaiser, M. Y. Malik and U. Ali, Numerical communication for MHD thermally stratified dual convection flow of Casson fluid yields by stretching cylinder. *Chin. J. Phys.* 55(4) (2017)1605-1614.
- [117]S. Nadeem, R. U. Haq and C. Lee, MHD flow of a Casson fluid over an exponentially shrinking sheet. *Sci. Iranic.* 19 (2012) 1550-1553.
- [118]S. Mukhopadhyay, MHD boundary layer flow and heat transfer over an exponentially stretching sheet embedded in a thermally stratified medium. *Alexandria Eng. J.* 52(3) (2013) 259-265.

- [119]B. Bidin, R. Nazar, Numerical solution of the boundary layer flow over an exponentially stretching sheet with thermal radiation. *Eur. J. Sci. Res.*33(4) (2009) 710-717.
- [120]M. S. Abel, M. M. Nandeppanavar, Heat transfer in MHD viscoelastic boundary layer flow over a stretching sheet with non-uniform heat source/sink. *Commun. Nonlinear Sci. Numer. Simulat.* 14 (2009) 2120-2131.
- [121]N. Muhammad, S. Nadeem, R. U. Haq, Heat transport phenomenon in the ferromagnetic fluid over a stretching sheet with thermal stratification. *Results Phys.* 7 (2017) 854-861.
- [122]T. Hayat, S. Ahmad, M. I. Khan and A. Alsaedi, Simulation of ferromagnetic nanomaterial flow of Maxwell fluid. *Results Phys.* 8 (2018) 34-40.